Contaminant reduction by iron oxide nanoparticles: Environmental variables and evolving reactivity

A DISSERTATION
SUBMITTED TO THE FACULTY OF
UNIVERSITY OF MINNESOTA
BY

Jennifer Helen Strehlau

IN PARTIAL FULFILLMENT OF THE REQUIREMENTS
FOR THE DEGREE OF
DOCTOR OF PHILOSOPHY

R. Lee Penn, William A. Arnold

May, 2016

Acknowledgments

This dissertation is far more than words summarizing my years spent in graduate school. It represents the unending support from mentors, colleagues, family, and friends. A great number of people have contributed to its production.

First and foremost, I would like to thank my advisors Lee Penn and Bill Arnold for providing invaluable guidance and support over the years. Your geochemical studies provided the perfect research setting for me and I am truly excited about the science we have produced together. I would also like to thank collaborators Josh Feinberg and Brandy Toner, who have provided me more opportunities to explore research from a unique and interdisciplinary perspective. Lindsay Hegner and Jonathan Schultz were outstanding undergraduate students and I am grateful to have been given the opportunity to advise them. Their work has provided vital contributions to these chapters and I look forward to seeing their bright futures.

Professors Michelle Driessen and Barb Nielsen have been invaluable mentors during my transition from graduate student to a career in academia. Their commitment to fruitful learning and inspirational teaching is contagious. Additionally, the faculty at University of Wisconsin – River Falls have all contributed to my achievements. During my four years there, I was continuously motivated to achieve success and encouraged to attend graduate school, and for that, I am forever grateful.

My daily workday was never dull with an amazing group of fellow labmates, always making our office and lab space a welcoming and good-humored environment. I couldn't imagine a better group to spend the majority of my graduate school time with. I

am also indebted to the researchers at the Institute for Rock Magnetism for providing the resources for me to study the awesome field of magnetism, which has been a fun and unique addition to this thesis. Specifically, to my partner-in-crime and confidant, Becky Strauss, thanks for sticking it out with me over the years. Our initial collaboration turned into a valuable friendship. The hard days would have been harder if not for your open ears and our mutual interest in coffee/tea and good food.

But most importantly, a huge thank you to my family and friends for all of your love and patience over the years. My husband has graciously been there day in and day out, supporting me through this journey. To my mom and dad, thank you for teaching me *to want* to be the best person I can be, instead of just teaching me how. Because of you, I always have a reason to pursue my dreams. To my brother, whose humor even in the stickiest of situations never fails to make me laugh, you're awesome. And Joe, Carla, Tyler, and Haley, thank you for accepting me into your life like I was your own daughter and sister, your love is unfailing and I'm grateful to be a part of your family.

Without all of you, this accomplishment would have been incredibly difficult. I will forever be appreciative of that.

Finally, a whimsical thank you to J. K. Rowling, who might read this thesis when I finally stumble across a bowtruckle. I personally relate to her character's drive for knowledge and excitement for the unknown. I am certain that reading her books at a young age inspired me in some way. In addition, those seven brilliant books led to a series of wildly entertaining cinema, all of which brought acromantulas, horcruxes, snitches, and hippogriffs to life during the writing of this thesis.

Dedication

This dissertation is dedicated to the many teachers and professors who have encouraged and inspired me throughout the years.

This would not have been possible without you.

Abstract

Iron oxide nanoparticles are a promising resource for solving some of today's most pressing global challenges in the developed and developing world, including the removal of toxins from drinking water resources, treatment of mining wastes, and remediation of groundwater contaminated by industrial activity. There is still much to be understood, however, about the reactivity of iron oxide nanoparticles in actual groundwater systems, where mineralogy and solution conditions are complex and variable over time. In this thesis, iron oxide nanoparticle reactivity was measured as a function of environmental variables, including pH, ionic strength, and the presence of organic matter or secondary mineral phases. The chosen variables simulate severe and impacted environments, such as pesticide-polluted groundwater and acid mine drainage. Additionally, kinetic studies paired with complementary solid-state characterization were used to elucidate evolving reactivity (changes in reactivity and iron oxide properties over time) as a function of environmental variables. This interdisciplinary research incorporated analytical quantification, diffraction, magnetism, microscopy, statistical analyses, cryogenic microscopy, and fluorescence spectroscopy. The overall result of this thesis demonstrated that the reactivity of iron oxide nanoparticles towards contaminants in aqueous systems is dynamic with respect to environmental variables and reaction extent. By increasing our understanding of how iron oxide nanoparticles will react in the subsurface, predictions of efficiency and expected outcome of environmental remediation will improve.

Table of Contents

List of Tables

List of Figures

List of Abbreviations

4-ClNB.....4-chloronitrobenzene

Ak.....akaganeite

amorph. .....amorphous

ARSA.....accessible reactive surface area

ASE.....accelerated solvent extraction

BET.....Brunner, Emmett, and Teller

Cal.....calcite

CCD .....charge coupled device

CRM.....chemical remanent magnetization

cryo-SEM.....cryogenic scanning electron microscopy

cryo-TEM.....cryogenic transmission electron microscopy

CSIA .....compound specific isotope analysis

DLVO .....Derjaguin, Landau, Verwey, and Overbeek

DLS.....dynamic light scattering

DRM .....detrital remanent magnetization

EDS.....electron dispersive spectroscopy

EEM.....excitation emission matrix

FC-ZFC.....field cooled-zero field cooled

Fh .....ferrihydrite

FTIR.....Fourier transform infrared spectroscopy

GC.....gas chromatography

GISAXS .....grazing incidence small-angle X-ray scattering

Gth.....goethite

Hem.....hematite

HS .....humic substance

HRTEM.....high resolution transmission electron microscopy

IOCS .....iron oxide coated sand

IRM .....isothermal remanent magnetization

Kln.....kaolinite

KQT .....kaolinite, quartz, and titanium dioxide

K-S .....Kolmogorov-Smirnov

LC .....liquid chromatography

Mag .....magnetite

MB .....methylene blue

MPMS .....magnetic property measurement system

NDIR.....nondispersive infrared

PARAFAC .....parallel factor analysis

PDF .....powder diffraction file

PRB .....permeable reactive barrier

PZC .....point of zero charge

Q.....benzoquinone

QH_2 .....hydroquinone

Qz.....quartz

RTSIRM.....room temperature saturation isothermal remanent magnetization

SAED .....selected area electron diffraction

SAXS .....small-angle X-ray scattering

SEM .....scanning electron microscopy

SQUID .....superconducting quantum interference device

TEM .....transmission electron microscopy

TMag.....titanomagnetite

TOC.....total organic carbon

VSM.....vibrating sample magnetometer

Vtr .....vaterite

XRD .....X-ray diffraction

ZVI.....zero valent iron

List of Symbols

D.....difference as calculated by the K-S test

Z .....fluorescence intensity

g.....g-force

ΔG .....Gibbs free energy

M .....magnetization

N.....number of particles

p.....probability

k_{obs} .....pseudo-first order reaction rate

$E_{H,\ pH\ 7}$.....reduction potential at pH 7

$E_{H,\ pH\ 4.5}$.....reduction potential at pH 4.5

E_H^0 .....standard reduction potential

Chapter 1. Contaminant degradation by aqueous Fe(II) and iron oxide nanoparticles and their evolving reactivity in environmental systems

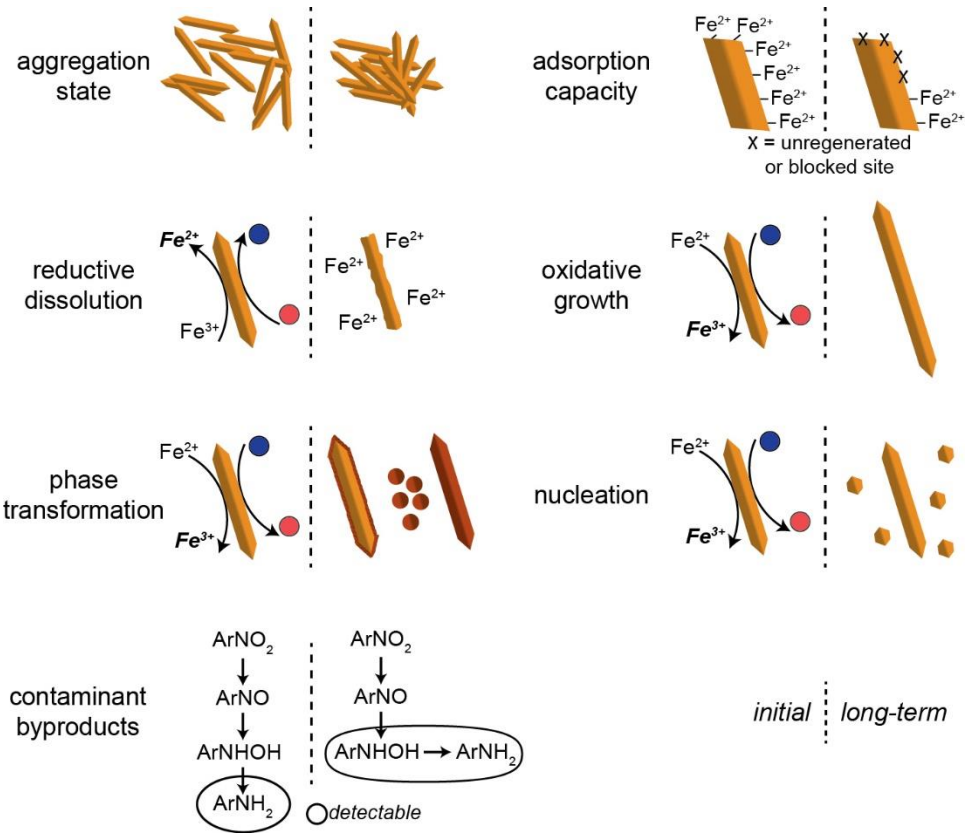

This chapter provides a critical review as written by Jennifer H. Strehlau advised by R. Lee Penn and William A. Arnold.

Introduction

A recent United States Geological Survey report estimated that 76 billion gallons of groundwater were pumped per day across the United States and that nearly 14% of Americans rely solely on fresh groundwater for domestic use, especially in rural zones.[1] Significant population growth and rising food demand has threatened groundwater resources with chemical contamination from a variety of sources, including industrial wastes and agricultural runoff.[2,3] Increasing attention on groundwater contamination and the associated negative health repercussions validate the demand for an efficient and realistic remediation method. For example, a brief literature search for the research topic "environmental remediation" using the SciFinder Database® reveals a rising trend in the development of remediation methods in the scientific communtiy (Figure 1.1), particularly in the last decade.[4]

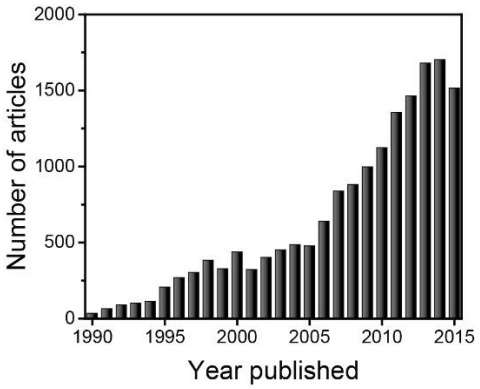

Figure 1.1: Frequency of articles per year with research topic "environmental remediation", 1990-2015, using the SciFinder Database®.

Current remediation methods can be categorized as either ex situ or in situ, and ex situ methods (e.g., above ground pump-and-treat) can be costly, time intensive, and

impractical.[5] Consequently, there is considerable focus on the development of in situ remediation methods, such as below ground chemical transformations using natural sediment materials or engineered systems.[6,7] For example, one in situ route for transforming oxidized contaminants, such as nitroaromatic compounds (NACs), is through chemical reduction by aqueous Fe(II), a common groundwater ion.[7] Previous work has demonstrated that Fe(II) can reductively degrade oxidized contaminant molecules and, in particular, rates of reaction increase dramatically when iron oxide or oxyhydroxide mineral surfaces are present.[8] Nanoparticles of these minerals, hereafter collectively referred to as iron oxides, are even more promising for in situ remediation due to their relatively higher specific surface areas, natural presence in sediments, and relative ease of synthesis.[6,9]

The reduction of oxidized contaminants by Fe(II) in the presence of an iron oxide mineral surface occurs via three steps (Figure 1.2). First, adsorption of Fe(II) occurs by complexation to surface hydroxyl groups on the iron oxide. An overlap in Fe(II) and Fe(III) d-orbitals results in electron delocalization and an overall decrease in the redox potential of Fe(II)−Fe(III), therefore stabilizing the Fe(III) oxidation state and making the transfer of an electron from Fe(II) more favorable.[10–13] Specifically for minerals that contain Fe(III) in their bulk structure, like iron oxides, electron delocalization is not always limited to the mineral surface but instead can occur within the bulk mineral. This second stage is described as interfacial electron transfer.[14] Interfacial electron transfer has been demonstrated for various iron oxides in the presence of aqueous Fe(II), including hematite, goethite, and others.[14,15] In addition, reduction of NACs by magnetite

$(Fe(III)_2Fe(II)O_4)$ in the absence of aqueous Fe(II) is expected to be due to interfacial electron transfer within the Fe(II) and Fe(III) in the bulk mineral.[16,17] Finally, during the third stage, the contaminant species nears the surface of the iron oxide and electron transfer occurs, resulting in a chemically reduced contaminant.

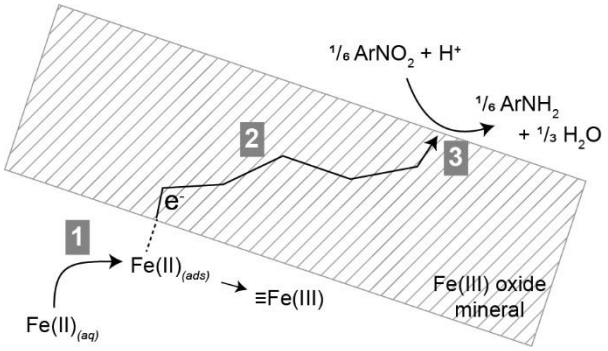

Figure 1.2: Illustration showing the reduction of a nitroaromatic compound by surface-mediated reaction with Fe(II). 1) Adsorption of Fe(II) and electron delocalization at the mineral surface. 2) Interfacial electron transfer within the bulk mineral. 3) Approach of a nitroaromatic compound at the mineral surface and subsequent electron transfer.

A great number of studies have investigated the reactions of Fe(II) adsorbed on iron oxide nanoparticles with various contaminants, either in abiotic, biotic, or photocatalyzed environments. Example contaminant classes that have been abiotically reduced by adsorbed Fe(II) on iron oxides include explosives,[18–20] pesticides and fertizilers,[21–24] drinking water disinfection byproducts,[25–27] toxic metal ions,[28,29] and chlorinated solvents.[30–32] Similar microbe-mediated reactions are possible when coupled with dissimilatory Fe(III) reduction and subsequent Fe(II) adsorption on an iron oxide.[33,34] In natural surface waters, redox transformations can also occur through photocatalyzed Fe(II) oxidation.[35,36] In dark groundwater systems, Garg et al. demonstrated that photocatalyzed organic matter is relatively stable in acidic waters and

can even contribute to the Fe(II)/Fe(III) cycle in dark systems hours later.[37] In summary, all of these studies demonstrate the potential of Fe(II) as an efficient chemical reductant for groundwater contaminants in the presence of iron oxide nanoparticles.

Given the widespread occurrence of iron oxide nanoparticles in soils and bedrock and the ease by which they can be synthesized, their application in the reduction of oxidized contaminants is promising. A major challenge to their application, however, is predicting their performance in environmental settings, where several variables including groundwater chemistry, exposure time, and fluctuations in exposure must be considered. For instance, the accessible reactive surface area (ARSA) of iron oxide nanoparticles is a controlling factor in reactivity but also greatly depends on the groundwater chemistry. Also, while there is a significant amount of information detailing the reactivity of Fe(II), oxidized molecules, and iron oxide nanoparticles in laboratory settings, few have considered the effects of extended reaction periods as well as fluctuating exposure. Thus, the aims of this review are two-fold. First, what is currently known about the ARSA of iron oxides in the presence of Fe(II) and groundwater contaminants is evaluated, with specific attention on how it has been measured and the influence of common environmental variables. Second, the evolving reactivity, or changes in the properties or chemistry of Fe(II)/iron oxide reactive systems with time or extent of exposure, is described. Not much is known about the evolving reactivity of these systems, despite its understanding being an essential step towards predicting reactivity in natural environments. Therefore, possible mechanisms of change and the experimental designs and characterization techniques available to detect these changes are described. With

further study into the effects of environmental variables and extended reaction properties, predictions of environmental reactivity for in situ contaminant transformations will be improved.

Accessible reactive surface area (ASRA) of iron oxide nanoparticles

The iron oxides are a class of minerals, comprising of a variety of crystal structures, sizes, and morphologies. Although there are many iron oxide minerals, some of the most common iron oxides studied for their reactivity in groundwater systems include goethite, hematite, and ferrihydrite. For instance, goethite (α-FeOOH) is one of the most frequently used iron oxides for environmental studies due to its common occurrence and stability in the environment. Typical synthetic goethite nanoparticles are acicular (rod-like) and can range in length and width.[38,39] The {110} and {100} faces dominate the sides of the particle, enclosed by a diamond-like cross section of predominantly {021} terminations.[38,40] Hematite (α-Fe_2O_3), another common iron oxide, often grows as rhombohedra or hexagonal plates, with the (001) face serving as the basal planes. In contrast, ferrihydrite ($Fe_{10}O_{14}(OH)_2$) nanoparticles have a uniquely low structural order and elusive crystal structure.[41] Akaganeite and lepidocrocite, less thermodynamically stable polymorphs of goethite, are not as frequently studied but exhibit remarkable reactivity in the presence of Fe(II). Akaganeite (β-FeOOH) nanoparticles can be synthesized as somatoids (cigar-shaped) or acicular rods, and lepidocrocite (γ-FeOOH) crystallizes as platy or tabular nanoparticles.[38] Magnetite (Fe_3O_4), a mixed-valent iron oxide mineral, forms as octahedral nanoparticles and

displays unique properties compared to other iron oxides due to both octahedral and tetrahedral structural iron species.[38]

Considering their unique composition, crystallography, and morphology, iron oxide nanoparticles vary greatly in their ARSA, which can be defined as the number of surface sites directly exposed to the solution phase in combination with a composition and structure that can participate in the reaction. When adsorbed Fe(II) is the reductant in aqueous systems, the measure of ARSA is largely determined by the aggregation state and Fe(II) adsorption capacity of the iron oxide, and both of these properties are dependent on the mineral morphology, size, and crystallography. In addition, the surrounding environment is a critical variable in reactivity, with pH, ionic strength, organic matter, and even the presence of other mineral phases impacting ARSA.

Quantifying ARSA

For nanoparticles in aqueous systems, a major challenge in quantifying ARSA is the variable adsorption capacity and aggregation state with even minor changes in iron oxide structure or environmental conditions. This means detailed characterization of the nanoparticles and their properties in the aqueous media is essential to quantifying ARSA. For example, reactive surface area can be described by measuring Fe(II) adsorption capacity and using structural analyses such as crystallographic modeling with Fourier transform infrared (FTIR) spectroscopy, both describing the total number of reactive adsorbed Fe(II) surface sites. To quantify accessible surface area, examination of aggregation state as the particles exist in the aqueous media is essential. Other techniques that measure surface area on dried particles may not be accurate estimates of accessible

surface area (e.g., gas adsorption with Brunauer-Emmett-Teller (BET) analysis). Advancements towards quantifying ARSA of iron oxide nanoparticles in reactive aqueous systems are described in the following paragraphs, including Fe(II) surface complexation, Fe(II) adsorption capacity, and particle aggregation state.

Fe(II) sorption can provide a measure of reactive surface area, and several surface complexation models and adsorption isotherms for Fe(II) on iron oxides have been developed. For instance, adsorption of Fe(II) may occur through mono- and/or bi-dentate complexation with surface hydroxyl groups and may be favored on particular crystal faces.[29,42,43] These surface complexation models provide fundamental insight into Fe(II) adsorption at the mineral-water interface, but empirical studies of Fe(II) adsorption capacity can provide a different means for estimating the total number of reactive sites. For example, Figure 1.3a provides an experimental adsorption isotherm for Fe(II) on goethite nanoparticles, providing an estimate of the total number of Fe(II) reactive sites as a function of particle loading. Other studies of Fe(II) adsorption on goethite,[44] hematite,[45–48] ferrihydrite,[29,49,50] and magnetite[51–53] have been performed, the results of which vary greatly depending on the nanoparticle properties and experimental conditions. In some cases, the addition of Fe(II) to iron oxide suspensions (e.g., akaganeite, lepidocrocite) induces phase transformations.[24,54–58] Together, these studies demonstrate that estimates of reactive surface area require an understanding of both microscopic complexation mechanisms and experimental adsorption studies.

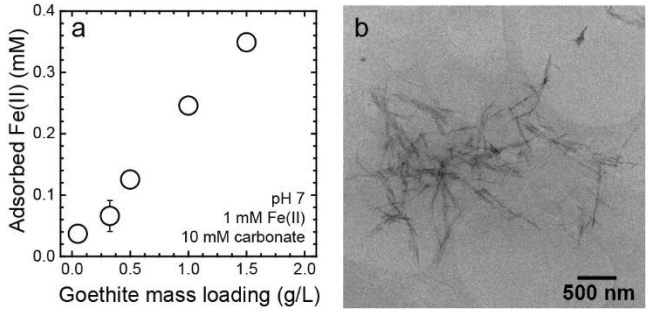

Figure 1.3: Experimental estimates of ARSA through a) Fe(II) adsorption capacity and b) cryogenic transmission electron microscopy (cryo-TEM) for goethite nanoparticles suspended in 10 mM carbonate buffer at pH 7 and initial Fe(II) concentration of 1 mM. *Figures adapted from Chapter 3.*

Aggregation state can provide an estimate of the accessible surface area. Techniques measuring aggregation state in aqueous systems, such as cryogenic microscopy or dynamic light scattering (DLS), are often used. For instance, goethite aggregates of various sizes and densities have been directly imaged using cryogenic microscopy and measured using DLS in a variety of aqueous media.[59,60] An example cryogenic transmission electron microscopy (cryo-TEM) image of goethite nanoparticles is shown in Figure 1.3b, showing side-to-side particle contacts which may suggest a decrease in accessible surface area relative to that of the dispersed nanoparticles, especially for the {110} and {100} side crystal faces. Previous work has demonstrated that the percentage of side-to-side contacts can be quantified by measuring the contact angles of goethite nanoparticles.[59] Researchers have also reported estimates of aggregation state for ferrihydrite[61–63] and hematite[64] in aqueous media. There is limited information, however, on the native state of other iron oxide aggregates in aqueous systems. For instance, while interesting aggregate structures have been observed in situ

for surfactant-coated magnetite nanoparticles (ferrofluid),[65] uncoated magnetite aggregation in aqueous media with Fe(II) has not yet been resolved. Given the broad study of iron oxides in reactive aqueous systems, however, more in situ evidence of iron oxide aggregate formation is expected in the coming years.

In summary, in situ observations of iron oxide surface chemistry, Fe(II) adsorption, and aggregation state have offered a means to quantify ARSA of iron oxide nanoparticles for the reduction of oxidized groundwater contaminants by adsorbed Fe(II). This review of the literature, however, suggests that all three properties are also highly dependent on the surrounding environment, which varies considerably between natural groundwater systems.

Impact of environmental variables on ARSA

In contaminated groundwater zones, there are several variables that control aggregation state and adsorption capacity of iron oxides nanoparticles, including solution parameters such as pH and ionic strength. While organic matter makes up only a small fraction of the total subsurface, it can greatly influence iron oxide nanoparticle surfaces and their resultant reactivity. Additionally, the presence of secondary mineral phases (e.g., binary or heterogeneous mineral mixtures) is not as commonly explored in relation to Fe(II)/iron oxide reactivity, yet the ubiquity of complex mineral mixtures in the subsurface advocates for future work in this field.

pH and ionic strength. Solution chemistry is an important consideration for surface-mediated reactions in groundwater systems, where small changes in pH and ionic strength or composition can lead to large deviations in ARSA. The point of zero charge

(PZC) determines the surface charge of an iron oxide at a given pH and when the pH is near the PZC (generally 6 – 9 for iron oxides[66]), particles hold a near neutral surface charge. Thus, Fe(II) adsorption (which occurs through surface hydroxyl groups) generally increases as pH increases, with each curve dependent on mineral phase, mass loading, specific surface area, and other solution variables.[20,42,44,50,57,67] While little detectable adsorption of Fe(II) occurs at pH values lower than 5, isotope tracer experiments demonstrated that some interfacial electron transfer still occurs.[68,69] In addition to adsorption, the pH of the system has been regarded as a master variable for predicting aggregation state, leading to estimates of colloidal stability.[70] When the pH is near the PZC, iron oxides tend to form larger aggregates due to less surface charge repulsion, which can result in decreased accessible surface area.[66,71–74]

Ionic strength and composition also affect the Fe(II) adsorption capacity and aggregation state of iron oxides. Several works have identified adsorption of anions and other metal cations on iron oxide surfaces.[75–77] Competitive reduction of NACs and nitrate ions by adsorbed Fe(II) on iron oxides has also been detected.[24,78] Likewise, aggregation is influenced by the ionic strength and can be promoted by compression of the electric double layer and/or charge neutralization, affecting the colloidal stability, transport, and reactivity of iron oxides in the subsurface.[62,79,80] One unique case of iron oxide aggregation induced by ionic strength with significant environmental relevance is estuaries, where induced iron oxide aggregation and settling following the mixing of freshwater with seawater is known to affect the availability of iron in the ocean.[81–83] Given this brief summary of the literature, it is clear that both pH and ionic strength are

important parameters to reporting ARSA of iron oxides and that many studies have examined the influence of these variables in great detail.

Organic matter. The presence of organic matter (OM) can also alter the properties and reactivity of iron oxides in aquatic systems.[84] OM is produced by microbes and the decay of terrestrial organisms, and it is known to have a complex molecular structure consisting of varied functional groups.[85] Fractionation of OM on iron oxide surfaces is possible (e.g., adsorption of OM fractions with high molecular weights[86,87]), and OM adsorption may be favored for a particular iron oxide (e.g., goethite over ferrihydrite when normalized to BET surface area[88]). These studies demonstrate that OM can decrease the amount of ARSA through coverage of the reactive sites and/or changes in aggregation state. In addition, Fe(II) can strongly bind to OM, impacting the concentration of aqueous Fe(II) available for sorption on iron oxides.[89,90] In some cases, this competitive adsorption may decrease the number of sorbed Fe(II) sites on an iron oxide, thus decreasing the amount of ARSA. On the other hand, OM can act as an electron shuttle and promote reaction contaminant reduction by further decreasing Fe(II)-Fe(III) redox potentials.[91]

Several studies have demonstrated changes in reactivity of adsorbed Fe(II) on iron oxides towards contaminants or model organic compounds when in the presence of OM. In Luan et al., the presence of humic acid (a fraction of OM) significantly slowed the reduction rate of nitrobenzene by Fe(II) sorbed on goethite, hematite, and magnetite.[92] They proposed two possible mechanisms: competitive Fe(II) complexation by humic acid and/or interference with electron transfer through humic acid adsorption on the iron

oxide. This is supported by earlier works demonstrating decreased NAC reduction rates in the presence of OM.[93,94] Recently, it has been shown that the character of OM (e.g., aromaticity or carbon content) can be used as a predictor for reaction rates between 4-chloronitrobenzene and Fe(II) sorbed on goethite in the presence of different OM fractions.[95] These results highlight the importance of OM in the environmental remediation of contaminants by Fe(II)-iron oxide complexes. A recent review by these authors summarizes in greater detail the interactions between iron oxides and OM in relation to environmental reactivity.[85]

Presence of secondary minerals. The mineralogy of the subsurface is heterogeneous and complex, and iron oxides are rarely the sole mineral to consider during in situ environmental reactions. Since oxygen, silicon, aluminum, and iron are the most common elements of the Earth's crust, mixtures of aluminosilicate clays and iron oxides are common in many environments, both produced by chemical weathering processes.[38,96,97] Figure 1.4 demonstrates four possible mechanisms by which clays might affect the surface-mediated reactions of adsorbed Fe(II) on iron oxide nanoparticles in the presence of groundwater contaminants. Clays with structural Fe(III), such as montmorillonite with Fe(III) substitution in the octahedral layer, can enhance the reduction of contaminants through Fe(II) adsorption and subsequent interfacial electron transfer,[10] although these clay minerals are often less effective when compared to iron oxides tested under the same conditions.[8,23,32,98–101] On the other hand, clay minerals with or without structural iron can affect Fe(II)/iron oxide reactivity through several nonreactive processes. For example, adsorption of Fe(II) or the targeted contaminant on

clay minerals is possible through several processes, such as ion-exchange in the intercalation spaces, electrostatic attraction on edges and basal planes, or coordination to interlayer cations.[102–104]

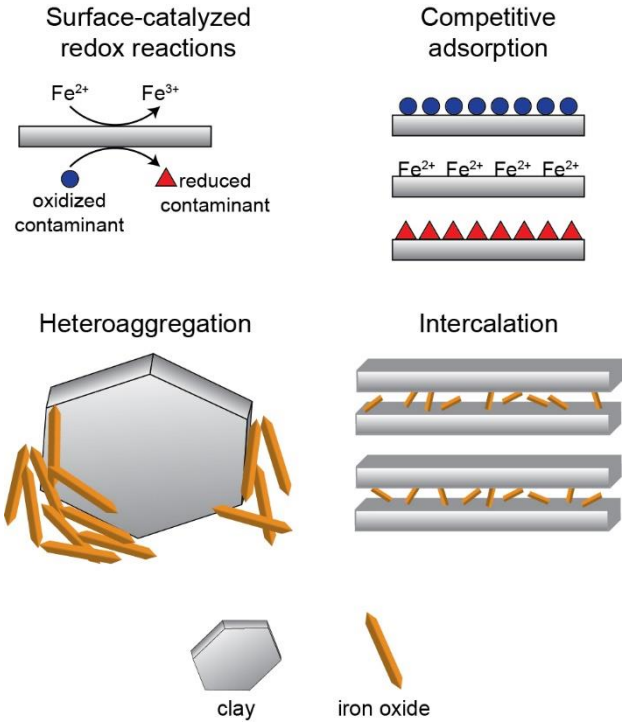

Figure 1.4: Possible mechanisms by which a clay mineral can affect the surface-mediated reactions of adsorbed Fe(II) on iron oxides nanoparticles.

Additionally, clay-iron oxide particle interactions, including intercalation or heteroaggregation, are possible. Intercalated or "pillared" iron oxide nanoparticles can be achieved when particles are thermally annealed in the presence of the clay, creating a hybrid material with relatively high ARSA.[105,106] In these hybrid materials, iron oxides are present in the interlayer spaces of the clay mineral and therefore cannot aggregate or grow to large diameters. In contrast, the heteroaggregation of clays and iron oxides could result in a decrease in ARSA, although few studies have directly imaged these

heteroaggregates in aqueous suspension.[107–109] Despite the evidence of clay-iron oxide interactions, few have exclusively studied binary mixtures of nonreactive clays and iron oxides in the presence of aqueous Fe(II) and oxidized contaminants. In *Chapter 3*, addition of the clay mineral kaolinite (shown to be nonreactive in this study) decreased the reactivity of Fe(II) on goethite towards 4-chloronitrobenzene, the result of competitive Fe(II) adsorption on kaolinite.[110] In situ observations using cryo-TEM suggested insignificant loss of accessible surface area through heteroaggregation. The common occurrence of clay minerals and their potential to affect ARSA of iron oxide nanoparticles through multiple mechanisms make heterogeneous mineral mixtures equally important to study.

Other common minerals have affected the surface-mediated reactions of Fe(II) and iron oxides. Some such as quartz (SiO_2) contain no structural iron, are considered nonreactive, and affect reactions of adsorbed Fe(II) on iron oxides similar to the mechanisms by which clays with no structural iron influence reactivity. While Klausen et al. described the observed increased reactivity of silica suspensions in the presence of aqueous Fe(II), they predicted it was the result of goethite precipitation on the silica surface, resulting in an iron oxide coated sand (IOCS).[8] IOCSs are as important for the fate and adsorption of contaminants. These hybrid materials, whether synthesized or natural, have different surface and transport properties in environmental systems than their iron oxide or sand counterparts.[111,112] Moreover, other minerals that contain structural Fe(II), some also with Fe(III), have demonstrated catalytic surface reactivity towards contaminants (e.g., pyrite (FeS_2) or sulfate green rust

($Fe^{II}_4Fe^{III}_2(OH)_{12}SO_4 \cdot 4H_2O$)).[32] These examples are only a small sampling from the list of minerals that can co-exist with iron oxides, leaving many other likely mineral combinations yet to be explored.

This section has emphasized that both the iron oxide properties and the surrounding groundwater chemistry are key factors in the reactivity of adsorbed Fe(II) towards oxidized molecules, linking reactivity with ARSA. Many of these studies, however, have measured ARSA in fixed or controlled laboratory systems with application to short-term (e.g., a single addition of a NAC) reactivity studies. As a result, many questions remain about the long-term results of in situ remediation using Fe(II) and iron oxide nanoparticles in dynamic environmental systems, where reaction time and extent of exposure will fluctuate.

Evolving reactivity of Fe(II) and iron oxides

Depending on the degree of contamination and the properties of the contaminant, in situ remediation systems may remain operational for extended periods of time. In some engineered systems, for example, the reactive material is continually exposed to the targeted contaminant for years or even decades.[113] As the duration or extent of exposure increases, properties such as the stability, structure, and composition of the reactive material, the reaction rate, and the reaction products may evolve over time.

Figure 1.5 illustrates several possible mechanisms of evolving reactivity in contaminant reduction by adsorbed Fe(II) on iron oxides. Reactivity can evolve at the solid-state level, including changes resulting from oxidative growth, reductive dissolution, phase transformation, and nucleation of new particles. In addition, ARSA is

affected by reaction extent, either through varying solution chemistry or solid-state properties, which may in turn affect the reaction rate and organic byproducts over time.

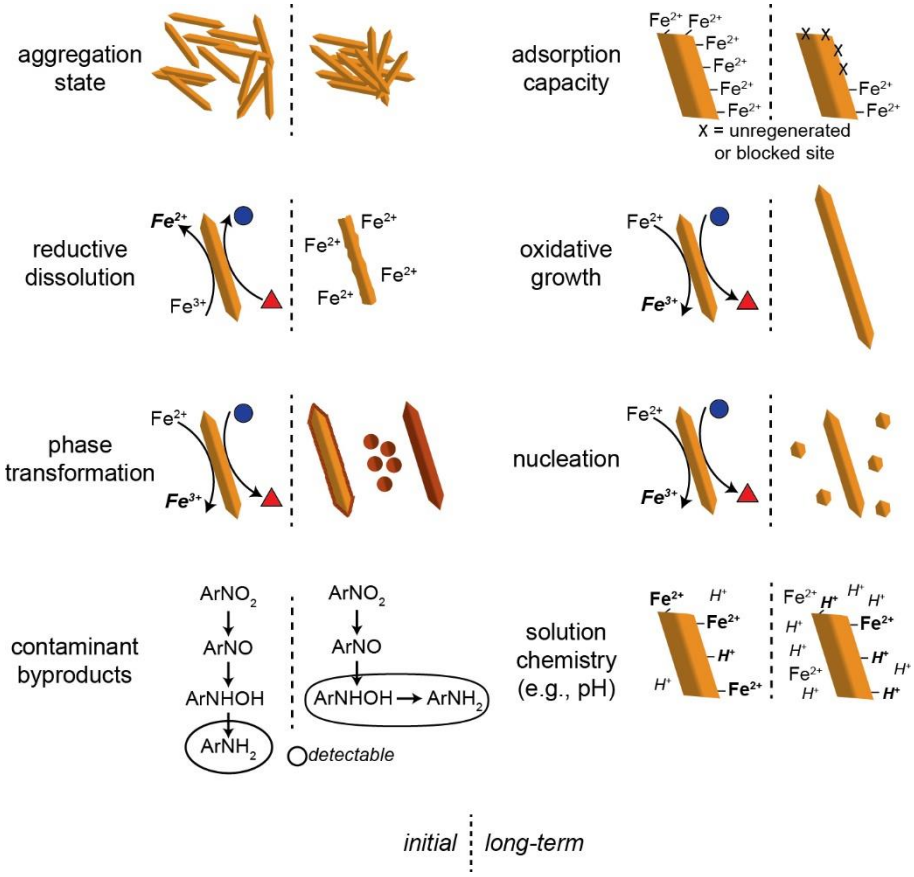

Figure 1.5: Possible mechanisms of evolving reactivity in the possible reactions between Fe(II), iron oxide nanoparticle surfaces, oxidized organic species (circles), and reduced organic species (triangles).

Solid-state changes

In reactions between oxidized contaminants, Fe(II), and iron oxide nanoparticle surfaces, chemical reactions occur at the mineral-water interface in a variety of ways. When adsorbed Fe(II) is the reductant, Fe(III) is produced, which results in three potential processes: new oxidative mineral growth on existing nanoparticles, new mineral phases, and/or new nucleated particles. In the reverse reaction, lattice-bound Fe(III) is the

oxidant and reductive mineral dissolution occurs. In either case, the total ARSA in the system will change, a property often overlooked in current kinetic studies which are limited to short-term reactions.

Oxidative mineral growth is the result of produced Fe(III) incorporated as the same mineral phase on existing nanoparticles. On the condition that all facets of the iron oxide have identical surface chemistry and crystallography, oxidative mineral growth can occur evenly on the nanoparticle surface. It is known, however, that the arrangement and density (sites/nm^2) of the reactive sites for each facet will differ, which is expected to result in preferential oxidative mineral growth on a particular face or faces. Several works from this group have detailed the oxidative growth of goethite and demonstrated the generally most reactive sites were on the tips, or {021} faces, resulting in growth along the *c* direction.[114,115] In *Chapter 2*, it was demonstrated that variable environmental conditions affected the relative reactivity of major types of goethite crystal faces, at times resulting in the relative contribution of growth rate for {021} faces decreasing compared to {110} or {100} faces (i.e., growth on side crystal faces became detectable).[116] Nevertheless, the role of the reactive faces is still unclear from these studies. It is possible that adsorption of Fe(II) and electron transfer to the contaminant both occur at the {021} face. On the other hand, adsorption may occur and then, through interfacial electron transfer, the electron may wander toward a different crystal face before transferring to the contaminant. These evolving solid-state results have only sparked more questions about the specific interactions between aqueous Fe(II) and iron oxide mineral surfaces in aqueous systems.

Phase transformations can lead to dramatic changes in ARSA. Phase transformations can occur in aqueous suspensions containing Fe(II), either with or without an oxidized contaminant. It has been proposed that interfacial electron transfer causes a decrease in crystal lattice stability, leading to mineral dissolution and precipitation of a more favorable iron oxide mineral phase.[117] Jeon et al. reported partial hematite conversion to magnetite that may result in rapid electron transfer with Fe(II),[67,118] a possibility that is particularly significant for reactions between oxidized contaminants and adsorbed Fe(II). Phase transformation in the presence of Fe(II) was also observed for other iron oxides such as ferrihydrite, goethite, and lepidocrocite[55,119–121] as well as recently for akaganeite (*Appendix B*).[58] Preferential phase transformation on certain crystal faces has been reported in some studies, which could greatly vary the ARSA over time depending on the crystallography of the new mineral face.[122,123] These studies show that by altering the ARSA, phase transformations could greatly change the reaction rate and mechanisms of reaction for iron oxide suspensions in contact with Fe(II) and oxidized contaminants.

Finally, in cases where the iron oxide is the electron acceptor, lattice-bound Fe(III) is reduced to Fe(II). The produced Fe(II) may remain surface-bound or be released into solution. The latter process, called reductive dissolution, has been observed in the oxidation of reduced organic species, such as phenols and oxalates, by a variety of iron oxides.[124–127] These functional groups have been detected in OM, thus reductive dissolution is an important process in groundwater systems. Similar to oxidative growth, dissolution on preferred crystal faces is likely depending on the character of the reactive

sites. Larsen and Postma measured length and width distributions of lath-like lepidocrocite nanoparticles at different stages of reaction with ascorbic acid and found that both size and morphology evolved with reaction time.[127] Preferential reductive dissolution of hematite has also been observed at crystal defects and rhombahedra corners.[128] Changes to mineral morphology and surface structure via reductive dissolution will likely affect ARSA and should be considered when interpreting long-term stability and transport of iron oxides in the environment.

Changes to the structure or phase composition of iron oxides will have repercussions for current models and kinetic studies on in situ reactions of Fe(II)/iron oxides in the presence of oxidized contaminants. If only initial reactions are explored, it will be difficult to predict the effect of long-term reactions between contaminants and iron oxides with a limited understanding about the evolving solid-state properties. For example, mineral dissolution may decrease the ARSA and thus reaction rate. In contrast, the emerging reactive sites may be relatively more reactive and demonstrate an increase in reaction rate. Before predictions can be made for in situ environmental applications, evolving reactivity must be quantified at the solid-state level. Changes to iron oxides will influence their reactivity and transport properties, affecting the fate and transport of natural or engineered nanoparticles in the environment.

Changes in ARSA and solution chemistry

Many kinetic studies have assumed that the initial reactive sites are identical to the post-reaction sites, imparting a steady-state assumption on the ASRA. With the evolving solid-state properties of iron oxides, the possibility that the steady-state

assumption will fail should be considered, especially in cases where contaminant exposure is extensive. The major variables controlling ARSA, such as solution chemistry (e.g., pH, Fe(II) concentration), particle morphology, and particle size, are likely to evolve. Many of these evolving variables have not been explicitly explored in long-term reactions of Fe(II)/iron oxides in context of ARSA.

If, for instance, the reduction of contaminants by adsorbed Fe(II) produces or consumes protons, the pH will vary locally depending on the degree of reaction and groundwater flow rate, among other variables. Spatial variations in pH would affect ARSA. For example, a decrease in pH would result in a decrease in the number of reactive sites (as seen in *Chapter 2*, with the net reaction between a NAC and adsorbed Fe(II) on goethite decreasing the pH[116]). Alternatively, aggregation or disaggregation of particles can be driven by similar changes in pH, which would also affect the accessibility of the reactive sites. With PZC values of 6 – 9 for most iron oxides, minor pH changes in circumneutral groundwater will considerably alter the aggregation state and particle stability, and therefore, the ARSA. The data of Palomino and Stoll reveal that a decrease in pH from 8 to 6, for example, would result in a decrease in hematite aggregate sizes from 1.2 μm to 200 nm, possibly increasing the ARSA and thus reactivity of hematite over time.[74]

Changes in ARSA can also be induced by the evolving characteristics of the nanoparticles themselves, such as growth or dissolution on certain crystal faces, further emphasizing that the observed change in reactivity is generally a sum of different mechanisms of evolving reactivity. If growth or dissolution occurs on a preferential face,

more complex situations may be considered, such as elongation of acicular goethite crystals resulting in drastic changes to particle stability and relatively rapid increases in aggregate size. Additionally, phase transformations or nucleation of new particles may result in changes to adsorption capacity or even affect interfacial electron transfer processes, further affecting ARSA.

A significant gap in the current literature is the exploration of evolving contaminant byproducts over the extent of reaction. In the reduction of 4-chloronitrobenzene by adsorbed Fe(II) on iron oxides, the intermediate 4-chlorophenylhydroxylamine was detected at initial stages of reaction and then later completely reduced to 4-chloroaniline.[8] In similar evolving reactivity experiments, complete conversion to the aniline was maintained after five sequential additions of 4-chloronitrobenzene to the same reaction system.[114] While complete conversion of nitrobenzene to aniline was shown to continue under these conditions, other contaminant reactions may not follow this trend. For instance, in a long-term field assessment of trichloroethene reduction by zero-valent iron (ZVI), increasing concentrations of certain daughter products (e.g., 1,2-*trans*-dichloroethene) were observed at different sampling localities and at different times.[129] The amount of research exploring the persistence of certain contaminant byproducts is limited for the Fe(II)/iron oxide system, making future explorations important for elucidating evolving reaction byproducts in contaminated groundwater.

The many mechanisms of evolving reactivity and limited understanding of the use of iron oxide nanoparticles for long-term environmental applications means the future

outlook must involve both fundamental analyses through controllable laboratory experiments as well as representative samplings from natural settings. The conflicting predictions of how ARSA might change with evolving properties (e.g., acidity, oxidative mineral growth) underscore the importance of expanding current studies to include long-term reactions. In this section, possible mechanisms have been described, including the results of current studies that recently explored evolving reactivity for Fe(II)/iron oxide systems. The following section aims to review methods of quantifying evolving reactivity which will enable elucidation of the many questions remaining.

Quantifying evolving reactivity

While it is speculated that evolving properties will have great significance on the reactions between Fe(II), iron oxides, and contaminants, it is impossible to make accurate predictions of in situ observations without more research using approaches specifically designed for detecting evolving reactivity. One of the most challenging aspects of studying evolving reactivity is determining how to model natural settings using controllable laboratory experiments while allowing for analysis at multiple stages and extents of reaction. It is not surprising that with several properties and variables to consider, experimental design often begins with a less complex approach and then increases the number of variables to consider. In addition, analysis of multiple reaction properties and components means complementary characterization is required, often through combinations of analytical quantification, microscopy, diffraction, spectroscopy, and other less common but promising techniques.

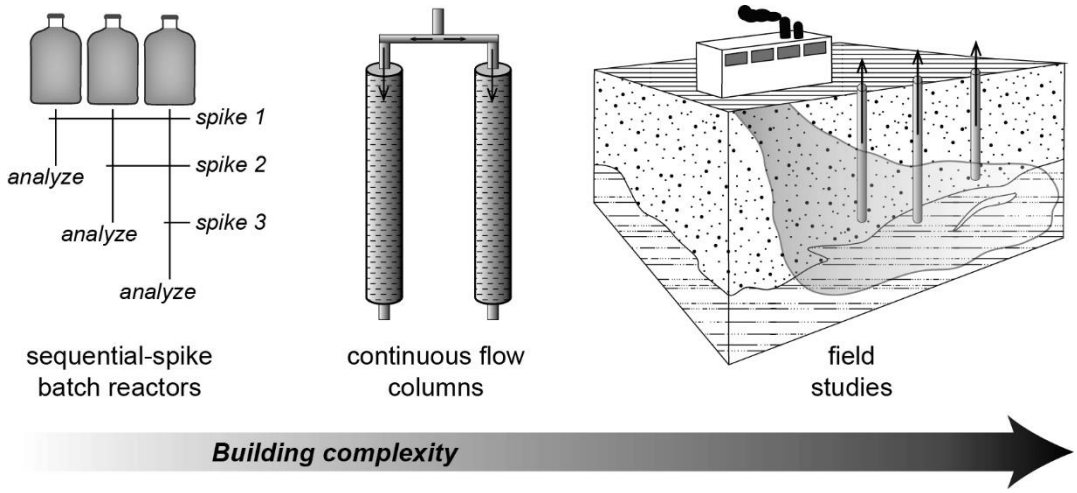

Figure 1.6: Three experimental designs used to study evolving reactivity of groundwater contaminant degradation by a reactive material, adding more variables to consider from left to right.

Experimental design

Three experimental designs have emerged for exploring evolving reactivity: sequential-spike batch reactors, continuous flow columns, and field studies (Figure 1.6). Each design has its own advantages and disadvantages, and using a combination of approaches will allow for a more thorough interpretation of the evolving reactivity in a given environment.

Sequential-spike batch reactors. Evolving reactivity as the result of a consecutive number of contaminant exposures, often referred to as spikes, to a single reaction system is observed via sequential-spike batch reactors. In these experiments, replicate batch reactors containing a closed, well-mixed suspension of Fe(II) and iron oxide nanoparticles are prepared and reacted with a known amount of contaminant or model contaminant species. These reactors are buffered around an environmentally relevant pH

using organic or, less commonly, carbonate buffers. One reactor may be sacrificed for analyses of reaction rate, products, and particle properties. The remaining unsacrificed reactors are replenished (e.g., Fe(II) concentration brought back to initial conditions) following complete degradation of the spike contaminant and then subjected to a second spike of contaminant. This procedure is repeated, sacrificing reactors after a certain number of spikes during the process, until no more reactors remain.

There are some variations to the procedure. For example, Vikesland and Valentine measured Fe(II) reduction of monochloramine by preparing sequential-spike batch reactors with a large excess of monochloramine and spiking Fe(II).[130] Chun et al. prepared a single reactor of Fe(II), goethite, and model contaminant, with a total of five spikes analyzed from the same reactor and accounting for the volume change between spikes.[114] In *Chapter 2*, additional steps were taken to ensure the system was brought back to near-initial conditions, including adjusting the pH back to initial values with acid or base if necessary.[116]

Sequential-spike batch reactors are relatively simple to prepare and offer the advantage of systematic data collection following exposure to exact quantities of contaminant in replicate systems. In addition, certain groundwater variables such as flow and mixing rate are disregarded so that elementary mechanisms of evolving reactivity are more easily explored. By using sequential-spike batch reactors, these works studied evolving properties such as reaction rate, oxidative mineral growth, and ASRA. A key element, which is generally not achieved in single-spike reactions, is that sufficient reaction occurs such that post-reaction solid-state characterization is useful. In other

words, there is a detectable amount of change to the particles, allowing for resolution of the primary reactive sites on iron oxide surfaces. In Chapter 2, for instance, the relative reactivity of different goethite crystal faces was elucidated given sufficient Fe(III) production to measure growth from microscopic images.

Continuous flow columns. To include variables such as groundwater flow and sediment porosity in a laboratory setting, a column-based approach is necessary. Column design varies depending on the aims of the research.[34,131–134] One of the simpler designs is a single column packed with a reactive material that has a solitary inlet and outlet. Solutions are passed through the column and the effluent is analyzed in intervals to attain breakthrough curves. The influent may contain both Fe(II) and contaminant or be divided into a two-stage process, where one component is passed through the column and equilibrated before initiating the reaction by introducing the other component. In more complex designs, parallel columns may be constructed, either sharing the same inlet to offer comparative studies between different packing materials or with separate inlets. To analyze effluent at different distances traveled, the column may be additionally fitted with several sampling ports. Fitting experimental data to geochemical models is complicated depending on the complexity of column design. Some have applied versions of advection-dispersion equations to account for linear velocity of the influent, porosity, and dispersion coefficient, among other variables.[131,135–137]

Continuous flow columns introduce several more variables over sequential-spike batch reactors and should be used as an intermediate step towards the study of reactivity in natural settings. For instance, Simon et al. determined rates of p-cyanonitrobenzene

reduction in natural sediment columns, which were designed with ten sampling ports to measure reactivity as a function of column depth.[138] The aggregation of iron oxide nanoparticles in continuous flow columns has been studied to elucidate their colloidal stability and transport in groundwater zones.[62,139] Some researchers have used column studies to determine the role of surface corrosion products and Fe(II) produced from reactions between ZVI and groundwater contaminants.[140,141] Given these preliminary studies, it is possible to study several mechanisms of evolving reactivity, such as reaction rate, solid-state properties, and aggregation state, while still including some groundwater variables by using continuous flow columns.

Field studies. A direct method to study evolving reactivity during in situ contaminant degradation by adsorbed Fe(II) on iron oxides is to evaluate their reactivity directly in the field. Few researchers, however, have exclusively explored the reactivity of Fe(II) in natural iron oxide systems using field studies, despite being noted as a main compartment of contaminant degradation in the environment.[142] Additionally, applications of ZVI in more than 50 pilot and full-scale operations[143] have determined iron corrosion products are formed following contaminant reduction.[144,145] This lends even more importance to studying long-term reactions of Fe(II)/iron oxides in environmental systems. While the benefit to performing field studies is the direct relevance to predicting reactivity in environmental systems, disadvantages include the necessary regard for numerous complex variables as well as the costs and permissions of operation. Despite these challenges, field tests focused on evolving reactivity of iron

oxides are an essential step towards improving predictions about reactivity and thus fate and transport of groundwater contaminants and reactive nanoparticles.

Characterization

Sequential-spike batch reactors, continuous flow columns, and field studies all have in common the advantage of data collection as a function of reaction time and extent as well as for different components (i.e., solution and solid-state reactants). The combination of several methods facilitate interpretation of evolving reactivity and comprise both analytical techniques and solid-state characterization.

Analytical techniques. Andreu and Picó identified several challenges to quantifying contaminants in natural settings, such as the low concentrations, diverse molecular structures, and adsorption properties of the analytes.[146] Efficient extraction along with selective and sensitive analytical methods that suit the nature of a wide range of contaminants are required. Pesticides, for example, have been extracted using accelerated solvent extraction (ASE), which saves both time and solvent volume.[147] Quantification using gas chromatography (GC) and liquid chromatography (LC) methods is most common.[146] Several reviews are available for other contaminant molecules, although similar GC and LC methods are used depending the nature of the contaminant and byproducts.[148–150]

Specific to evolving reactivity, analytical quantification paired with stable isotope analyses provides detailed insight into not only the mechanisms and kinetics of contaminant degradation on iron oxide surfaces but also the transport behavior and byproducts of contaminants. Isotopic fractionation of model organic species through

processes such as chemical reaction, sorption, and diffusion in groundwater systems offers unique opportunities for use of compound specific stable isotope analysis (CSIA). CSIA with carbon, hydrogen, and nitrogen isotopes has been applied for quantifying contaminant degradation in a variety of polluted waters, such as those contaminated with monoaromatic hydrocarbons, chlorinated solvents, fuel additives, and explosives.[151,152] CSIA may also enable the elucidation of evolving organic byproducts over time and distance traveled by facilitating identification of specific bonds broken and sources of contamination.

Microscopy. Microscopy is useful for detection of evolving solid-state properties, particularly when there is sufficient change to the nanoparticles from extended reaction periods. Commonly used microscopic techniques include transmission electron microscopy (TEM) and scanning electron microscopy (SEM). Advancements in cryogenic sample preparation and imaging have also led to unique in situ investigations of particle-particle interactions in aqueous media, where the reaction suspension is rapidly cooled to vitrify the water and particles are trapped in their native aggregation state.

Conventional TEM is used to detect and quantify iron oxide growth, dissolution, or phase transformations on bulk crystal faces of nanoparticles. To compare growth or dissolution on different crystal faces, measuring particle dimensions from conventional TEM images can assess deviations in the average size of iron oxide nanoparticles, like the lengths and widths of acicular nanoparticles (e.g., goethite, akaganeite, and lepidocrocite). For example, the initial and post-reaction length and width distributions

have been compared for acicular iron oxide nanoparticles participating in the oxidation or reduction of organic species.[114,127] In *Chapter 2*, collection of a representative data set and application of appropriate statistical analyses was described.[116] Measurement of 400 – 500 particles at minimum using blind analysis was recommended, along with additional assessments to check for user-based uncertainties or bias. Data are generally represented as histograms of normalized frequency as a function of length or width and can be statistically compared (e.g., nonparametric tests) to other histograms to describe changes in particle morphology. Figure 1.7, adapted from *Chapter 2*, provides examples of histograms showing the oxidative growth of goethite in identical systems except with added OM in one set of experiments. By applying the Kolmogorov-Smirnov (K-S) test, it was statistically determined that the growth rate on the side crystal faces was relatively faster when OM was present.

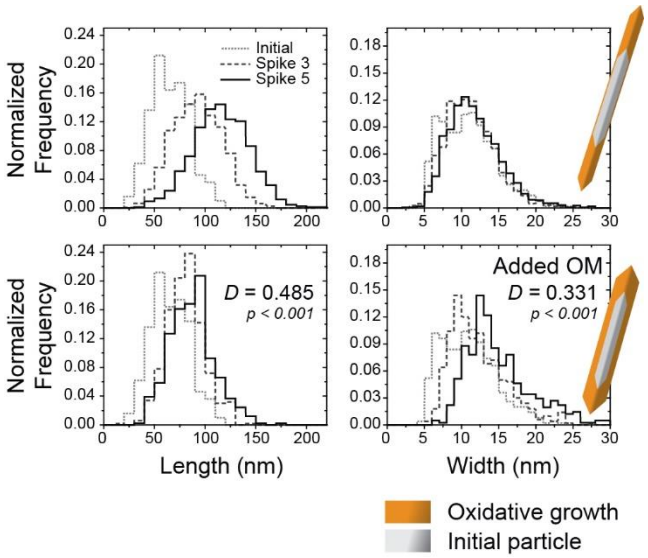

Figure 1.7: Normalized frequency of goethite (0.325 g/L) length and width reacted with 4-chloronitrobenzene (0.1 mM) in 1 mM Fe(II) and 10 mM carbonate buffer at pH 7 using sequential-spike batch reactors. Bottom histograms collected from when 10 ppm Suwannee River natural organic matter was added in the same conditions. Using the K-S test, the relative extent of difference, *D*, between the two Spike 5 histograms and the probability, *p*, that the two histograms are statistically the same are provided to compare both length and width of the particles after reaction.

Conventional TEM often results in aggregation of particles due to the removal of the solvent, making cryogenic TEM (cryo-TEM) and cryo-SEM more conclusive techniques for assessing aggregation state of nanoparticles in their native state.[153] This is accomplished by either comparative observations or statistical analysis. Qualitative comparisons of cryo-TEM images identifying differences in aggregation state of iron oxide nanoparticle suspensions in different aqueous media have been provided.[95,110] On the other hand, Stemig et al. quantified frequency of side-to-side contacts of goethite nanorods and particle density using aggregate measurements from cryo-TEM images.[59] In addition, cryo-TEM provides detailed information about iron oxide nanoparticles at subnanometer scale, including growth and phase transformations.[154] On the other hand,

cryo-SEM has been applied more frequently in industrial and biomedical fields, providing powerful in situ imaging of diverse materials like cheese microstructures or encapsulated bacteria.[155,156] The application of cryo-SEM in nanoparticle studies is less common, due to the relatively small particle sizes, but has potential to elucidate nanoparticle aggregation, and more specifically heteroaggregation or porosity, in natural systems which contain larger sediment materials.[157,158] In *Chapter 3*, cryo-SEM was used to image heteroaggregation of goethite and the clay mineral kaolinite in aqueous reactive media, although more work was needed to optimize the technique at the studied particle loadings.[110]

Other solid-state characterization. Other techniques detect the evolving properties of nanoparticles following reaction with contaminants in groundwater systems, including diffraction and magnetism. Diffraction techniques, such as X-ray diffraction (XRD), provide information on evolving mineral composition, crystallography, size, and other characteristics. Powder XRD is frequently used for characterizing nanoparticles, with detection limits for quantitative phase analysis between 1 and 5%.[159] Crystallite size can also be estimated from peak widths using the Scherer equation.[160] This technique may reveal evolving solid-state properties through detection of secondary iron oxide products or through broadening or narrowing of certain peaks, indicating solid-state changes with extent of reaction.

Other diffraction methods have been applied to characterize iron oxides. For example, Jun et al. evaluated iron oxide nucleation, distribution, and topology on quartz substrates using an in situ time-resolved characterization technique that simultaneously

combined small-angle X-ray scattering (SAXS) with grazing incidence SAXS (GISAXS).[161] This technique was later used to quantify evolving characteristics of nucleating iron oxide nanoparticles as a function of environmental variables.[162]

Magnetic characterization can be used to detect and often quantify vanishingly small amounts of magnetic minerals (with one reported detection limit of < 0.01 % in natural calcites[163]) while maintaining sufficient information for identification.[116,164] The unique magnetic properties of iron oxides provide reason to apply magnetic instrumentation such as a Magnetic Property Measurement System (MPMS) with a superconducting quantum interference device (SQUID) magnetometer or a vibrating sample magnetometer (VSM). Observable magnetic transitions, such as the Morin transition for hematite and Verwey transition for magnetite, can indicate whether trace secondary iron oxide phases are present.[38,154] Smaller particles may display superparamagnetic behavior, detectable through low-temperature and room-temperature measurements.[165–167] Different magnetic properties have also been measured for various morphologies of the same iron oxide phase.[168,169] Thus, magnetic characterization offers a highly sensitive alternative to diffraction techniques like XRD.

Spectroscopy. Lastly, spectroscopy, especially Mössbauer spectroscopy, has proven a powerful technique for monitoring interfacial electron transfer between Fe(II) and iron oxide nanoparticles. Just over a decade ago, Scherer and coworkers used Mössbauer spectroscopy to demonstrate interfacial electron transfer in Fe(II)/iron oxide systems and have since published a range of works investigating variables affecting electron transfer.[10,14,48,101,170] Mössbauer spectroscopy could also enable elucidation of

evolving interfacial electron transfer and the environmental variables that affect it. Larese-Casanova and Scherer proposed that for hematite, interfacial electron transfer is limited when Fe(II) surface saturation is achieved, which may be due to the formation of a new layer of hematite that is somehow different from the bulk structure. It is not yet known whether similar observations would be seen in systems with oxidative growth or phase transformations after extended reaction with groundwater contaminants. Additionally, Latta et al. determined over 10% Al substitution in goethite decreased the amount of interfacial electron transfer over long reaction periods.[171] This would be particularly relevant for Fe(II)/goethite heterogeneous systems with clay minerals, which has been shown to result in Al and Si incorporation into the goethite crystal structure during oxidative growth as a result of clay dissolution.[110] It remains clear that the pioneering work using Mössbauer spectroscopy to elucidate Fe(II)/iron oxide interactions has only paved the way for its future use as a promising characterization tool in studying evolving reactivity.

X-ray spectroscopy facilitates structural characterization of iron oxide surfaces and interactions with complexing ligands, offering an atom selective and nondestructive approach to study evolving reactivity at the mineral surface–water interface. Modifications in local coordination geometry or oxidation state for a suite of iron oxides and adsorbates has been elucidated using X-ray absorption near edge structure (XANES). The redox transformations of arsenic by adsorbed Fe(II) on goethite were investigated by Amstaetter et al. using XANES, observing As(III) oxidation in the presence of goethite only when aqueous Fe(II) was added.[172] Using XANES and extended X-ray absorption

fine structure (EXAFS) spectroscopy, Boland et al. identified incorporation of U(V) into the newly formed goethite during reduction of U(VI) by Fe(II) in the presence of ferrihydrite, which catalyzed phase transformation.[173] In Li et al., different atomic surface structures and Pb(II) coordination chemistry between different crystal phases of Fe_2O_3 was identified using EXAFS and X-ray photoelectron spectroscopy (XPS).[174] No matter the technique, X-ray spectroscopy can elucidate chemical surface interactions between Fe(II), iron oxides, and contaminants at a fundamental level and, more importantly for evolving reactivity, at different stages of reaction.

A recent shift in the literature has focused on OM interactions with iron oxide surfaces and the resultant effect on short- and long-term reactions with contaminants. Excitation-emission matrix (EEM) fluorescence spectroscopy has an advantage over other techniques to characterize OM content in that sample preparation is relatively simple. For example, Cory and McKnight collected EEMs for nearly 400 natural samples and applied parallel factor analysis (PARAFAC), which divides complex EEMs into components that represent certain functional groups, to reveal a universal presence of quinone-like components in natural waters.[175] In this context, EEMs enabled characterization of a class of materials that is heterogeneous over both time and location. Using EEM spectroscopy, OM interactions with contaminants and iron oxides has been detected.[176–178] In some cases, fractionation onto iron oxides is also observable and, at times, quantifiable given advancements in fluorescence integration.[179] One disadvantage of using EEMs is its relative novelty, yet development in technique and data interpretation is ongoing.[180] For example, Poulin et al. provided a solution to the

interference of aqueous iron fluorescence in EEM spectra.[181] Despite these challenges, the mechanisms of OM interactions on iron oxide surfaces using EEM spectroscopy is likely in the coming years.

In conclusion, this section has outlined potential routes for quantifying evolving reactivity, including a variety of experimental designs and characterization techniques. The majority of current studies on Fe(II)/iron oxide nanoparticle systems are limited to short-term observations, and while they have provided critical information regarding the mechanisms of reactivity, we have only started to describe the influence of time and reaction extent. The techniques provided herein provide a guide to future exploration of these systems for environmental applications, such as in situ groundwater remediation.

Future outlook

As described in the earlier sections of this review, the current literature showcases a broad understanding of iron oxide nanoparticles as reactive surfaces for single, short-term contaminant reactions in different environmental conditions. Yet, efforts to describe evolving reactivity have led to more questions regarding the mechanisms of long-term changes in reactivity of Fe(II) and iron oxide nanoparticles. In view of recent work demonstrating that the properties of Fe(II)/iron oxides evolve in aqueous systems, it is critical to explore long-term reactions further using different experimental designs and complementary characterization. Results will facilitate improved predictions for actual groundwater applications. For instance, although results collected in the laboratory have revealed fundamental mechanisms of reaction, they are not always translated in field

studies. A number of reviews in the last year have identified this challenge for various groundwater remediation methods.[182–185]

Prior to this review, potential causes and effects of evolving reactivity for Fe(II)/iron oxide systems had not been summarized. The studies mentioned herein have all taken steps toward the exploration and quantification of evolving reactivity for Fe(II)/iron oxide systems, providing novel procedures, techniques, or results to guide future work in this field. Some studies have started to characterize core components of evolving reactivity, such as mineral growth on select crystal faces, causes of declining reaction rates, or sources of variability in aggregation state. As evidenced by these works, environmentally relevant variables, including pH, ionic strength, presence of secondary minerals, and reactant identity and concentrations, remain critical variables in predicting remediation efficiency at different stages of reaction.

The future for this field of research must incorporate complementary analyses to systems with variable solution conditions and mineral phases in order to elucidate evolving reactivity in groundwater systems. For example, sequential-spike batch reactors with systematic characterization of properties at the solid-state and solution level can establish how experimental parameters fundamentally influence these systems at different reaction stages. Cryogenic microscopy can provide information on the mechanisms of mineral growth, dissolution, and phase transformation, and magnetic measurements can detect trace phase transformations, which could have a considerably larger impact at field scale. X-ray absorption spectroscopy can reveal unique changes in surface chemistry and cation complexation with changes in groundwater chemistry over reaction time. These

types of smaller-scale, laboratory studies may be more feasible in the approaching years and would begin to elucidate the complex combination of numerous evolving properties that produce a net change in reactivity. The rising number of these studies would then make opportunities for local- or regional-scale field tests more possible. By using a suite of methods and models, including broad sampling practices, stable isotopic analyses, product characterization, and advection-dispersion models, a clearer understanding of evolving reactivity in natural studies can be achieved.

In conclusion, this review has summarized the environmental variables that influence the short-term reactions between Fe(II), iron oxide nanoparticles, and groundwater contaminants and also described where the literature falls short at the present moment (i.e., long-term studies). Given that in situ remediation techniques are one of the most promising pathways to addressing issues of contaminated groundwater and that they often correspond to extensive reaction periods, possible mechanisms of evolving reactivity in the Fe(II)/iron oxide system and details on how to quantify it were described. The recent examples of studies exploring evolving reactivity have sparked a movement in connecting fundamental interpretations to observations in the natural environment, and more research in this area is anticipated. In addition, given the vast amount of evidence that has been collected about synthetic iron oxide nanoparticles, future research will likely incorporate such factors like the use of natural soils in comparison to synthetic counterparts, continuous flow columns with unique and complex design, and regionally applicable field tests. That is not to say that the number of fundamental studies will decline. The imminent advancements of instrumentation with

higher resolution and exceptional selectivity will only improve our capability of studying finer details of the interactions between Fe(II), iron oxides, and contaminants. With additional investigations, the link connecting microscopic observations of iron oxide reactivity to regional-scale predictions of remediation may be illuminated.

Chapter 2. Facet-dependent oxidative goethite growth as a function of aqueous solution conditions

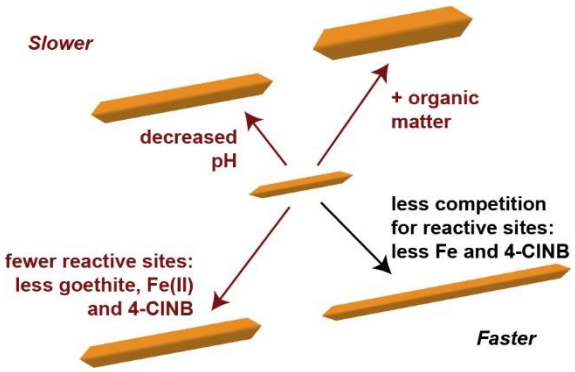

This chapter describes the outcome of a research project carried out by Jennifer H. Strehlau, Melissa S. Stemig, advised by R. Lee Penn and William A. Arnold. Supporting information is located in Appendix B.

Summary

Nitroaromatic compounds are groundwater pollutants that can be degraded through reactions with Fe(II) adsorbed on iron oxide nanoparticles, although little is known about the evolving reactivity of the minerals with continuous pollutant exposure. In this work, Fe(II)/goethite (α-FeOOH) reactivity towards 4-chloronitrobenzene (4-ClNB) as a function of pH, organic matter presence, and reactant concentrations was explored using sequential-spike batch reactors. Reaction rates for all reaction conditions did not change with the number of 4-ClNB spikes but were slower with lower pH, introduction of organic matter, and diluted reactant concentrations. Under all conditions, oxidative goethite growth was demonstrated through X-ray diffraction, magnetic characterization, and transmission electron microscopy. Nonparametric statistics were applied to compare histograms of lengths and widths of goethite nanoparticles as a function of varied solution conditions. The conditions that slowed the reaction also resulted in statistically shorter and wider particles than for the faster reactions. Additionally, added organic matter interfered with particle growth on the favorable {021} faces to a greater extent, with statistically reduced rate of growth on the tip facets and increased rate of growth on the side facets. These data demonstrate that oxidative goethite growth is dependent on major groundwater variables, which could implicate current models of nanoparticle fate and transport in contaminated groundwater.

Introduction

Whether naturally occurring or engineered, iron oxide and oxyhydroxide (herein referred to as iron oxide) nanoparticles are of interest for their contributions to subsurface

oxidation/reduction chemistry. Aqueous Fe(II) adsorbed on iron oxide nanoparticles in natural groundwaters or simulated systems has been shown to efficiently reduce oxidized contaminants.[1] Specifically, Fe(II) adsorbed on goethite (α-FeOOH) can reduce nitroaromatic compounds (NACs), such as those used as pesticides and explosives.[2–5] In the reduction of NACs by Fe(II)/goethite, decreases in pH lead to slower reaction rates as a result of less Fe(II) adsorption and less net proton production.[5–7] The presence of organic matter is known to interact with the nanoparticle surface and affect reactive sites, although the exact mechanism of interaction remains elusive given the complexity of organic matter.[8–11] Furthermore, Fe(II) concentration and nanoparticle properties including mass loading, aggregation state, size, and shape directly influence the amount of accessible reactive surface area.[12,13]

Questions remain about the evolving reactivity of the Fe(II)/goethite system in polluted groundwater, particularly, the changing physical and chemical properties as a result of continuous reaction with pollutants. Evolving reactivity is a critical consideration when interpreting environmental processes using the results of laboratory studies. Several field studies have demonstrated changing characteristics of permeable reactive barriers containing zero-valent iron, including declining remediation efficiency and oxidized iron corrosion products.[14,15] In contrast, long-term effects of reactions between oxidized contaminants, aqueous Fe(II), and iron oxide nanoparticles in polluted groundwater zones have not been explored in detail. From the solid-state perspective, evolving reactivity in these systems can manifest as mineral phase transformations,[16] oxidative growth,[17,18] reductive dissolution,[19,20] and varying aggregation state and

adsorption capacity.[21–24] In addition, reaction rate, contaminant byproducts, and solution chemistry may vary over time.[17,18,25]

Few studies have specifically explored evolving reactivity for the reaction between adsorbed Fe(II) on goethite and NACs. It has been demonstrated that produced Fe(III) is incorporated into the bulk mineral, a process defined as oxidative mineral growth when the new surface-bound Fe(III) is integrated as goethite.[17,26] Acicular goethite nanoparticles are bound by {110} faces on the sides with ends comprised mostly of {021} planes.[27] Earlier work demonstrated that oxidative mineral growth for goethite occurs primarily along the c-direction with the most reactive sites residing on the {021} faces.[17] The results were limited, however, in that the work only studied one set of reaction conditions and did not explore the effect of environmental variables. For example, the aggregation state and reactivity of iron oxides in the presence of various humic substances was determined to be sensitive to the properties of the humic substance (e.g., carboxyl concentration, aromatic content).[9] Given the complexity of natural systems, further exploration into evolving reactivity as a function of environmentally relevant variables will advance our understanding of the long-term sustainability of reactions mediated by iron oxides in polluted groundwater zones.

In this work, the evolving reactivity of goethite as a function of 4-chloronitrobenzene (4-ClNB) exposure was explored using complementary techniques while systematically varying reaction conditions. Sequential-spike batch reactors were prepared with differing goethite mass loading, pH, Fe(II) concentration, and Suwannee River natural organic matter (SRNOM) concentration. Each sample was reacted with 1 –

10 cycles of 4-ClNB such that the initial [Fe(II)] to [4-ClNB] ratio was always 10 to 1 and with re-equilibration of Fe(II) and pH in between each reaction cycle with 4-ClNB. Rates of 4-ClNB reduction were quantified and solid-state products characterized using diffraction, magnetic analyses, and microscopic imaging. Oxidative goethite growth was elucidated as a function of reaction conditions through measurements of particle lengths and widths following spikes of 4-ClNB. In addition, a protocol was established for the collection, quantification, and analysis of a statistically representative data set when comparing nanoparticle growth between experiments. The results offer new insight into the relative reactivity of goethite crystal faces under different conditions and also establish new practices for quantifying evolving reactivity, with sequential-spike experiments enabling direct characterization of reactive surfaces on iron oxide nanoparticles give the production of sufficient mass.

Experimental

Materials

Goethite nanoparticles were synthesized by the method of Anschutz and Penn[28] and stored as an aqueous suspension at pH 4 with known mass loading. Sources of materials and preparation of the carbonate buffer (10 mM, pH 7.0), stock Fe(II) solution (175 mM), and ferrozine solution (5 mg/mL) are described in the Supporting Information (Section C.1). All experiments and stock solutions were housed in an anaerobic glove bag (Coy, 95% N_2/5% H_2).

Kinetic experiments

Sequential-spike batch reactors were performed in triplicate for each set of reaction conditions. For the *reference* condition, goethite nanoparticles (0.325 g/L, denoted G_{325}) were volumetrically added to three 120 mL serum bottles and then transferred to the glove bag. Freshly made carbonate buffer (pH_7) was added so that the final volume was 120 mL, including the volume to come from Fe(II) and 4-ClNB additions. Reactors were capped with Teflon stoppers and only removed during sampling for a minimum amount of time to avoid outgassing. To each of the triplicate reactors, 0.686 mL Fe(II) stock solution was added for an initial concentration of 1 mM (Fe_1) and equilibrated for 21 to 24 h. The reference condition is denoted as $G_{325}Fe_1pH_7$.

Spike 1 was initiated by adding 1.2 mL (1% by volume) of a 10 mM 4-ClNB stock solution in methanol to all three reactors (0.1 mM 4-ClNB per spike). One of the three reactors was sacrificed for analysis via high pressure liquid chromatography (HPLC) and characterization of the solids, labeled Spike 1, while the other two reactors were not sampled. HPLC analysis involved withdrawing 0.5 mL with a plastic syringe periodically over 2 h and filtering (13 mm Acrodisc filters with 0.22 μm nylon membrane) into amber HPLC vials (HPLC method in Supporting Information). Each day thereafter, 0.5 mL of all three reactors were withdrawn, filtered, and analyzed by HPLC until no detectable amounts of 4-ClNB remained (<0.001 mM, typically after 2 d). The remaining aqueous Fe(II) concentration was quantified by the ferrozine method, with absorbance measured at 562 nm on an Agilent 8453 UV-Visible spectrometer.[29] Solids from Spike 1 were collected by centrifuge (Eppendorf 5804 at 7000 rpm for 3 min),

washed, and dried for characterization. For the remaining two reactors, the pH was adjusted back to 7.0 with 0.5 M NaOH (~ 0.1 mL), and the appropriate amount of Fe(II) stock was added to bring the aqueous Fe(II) concentration back to 1 mM (~ 0.5 – 0.7 mM was consumed). After 21 to 24 h equilibration, Spike 2 was initiated by adding 1.2 mL of freshly prepared 10 mM 4-ClNB methanolic stock solution to yield a 4-ClNB concentration of 0.1 mM. This process was repeated, sacrificing one reactor after Spike 3 and the last reactor after Spike 5. A flowchart depicting the entirety of this process is provided in the Supporting Information (Figure B.1).

To characterize the impact of pH, organic matter, particle loading, and reactant concentration, all subsequent experiments were compared to $G_{325}Fe_1pH_7$. The kinetics and characterization of four different systems were evaluated in the same manner except with the following modifications. To test the effect of pH, the carbonate buffer was prepared at pH 6.5 and the reactors were adjusted to pH 6.5 following each 4-ClNB spike ($G_{325}Fe_1\mathbf{pH_{6.5}}$). To test the effect of SRNOM (10 ppm organic carbon; $G_{325}Fe_1pH_7\mathbf{NOM_{10}}$), 0.6 mL of 2000 ppm organic carbon SRNOM was added following goethite addition. To test the effect of reactant concentration, two systems were studied: 1) half of the goethite, Fe(II), and 4-ClNB ($\mathbf{G_{163}Fe_{0.5}}pH_7$) and 2) the same goethite mass loading but with half Fe(II) and 4-ClNB ($G_{325}\mathbf{Fe_{0.5}}pH_7$). For the latter, ten 4-ClNB spikes were performed so as to produce an equivalent mass of Fe(III) per goethite surface area as compared to the other systems. In all systems, the amount of carbonate buffer was adjusted so the final volume remained 120 mL for all reactors. The reaction conditions are compiled in Table 1.

Table 2.1: Matrix of reaction conditions explored using batch reactors in 10 mM carbonate buffer. For each reaction cycle, the solution conditions were re-adjusted to the initial pH and Fe(II) concentrations before spiking in the 4-ClNB to initiate the next reaction.

Sample	**Goethite (g/L)**	**pH**	**$Fe(II)_{aq}$ (mM)**	**4-ClNB (mM)**	**SRNOM (ppm[a])**
$G_{325}Fe_1pH_7$	0.325	7.0	1.0	0.10	0
$G_{325}Fe_1$**$pH_{6.5}$**	0.325	6.5	1.0	0.10	0
$G_{325}Fe_1pH_7$**NOM_{10}**	0.325	7.0	1.0	0.10	10
$G_{163}Fe_{0.5}$ pH_7	0.163	7.0	0.5	0.05	0
G_{325}**$Fe_{0.5}$**pH_7	0.325	7.0	0.5	0.05	0

[a] SRNOM represented as parts per million organic carbon.

Diffraction and magnetic characterization

X-ray diffraction patterns were collected using a PANalytical X'Pert Pro X-ray diffractometer with a cobalt source (wavelength 1.79 Å) and X'Celerator detector. Post-reaction solids were analyzed from 20° to 80° 2θ over a collection time of 75 min and compared to the goethite powder diffraction file #29-0713. Low-temperature magnetic characterization was completed on a Quantum Designs Magnetic Property Measurement System (MPMS) cryogenic magnetometer (10^{-10} Am^2 sensitivity). Field cooled-zero field cooled (FC-ZFC) analyses were performed with a 2.5 T applied field as previously described.[30]

Microscopy

For TEM characterization, samples were prepared by resuspending a small amount of dried post-reaction solid in 1 mL Milli-Q water (~ 0.1 mg/mL), sonicating for 20 s, and drop-casting to a 3 mm holey carbon-coated copper grid (SPI supplies). Grids were imaged using a FEI T12 TEM at 120 kV, collecting at least 20 images from a minimum of 4 locations and using the same magnification.

Particle measurements

Particle lengths and widths were measured using ImageJ software (National Institute of Health, 1.47v). To obtain a representative distribution of particle lengths and widths, measurements were made for at least 400 particles per sample, stopping after either 500 particles or 20 analyzed images. Length and width measurements were plotted as histograms of 10 nm and 1 nm bins, respectively. A series of pairwise Kolmogorov-Smirnov (K-S) tests were performed to assess the degree to which the particle length and width for the last spike of 4-ClNB in experimental conditions differed from those in the reference condition. Eight K-S tests in total (4 conditions × 2 outcomes) were conducted. The hypothesis that all experimental conditions would result in particles that were shorter and wider than those under the reference condition was tested.

Several controls were instituted to provide statistically representative sampling. To prevent user-based bias, sample images were randomly assigned (i.e., unrelated file names) by another individual and decoded following measurement (blind analysis). The same ten particles were measured 20 times on separate days to quantify user-based uncertainty. Finally, the method by which grids were prepared was tested, comparing grids prepared from previously washed and dried solids (as described above) to grids prepared from diluting ~ 10 μL of sample withdrawn directly from the reactor.

Results and Discussion

Nitrobenzene reduction rates

Relative reaction rates were dependent on the number and availability of reactive sites, and the two strongest inhibitors of reactivity were decreased pH and the presence of

organic matter. Further, the rates did not change over many sequential spikes. Average pseudo-first order reaction rates (k_{obs}) for each sample as a function of the number of 4-ClNB spikes are provided in Figure 2.1 (all k_{obs} values and uncertainties are provided in Table 2.2). The reactors maintained at pH 6.5 ($G_{325}Fe_1$**$pH_{6.5}$**) had slower reaction rates than the reference condition ($G_{325}Fe_1pH_7$). Because there is proton production during the reduction of 4-ClNB by adsorbed Fe(II), a lower pH would shift the equilibrium for the reaction. Additionally, there is less Fe(II) adsorption on goethite at more acidic pH,[6] reducing the overall number of reactive sites. The addition of 10 ppm SRNOM also decreased overall reaction rates, an observation which has been previously attributed to either blocking of Fe(II)-goethite surface complexes or alteration of the reactive sites by certain humic substances, including SRNOM.[9]

The concentration of Fe(II) and goethite mass loading also affected average rates of 4-ClNB reduction, depending on the Fe(II) to goethite ratio. At pH 7 and without SRNOM, results tracking Fe(II) adsorption demonstrated that similar Fe(II) density (0.2 – 0.3 mmol m^{-2}) resided on the particle surface (Appendix C) for the $G_{325}Fe_1$, **$G_{163}Fe_{0.5}$**, and G_{325}**$Fe_{0.5}$** conditions. The k_{obs} values, in increasing order, were **$G_{163}Fe_{0.5}$** < $G_{325}Fe_1$ < G_{325}**$Fe_{0.5}$**. Compared to the reference condition, **$G_{163}Fe_{0.5}$** reactors were slower due to the lower concentration of the reductant (and thus fewer reactive sites) present. In contrast, the reference goethite loading with half Fe(II) concentration reactors were faster due to a greater ratio of adsorbed Fe(II) to 4-ClNB (because the 4-ClNB was lowered to 0.05 mM to maintain a 10:1 Fe(II):4-ClNB ratio). If the reaction at the surface is the rate limiting

step, a lower 4-ClNB concentration will lead to faster reaction kinetics due to less competition for reactive sites.[31]

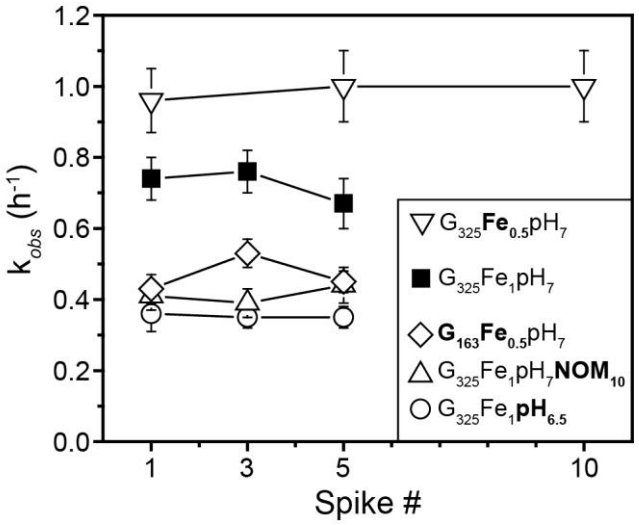

Figure 2.1: Average pseudo-first order reaction rates from triplicates of 4-ClNB reduction by Fe(II)/goethite in different reaction conditions as a function the number of 4-ClNB spikes. In the legend, the subscripts refer to goethite (G) loading in mg/L, the Fe(II) concentration (Fe) in mM, the pH, and the added Suwannee River NOM concentration (ppm organic carbon).

Table 2.2: Pseudo-first order reaction rates and length and width measurements for reduction of 4-ClNB by adsorbed Fe(II) under different reaction conditions. R^2 values were greater than 0.97 for all k_{obs} values.

Sample	Stage	k_{obs} (h^{-1})	Length (nm)	Width (nm)	N
Initial	-	-	65 ± 18	11 ± 4	500
$G_{325}Fe_1pH_7$	Spike 1	0.74 ± 0.06	-	-	-
	Spike 3	0.76 ± 0.06	93 ± 24	11 ± 4	1449
	Spike 5	0.67 ± 0.07	116 ± 28	12 ± 5	1500
$G_{325}Fe_1$**pH$_{6.5}$**	Spike 1	0.36 ± 0.05	-	-	-
	Spike 3	0.35 ± 0.03	89 ± 23	12 ± 4	450
	Spike 5	0.35 ± 0.03	104 ± 28	14 ± 7	457
$G_{325}Fe_1pH_7$**NOM$_{10}$**	Spike 1	0.41 ± 0.04	-	-	-
	Spike 3	0.39 ± 0.04	81 ± 18	12 ± 4	500
	Spike 5	0.44 ± 0.05	87 ± 23	15 ± 4	410
G$_{163}$Fe$_{0.5}$ pH_7	Spike 1	0.43 ± 0.04	-	-	-
	Spike 3	0.53 ± 0.04	86 ± 22	12 ± 4	458
	Spike 5	0.45 ± 0.03	101 ± 26	13 ± 5	500
G_{325}**Fe$_{0.5}$**pH_7	Spike 1	0.96 ± 0.09	-	-	-
	Spike 5	1.0 ± 0.1	88 ± 25	12 ± 4	500
	Spike 10	1.0 ± 0.1	110 ± 31	12 ± 6	500

Length and widths were not measured for Spike 1
N = number of particles measured for each data set

Reaction rates were constant over all 4-ClNB spikes for all reaction conditions. This was initially surprising due to previous work of similar experimental design observing decreases in reaction rate of 4-ClNB reduction with the number of contaminant spikes.[17,18] We hypothesize that the steady k_{obs} values seen herein were the result of additional steps taken to maintain pH between spikes. The pH was measured at the end of each spike and readjusted to initial pH (7 or 6.5, depending on the sample) before adding the necessary amount of Fe(II). The pH was then measured again after the equilibration period, immediately prior to 4-ClNB addition, to ensure pH was ± 0.1 from the initial value before the start of the spike. These results highlight the importance of monitoring and reporting solution parameters in sequential-spike series, especially those that may

vary with extent of reaction. The 10 mM carbonate buffer chosen based on environmental values for carbonate concentrations in groundwater did not provide sufficient buffer capacity to maintain the pH, which dropped to 6.6 ± 0.1 and 6.8 ± 0.1 for each spike when Fe(II):4-ClNB was 1:0.1 mM and 0.5:0.05 mM, respectively. When left unadjusted, the pH would continue to decrease, which would cause a decrease in the number of reactive sites (due to lower Fe(II) sorption) and may even alter the relative abundance of different protonation states of the reactive sites.

Mineral identification

Both XRD and magnetic analyses determined that oxidative mineral growth occurred, rather than precipitation of new phases or nucleation of new goethite nanoparticles. XRD results (Figure 2.2a) demonstrate no detectable difference in phase composition of the pre-reaction and post-reaction materials. In addition, control particles that were stirred for 18 days in carbonate buffer with Fe(II) but were not reacted with 4-ClNB provided no indication that phase transformation occurred (Appendix C).

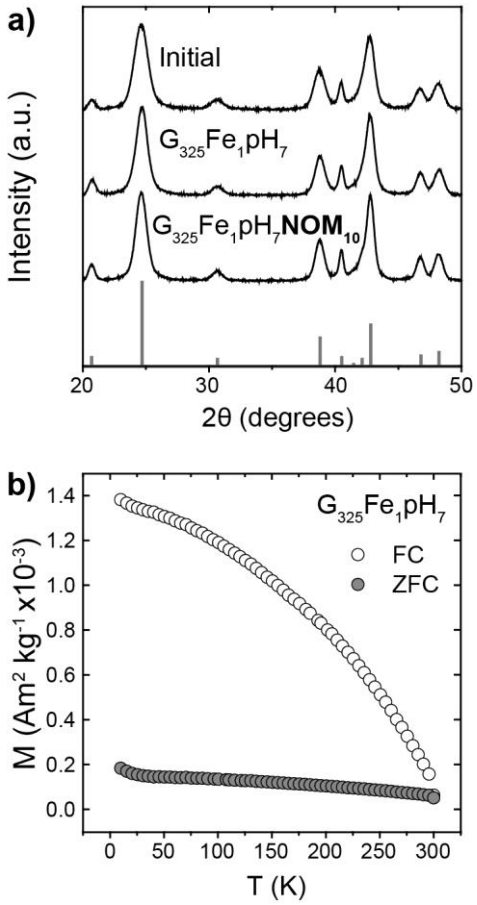

Figure 2.2: a) XRD patterns of the initial (unreacted) nanoparticles and samples $G_{325}Fe_1pH_7$ and $G_{325}Fe_1pH_7$**NOM$_{10}$** (10 ppm organic carbon SRNOM added) after five spikes of 4-ClNB compared to the powder diffraction file for goethite (#029-0713, straight lines). b) Low-temperature magnetic characterization of sample $G_{325}Fe_1pH_7$ following five spikes of 4-ClNB. Field cooling = FC, open circles. Zero-field cooling = ZFC, filled circles. Both panels demonstrate goethite was the only mineral present before and after reaction.

XRD is a relatively quick technique for the detection of phase transformations but it has a relatively high detection limit of ca. 1 – 5%, depending on the particle size and phases of the materials characterized.[32] Magnetic methods have substantially lower detection limits for iron oxides; therefore, low-temperature magnetic characterization was used to detect possible formation of new phases at much higher sensitivities. We have

previously used this technique to detect trace magnetic minerals in speleothem samples, which contained < 0.01% magnetic mineral concentration by mass.[30] Figure 2.2b provides a representative FC-ZFC plot for $G_{325}Fe_1pH_7$ after five spikes of 4-ClNB, which was similar in pattern to all other samples after five spikes of 4-ClNB. The observed separation of the FC and ZFC curves is characteristic of goethite.[33] In addition, no other transitions were observed (e.g., Morin transition for hematite or Verway transition for magnetite), indicating that goethite was the primary product (at least > 99.9%). Nucleation of new goethite particles was not observed in TEM images of goethite nanoparticles following five spikes of 4-ClNB (Figure 2.3). Thus, this system underwent oxidative mineral growth up to the measured number of 4-ClNB spikes.

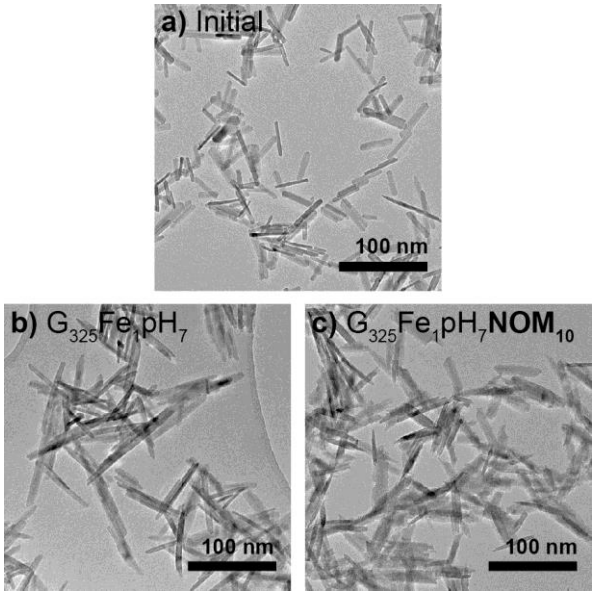

Figure 2.3: Representative TEM images of a) initial (unreacted) nanoparticles, b) after five spikes of 4-ClNB for 0.325 g/L goethite, 1 mM Fe(II) and pH 7, and c) after five spikes of 4-ClNB for 0.325 g/L goethite, 1 mM Fe(II), pH 7, and 10 ppm SRNOM. Scale bars are equal.

Quantifying oxidative mineral growth

The dynamics of oxidative mineral growth of goethite nanoparticles was dependent on the reaction conditions, with slower reactions leading to shorter and wider particles after five spikes of 4-ClNB. The presence of organic matter had the largest impact on the relative reactivity of goethite crystal faces, resulting in the shortest and widest particles. Examples of measured TEM images are shown in Figure 2.3. Immediate observations suggest elongation of the particles in both samples after five 4-ClNB spikes compared to the initial particles, although significant differences between the two post-Spike 5 samples were not easily observable by eye. Statistical analyses were therefore necessary to explore the effect of reaction conditions on oxidative goethite growth.

Average length and width measurements (Table 2.2) demonstrated that length increased gradually with the number of 4-ClNB spikes, regardless of the reaction conditions. Direct comparisons between reaction conditions were difficult to summarize given the large standard deviations in the averages, therefore histograms were plotted (Figure 2.4) and statistically compared using the nonparametric K-S test. Length histograms for the last measured spike of 4-ClNB in each reaction condition were statistically compared to the length histogram for the fifth spike of 4-ClNB in the reference condition. In Figure 2.4, this process is visualized as the comparison between the solid black line for $G_{325}Fe_1pH_7$ length and the solid black line for length for the other four reaction conditions. The same process was then repeated except for the width histograms. The K-S test was applied with the hypothesis that lengths or widths are different from the reference condition, providing a test statistic *D*, which corresponded to

the extent of difference between the two histograms, and *p*, the probability that the two histograms are statistically the same. Much like reaction rate, the dynamics of oxidative mineral growth were strongly dependent on the reaction conditions. Relative differences are evident through the magnitude of *D*, where a larger *D* means that the histogram is more different from that of the reference condition ($G_{325}Fe_1pH_7$). Differences between each condition, therefore, followed:

$$G_{325}Fe_1pH_7 \approx G_{325}\mathbf{Fe_{0.5}}pH_7 < \mathbf{G_{163}Fe_{0.5}}pH_7 \approx G_{325}Fe_1\mathbf{pH_{6.5}} < G_{325}Fe_1pH_7\mathbf{NOM_{10}}$$

In other words, the reaction condition that caused the most difference in length (negative difference, shorter) and width (positive difference, wider) was added SRNOM. In other words, goethite particles in the presence SRNOM have a faster growth rate on side facets and slower growth rate on tip facets compared to those in the absence of SRNOM, holding all other variables constant.

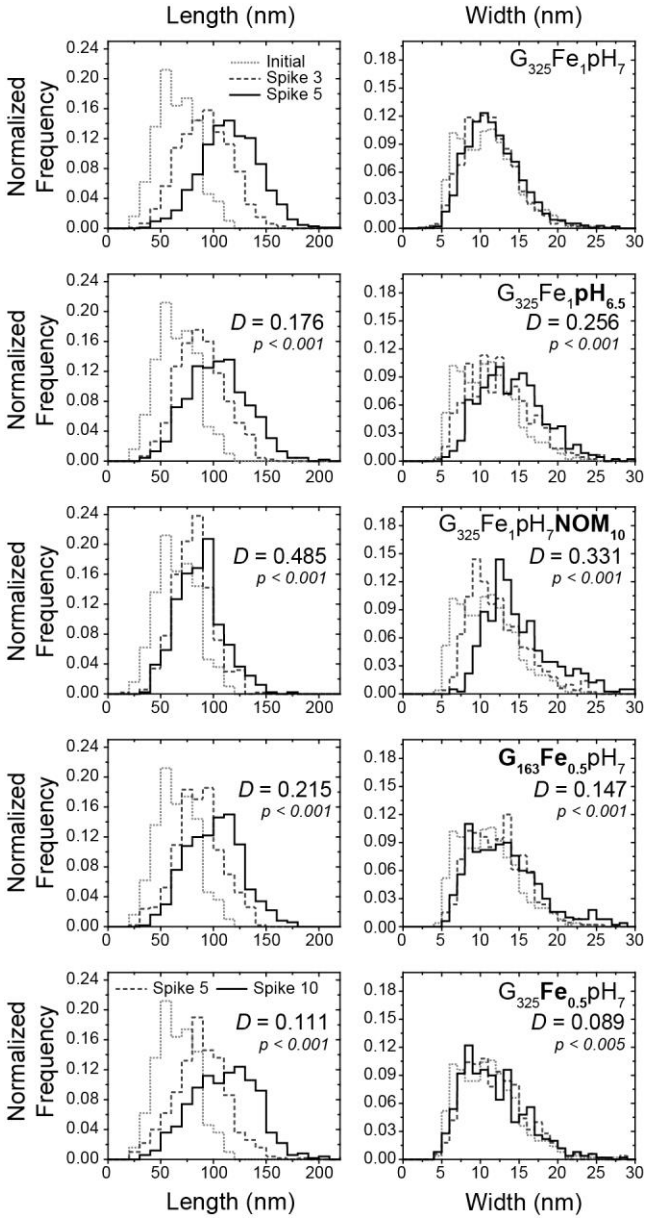

Figure 2.4: Normalized frequency of goethite length and width reacted with 4-ClNB in different reaction conditions compared to the initial goethite nanoparticles (dotted line). Reference conditions were 0.325 g/L goethite, 1 mM Fe(II):0.1 mM 4-ClNB, pH 7, and 0 ppm SRNOM ($G_{325}Fe_1pH_7$). Top four sets are measurements after Spike 3 (dashed line) and Spike 5 (solid line). Last set ($G_{325}\mathbf{Fe_{0.5}}pH_7$) are measurements after Spike 5 (dashed line) and Spike 10 (solid line). The relative extent of difference, *D*, between the corresponding Spike 5 (or 10) to the reference condition Spike 5 and the probability, *p*, that the two histograms are statistically the same are provided. Larger *D* values indicate greater difference from the reference condition.

Protocols were established to eliminate bias in the measurement of particle lengths and widths. Besides setting extensive criteria for collecting representative data, several controls were implemented (data in Appendix C). By encoding the image file labels, any tendency to measure certain samples in a predisposed way given the knowledge of sample identity was eliminated. In addition, measurements from three different trials of $G_{325}Fe_1pH_7$ show little variability in length and width histograms (Figure B.4). The uncertainty for both length and width measurements was ~ 1.3 pixels, equivalent to ~ ± 0.8 nm at the magnification in this study (Table B.1). Finally, resultant length and width histograms from two TEM grid preparation techniques were compared. In our previous works, grid preparation involved sampling directly from the reactor, diluting, and drop-casting on a TEM grid.[17,18] This method resulted in grids with highly aggregated particles induced by drying, making measurements especially tedious. Here, particles were first washed and dried before grid preparation. The same sample prepared using these two different methods showed very little difference in length and width histograms (Figure B.5). While the averages were nearly identical, there was some variation in width distributions. In this work, measurements were easier to obtain and perhaps even more accurate given reduced aggregation. Thus, consistency in technique was critical.

Due to the duration of the sequential-spike experiments (~ 2 – 3 weeks), the effect on goethite lengths and widths from extended contact with Fe(II) and carbonate buffer at pH 7 was investigated. Histograms (Figure B.6) reveal that the Fe(II)/goethite system was

relatively unreactive when 4-ClNB was absent. Consequently, the observed particle growth seen in the sequential-spike batch reactors must be the result of oxidative mineral growth caused by the reaction of Fe(II) and 4-ClNB.

Factors controlling relative reactivity of goethite crystal faces.

These results suggest that the surface-mediated reactions between Fe(II)/goethite and NACs are even more complex than previously understood. While changes in several parameters (e.g., rate constant) have been attributed to changes in solution conditions, these results demonstrate that even the relative reactivity of certain crystal faces are also dependent on common environmental variables. Compared to the reference conditions, particles were shorter and wider when the pH was more acidic, organic matter was added, and the Fe(II), goethite, and 4-ClNB concentrations were decreased by a factor of two. The pseudo-first order reaction rates for these conditions were also slower. In contrast, when goethite mass loading was left the same but the Fe(II) and 4-ClNB concentration decreased, the reaction rate was faster and the particles were less different from the particles reacted in the reference condition. Reaction rate (or blockage/reduction in the number of highly reactive sites), therefore, appears to be a controlling factor in the oxidative mineral growth of goethite, specifically the crystal face on which reaction occurs.

Another controlling factor may be the pH and point of zero charges for each crystal face. Weidler et al. discussed the favorable atomic structure of the {021} faces for Fe(II) adsorption but emphasized that the relative reactivity of each goethite face is dependent on several factors, including surface charge and pH.[34] Others have explored

the point of zero charges, proton affinities, and Fe(II) adsorption capacities for goethite crystal faces, although values vary depending on the applied model and set parameters.[35–38] Goethite commonly forms acicular particles, elongated in the c-direction, meaning the {021} faces are observably the most reactive sites, with the edge faces {110} and {100} less reactive. Our results demonstrate that {021} is still reactive but the ratio of {021}:edge reactivity varies in different conditions. Barrón and Torrent determined that the surface hydroxyl density was 8.2 and 3.0 m^{-2} for {021} and {110}, respectively.[39] A larger proton affinity for {021} could therefore make growth on the edge {110} faces more favorable in acidic pH, due to displacement of Fe(II) from the {021} face.

The addition of 10 ppm SRNOM had the largest effect on the length:width growth ratio (i.e., shortest and widest particles after five spikes of 4-ClNB). The exact mechanism of SRNOM attachment or interaction on goethite nanoparticles remains unknown. Due to the complex structure of organic matter, few studies have conclusively modeled trends in organic matter affinities for different goethite crystal surfaces. Despite this, there is general agreement that ligand exchange is possible between organic matter, particularly carboxylic functional groups, and goethite surface hydroxyl groups.[40,41] With the higher surface hydroxyl density on the {021} than on {110}, this could lead to preferential inhibition of Fe(II) adsorption on the acicular tips and thus decreased {021} reactivity. This is supported by our length and width measurements, which demonstrate that the {110} becomes more reactive in the presence of added organic matter.

In addition, the volume of goethite produced was estimated from average length and width measurements in Table 2.2 (assuming a density of 4.26 g/cm^3 for goethite[27]

and a cross-sectional rhombus composed only of {110} faces[28]) to calculate experimental Fe(III) produced, which was compared to theoretical values based on reaction stoichiometry (Figure B.7). The reaction conditions that resulted in wider particles (**$G_{325}Fe_1$pH$_{6.5}$** and $G_{325}Fe_1pH_7$**NOM$_{10}$)** overestimate the amount of Fe(III) produced. This is likely because if {100} faces are present, the assumption of a rhomboid shape composed only of {110} faces leads to an overestimation of the cross sectional area (and thus volume), especially because growth on {110} faces would result in expansion of the {100} faces as the reaction proceeds (see schematic in Figure B.7).

This work demonstrated that oxidative goethite growth in the reduction of NACs is dependent on the reaction conditions, such as pH, organic matter, and reactant concentration. While oxidative mineral growth on the {021} faces occurred in all cases, slower reactions had relatively more reactive {110} side faces than faster reactions and therefore particles grew statistically wider as well. This was observed for more acidic pH and dilute reactant concentrations. Organic matter, while also causing slower reaction rates, interfered to a greater extent, preferentially blocking or complexing to the more reactive {021} sites and therefore the {110} faces were relatively more reactive than for the other slower reaction conditions.

With these results, the redox transformations of NACs or other oxidized contaminants by adsorbed Fe(II) on iron oxides nanoparticles, including both the reaction efficiencies and nanoparticle properties, are more complicated at a mechanistic level. Not only will estimates of reaction rate be affected by groundwater chemistry, predictions of iron oxide nanoparticle fate and transport will be greatly influenced by the environmental

conditions. Differences in growth of certain crystal faces may influence the aggregation state of the reacted nanoparticles and subsequently the colloidal stability in groundwater systems. On the other hand, the assumption that the initial reactive sites on iron oxides are equivalent to the reacted sites may not hold if oxidative mineral growth influences the chemistry of the surface. Additionally, the reaction efficiency of goethite did not decrease with continuous exposure, although this was only observed for the 5 – 10 spikes administered. With longer reaction, reaction efficiency may change from a variety of factors, including evolving particle morphologies, aggregation state, or adsorption capacity. The evolving reactivity of goethite, therefore, may be more difficult to predict than previously thought.

Acknowledgments

This work was supported by National Science Foundation grant ECS-1012193 (R.L.P. and W.A.A.) and the Graduate School Doctoral Dissertation Fellowship at the University of Minnesota (J.H.S.). Magnetic characterization was performed at the Institute for Rock Magnetism (IRM) at the University of Minnesota with assistance from Becky E. Strauss. The IRM is a US National Multi-user Facility supported through the Instrumentation and Facilities program of the National Science Foundation, Earth Sciences Division, and by funding from the University of Minnesota. Parts of this work were carried out in the Characterization Facility, University of Minnesota, a member of the NSF-funded Materials Research Facilities Network (www.mrfn.org) via the MRSEC program.

Chapter 3. Influence of kaolinite on the reduction of 4-chloronitrobenzene by Fe(II) in goethite-kaolinite heterogeneous suspensions

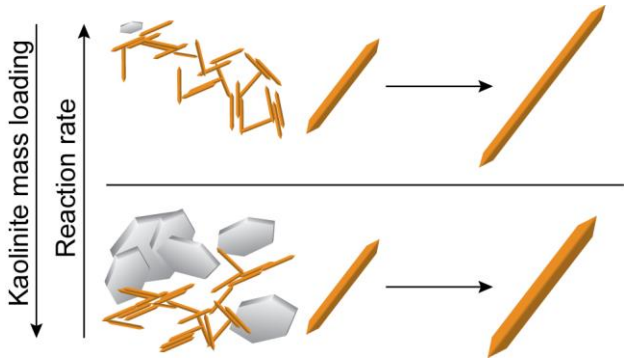

This chapter describes the outcome of a research project carried out by Jennifer H. Strehlau, Jonathan D. Schulz, and Amanda M. Vindedahl advised by William A. Arnold and R. Lee Penn. Supporting information is located in Appendix C.

Summary

The surface-mediated reduction reactions of Fe(II) adsorbed on iron oxides are important for groundwater systems, which contain both natural and anthropogenic oxidized molecules. The effect of heterogeneous mineral mixtures on these reactions is less understood, despite being environmentally relevant. The effect of kaolinite ($Al_2Si_2O_5(OH)_4$), a clay mineral, on the reactions of Fe(II) and 4-chloronitrobenzene (4-ClNB) in goethite (α-FeOOH)-kaolinite suspensions was explored. Increasing the amount of kaolinite present decreased the reduction rate of 4-ClNB and competitive Fe(II) adsorption on kaolinite occurred. Cryogenic transmission and scanning electron microscopy (cryo-TEM and cryo-SEM) images did not reveal significant loss of accessible reactive surface area as a result of heteroaggregation. Sequential-spike batch reactors revealed that in the presence of kaolinite, 4-ClNB reduction rate decreased with extended reaction, the result of kaolinite dissolution and consequential incorporation of Al and Si in goethite or on the goethite surface. The reactive sites residing on the {110} faces were therefore relatively more reactive in the presence of a large loading of kaolinite, resulting in shorter and wider goethite particles after reaction. These results elucidate the mechanisms by which nonreactive clays affect the reactions of Fe(II)/iron oxides in aquatic systems, indicating that nonreactive clays are not passive participants.

Introduction

Fe(II) adsorbed on iron oxides affects the reduction of oxidized molecules in groundwater systems, including nitroaromatic compounds (NACs) which are commonly used as explosives and pesticides.[1–3] In these systems, Fe(II)-Fe(III) electron transfer

occurs at the iron oxide-water interface, leading to lower reduction potentials.[4] Through a similar mechanism, iron-containing clay minerals can also serve as effective reductants.[5–8] Because clay minerals are commonly found in sediments that are rich with iron oxides,[9] the effect of heterogeneous clay-iron oxide mixtures on the reduction of oxidized molecules by Fe(II) are important for predicting reactions in the natural environment. The mechanisms by which nonreactive clays, such as kaolinite ($Al_2Si_2O_5(OH)_4$) and other clays that contain no or trace redox active metal cations, affect the redox reactions of Fe(II) in mixed mineral suspensions with iron oxides have not yet been studied. Potential mechanisms by which nonreactive clays could influence redox reactions on iron oxide surfaces include reducing available Fe(II) or NAC by adsorption onto the nonreactive mineral surface, poisoning reactive surfaces by dissolved species produced by clay dissolution, or decreasing accessible surface area of reactive surfaces by way of heteroaggregation.

Firstly, competitive adsorption of certain ions and NACs has been previously shown for heterogeneous suspensions containing clays and iron oxides. For instance, co-adsorption of various ions (e.g., phosphate, Pb(II)) has been modeled and experimentally determined for kaolinite in the presence of iron oxide minerals,[10–12] but Fe(II) adsorption in iron oxide-kaolinite heterogeneous systems has not been presented. Additionally, adsorption of NACs on kaolinite has also been demonstrated, particularly for substituted kaolinites.[13,14] Secondly, dissolution of aluminosilicate minerals can occur at circumneutral pH.[15] The release of Al and Si ions would alter the solution chemistry, and the presence of Al and Si ions during iron oxide growth has been shown to affect the size,

morphology, and composition of resulting particles, which may in turn alter the relative reactivity of iron oxide surfaces for reduction of NACs by Fe(II).[16,17]

Lastly, heteroaggregation, or the formation of aggregates composed of a heterogeneous mineral mixture, could decrease the number of accessible reactive surface sites.[18–20] Points of zero charge depend on various factors, but iron oxides are generally neutral at pH 6 – 9 and kaolinite at pH 3 – 4.[21,22] At circumneutral pH, therefore, these two minerals could be expected to heteroaggregate based on attractive surface charges. The best technique for directly imaging aggregates as they exist in aqueous suspension is cryogenic microscopy,[23] such as cryogenic transmission and scanning electron microscopy (cryo-TEM and cryo-SEM). Cryogenic microscopy has been previously used to study aggregation in solely iron oxide aqueous suspensions,[24,25] but few have imaged mixed iron oxide-clay suspensions in their native state using cryo-SEM.[26] At this time, no studies have been found that provide cryo-TEM images of clay-iron oxide suspensions in solutions with chemistry similar to groundwater.

The objective of this work was to elucidate mechanisms by which nonreactive clays affect the surface-mediated redox reactions of Fe(II)/iron oxides in groundwater systems. The kinetics of 4-chloronitrobenzene (4-ClNB) reduction by Fe(II) in suspensions containing goethite (α-FeOOH) and/or kaolinite were quantified. Cryogenic SEM and TEM were used to examine the aggregation state of the suspended mineral particles. The oxidative growth of goethite was quantified from calibrated TEM images and the relative rates of growth along and perpendicular to the long axis of the goethite particles quantified. The results, coupled with elemental analysis of supernatants,

demonstrate that the most important control parameter is the solution chemistry, with dissolved species generated by partial dissolution of the kaolinite particles serving to alter the relative reactivity of goethite crystal faces. The results offer novel insight into the influence of nonreactive clay minerals in iron oxide suspensions at different stages of reaction with NACs.

Experimental

Materials

Chemicals were purchased from the following sources: $FeCl_2 \cdot 4H_2O$, NaOH, methanol, and acetonitrile from Fisher, HCl from BDH Aristar, ammonium acetate and H_2SO_4 from Mallinckrodt, $NaHCO_3$ from Sigma Aldrich, and ferrozine from Alfa Aesar. All solvents were HPLC grade. Ultrapure water (18.2 MΩ·cm, Milli-Q) was the only water source used. Acrodisc syringe filters (0.2 μm nylon membrane) were purchased from PALL Life Sciences. Goethite nanoparticles were prepared by the method of Anschutz and Penn and stored at 4 °C in Milli-Q water with known mass loading.[27] Well-crystallized kaolinite (KGa-1b, Washington County, Georgia) was purchased from The Clay Mineral Society with characterization provided by Pruett and Webb.[28] Kaolinite stock suspensions were prepared fresh by weighing kaolinite in 20 mL scintillation vials and diluting with ultrapure water. A concentrated stock (80 g/L) was used for preparation of reactors with high kaolinite loadings. When the desired mass loading was low, a dilute stock (8 g/L) was prepared by diluting the concentrated stock. Magnetic stirring was maximized to eliminate settling effects. Controls were performed periodically to ensure that the delivered volume provided the expected mass of kaolinite.

Single-spike reactors

All reactions were performed in an anaerobic environment (Coy glovebag, 95% N_2/5% H_2) and prepared in 10 mM carbonate buffer at pH 7, made on the same day by adding 0.840 g $NaHCO_3$ to 1 L ultrapure water and adjusting pH with 1 M H_2SO_4. Five 120 mL glass reactors were prepared, including one with no minerals, one with only 0.325 g/L kaolinite, one with only 0.325 g/L goethite and two mixed mineral suspensions (0.325 g/L goethite with either 0.05 or 2 g/L kaolinite). The final reactor volume was 120 mL. The general procedure for reactor preparation included adding the appropriate amount of goethite stock suspension to the reactors, followed by the necessary amount of kaolinite stock suspension. Carbonate buffer was added to reach 118.11 mL and the reactors were immediately capped with Teflon plugs to prevent outgassing. To each reactor, 0.686 mL of a fresh stock solution of 175 mM Fe(II) made from $FeCl_2 \cdot 4H_2O$ in 30 mM HCl was added (reactor concentration of 1 mM Fe(II)). After the reactors were magnetically stirred for 21 – 24 hours, 1.2 mL of a 10 mM methanolic 4-ClNB solution was spiked in to initiate the reaction (initial reactor concentration of 0.1 mM 4-ClNB).

After the initial spike of 4-ClNB, samples were withdrawn periodically over 2 h using a plastic syringe and filtered into amber glass HPLC vials. An Agilent 1100 Series system with UV detector and Zorbax SB-C18 column (4.6 mm × 150 mm, 5 μm) was used to quantify 4-ClNB concentration from a five-point calibration curve (0.02 – 0.1 mM). HPLC parameters included a 20 μL injection, 70% acetonitrile and 30% ammonium acetate (1 g/L, pH 7) mobile phase, detection wavelength of 254 nm, and 7 min separation time.

When the effects of kaolinite dissolution were tested, the same amount of kaolinite stock suspension was added during reactor preparation except filtered beforehand. To a 20 mL scintillation vial, filtrate was added from ~ 5 mL of the kaolinite stock suspension (either 1 or 7 d old) using a 0.2 μm nylon membrane. Then, the appropriate amount of the filtrate was added directly to the reactors.

Fe(II) quantification

Fe(II) adsorption was determined using a ferrozine colorimetric assay.[29] For adsorption capacity in each reactor, ~ 1 mL of a prepared reactor described above before 4-ClNB addition was filtered into a vial for analysis. For adsorption isotherms, separate vials containing various mass loadings (0 – 2 g/L) of goethite or kaolinite were prepared anaerobically in the carbonate buffer (15 mL total volume). To each vial, 0.2 mL of 175 mM Fe(II) was spiked and equilibrated for 21 h before samples (~ 1 mL) were withdrawn and filtered for analysis. The general procedure for ferrozine analysis added 0.2 mL filtrate, 2.4 mL Milli-Q water, and 0.2 mL ferrozine stock solution (5 mg/mL in Milli-Q water) into a polystyrene cuvette. Each cuvette was capped, inverted three times, removed from the glovebag, and analyzed with an Agilent 8452 UV-Visible spectrometer at 562 nm. Aqueous Fe(II) was quantified from a five-point calibration curve (0.01 – 0.08 mM) and average adsorbed Fe(II) calculated from the difference between controls that contained no particles and resultant aqueous Fe(II) from three trials.

Sequential-spike batch reactors

Triplicate sequential-spike batch reactors were prepared in a process identical to the single-spike experiments. Two mixed mineral systems were tested, 0.05 or 2 g/L

kaolinite with 0.325 g/L goethite, for a total of six reactors for one trial (3 reactors × 2 mass loadings). After preparation, Fe(II) addition, and equilibration as described above, 4-ClNB (0.1 mM) was added to all six reactors, defined herein as a 4-ClNB spike. One reactor of each kaolinite loading was then sacrificed for analysis, which included sampling for HPLC and solid collection (described below). The other reactors were sampled minimally (1 – 3 times) to monitor the reaction progress. Once 4-ClNB concentration was < 0.001 mM, the remaining aqueous Fe(II) was quantified, the pH raised to 7 using 0.5 M NaOH, and the appropriate amount of Fe(II) stock added to replenish the reactor back to 1 mM Fe(II). After 21 – 24 h equilibration, the pH was checked to ensure a value of 7.0 ± 0.1 and the second spike of 4-ClNB was added. This process was repeated for a total of five 4-ClNB spikes, sacrificing reactors after one, three, and five 4-ClNB spikes.

Filtrates of suspensions from both kaolinite loadings after one and five spikes of 4-ClNB were analyzed by inductively coupled plasma optical emission spectroscopy (ICP-OES) to quantify dissolved Si and Al concentrations. Additionally, a separate experiment involved adding 0.325 g/L goethite and 1 mM Fe(II) to a 250 mL Erlenmeyer flask, diluted to 200 mL with carbonate buffer. In a dialysis membrane, 20 mL of a 22 g/L kaolinite suspension in the same carbonate buffer was added (the equivalent amount for 2 g/L in 220 mL). The membrane was closed and added to the flask containing goethite. The flask was capped and stirred magnetically inside the glove bag. After 14 d, ~ 5 mL of the goethite suspension was filtered for ICP-OES analysis. The solid goethite was collected as described below and analyzed by ICP-OES. Major elemental analyses of

filtrates and solids were performed using a Thermo Scientific iCAP 6500 duo optical emission spectrometer with simultaneous charge induction detection from five replicate sample injections. Samples were acidified prior to analysis and an internal standard of yttrium was added.

Solid collection and characterization

Solid collection included centrifuging (7000 rpm for 3 min), washing (3 × 20 mL ultrapure water), and air drying the particles. Post-reaction solids for goethite reactors containing 0.05 or 2 g/L kaolinite after five spikes of 4-ClNB were characterized by low-temperature magnetic characterization (10 – 300 K) on a Quantum Designs Magnetic Property Measurement System (MPMS) cryogenic magnetometer (10^{-10} Am^2 sensitivity) with a 2.5 T applied field for field cooled-zero field cooled (FC-ZFC) analyses.

Microscopy

Conventional TEM was performed on a FEI Tecnai T12 TEM microscope at 120 kV with a LaB_6 electron source and Gatan charge-coupled device (CCD) camera. Samples were prepared by diluting ~ 10 μL of reactor suspension to 1 mL, sonicating 20 s, and air drying a single drop on a holey carbon 200 mesh copper grid (SPI Supplies). Goethite length and width measurements (~ 500 particles per sample) were collected from a minimum of 20 images at 4 grid locations and the same magnification using ImageJ (National Institute of Health, v1.47). Cryo-TEM was performed using a FEI Technai G^2 Spirit BioTWIN TEM with a LaB_6 source and Eagle 2k CCD camera. Grids were prepared by dropping ~ 3 μL of sample on a 3 mm 200-mesh lacey carbon coated copper grid (SPI Supplies), blotting with filter paper for 1 s using a Vitrobot Mark IV

(FEI), plunging into liquid ethane, and transferring to a cryo-TEM holder under liquid nitrogen. Grids were imaged at 120 kV on a cryo stage.

Conventional SEM was performed on a Hitachi S-4700 SEM microscope with cold field emission gun at 3 kV. Samples were prepared by drying a drop of the reactor suspension directly onto copper tape. Cryo-SEM was performed on the same microscope, imaged at 3 kV and -160 °C. A drop of reactor suspension was placed on a Si wafer chip (5 × 7 mm), which was previously scored in the center and cleaned by 30 sec of plasma glow discharge in a DV-502A Denton Vacuum system. The chip was then manually plunged into liquid ethane and transferred immediately to liquid nitrogen. Under liquid nitrogen, the chip was placed into a cryo-SEM sample holder and cracked in half along the score with precooled tweezers, revealing a cross section of the sample. The sample holder was then cryogenically moved to an Emitech K-1250 Cryo Preparation Unit, sublimed at -96 °C for 10 min, sputtered with Pt (~ 2 nm layer), and transferred to the microscope for imaging.

Results and discussion

Effect of kaolinite on initial 4-ClNB reduction by Fe(II)/goethite

Pseudo first-order rate constants (k_{obs}) of 4-ClNB reduction by Fe(II) for the goethite-containing reactors are provided in Table 3.1. Initial reduction rate of 4-ClNB by adsorbed Fe(II) on goethite was slower in the presence of 2 g/L kaolinite. Three viable hypotheses that could explain the decrease in reactivity are adsorption of 4-ClNB or Fe(II) onto kaolinite, which may limit the availability of 4-ClNB or Fe(II) at the goethite-water interface; heteroaggregation, which could effectively sequester some goethite

surface area from the aqueous medium; and kaolinite dissolution, which would result in the production of dissolved species that could interfere with Fe(II) adsorption or oxidation.

Table 3.1: Average pseudo-first order rates for 4-ClNB reduction by Fe(II) adsorbed on goethite and resultant length and width measurements in suspensions containing goethite (0.325 g/L) and various kaolinite mass loadings. Reactions were performed in 10 mM carbonate buffer at pH 7 with initial Fe(II) concentration of 1 mM.

Kaolinite (g/L)	Stage	k_{obs} (h^{-1})	Length (nm)	Width (nm)	N
0	Before reaction	NA	110 ± 41	12 ± 5	500
	Spike 1	0.75 ± 0.04	NM	NM	NM
0.05	Spike 1	0.74 ± 0.04	NM	NM	NM
	Spike 3	0.42 ± 0.04	146 ± 46	12 ± 5	500
	Spike 5	0.26 ± 0.01	177 ± 56	13 ± 4	405
2	Spike 1	0.55 ± 0.05	NM	NM	NM
	Spike 3	0.11 ± 0.01	133 ± 41	14 ± 4	413
	Spike 5	0.069 ± 0.006	157 ± 46	18 ± 4	473

Rate constants were determined by linear regression, where errors are the 95% confidence intervals and R^2 values were greater than 0.98.
For lengths and widths, errors are the standard deviations and N is the number of particles measured.
NA = not applicable.
NM = not measured.

Adsorption of 4-ClNB by kaolinite was not detected and reactors containing no particles or only kaolinite with 4-ClNB and Fe(II) were relatively unreactive (Figure C.1), evidence that Fe(II) adsorbed specifically on the goethite surface was the reductant. Kaolinite dissolution and the release of Al and Si ions has been previously observed and kinetically modeled at circumneutral pH.[15,30,31] In this study, when Fe(II), goethite, and 4-ClNB were reacted in the presence of the filtrate from the kaolinite stock suspension which was equilibrated for < 1 day, no differences in reactivity were observed (Figure C.2). Filtrate from the kaolinite suspension after 7 days of equilibration, however, resulted in a slight decrease in reaction rate. Kaolinite dissolution over time and resultant variations in solution chemistry could influence Fe(II)/goethite reactivity for aged

systems, such as in the sequential-spike experiments or natural environmental settings, but not on the single-spike reactions, which are freshly prepared and reacted in < 2 days.

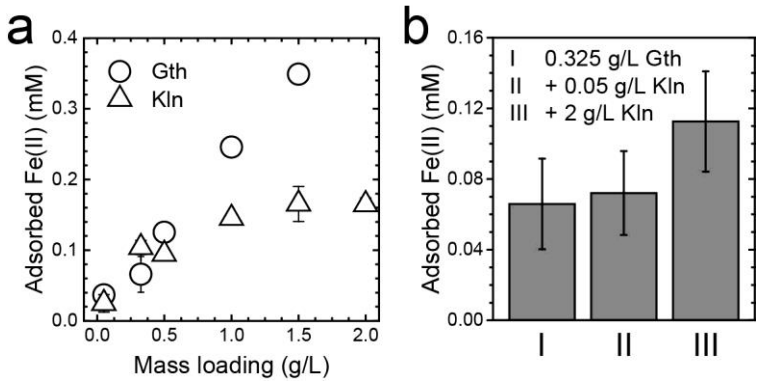

Figure 3.1: a) Fe(II) adsorption isotherms on either goethite (Gth) or kaolinite (Kln) as a function of particle mass loading. b) Adsorbed Fe(II) in systems containing, I: 0.325 g/L Gth only, II: 0.325 g/L Gth with 0.05 g/L Kln, or III: 0.325 g/L Gth with 2 g/L Kln. Error bars are the standard deviations from triplicate trials. Both studies were performed in 10 mM carbonate buffer at pH 7 with an initial Fe(II) concentration of 1 mM.

Competitive Fe(II) adsorption between goethite and kaolinite was quantified through adsorption isotherms and measurement of adsorbed Fe(II) in the reactors (Figure 3.1). Adsorption isotherms (Figure 3.1a) as a function of particle mass loading revealed that both goethite and kaolinite adsorbed Fe(II) in the 10 mM carbonate buffer at pH 7. In the reactors (Figure 3.1b), those with only goethite and those with goethite and 0.05 g/L kaolinite had similar adsorption capacities for Fe(II). When kaolinite loading was 2 g/L, a greater amount of Fe(II) was adsorbed, consistent with co-adsorption of Fe(II) by goethite and kaolinite. Competitive adsorption of Fe(II) on kaolinite could influence the competition for reactive sites on goethite, therefore decreasing the reaction kinetics of 4-ClNB reduction.

Although Fe(II) adsorbed onto kaolinite, it was still relatively unreactive towards 4-ClNB (Figure C.2). In contrast, Klausen et al. described the detectable reactivity of Fe(II) on kaolinite towards similar NACs.[1] The difference between the study described here and that of Klausen et al. could be the source of kaolinite (i.e., extent of iron isomorphic substitution) and/or the production of an iron oxide coating as stated in Klausen et al., both of which would lead to increased NAC reduction rates. The results shown in this study demonstrated that certain kaolinite samples can serve as nonreactive competitors for Fe(II) sorption in a heterogeneous mineral system, thereby influencing overall rates of reduction by reducing the number of Fe(II) species on the iron oxides.

Finally, heteroaggregation is possible given the attractive electrostatics of goethite and kaolinite in aqueous media at pH 7, which may decrease the accessible surface area of goethite for reaction. Figure 3.2a and 3.2b show representative images using conventional SEM and TEM, respectively. While it appeared that considerable heteroaggregation occurred, conventional microscopy cannot directly reveal particle aggregates in their native state due to drying effects, such as aggregation induced from the removal of the solvent.[23] Thus, the application of cryogenic techniques was critical to obtaining accurate representations of aggregation state.

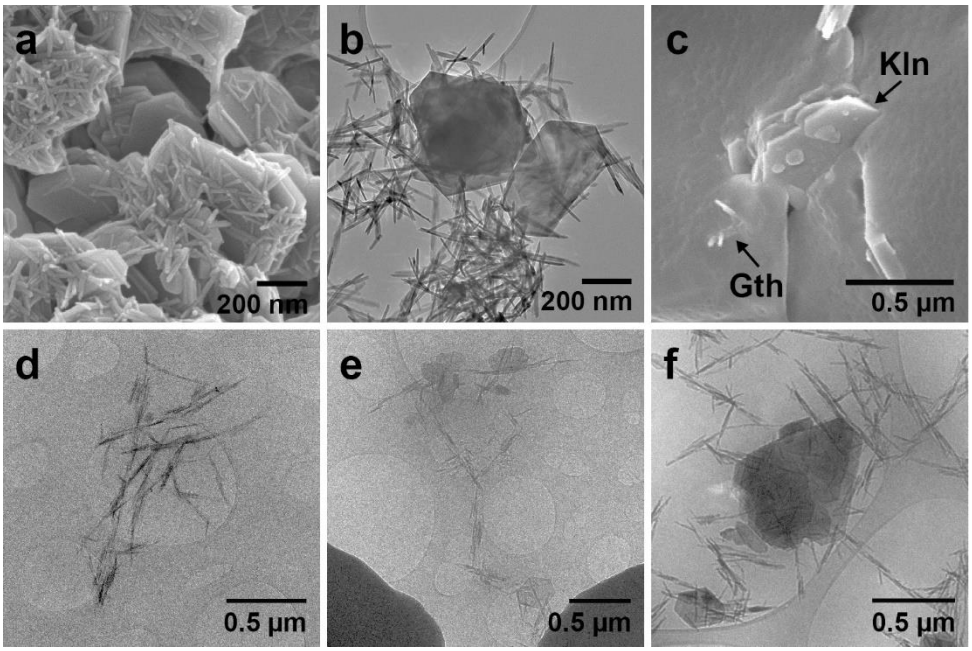

Figure 3.2: Images of goethite (Gth) and kaolinite (Kln) mixed-mineral suspensions in 10 mM carbonate buffer at pH 7 using microscopic techniques at different mass loadings. (a-c) Goethite and kaolinite (0.325 g/L of each) taken by a) SEM, b) TEM, and c) cryo-SEM. (d-f) Cryo-TEM images of 0.325 g/L goethite and either d) 0.05 or e-f) 2 g/L kaolinite.

Cryo-SEM (Figure 3.2c) was used due to the larger particle size of kaolinite, although the methodology is not yet developed for aqueous clay-iron oxide suspensions similar to the particle loadings used here. Thus, more work is needed to optimize sample preparation. The few images that were obtained did not show evidence of extensive heteroaggregation. In addition, the SEM was not equipped with energy-dispersive X-ray spectroscopy (EDS), making particle morphology and size the only two identifiers available to distinguish the larger kaolinite platelets and goethite acicular nanoparticles from the surrounding matrix.

Cryo-TEM images also did not provide evidence of extensive heteroaggregation or loss of accessible goethite surface area (Figure 3.3d-f). Kaolinite was distinguished from hexagonal ice formations by purposeful beam damage (examples in Figure C.3). Despite extensively searching through multiple grids, no kaolinite platelets were found in the cryo-TEM images of reactors containing goethite and 0.05 g/L kaolinite. In the reactors with 2 g/L kaolinite, all goethite aggregates were found in contact with at least one kaolinite platelet (forming heteroaggregates) but goethite aggregation state did not differ from those imaged in 0.05 g/L kaolinite, indicating minimal loss of accessible goethite surface area as a result of heteroaggregation. In addition, preferential heteroaggregation between goethite and either the basal planes or the edges of kaolinite was not observed.

As revealed primarily through cryo-TEM images, the extent of heteroaggregation in the goethite-kaolinite mixed-mineral reactors was minimal, which means heteroaggregation cannot explain the significant decrease in reduction rate of 4-ClNB by adsorbed Fe(II) on goethite in higher kaolinite loading. Therefore, competitive Fe(II) adsorption is the only cause with substantive evidence to explain the slower 4-ClNB reduction rates during single-spike reactions.

Relative reactivity of goethite crystal faces in suspension with kaolinite

Sequential-spike reactions were performed to provide sufficient reaction to quantify relative reactivity of goethite crystal faces as a function of kaolinite loading. Reduction rates for 4-ClNB in both 0.05 and 2 g/L kaolinite loadings decreased with each sequential spike of 4-ClNB (Figure 3.3, k_{obs} values provided in Table 3.1). We have

previously demonstrated that reduction rates in identical conditions except in the absence of kaolinite did not decrease with the number of 4-ClNB spikes,[32] therefore the presence of kaolinite was the controlling factor for the declining rates.

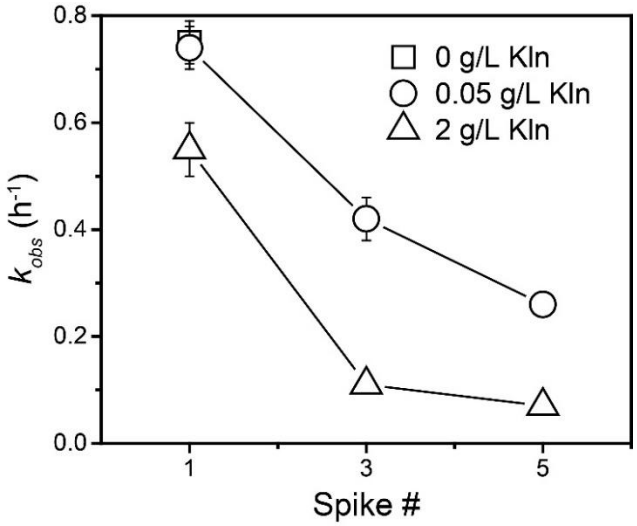

Figure 3.3: Pseudo first-order reduction rates of 4-ClNB in reactors containing goethite (0.325 g/L) and various loadings of kaolinite (0, 0.05, or 2 g/L Kln) as a function of the number of 4-ClNB spikes in 10 mM carbonate buffer at pH 7 and initial Fe(II) concentration of 1 mM.

A decrease in rate was observed when the filtrate from an aged kaolinite stock suspension was added to the goethite reactors (Figure C.2), therefore, it was hypothesized that kaolinite dissolution occurred in the sequential-spike reactors and that the released ions affected the surface chemistry of goethite. Several filtrates and solids were digested and analyzed by ICP-OES (Table C.1), revealing that Al and Si ion concentrations increased with the number of equilibration days. The dialysis experiment, which allowed goethite to contact dissolved ions of kaolinite but kept the two minerals separated by a dialysis membrane, demonstrated that the goethite particles also contained Al and Si after several weeks in suspension.

The similar ionic radii of Al and Fe(III) (0.67 and 0.78 Å, respectively[17]) suggest that Al could substitute into the goethite crystal structure, and aluminous goethite is known to occur naturally in sediments and can be synthesized in the laboratory.[33,34,16] Although the ionic size of Si (0.54 Å) is smaller than that of Al, its incorporation into the octahedral sites of goethite has been previously noted.[17,35] In all of these studies, the reactive properties of Al- or Si-goethite differed from its unsubstituted counterpart, depending on the extent of isomorphic substitution. For example, the amount of atom exchange and interfacial electron transfer in aluminous goethite was less than that for goethite.[16] In Quin et al., acicular goethite nanoparticles with 2.5 mole % Si were shorter in length as compared to goethite with no Si substitution, with preferential adsorption of Si ions occurring on the tips of the goethite. Similar variations in goethite nanoparticle morphology has been observed for Al-substituted goethite, with more Al substitution resulting in shorter and wider nanoparticles.[36] In this study, Al and Si incorporation into goethite or adsorption on the goethite surface led to fewer reactive surface sites, inhibition of interfacial electron transfer, or a combination of both, thereby decreasing observed 4-ClNB reduction rates.

The conclusion that extent of Al and Si substitution controlled 4-ClNB reaction rates was further supported by quantitative analysis of oxidative mineral growth, or formation of new goethite from produced Fe(III) on the existing particles. Oxidative growth occurred preferentially on certain goethite crystal faces depending on the amount of kaolinite present. No evidence of new particle nucleation was seen in conventional TEM images (Figure 3.4) and no magnetic transitions indicative of other iron oxide

mineral phases were present in magnetic analyses (Figure C.4) of solids after five spikes of 4-ClNB. Magnetic characterization was used over other more commonly applied techniques (e.g., X-ray diffraction) for its very low detection limit even when a large amount of kaolinite is present.[37] Both samples (goethite with 0.05 or 2 g/L kaolinite) have similar FC and ZFC curves when normalized to the maximum magnetization, and the minor differences are more likely attributed to variations in grain size and morphology than isomorphic substitution.[38]

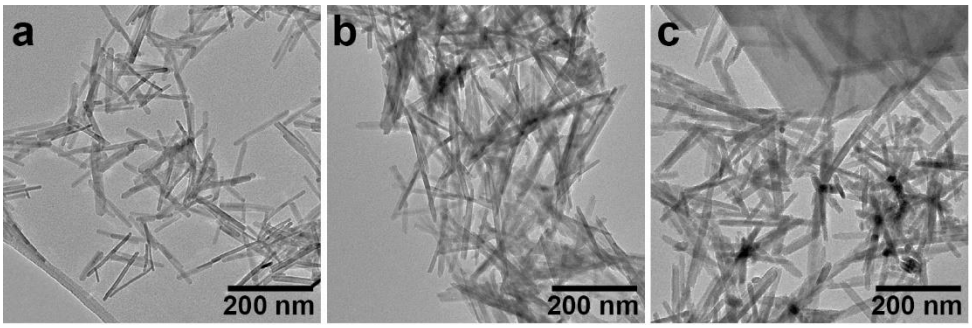

Figure 3.4: Representative conventional TEM images of 0.325 g/L goethite nanoparticles in 10 mM carbonate buffer at pH 7 either a) before reaction with 4-ClNB or b-c) after five spikes of 4-ClNB. b) 0.05 g/L kaolinite. c) 2 g/L kaolinite.

The conventional TEM images in Figure 3.5 show that goethite nanoparticles grew with the number of 4-ClNB spikes, with the particles becoming significantly longer. In previous work which quantified oxidative mineral growth for acicular goethite nanoparticles, growth dominated on the {021} faces located on the tips of the particles.[39] In the 2 g/L kaolinite reactors, however, goethite nanoparticles also appeared to grow on the edges, or {110} and {100} faces, in comparison to goethite in the 0.05 g/L kaolinite reactors. Goethite growth for each kaolinite loading was quantified from length and width measurements of goethite nanoparticles (Figure 3.5, averages and standard deviations

provided in Table 3.1). The histograms provide quantitative evidence that at both kaolinite loadings, growth on the {021} faces occurred. Goethite nanoparticles with 2 g/L kaolinite, however, grew relatively less long and significantly more wide with each 4-ClNB spike as compared to goethite particles with 0.05 g/L kaolinite.

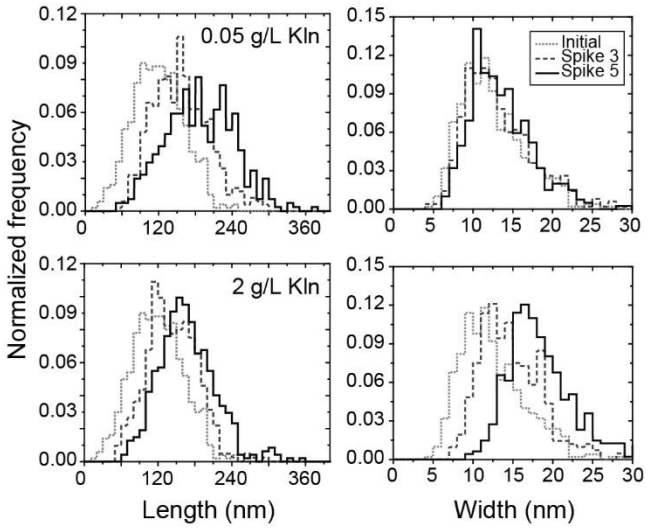

Figure 3.5: Histograms of goethite length and width measurements, normalized to the number of particles measured, in suspension with either 0.05 or 2 g/L kaolinite before reaction (initial), after three spikes of 4-ClNB, and after five spikes of 4-ClNB in 10 mM carbonate buffer at pH 7 and 1 mM initial Fe(II).

Given the results of chemical analyses and occurrence of kaolinite dissolution, isomorphic Al and Si substitution occurred simultaneously with oxidative goethite growth. Since oxidative growth is favorable on the {021} faces,[39] those sites may be initially susceptible to Al or Si incorporation. On the other hand, Si and Al incorporation or adsorption could be preferential on the {021} faces due to crystallographic constraints, as was seen for Si on goethite nanoparticles in Quin et al.[17] In both scenarios, oxidative

mineral growth on the side crystal faces of goethite would be more favorable than for goethite in the absence of dissolved Al or Si ions, forming shorter and wider goethite particles when more kaolinite is present. The results of the sequential-spike reactions demonstrated that even trace or slowly occurring changes in ionic composition and strength of aqueous media can drastically vary the reactivity of iron oxides in groundwater systems. In addition, these results emphasize the importance of including long-term studies when interpreting iron oxide reactivity in natural systems. Kaolinite dissolution, which led to Al and Si incorporation during oxidative growth, declining reaction rates, and variable goethite particle dimensions, was only observed after additional spikes of 4-ClNB were performed. Consideration of the variable particle dimensions following redox reactions with contaminants is especially important for current models predicting the transport of nanoparticles in environmental systems.

This study has demonstrated that the presence of nonreactive clay minerals like kaolinite can significantly affect the surface-mediated reactions of Fe(II) on iron oxides with NACs in groundwater systems. Fe(II) on kaolinite was not an effective reductant for 4-ClNB; thus, the mechanisms by which it affected the reactions between adsorbed Fe(II) on goethite and 4-ClNB was explored. Kaolinite initially only served as a competitor for Fe(II) adsorption, thus increasing competition for reactive sites on goethite and slowing 4-ClNB reduction rates. The first cryo-TEM images of a clay and iron oxide mixed-mineral (to the best of our knowledge) revealed that heteroaggregation did not affect the accessibility of goethite reactive sites at the explored particle loadings. Kaolinite dissolution had a greater effect on the Fe(II)/goethite system during reactions of longer

equilibration time, and Al and Si were incorporated into goethite during oxidative mineral growth, especially at higher kaolinite loadings. As a result, reactive sites were inhibited and 4-ClNB reduction rates slowed considerably with time. In addition, the incorporation of Al and Si varied the chemistry of the goethite crystal faces, with oxidative mineral growth occurring more on side crystal faces and less on the tip faces when the kaolinite loading was relatively higher.

In natural groundwater systems, clays that are nonreactive towards oxidized molecules should not be assumed as passive participants during interpretations of iron cycling in environmental systems. In other nonreactive clay and iron oxide systems, competitive Fe(II) adsorption, heteroaggregation, and/or clay dissolution may be more significant. While kaolinite and goethite did not heteroaggregate, other clays with greater negative surface charge at circumneutral pH may be more likely to heteroaggregate with positively charged goethite.[40] These interactions could impact the accessible surface area as well as the transport properties of iron oxides more so than the kaolinite-goethite mixed-mineral suspensions studied here. In addition, the extent of isomorphic substitution or crystal defects in kaolinite, or another nonreactive clay, as well as in the iron oxides themselves can greatly change its chemical and physical properties.[41,42] Further investigations and microscopic analyses of evolving reactivity in Al and Si substituted iron oxide suspensions will elucidate the specific mechanisms defining the relative reactivity of each goethite crystal face.

Acknowledgments

This work was funded by NSF grant ECS-1012193 (R.L.P. and W.A.A.), the Graduate School Doctoral Dissertation Fellowship at the University of Minnesota (J.H.S.), and the Undergraduate Research Opportunity Program at the University of Minnesota (J.D.S.). Cryo-SEM was performed with the invaluable assistance of Chris Frethem (Characterization Facility, University of Minnesota). Magnetic characterization was performed at the Institute for Rock Magnetism (IRM) at the University of Minnesota with support from Becky E. Strauss, Joshua M. Feinberg, and Mike Jackson. The IRM is a US National Multi-user Facility supported through the Instrumentation and Facilities program of the National Science Foundation, Earth Sciences Division, and by funding from the University of Minnesota. Analyses by ICP-OES were performed by Rick Knurr with the Analytical Geochemistry Lab, part of the Department of Earth Sciences at the University of Minnesota. Parts of this work were carried out in the Characterization Facility, University of Minnesota, a member of the NSF-funded Materials Research Facilities Network (www.mrfn.org) via the MRSEC program.

Chapter 4. Adsorption of humic substances on goethite observed by excitation-emission matrix (EEM) fluorescence spectroscopy with methylene blue

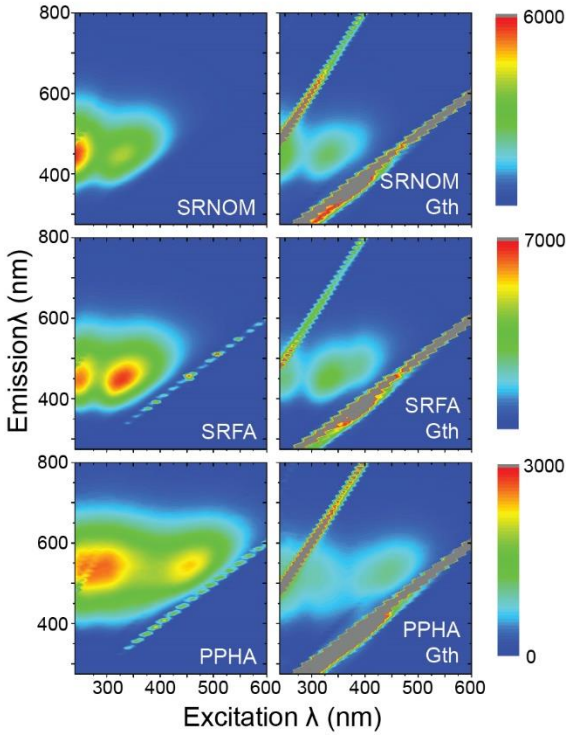

This chapter describes the preliminary data of a research project carried out by Jennifer H. Strehlau, Clare Johnston, and Andrew McCabe advised by William A. Arnold and R. Lee Penn.

Summary

The use of excitation emission matrix (EEM) fluorescence spectroscopy can elucidate organic matter adsorption onto reactive iron oxide surfaces, yet the effect of trace iron oxide nanoparticles in EEM spectroscopy is unknown. The following work details preliminary data quantifying humic substance (HS) adsorption on goethite nanoparticles by centrifuging HS-goethite (α-FeOOH) suspensions after various equilibration times. The supernatants, however, contained residual goethite nanoparticles (~ 0.5 – 3% of the original mass loading) which may quench HS fluorescence. Methylene blue was proposed as a possible internal standard, and while methylene blue-HS interactions were observed by EEM and UV-Vis spectroscopy, HS concentration was still quantifiable after EEM spectra were normalized to the maximum peak intensity of methylene blue. Methylene blue-goethite interactions have not yet been explored. Maximum adsorption of Suwannee River natural organic matter (SRNOM), humic acid (SRHA), and fulvic acid (SRFA) on goethite likely occurred within 2 h of equilibration, observed with and without normalization to the internal standard, and no fractionation was detected. Time was a constraint, therefore highlighting an important next step of performing these experiments in triplicate. In any case, these results present a novel and potentially promising characterization tool for quantifying OM adsorption and fractionation on iron oxide surfaces in environmental systems.

Introduction

Iron oxide nanoparticles in the presence of aqueous Fe(II) are known to mediate the reductive transformations of a variety of oxidized molecules in groundwater, including contaminants from agricultural and industrial sources.[1–6] The rate of reduction by Fe(II) increases when iron oxide mineral surfaces are present, with adsorption of Fe(II) resulting in a lowered reduction potential promoted by electron delocalization within the bulk mineral.[7–9] Reduction rate is dependent on the available surface area and amount of adsorbed Fe(II) on iron oxides. Nanoparticles of iron oxides, which occur naturally in many environments, contribute even higher specific surface areas compared to bulk minerals and are consequently of particular interest in these studies.[10–12]

It is well known that these surface-mediated reactions are influenced by certain solution variables (e.g., pH, ionic strength), which affect the properties and accessible reactive surface area of iron oxides.[13–15] The influence of organic matter, however, is less understood. Organic matter (OM) is a diverse component of all groundwater, produced by aquatic organisms or through the decay of terrestrial organic matter and composing of several fractions including humic and fulvic (smaller and more highly charged) acids.[16] The molecular structure of OM is complex, including various functional groups such as carboxylic acids, alcohols, esters, and amines, to name only a few.[17] Interactions between OM and iron oxide nanoparticle surfaces have been previously researched, although many questions regarding the extent and mechanisms of these interactions remain given the complexity of OM in natural systems.[18,19]

In the effort to describe OM properties and its interactions with other subsurface components like iron oxide nanoparticles, fluorescence spectroscopy has proven to be a promising tool. For instance, excitation-emission matrices (EEMs) not only provide intensity of fluorescence, which can be related to OM concentration, but also valuable information about the composition and molecular structure of OM from the matrix peak positions.[20,21] For these reasons, EEM spectroscopy offers several advantages for the characterization of OM, including high sensitivity and selectivity with rapid measurement times.[20] Several challenges exist, particularly in protocols for correction of instrument-response and solution variables that quench OM fluorescence.[22] For example, aqueous Fe(II) and Fe(III) are known to quench OM fluorescence in EEM spectroscopy.[23,24] To date, no works have presented similar effects on OM fluorescence by the presence of iron oxide nanoparticles in suspension with OM.

This work summarizes preliminary data toward elucidation of OM adsorption and fractionation processes on iron oxide nanoparticles using EEM fluorescence spectroscopy. The main goal was to describe the adsorption of various OMs (as purchased humic substances (HS) from the International Humic Substance Society) on goethite. Suspensions of goethite and HS were prepared, equilibrated for certain time periods, and centrifuged. Centrifugation allows for EEM characterization of the supernatant, which in theory would contain the fraction of HS that did not adsorb on goethite. Trace goethite nanoparticles in suspension, however, could affect measured HS fluorescence. A possible solution to this challenge will be an internal standard, and the following work details the potential use of methylene blue in EEM spectroscopy.

Although there is much work remaining, these results may lead to a novel route for characterizing complex OM-iron oxide interactions in environmental systems.

Experimental

Goethite-HS suspensions

Acicular goethite nanoparticles were prepared using the method of Anschutz and Penn[25] and have been previously characterized as 65 ± 18 by 11 ± 4 nm in size.[13] They were stored in suspension at 5 ºC with known mass loading (27.4 ± 0.1 g/L). All humic substances, including Suwannee River humic acid II (SRHA), Suwannee River fulvic acid II (SRFA), Suwannee River natural organic matter (SRNOM), Pahokee Peat humic acid (PPHA), and Pahokee Peat fulvic acid (PPFA), were purchased from the International Humic Substances Society. Only ultrapure water (Millipore, 18.2 Ω·cm) was used. All suspensions were prepared in fresh carbonate buffer, made by dissolving 0.841 g $NaHCO_3$ (Sigma Aldrich) in 1 L deoxygenated water and adjusting pH to 7 with 1 M H_2SO_4 (Mallinckrodt) on the same day as suspension preparation. Goethite-HS suspensions were prepared at different mass loadings and concentrations, depending on the nature of the study, as described below.

Methylene blue controls: To 20 mL scintillation vials, appropriate amounts of carbonate buffer and 20 ppm HS stock solution (in ppm organic carbon) were added in order to achieve a range of HS concentrations (0 – 10 ppm). When exploring the effect of methylene blue on EEM spectroscopy of HS-goethite suspensions, 0.1 mL of 20 ppm methylene blue stock solution (in ppm of total methylene blue mass, stored in a Nalgene

bottle in the dark) was added to 4.9 mL of the sample immediately before analysis (0.4 ppm methylene blue, < 5 min of total exposure including analysis time).

HS adsorption on goethite: When determining the adsorption of HS on goethite over time, 1.42 mL of goethite stock suspension was volumetrically added to 120 mL glass serum bottles and diluted with 118 mL carbonate buffer. Within 2 min, 0.6 mL of a 2000 ppm HS stock solution (in ppm organic carbon) was added to each bottle (either SRHA, SRFA, SRNOM, PPHA, or PPFA). The bottles were immediately capped with Teflon stoppers and magnetically stirred. At 2, 24, and 72 h, ~ 40 mL of each reactor was transferred to a polystyrene centrifuge tube and centrifuged for 20 min at 7000 rpm using an Eppendorf 5804 centrifuge. The supernatant was carefully collected by pipette, added to 20 mL scintillation vials, capped, and stored at 5 °C in the dark until analysis.

Spectroscopy

EEM fluorescence spectroscopy was performed using a Horiba Scientific Aqualog fluorimeter with an excitation range of 240 – 600 nm with a 3 nm increment and emission range of 275 – 800 nm. Bin size was set to 2.33 and integration time was 1 s. Spectrosil® Quartz cuvettes (1 cm, 4 clear sides) were used. If methylene blue was added to the sample, the EEM was normalized by dividing the entire matrix by the intensity (Z) of the highest peak at 291 and 682 – 687 nm for excitation and emission wavelengths, respectively. UV-Vis spectroscopy was performed using an Agilent 8453 UV-Visible spectrophotometer in 1 cm polystyrene cuvettes, scanning absorbance from 300 – 800 nm.

Iron quantification

Dissolved Fe(II), dissolved Fe(III), and total Fe were quantified using a method adapted from Viollier et al.[26] The ferrozine reagent (0.01 M) was prepared in 0.1 M ammonium acetate. The hydroxylamine reagent (1.4 M) was prepared by dissolving hydroxylamine hydrochloride in 2 M HCl. The buffer (10 M ammonium acetate, pH 9.5) was prepared by dissolving ammonium acetate in ultrapure water and adjusting pH using 30% ammonium hydroxide. For all cases, the ferrozine–Fe(II) complex was quantified by UV-Vis spectroscopy. Absorbance was measured at 562 nm and standards for a five-point calibration curve (5 – 50 μM) were prepared by diluting 1 mM $FeCl_2 \cdot 4H_2O$, with each cuvette containing 0.2 mL ferrozine reagent.

Step 1, dissolved Fe(II): For dissolved Fe(II) species, supernatants (~ 2 mL) were filtered through Acrodisc 13 mm syringe filters with a 0.22 μm nylon membrane (Pall Life Sciences). To a polystyrene cuvette, 1 mL of the filtrate, 0.2 mL ferrozine reagent, and 1.8 mL ultrapure water were added. The cuvette was capped, inverted three times, and analyzed.

Step 2, dissolved Fe(III): To the same cuvette from *Step 1*, 0.3 mL hydroxylamine reagent was added. The cuvette was capped, inverted three times, and allowed to react. After 10 min, 0.1 mL of the ammonium acetate buffer was added and the cuvette was inverted before analysis. Dissolved Fe(III) was quantified by subtracting the concentration determined from *Step 1* (dissolved Fe(II)) from the concentration determined from *Step 2* (dissolved Fe(II) + dissolved Fe(III)).

Step 3, total Fe: Total Fe (including residual iron oxide nanoparticles that remained in the supernatant) was determined by HCl digestion of the solids and subsequent colorimetric analysis. A sample of the supernatant (1 mL) was added to a 20 mL scintillation vial with 2 M HCl (2 mL), hydroxylamine reagent (0.5 mL), and ferrozine reagent (0.5 mL) and diluted to 10 mL with ultrapure water. The vial was tightly capped and aged at 40 °C for 6 d. After aging, the vials were cooled to room temperature, mixing periodically. Once cooled, the vials were opened and ammonium acetate buffer (1 mL) was added. The solution was transferred to a polystyrene cuvette and analyzed.

TOC analysis

Total organic carbon was measured using a Shimadzu TOC-L Total Organic Carbon (TOC) Analyzer operated in non-purgeable organic carbon mode. Samples were acidified with HCl, sparged with humidified air to remove inorganic carbon, and combusted at 680 ºC with Pd catalyst beads. CO_2 production was quantified using a nondispersive infrared (NDIR) detector and a calibration curve of potassium hydrogen phthalate (99.9%, Sigma).

Results and discussion

Challenges associated with EEM fluorescence spectroscopy of HS-goethite suspensions

HS sorption on goethite was characterized by EEM spectroscopy and results are consistent with no fractionation. While fluorescence for HS was detected in supernatants of HS-goethite suspensions equilibrated for 21 h, it remains unclear what effect the presence of iron (residual goethite that was not removed by centrifugation) had on the

intensity of HS fluorescence. Figure 4.1 provides representative EEM spectra for SRNOM, SRFA, and PPHA and corresponding supernatants from suspensions containing goethite and HS in carbonate buffer. Spectra for solutions containing only HS in carbonate buffer are different than for corresponding supernatants collected after equilibration with goethite for 21 h and then centrifuged. At first observation, the decrease in intensity of HS fluorescence may suggest that significant adsorption of HS on goethite occurred, therefore decreasing the concentration of HS in the supernatant.

On the other hand, a large increase in intensity of the first and second order Rayleigh scattering (elastic scattering) is notable in the supernatants. First order Rayleigh scattering occurs when emission equals excitation wavelength and second order when emission equals twice the excitation wavelength.[27] In addition, supernatants had a slightly orange tint, suggesting some goethite particles remained in suspension after centrifugation. As previously described, aqueous Fe(II) and Fe(III) are known to quench the fluorescence of OM.[23] Therefore, the decrease in intensity of OM may be due to either adsorption of OM on goethite resulting in less OM present after centrifugation or quenching of fluorescence by residual goethite (no dissolved Fe(II) or Fe(III) species were detected).

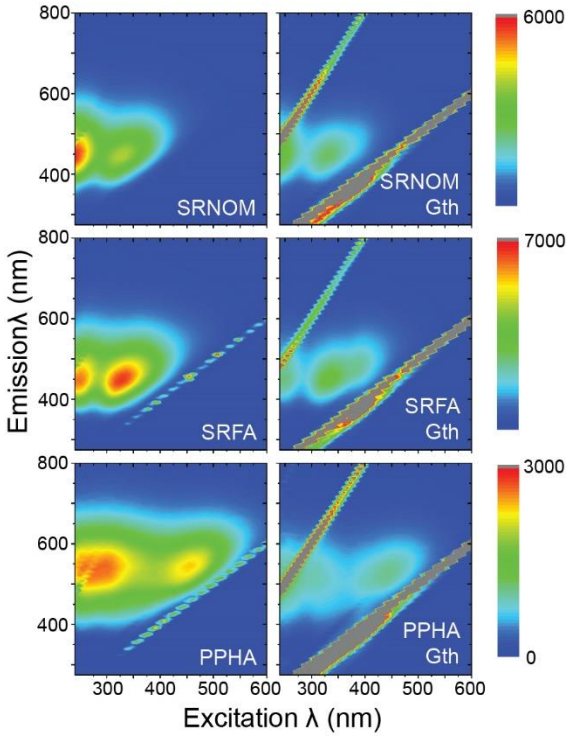

Figure 4.1: Representative EEM fluorescence spectra of SRNOM, SRFA, and PPHA (10 ppm OC) in 10 mM carbonate buffer at pH 7 (left panel) and the supernatant of the identical system except with 0.325 g/L goethite (Gth, right panel) equilibrated for 21 h.

Use of methylene blue as an EEM internal standard

The first step to facilitate quantitation of the HS concentration in solution is identification of a suitable internal standard, which may help distinguish between HS quenching and loss via sorption on goethite. An appropriate internal standard in EEM spectroscopy would be a molecule that has different fluorescence maxima than the suite of humic substances. As seen in Figure 4.1, the majority of HS fluorescence generally falls between emission wavelengths of 400 – 600 nm. Several different dye molecules were investigated, and only methylene blue had suitable fluorescence peak positions for

use as an internal standard. Because the use of an internal standard in EEM fluorescence spectroscopy is a new idea, the EEM spectra for all the dye molecules tested are provided in Figure 4.2. Excitation of methylene blue produced a peak with a reproducible maximum at excitation and emission wavelengths of 291 and 682 – 687 nm, respectively. This unique peak could make the parameters for fluorescence normalization particularly simple and repeatable. In contrast, Rhodamine B and 2',7'-dichlorofluorescein had emissions at wavelengths greater than 550 nm but lacked a clearly identifiable and reproducible maximum for which to normalize intensity. Brilliant blue and hydroxyterephthalic acid had overlapping fluorescence maxima as compared to the humic substances, and several other dyes were not detectable by EEM spectroscopy. Of the dyes tested, methylene blue had the most optimal properties for use as an internal standard for characterizing the fluorescence intensity of humic substances.

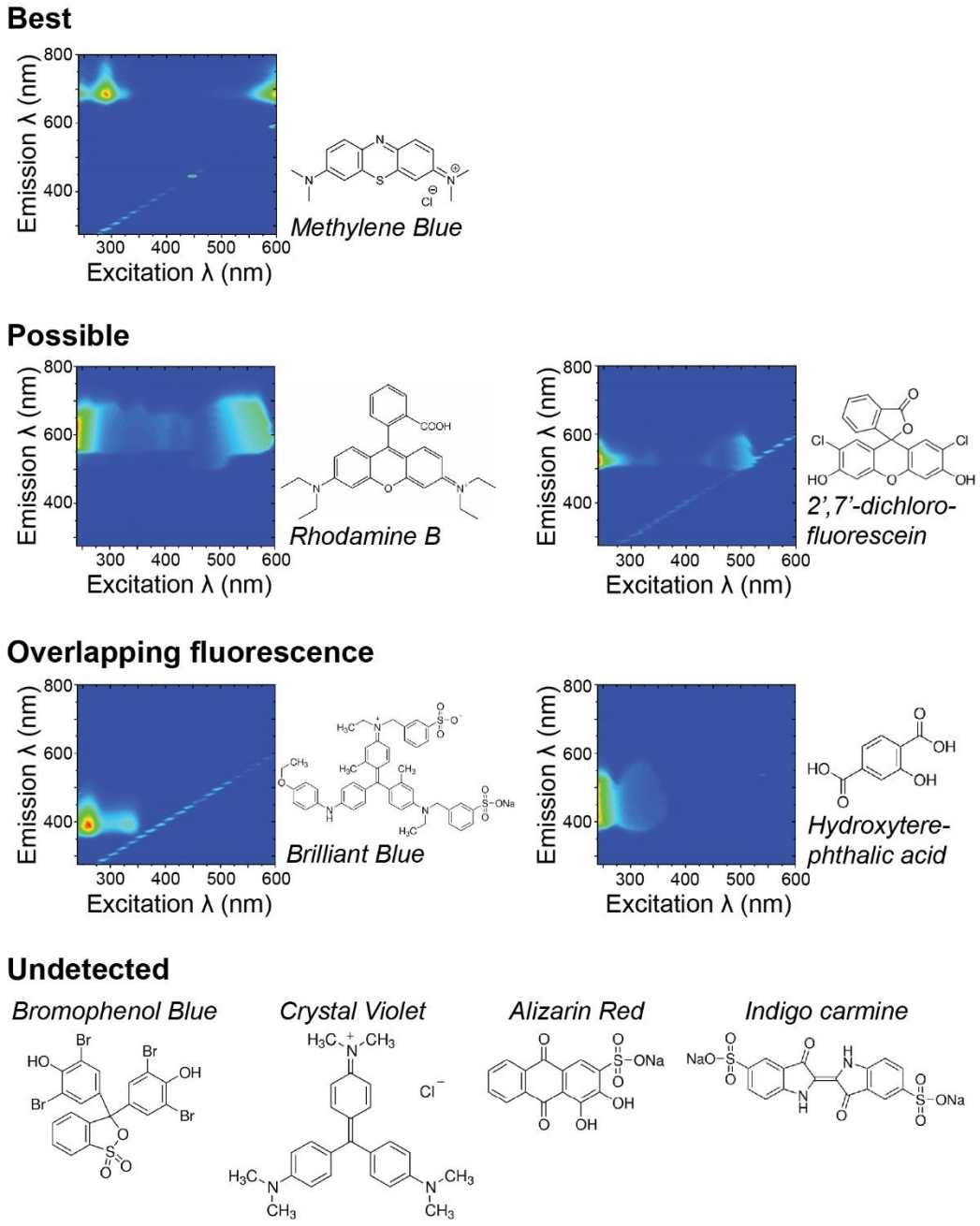

Figure 4.2: EEM spectra of various dyes categorized by their applicability as an internal standard in solutions containing humic substances (excitation range of 240 – 550 nm and emission range of 400 – 600 nm).

To determine whether methylene blue could be used as an internal standard in HS-goethite suspensions, two possible interactions needed to be explored: methylene blue-HS and methylene blue-goethite. While we have not yet explored methylene blue-goethite interactions, the effect of added methylene blue on the fluorescence of HS was tested at different SRNOM concentrations (Figure 4.3) in carbonate buffer at pH 7 and the absence of goethite. In Figure 4.3a, the fluorescence peak height (*Z*) of SRNOM was linear as a function of concentration, demonstrating that EEM spectroscopy can be used to quantify HS concentrations in suspensions free of iron. The fluorescence peak height of methylene blue, however, was not constant. Methylene blue was always added immediately before EEM spectra were taken (< 5 min). Because the amount of methylene blue did not change and yet the intensity decreased, methylene blue-HS interactions may be occurring in that short time period, resulting in the quenching of methylene blue fluorescence. UV-Vis spectroscopy of similar solutions provided a comparable story (Figure 4.3b), although the concentrations differed compared to those used in EEM spectroscopy (in UV-Vis spectroscopy, methylene blue concentration was 5 ppm to increase absorbance and decrease signal-to-nose ratio). Absorbance of methylene blue (550 – 700 nm) decreased as OM concentration increased, more evidence of methylene blue-HS interactions.

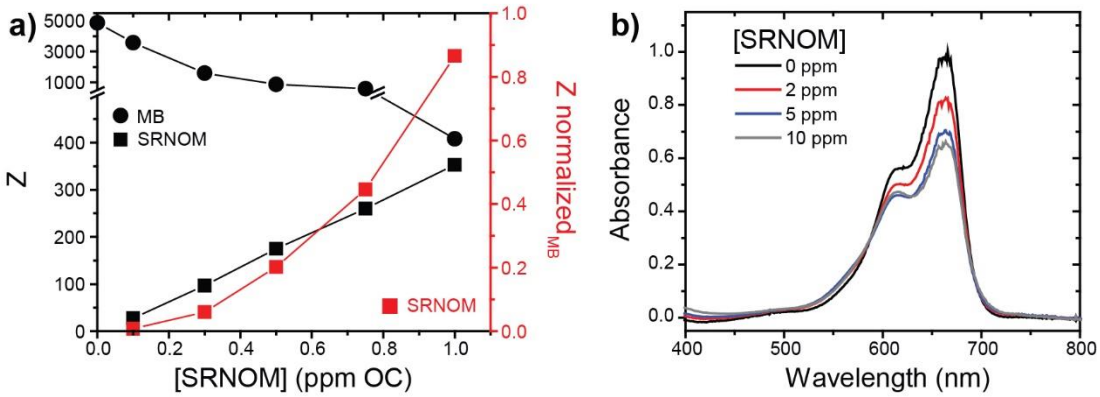

Figure 4.3: a) Fluorescence intensity (*Z*) of SRNOM and methylene blue (MB) and the normalized *Z* of SRNOM (Z_{SRNOM} divided by Z_{MB}), collected by EEM fluorescence spectroscopy. b) Absorbance of methylene blue (5 ppm) in solution with different concentrations of SRNOM, collected by UV-Vis spectroscopy. All solutions were prepared in 10 mM carbonate buffer at pH 7. No goethite or Fe(II)/Fe(III) species were present in these samples.

Significant interactions between humic acid and methylene blue have been observed in previous work. Exchange interactions between carboxylic acid groups of humic acids or electrostatic interactions with aromatic backbones of humic acids have been described as possible mechanisms of methylene blue-humic acid interactions.[28] Quenching of methylene blue fluorescence by HS does not necessarily mean that it is not a possible internal standard. When the fluorescence of HS was normalized to that of methylene blue, an exponential trend is observed between normalized maximum and HS concentration, suggesting that HS may still be quantifiable. Without knowing how methylene blue fluorescence changes in the presence of goethite, we cannot conclusively determine whether methylene blue is an appropriate internal standard for samples

containing residual iron oxide nanoparticles. The subject of future studies will include possible methylene blue-goethite interactions.

Preliminary data towards elucidating HS adsorption on goethite

The following preliminary data offer the first insight into characterizing interactions between HS and iron oxide nanoparticles using EEM fluorescence spectroscopy, suggesting no detectable fractionation occurred during HS sorption on goethite. Supernatants of HS-goethite suspensions were analyzed by EEM spectroscopy both with and without added methylene blue. It should be noted, however, that this data came from performing only one trial of the experiment, given the current time constraints of the researcher. Additionally, only Suwannee River humic substances are shown. Pahokee Peat humic and fulvic acid were analyzed but had strikingly more fluorescence compared to that of 0.4 ppm methylene blue, therefore requiring more work to optimize HS and methylene blue concentrations for EEM spectroscopy.

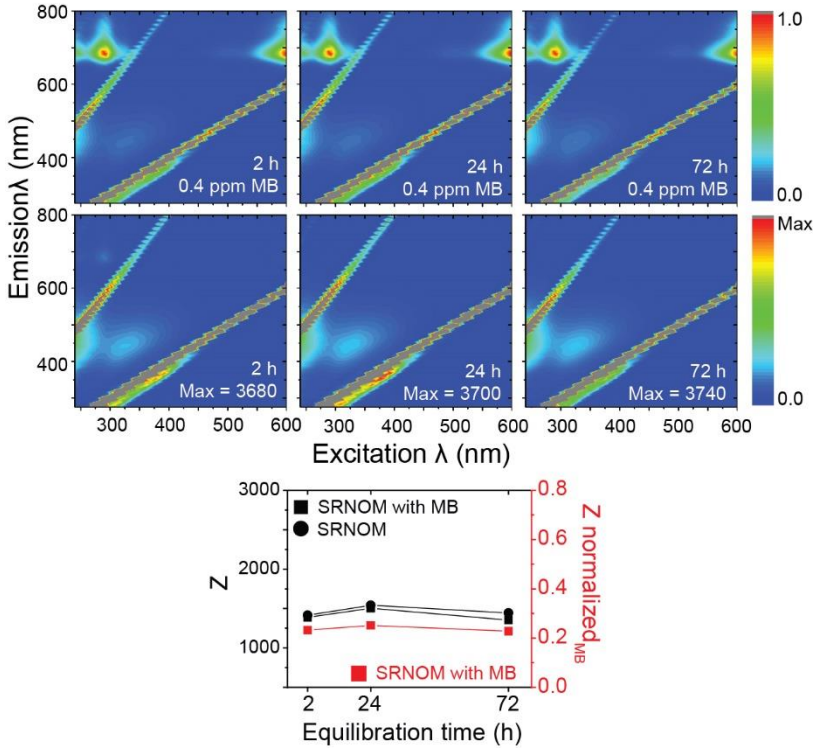

Figure 4.4: EEM spectra of SRNOM (10 ppm OC)/goethite (0.325 g/L) supernatants following 2, 24, and 72 h equilibration. Suspensions were prepared in 10 mM carbonate buffer at pH 7. Top panel contains 0.4 ppm methylene blue (MB). Plot shows fluorescence intensity (Z) of SRNOM with and without MB and the normalized Z of SRNOM (Z_{SRNOM} divided by Z_{MB}).

Figure 4.4 provides EEM spectra for supernatants of SRNOM-goethite suspensions after 2, 24, and 72 h equilibration. The fluorescence intensity remained relatively constant over time, and it did not make a significant difference if intensity was normalized to methylene blue. The data suggest that adsorption of SRNOM is either limited or occurred within the first 2 h of equilibration and then quickly stabilized. The former possibility is less likely; several studies in various experimental conditions have demonstrated that SRNOM adsorbs onto goethite nanoparticles and affects the reactivity and properties of goethite surfaces.[13,29,30] Chekli et al. described maximum adsorption of

SRNOM on hematite (α-Fe_2O_3) nanoparticles was achieved in under 2 h,[31] and Lv et al. showed a similarly quick increase in SRNOM adsorption on goethite (maximum adsorption in < 10 h).[32] Thus, it is likely that maximum adsorption of SRNOM on goethite was achieved by the time the first EEM spectra were taken.

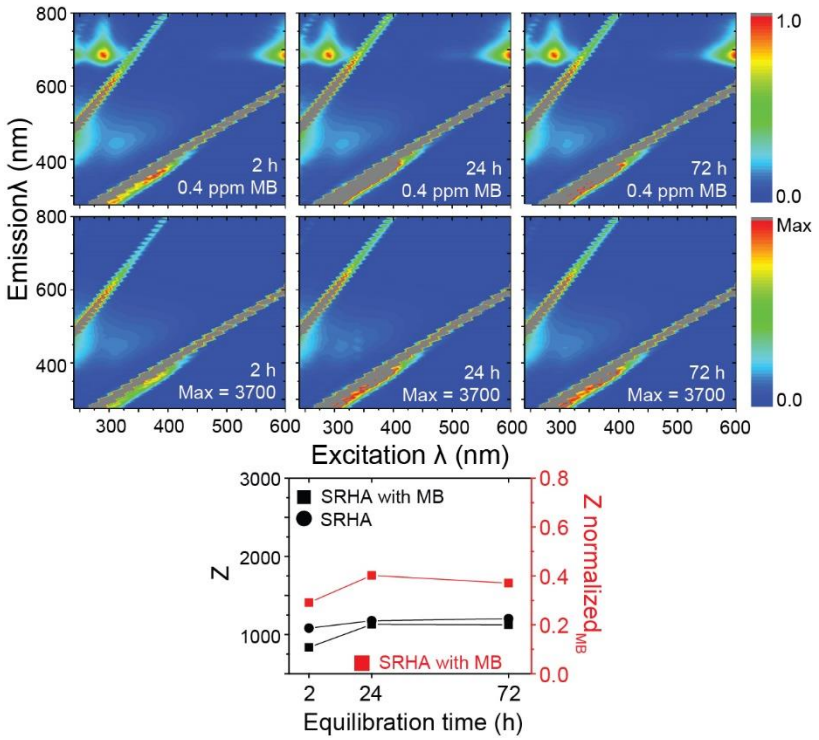

Figure 4.5: EEM spectra of SRHA (10 ppm OC)/goethite (0.325 g/L) supernatants following 2, 24, and 72 h equilibration. Suspensions were prepared in 10 mM carbonate buffer at pH 7. Top panel contains 0.4 ppm methylene blue (MB). Plot shows fluorescence intensity (Z) of SRHA with and without MB and the normalized Z of SRHA (Z_{SRHA} divided by Z_{MB}).

Identical experiments except with SRHA had a similar result. A change in SRHA intensity, whether or not it was normalized to methylene blue, was not observed as a function of equilibration time. SRHA-goethite interactions are similarly known,[30] and therefore equilibrium of SRHA adsorption on goethite may have been achieved in under

the 2 h point where our first measurements were made. In a recent paper from this group, the character of humic substances was related to its effect on aggregation and reactivity of goethite nanoparticles.[30] Humic acid fractions, as compared to fulvic acid fractions, had fewer interactions with goethite nanoparticles and weakly inhibited the reactions on goethite surfaces.

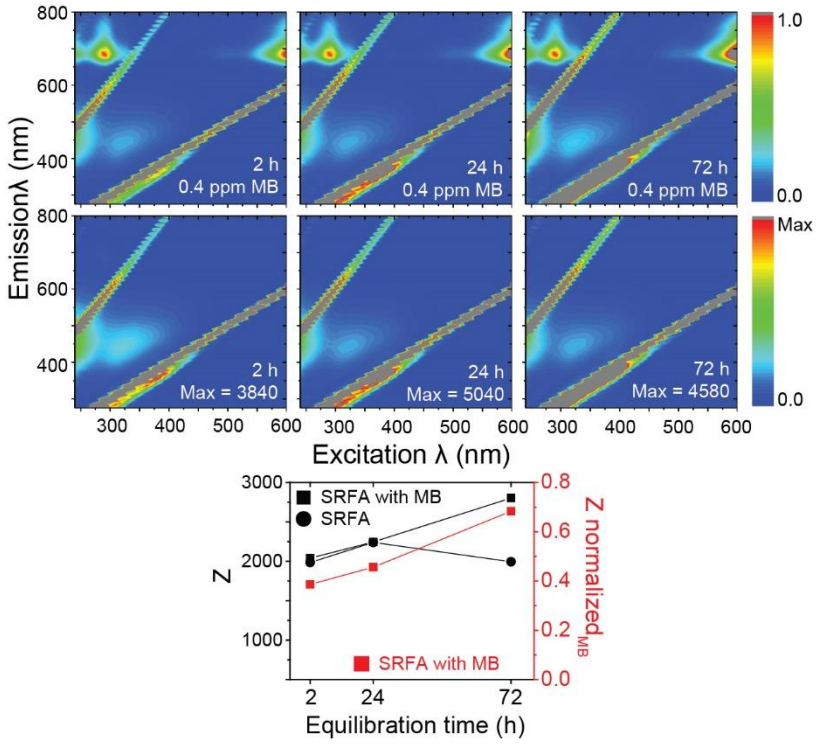

Figure 4.6: EEM fluorescence spectra of SRFA (10 ppm OC)/goethite (0.325 g/L) supernatants following 2, 24, and 72 h equilibration. Suspensions were prepared in 10 mM carbonate buffer at pH 7. Top panel contains 0.4 ppm methylene blue (MB). Plot shows fluorescence intensity (Z) of SRFA with and without MB and the normalized Z of SRFA (Z_{SRFA} divided by Z_{MB}).

In contrast to SRNOM and SRHA, the properties of SRFA adsorption as characterized by EEM spectroscopy were not as clear (Figure 4.6). In spectra normalized to methylene blue, concentration of SRFA in the supernatant generally increased,

suggesting desorption of SRFA on goethite over time. On the other hand, the spectra from supernatants in the absence of methylene blue were not comparable. These results may be the result of an experimental error (an unfortunate possibility given that time allowed for only one trial). Additional work is necessary to determine whether the data are consistent over multiple trials. Even more, TOC measurements do not reflect a steady concentration of HS as observed by EEM intensities for SRNOM, SRHA, and SRFA as a function of equilibration time (Figure 4.7). Given these discrepancies, more trials are required before suggestions of adsorption kinetics and mechanisms can be provided.

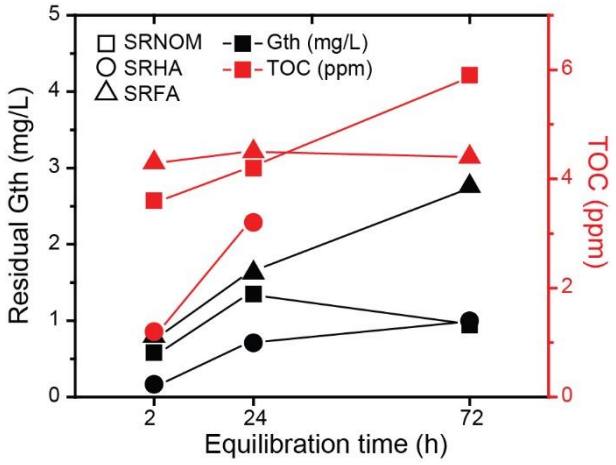

Figure 4.7: Plot of residual goethite (Gth) mass loading as measured by colorimetric analysis and TOC measurements for supernatants of SRNOM-, SRFA-, and SRFA-goethite mixtures after varied equilibration times. TOC measurement of SRHA at 72 h was unrealistic (TOC > 100 ppm) and therefore was not shown.

There is much work to be done before any conclusions can be drawn on HS adsorption on goethite or the use of methylene blue as an internal standard in EEM spectroscopy. No evidence for fractionation of HS on goethite was observed at the given equilibration periods. Evidence for fractionation would be apparent if the relative peak

intensities or even peak locations shifted as a function of equilibration time, meaning that a specific fraction (e.g., smaller, highly charged molecules like fulvic acids) preferentially adsorbed on to goethite. This could be observed regardless of the relative intensities. Since no changes in the relative "shape" of the peaks were observed in SRNOM, SRHA, and SRFA experiments, no detectable fractionation occurred within the equilibration period examined. Future work will include similar experiments with supernatants collected after < 2 h equilibration time to determine if changes in intensity or peak position occur.

The completion of this work may reveal unique characteristics of OM adsorption on goethite surfaces. While several studies have quantified OM and HS adsorption on goethite, few have looked at the preferential adsorption of certain fractions (e.g., greater adsorption of fulvic acids as compared to humic acids), and even fewer have applied EEM spectroscopy to answer these questions. Future work should include a detailed investigation into the interactions of methylene blue on goethite and its effect on EEM spectra. In addition, several more experiments are required in order to both confirm that methylene blue can be used as an internal standard for EEM and establish a protocol for its application. Once that has been determined, adsorption of OM on goethite can be explored in greater detail, including shorter equilibration periods and other humic substances like PPFA and PPHA.

Acknowledgments

This work was funded by NSF grant ECS-1012193 and the Graduate School Doctoral Dissertation Fellowship at the University of Minnesota to Jennifer Strehlau.

Chapter 5. Accessible reactive surface area of iron oxyhydroxides in acidic brines

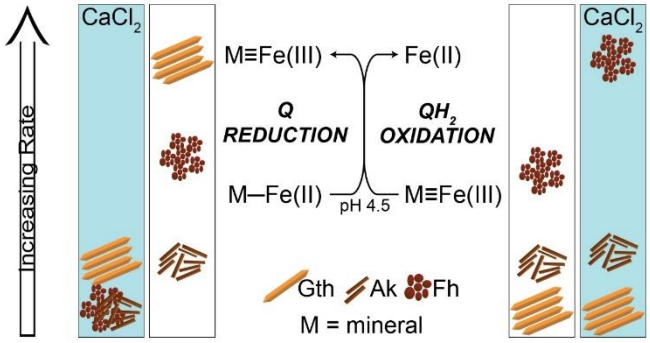

This chapter describes the outcome of a research project carried out by Jennifer H. Strehlau advised by Brandy M. Toner, William A. Arnold and R. L. Penn. Supporting information is located in Appendix D.

A report on this research has been submitted.

Strehlau, J. H.; Toner, B. M.; Arnold, W. A.; Penn, R. L.

Submitted, 2016.

Summary

The reactivity of iron oxyhydroxide nanoparticles in low pH and high ionic strength solutions was quantified to assess abiotic contributions to oxidation-reduction chemistry in acidic brine environments, such as mine groundwater seepage, lakes in Western Australia, and acid mine drainage settings, which are of global interest for their environmental impacts and unique geomicrobiology. Factors that influence accessible and reactive surface area, including Fe(II) adsorption and aggregate size, were measured as a function of pH and $CaCl_2$ concentration and related to the kinetics of redox reactions in aqueous suspensions of synthetic goethite (α-FeOOH), akaganeite (β-FeOOH), and ferrihydrite ($Fe_{10}O_{14}(OH)_2$) nanoparticles. Quinone species were used as redox sensors because they are well-defined probes and are present in natural organic matter. Fe(II) adsorption to the iron oxyhydroxide mineral surfaces from aqueous solution was measurable only at pH values above 4 and either decreased or was not affected by $CaCl_2$ concentration. Concentrations at or above 0.020 M $CaCl_2$ in acetate buffer (pH 4.5) induced particle aggregation. Assessment of Fe(II) adsorption and particle aggregation in acidic brine suggested that accessible reactive surface area may be limited in acidic brines. This was supported by observations of decreasing benzoquinone reduction rate by adsorbed Fe(II) at high $CaCl_2$ concentration. In contrast, the hydroquinone oxidation rate increased at high $CaCl_2$ concentrations, which may be due to suppressed adsorption of Fe(II) generated by the reaction. Results suggest that iron geochemical cycling in acidic brine environments will be substantially different than for iron oxyhydroxides in low-

saline waters with circumneutral pH. These findings have implications for acidic brine lakes and acid mine drainage locations that contain precipitated iron oxyhydroxides.

Introduction

Acidic brine environments form through rock alteration reactions in climates favoring evaporite deposition.[1] Development of acidic conditions in these natural waters is strongly linked to iron geochemistry and the onset of oxidizing conditions. Specifically, high acidity develops through pyrite oxidation or, in sulfide-limited systems, through oxidation of Fe(II) and hydrolysis of Fe(III). Naturally formed acidic waters with brine or hypersaline ionic strength (as high as 300,000 mg/L salt content[2]) have been reported in northern Chile and Bolivia,[3,4] Western Australia,[5,6] and the United States.[7] These acidic brines have been investigated for their environmental impacts as well as their potential to serve as Martian analogs of geology and microbiology.[1,4,8] Acidic brines also form in human-impacted settings, such as acid mine drainage and pit lakes of mines, which are of broad public concern and have been extensively studied.[9–11]

In some acidic brines, iron oxyhydroxide nanoparticles participate in the oxidation or reduction of organic contaminants or phenolic groups in natural organic matter through direct reaction with mineral surface sites or with adsorbed Fe(II).[12] Quinone moieties present in organic matter also act as electron shuttles between iron oxyhydroxides and redox active bacteria.[13,14] In human-impacted settings, such as polluted groundwater or acid mine drainage, the potential for iron oxyhydroxides to incorporate or degrade contaminants can be exploited for remediation efforts.[10,15] Several studies have demonstrated that the accessible and reactive surface area of iron

oxyhydroxides in aquatic systems depends on solution chemistry variables, such as ionic strength, pH, and concentration of reactive species,[16,17] but extreme environments such as acidic brines have yet been fully explored. Ionic strength and acidity likely impact the reactivity of iron oxyhydroxide nanoparticles by affecting processes such as ion adsorption and aggregation, which in turn influence accessible and reactive surface area.[18–21]

Understanding abiotic iron cycling in acidic brines has the potential to elucidate fundamental processes in geochemistry as well as lead to improved remediation methods. A significant challenge, however, is the occurrence of both biological and abiotic influences. For example, some iron-rich saline and hypersaline microbial mats, such as those found in hydrothermal vents and solar salterns, are the subject of geomicrobial research.[22–25] While the microbial reactivity in these iron-rich mats has been studied,[26,27] the chemical behavior of the iron oxyhydroxides in high ionic strength and low pH conditions has not yet been evaluated, making it difficult to elucidate the mechanisms controlling iron redox cycling.

In this work, we assess the abiotic redox reactivity of iron oxyhydroxide nanoparticles in acidic brines. To model a natural environment, experiments were performed using solution chemistry similar to groundwater seepages found in the microbial mats of Soudan Underground Mine, USA, which features an acidic brine environment with both microbial and abiotic contributions to iron cycling and where aqueous Fe(II) undergoes oxidation and hydrolysis upon exposure to the ambient air. Analysis of one location in the mine shaft with exposed groundwater seepage found three

iron oxyhydroxide mineral phases present: goethite (α-FeOOH), akaganeite (β-FeOOH), and ferrihydrite ($Fe_{10}O_{14}(OH)_2$[28]) In addition, the Fe(II) concentration was high (0.342 mM), the pH acidic (~ pH 3), and the ionic strength high (> 2 M).[29] Here, $CaCl_2$ was used to set ionic strength, and synthetic goethite, akaganeite, and ferrihydrite nanoparticles were prepared as model minerals. The first objective of this work was to characterize accessible reactive surface area as a function of low pH and high ionic strength by quantifying adsorbed Fe(II) and assessing aggregation state. The second was to quantify rates of *p*-benzoquinone (referred to as benzoquinone hereafter) reduction via adsorbed Fe(II) or hydroquinone oxidation by iron oxyhydroxides as a function of increasing ionic strength at low pH. The results, along with consideration of thermodynamics, allow us to elucidate the relationship between surface redox reactions and acidic brine solution conditions due to the influence on accessible reactive surface area. These results offer a unique perspective on iron cycling in extreme environments, highlighting the potential importance of abiotic reactivity in acidic brines.

Experimental

Materials

Chemical sources and purities are listed in the supplementary material. All solutions were prepared in ultrapure water. For delivering aqueous Fe(II) to experiments, a stock solution of 200 mM Fe(II) was freshly prepared each day under anaerobic conditions by adding 0.55 mol $FeCl_2 \cdot 4H_2O$ to 5 mL of water or 0.67 M $CaCl_2$ and 0.5 mL of 1 M HCl. When performing buffered experiments at pH 4.5, 40 mM acetate buffer was

prepared by diluting glacial acetic acid with ultrapure water and adjusting the pH to 4.5 with 1 M NaOH.

Nanoparticle synthesis and characterization

Details of the synthetic procedures summarized here are provided in the supplementary material. Goethite nanoparticles were synthesized using a modified version of the method from Anschutz and Penn (2005) by adding 0.48 M $NaHCO_3$ to 0.40 M $Fe(NO_3)_3 \cdot 9H_2O$ followed by aging and purification. Akaganeite nanoparticles were synthesized by aging 0.035 M $FeCl_3 \cdot 6H_2O$ in a hydrothermal bomb. Ferrihydrite nanoparticles were synthesized by forced hydrolysis and aging of a 0.20 M $Fe(NO_3)_3 \cdot 9H_2O$ solution as described in Schwertmann and Cornell (2000). The nanoparticles were stored as a suspension with known mass loadings in a Nalgene bottle at 5 °C to be delivered by volumetric pipette. Mass loading measurements were performed frequently to ensure accuracy. Considering ferrihydrite reactivity has shown to change as a function of particle age, fresh ferrihydrite nanoparticles were prepared after three weeks of storage.[32] Particle composition, size, morphology, and surface area were determined by a combination of X-ray diffraction (XRD), transmission electron microscopy (TEM), and nitrogen sorption analysis (see supplementary material).

Iron adsorption

Iron adsorption was measured by quantifying the remaining Fe(II) in solution after filtration using the ferrozine colorimetric analysis.[33] In brief, nanoparticle suspensions were prepared in either 0 M or 0.67 M $CaCl_2$ at pH 3 – 7 and equilibrated for 21 h. Following equilibration, an aliquot was filtered, added to cuvettes containing

ferrozine, and measured by UV-Vis spectroscopy. Details are provided in the supplementary material.

Aggregate size and zeta potential

Aggregate sizes and zeta potentials were collected by dynamic light scattering (DLS) as a function of $CaCl_2$ concentration using a ZetaPALS Zeta Potential Analyzer (Brookhaven) with the 90Plus/BI-MAS Multi Angle Particle Sizing Option installed. Goethite, akaganeite, or ferrihydrite samples (0.325 g/L) were prepared in 20 mL scintillation vials by volumetrically delivering particle stock suspension and 40 mM acetate buffer at pH 4.5 with either 0 or 0.67 M $CaCl_2$ so that the final $CaCl_2$ concentration ranged from 0 to ~ 0.67 M. The effect of added Fe(II) was examined by adding the Fe(II) stock solution so that the Fe(II) concentration was 0.342 mM. Aggregate sizes and standard errors were reported as mean number-based effective hydrodynamic diameters from 5 runs of 15 s each with a dust cut-off of 30 (instrumental parameter for filtering out rare intensity spikes most likely due to large dust particles). Average zeta potentials and standard errors were reported from 3 runs of 20 cycles. For monitoring aggregate size during reaction, a 3 mL sample from the reaction was measured using the same instrumental parameters.

Reaction kinetics

Benzoquinone reduction and hydroquinone oxidation experiments were run in 40 mM acetate buffer at pH 4.5 with either 0 or 0.67 M $CaCl_2$. To 38 mL glass serum bottles, the appropriate iron oxyhydroxide suspension was volumetrically delivered so that the final mass loading was 0.325 g/L. When all three iron oxyhydroxides were added

to one reactor, the total mass loading was either 0.325 or 0.975 g/L (equal mass ratios of each iron oxyhydroxide). Reactors were then transferred to an anaerobic chamber and diluted with 20 mL of 0 or 0.67 M $CaCl_2$ buffer. To vary the $CaCl_2$ concentration, appropriate ratios of the 0 and 0.67 M $CaCl_2$ buffers were added. For benzoquinone reduction, 0.342 mM Fe(II) was added using the Fe(II) stock solution. The reactors were then brought to a final volume of 35 mL with the appropriate buffer, crimp capped, and sonicated for 20 min outside of the anaerobic chamber. Following sonication, the reactors were wrapped in aluminum foil to block light and magnetically stirred in the anaerobic chamber for 21 h of equilibration.

Reactors were spiked with benzoquinone or hydroquinone (0.1 mM) from a 10 mM stock solution prepared in the appropriate buffer solution. Samples (1 mL) were withdrawn using a plastic syringe and filtered into an amber glass HPLC vial. Benzoquinone and hydroquinone were quantified at 235 nm using an Agilent 1100 series HPLC (see supplementary material). Benzoquinone reduction was analyzed using a pseudo-first-order rate model, and hydroquinone oxidation was analyzed using the rate of benzoquinone production. The post-reaction suspensions were transferred to centrifuge tubes and collected using an Eppendorf 5804 centrifuge (6000 g for 3 min). Samples were washed three times with deoxygenated Milli-Q water (only opening when inside the anaerobic chamber). Collected solids were dried at room temperature in air, ground using mortar and pestle, and characterized by XRD in the same manner as the unreacted minerals.

Results

Synthetic nanoparticle characterization

TEM micrographs and XRD patterns are shown in the supplementary material. The synthetic goethite particles have an acicular morphology with dimensions of 110 ± 41 nm in length and 12 ± 5 nm in width. The synthetic akaganeite nanoparticles are also acicular but smaller in size, with an average length of 36 ± 16 nm and width of 5 ± 2 nm. The synthetic ferrihydrite particles are 2 to 3 nm in diameter. No evidence of secondary phases was detected by XRD for any of the three samples. TEM surface area was determined to be 190 m^2/g, 240 m^2/g, and 510 m^2/g for goethite, akaganeite, and ferrihydrite, respectively, using the assumption that goethite rods are prisms similar in shape as described in previous work,[34] akaganeite rods are square cuboids (where $a = b \neq c$), and ferrihydrite dots are spheres. Nitrogen sorption-BET analysis yielded a specific surface area of 140 m^2/g for goethite, 278 m^2/g for akaganeite, and 130 – 280 m^2/g for ferrihydrite. The low and variable specific surface area measured for ferrihydrite by BET is consistent with considerable aggregation during drying, which would prevent condensation of N_2 on all mineral surfaces. For akaganeite, the higher specific surface area determined by BET analysis than by measurements from TEM images suggests that the square cuboid assumption may under-represent the akaganeite surface area. These akaganeite rods may be rounded at the ends or have a porous surface, similar to the more pronounced cigar-shape morphology and tunnel structure seen in larger akaganeite nanoparticles.[35]

Aggregation state vs. adsorbed Fe(II) and $CaCl_2$ concentration

Accessible surface area of iron oxyhydroxide nanoparticles in suspensions (buffered at pH 4.5) was monitored by DLS. Hydrodynamic diameter and zeta potential, which serve as proxies for aggregation state and surface charge, respectively, are shown in Figure 5.1. In general, aggregate size increased with increasing $CaCl_2$ (Fig. 5.1a), with the largest changes in size observed at lower concentrations of $CaCl_2$ (below 0.1 M). The maximum quantitative size of this DLS instrument (3000 nm, provided in the manual, indicated by a dashed line in Fig. 5.1a) was observed for most suspensions below or at 0.1 M $CaCl_2$. Additionally, suspensions prepared with and without Fe(II) were distinguishable at lower $CaCl_2$ concentrations but not statistically different above 0.1 M $CaCl_2$. The observed decrease in zeta potential with increasing $CaCl_2$ concentration (Fig. 5.1b), approaching 0 mV in suspensions with 0.67 M $CaCl_2$, indicates decreasing surface repulsion of the particles.

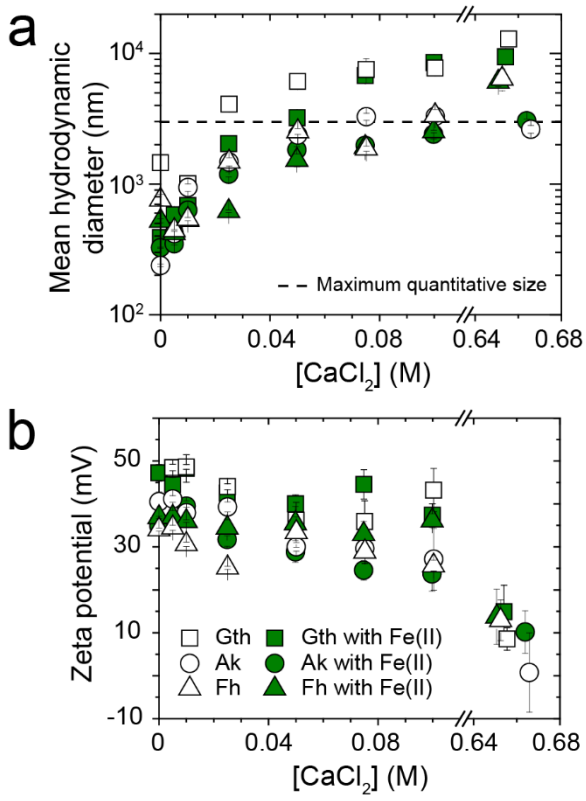

Figure 5.1. a) Log number-based mean hydrodynamic diameter and b) zeta potential of goethite (Gth), akaganeite (Ak), and ferrihydrite (Fh) as a function of $CaCl_2$ concentration as measured using dynamic light scattering. Open symbols are data obtained from suspensions with no Fe(II) and closed symbols with 0.342 mM Fe(II). Samples were prepared in 40 mM acetate buffer at pH 4.5. Note x-axis break between 0.10 and 0.64 M $CaCl_2$.

Iron adsorption vs. pH and $CaCl_2$

To characterize the reactive surface area as a function of pH and ionic strength, Fe(II) adsorption edges (Fig. 5.2a-c) were collected and normalized to the number of reactive sites for each mineral (Fig. 5.2d and 5.2e, see supplementary material for calculations).[36–38] Fe(II) adsorption onto all three iron oxyhydroxides increased with increasing pH and measurable Fe(II) adsorption did not occur until pH values were greater than 4, consistent with previous works.[39,40] Generally speaking, the degree of

adsorption was greatest on goethite and least on ferrihydrite when normalized to the total number of reactive sites. In the cases of goethite and ferrihydrite, Fe(II) adsorption decreased at high $CaCl_2$ concentration. In contrast, Fe(II) adsorption onto akaganeite was independent of $CaCl_2$ concentration, less than that observed for goethite, and greater than that observed for ferrihydrite.

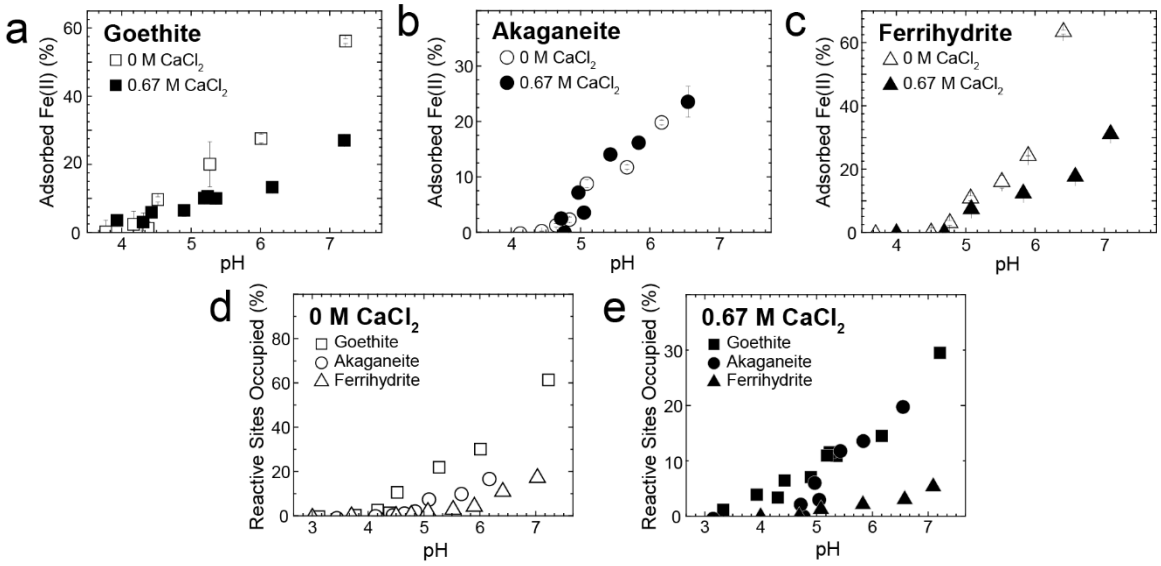

Figure 5.2. (a-c) Average percent of Fe(II) added that adsorbed on the mineral surface of a) goethite, b) akaganeite, or c) ferrihydrite as a function of pH, with either 0 M or 0.67 M $CaCl_2$. Initial conditions of 0.325 g/L particle loading and 0.342 mM Fe(II) in water. (d-e) Percent of reactive sites occupied on the mineral surface as a function of pH for each iron oxyhydroxide in d) 0 M $CaCl_2$ or e) 0.67 M $CaCl_2$.

Kinetics

Relevant one-electron transfer reduction reactions are summarized in Table 5.1, including the reduction potentials at pH 7 and pH 4.5. Thermochemical considerations of $E_{H,pH\ 4.5}$ are necessary when comparing the relative reaction rates of each iron oxyhydroxide mineral in an acidic brine environment. Based strictly on thermodynamics,

ferrihydrite is predicted to be the most favorable in iron oxyhydroxide reductive dissolution whereas goethite is predicted to be the most favorable in iron oxyhydroxide oxidative growth.

Table 5.1: Reduction potentials of half reactions at pH 7 and pH 4.5 (relevant for acidic brines) and 25 °C, calculated using the Nernst equation. Dissolved Fe(II) concentrations were set to 10^{-4} M, and sorbed Fe(II) sites set to 10^{-6} M. For the quinone reaction, concentrations of Q and QH_2 were set equal to each other.

Reaction	E_H^0 (V)	$E_{H,\ pH\ 7}$ (V)	$E_{H,\ pH\ 4.5}$ (V)
$Fe(III) + e^- = Fe(II)$	+0.77[b]	+0.77	+0.77
$^1/_2\ Q + H^+ + e^- = {}^1/_2\ QH_2$	+0.70[c]	+0.28	+0.43
Iron oxyhydroxide dissolution			
[Gth] α-$FeOOH + 3H^+ + e^- = Fe(II) + 2H_2O$	+0.68[calc]	-0.32	+0.12
[Ak] β-$FeOOH + 3H^+ + e^- = Fe(II) + 2H_2O$	+0.75[calc]	-0.25	+0.19
[Fh] amorph $Fe(OH)_3 + 3H^+ + e^- = Fe(II) + 3H_2O$	+0.97[calc]	-0.04	+0.41
Iron oxyhydroxide growth			
[Gth] α-$FeOOH + \equiv Fe(III)OH + 2H^+ + e^- = \equiv Fe(III)OFe(II)^+ + 2H_2O$	+0.17[d]	-0.60[a]	-0.30[a]
[Ak] β-$FeOOH + \equiv Fe(III)OH + 2H^+ + e^- = \equiv Fe(III)OFe(II)^+ + 2H_2O$	–	–	–
[Fh] $Fe(OH)_3 + \equiv Fe(III)OH + 2H^+ + e^- = \equiv Fe(III)OFe(II)^+ + 3H_2O$	+0.24[d]	-0.53[a]	-0.23[a]

[calc] Calculated from Gibbs free energies, where ΔG_f^0 is -488.6 kJ/mol[b] for Gth, -481.7 kJ/mol[e] for Ak, and -699 kJ/mol[b] for Fh

[a] Assuming $[\equiv Fe(III)OFe(II)^+]$ is 10^{-6} M (~ 1 % of initial [Fe(II)]) and $[\equiv Fe(III)OH]$ is 10^{-5} M (calculated from the site density[d] and the TEM surface area in Table 5.2)

[b] Brezonik and Arnold (2011)

[c] Schwarzenbach et al. (2003)

[d] Silvester et al. (2005)

[e] Navrotsky et al. (2008)

– Not found in the current literature

The kinetics of abiotic redox reactions were quantified to compare the redox reactivity of goethite, akaganeite, and ferrihydrite in acidic brine solutions. Benzoquinone reduction by adsorbed Fe(II) significantly decreased in 0.67 M $CaCl_2$ as compared to 0 M $CaCl_2$ (Fig. 5.3a). In contrast, the hydroquinone oxidation rate increased with higher $CaCl_2$ concentration (Fig. 5.3b) in the case of ferrihydrite, did not change with changing $CaCl_2$ concentration in the case of akaganeite, and was altogether undetectable in the case of goethite. Detailed reaction rate constants for each system and $CaCl_2$ concentration,

along with surface area measurements from TEM and BET, are provided in Table 5.2. To determine the effect of ionic strength, rates of benzoquinone reduction as a function of $CaCl_2$ concentration were determined for Fe(II)/goethite (Fig. 5.3c) and Fe(II)/ferrihydrite suspensions (Fig. 5.3d, rate constants in Table D.1). With both iron oxyhydroxides, reaction rates decreased with increasing $CaCl_2$ concentration.

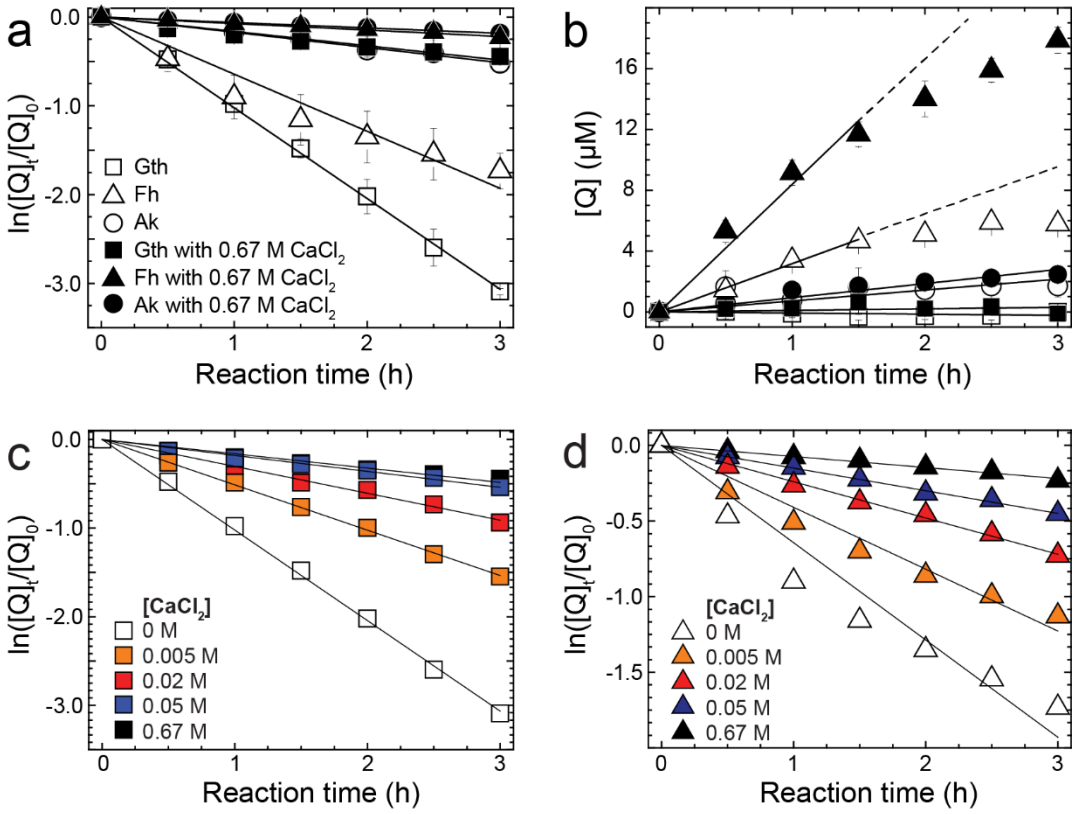

Figure 5.3. a) Degradation of benzoquinone (Q) by adsorbed Fe(II) on goethite (Gth), akaganeite (Ak), or ferrihydrite (Fh) and b) production of benzoquinone from the oxidation of hydroquinone by each iron oxyhydroxide as a function of time. Suspensions were prepared with either 0 M (open symbols) or 0.67 M (closed symbols) $CaCl_2$ in 40 mM acetate buffer at pH 4.5. Solid lines are results of linear regression (data summarized in Table 1). Error bars are standard deviations from triplicate trials. Dashed lines represent the extrapolation of initial rates over longer reaction times. c-d) Benzoquinone (Q) degradation by Fe(II) adsorbed on either c) goethite or d) ferrihydrite in varied $CaCl_2$ concentration and 40 mM acetate buffer at pH 4.5. Solid lines are results of linear regression (data summarized in Table S1).

Table 5.2. Pseudo-first-order rate constants of benzoquinone (Q) reduction by adsorbed Fe(II) or initial rate of hydroquinone (QH_2) oxidation by goethite (Gth), akaganeite (Ak), ferrihydrite (Fh), or a combination of all three minerals. Reaction suspensions were in 40 mM acetate buffer at pH 4.5. R^2 values are in parentheses. ND = not detectable. NA = not applicable.

Particle(s)	SA_{TEM} (m^2/g)	SA_{BET} (m^2/g)	Total mass loading (g/L)	$[CaCl_2]$ (M)	$Q \rightarrow QH_2$ k_{obs} (h^{-1})	$QH_2 \rightarrow Q$ d[Q]/dt (µM h^{-1})
Gth	190	140	0.325	0	1.02 ± 0.02 (1.0)	ND
				0.67	0.16 ± 0.01 (0.99)	ND
Ak	240	278	0.325	0	0.17 ± 0.01 (1.0)	0.72 ± 0.31 (0.84)
				0.67	0.061 ± 0.002 (1.0)	0.93 ± 0.15 (0.98)
Fh	510	130-280	0.325	0	0.64 ± 0.09 (0.98)	3.2 ± 0.3 (1.0)
				0.67	0.073 ± 0.004 (1.0)	8.4 ± 1.6 (0.99)
Gth+Ak+Fh			0.325	0	0.51 ± 0.01 (1.0)	NA
				0.67	0.091 ± 0.002 (1.0)	NA
Gth+Ak+Fh			0.975	0	0.85 ± 0.02 (0.99)	NA
				0.67	0.22 ± 0.01 (1.0)	NA

Rate constants for individual iron oxyhydroxides were also compared to the rate constants obtained using a mixture of three (Table 5.2, Fig. D.7), which is more analogous to the natural modeled system. Similar to the individual results, the addition of 0.67 M $CaCl_2$ decreased benzoquinone reduction rate by adsorbed Fe(II). The observed rate for suspensions containing all three iron oxyhydroxides at a total mass loading of 0.325 g/L was approximately equal to the sum of one-third the rates observed for each mineral alone at 0.325 g/L. When normalized to mass loading, benzoquinone reduction rate is faster for the lower mass loading (0.325 g/L versus 0.975 g/L), despite the identical amount of Fe(II) added.

Discussion

Accessible reactive surface areas of iron oxyhydroxides in acidic brines

Accessible surface area

Estimates of accessible reactive surface area for each iron oxyhydroxide in an acidic brine is fundamental to interpreting relative reactivity in such environments, among other factors, such as thermodynamic properties. Increasing $CaCl_2$ concentration led to the formation of larger aggregates as evidenced by increasing hydrodynamic diameters and decreasing zeta potentials. It has been shown that larger aggregate size correlates to decreases in accessible surface area of iron oxyhydroxide nanoparticles in typical aquatic systems.[45] Given these results, accessible surface area of goethite, akaganeite, and ferrihydrite nanoparticles is expected to decrease in natural acidic brine environments. While the amount of adsorbed Fe(II) is limited, the low amount of inner-sphere complexation of Fe(II) may change the surface potential enough to affect aggregation at low $CaCl_2$ concentrations, as seen nominally in Fig. 5.1. At high $CaCl_2$ concentrations, however, the ionic strength primarily controls aggregation.

In this study, we provide hydrodynamic diameters collected by DLS, which is an indirect but relatively efficient method for characterizing aggregate size in suspensions. At large aggregate sizes, however, the limitations of the technique[46] along with faster settling rates[21] must be acknowledged, especially in the case of high $CaCl_2$ concentrations seen here. Previous work indicated that when DLS results demonstrate aggregates in the 100 nm size range, data from DLS and cryogenic transmission electron microscopy (cryo-TEM), a direct method of characterizing aggregate sizes, match well. When DLS results demonstrate larger sizes in the micron size range, cryo-TEM can provide more detail regarding the size distribution, especially since DLS is so strongly dominated by the largest suspended objects, yet the results are qualitatively consistent.[45]

Reactive surface area

Extent of Fe(II) adsorption was measured to assess the amount of reactive surface area available for each iron oxyhydroxide in 0 and 0.67 M $CaCl_2$. Our results (Fig. 5.2) suggest only a small fraction of total Fe(II) resides on the iron oxyhydroxide surface at any given time in an extremely acidic brine environment (pH < 4), with the largest fraction of adsorbed Fe(II) sites on goethite. In moderately acidic (pH 4 – 6) settings,[6,47] a greater fraction of total Fe(II) residing on the surface may lead to faster kinetic rates of reactions involving adsorbed Fe(II) on iron oxyhydroxides.

The presence of 0.67 M $CaCl_2$ decreased overall adsorption for goethite and ferrihydrite. Possible causes include less accessible surface area and/or competitive Ca(II) adsorption. Previous studies have shown that iron oxyhydroxide minerals weakly sorb Ca(II)[48,49] but sorb other metal ions more strongly,[50,51] particularly when the pH is below the point of zero charge. This is the first study to our knowledge that has measured Fe(II) adsorption edges on akaganeite as a function of ionic strength and pH; although previous work has shown adsorption of other ions on akaganeite.[52,53] The fact that high $CaCl_2$ concentration did not decrease Fe(II) adsorption indicates that there is a unique chemistry for akaganeite, such as competitive ligand exchange with chloride tunnel ions as described in the works of Song and Boily[38,54] and Kozin and Boily.[55]

These adsorption edges were collected in the absence of a buffer to determine effect of pH. In the subsequent studies, 40 mM acetate buffer was used to maintain pH 4.5. While attempts were made to measure differences in Fe(II) adsorption on each mineral in this buffer, average dissolved Fe(II) concentrations were not statistically

different and were within the quantification limit of 0.01 mM Fe(II) for the method. Acetate adsorption on an iron oxide has been described as solvent-surface hydration-separated ion pairs and surface hydration-shared pairs, which are favorable in mildly acidic conditions.[56] Given what is known about acetate adsorption, we argue that overall Fe(II) adsorption decreases in our buffered system (consistent with our difficulty in detecting statistical differences in adsorption between minerals) but that the pH and ionic strength trends are expected to remain the same.

Iron oxyhydroxide reactivity in acidic brines

Benzoquinone reduction

For reduction of benzoquinone (Fig. 5.3a), reaction rates were fastest with goethite, followed by ferrihydrite and then akaganeite, which can be attributed to their individual reduction potentials and number of reactive sites. A reduction potential for Fe(II)-sorbed on akaganeite was not found in the literature; thus, it is difficult to compare akaganeite to goethite and ferrihydrite, although it is hypothesized that it would be less favorable given this data.

The presence of brine, in this case high $CaCl_2$ concentration, decreased the reaction rates for all three minerals. Exploration of reaction rate as a function of ionic strength for goethite and ferrihydrite (Fig. 5.3c and 5.3d) demonstrated that rates systematically decreased with increasing ionic strength, consistent with a loss of accessible reactive surface area due to either particle aggregation or decreased Fe(II) sorption. This trend is most evident in the comparison between reaction rates in 0.05 M and 0.67 M $CaCl_2$. For goethite, the two rates were statistically indistinguishable,

consistent with a relatively small difference in measured aggregate size as seen in Fig. 5.1. With ferrihydrite, aggregate size largely increased between the two $CaCl_2$ concentrations, and the rate was much slower at the higher ionic strength.

Hydroquinone oxidation

The fastest rate of oxidation by ferrihydrite is agreeable with the low degree of crystallinity and favorable reduction potential, which drives reductive dissolution. Akaganeite was also faster than goethite (longer reaction times in 0.67 M $CaCl_2$ are shown in Fig. D.5). In contrast to the benzoquinone reactions, hydroquinone oxidation by ferrihydrite was significantly faster in 0.67 M $CaCl_2$. Despite decreases in accessible surface area, the number of free reactive ≡Fe(III) sites increases in $CaCl_2$ with the inhibition of adsorbed Fe(II) (which drives the reverse benzoquinone reduction reaction), thus increasing oxidation rate.

In both redox systems, especially in the case of ferrihydrite (and after ~ 6 h for hydroquinone oxidation by akaganeite in Fig. D.5), pseudo-first-order reaction kinetics do not always produce excellent fits, suggesting possible phase transformation or changes in aggregation. No evidence for new mineral phases was observed by XRD (Fig. D.2, though a difference in preferred orientation was observed for the 0 M $CaCl_2$-benzoquinone-goethite and -akaganeite system, possible evidence of mineral growth). Although numerous studies have detected phase transformations in similar suspensions at circumneutral pH and aerobic conditions,[57,58] no work has demonstrated phase transformations at more acidic pH and anaerobic conditions. In addition, no evidence for changing aggregate size of ferrihydrite during reaction with hydroquinone in 0 M $CaCl_2$

(Fig. D.6) was detected. It is then likely that the nonlinearity of the reaction kinetics is caused by the reverse reaction. In other words, with benzoquinone reduction, the hydroquinone produced could react with new iron oxyhydroxide reactive sites. Because hydroquinone oxidation is thermodynamically favorable for ferrihydrite, the reverse reaction is expected to be significant. Concurrently, with hydroquinone oxidation, the benzoquinone product could react with adsorbed Fe(II) produced from the reaction and would be more significant in systems at 0 M $CaCl_2$.

Mixed mineral suspensions

Finally, mixed mineral suspensions provide a better comparison to natural acidic brine environments. Benzoquinone reduction rate was faster for 0.325 g/L total mass loading compared to 0.975 g/L. Both suspensions had the same amount of Fe(II) added and were well mixed based on the observation that the particles were completely suspended in the reactors. Also, DLS measurements aggregate size in 0 M $CaCl_2$ as measured by DLS was ~ 200 nm for both suspensions. For those reasons, it is more likely that differences in the amount and distribution of adsorbed Fe(II) among the three minerals is the cause, although attempts to quantify a statistical difference in Fe(II) adsorption were problematic due to the low degree of Fe(II) adsorption at pH 4.5, as observed for the single mineral studies. These results demonstrate that the consideration of the entire system, including all reactive minerals present, is necessary when predicting the abiotic contributions to iron redox cycling in acidic brines.

Implications for iron geochemical cycling in acidic brines.

The unique chemistry between iron oxyhydroxides and organic species in acidic brines is significant for several systems with potential environmental impact. In acidic brines such as those found in the Soudan Mine, reaction with between adsorbed Fe(II) on an iron oxyhydroxide mineral and an oxidized quinone species is expected to be minor. Significant adsorption of Fe(II) is limited under such acidic conditions and only decreases further in waters with high ionic strength. In contrast, reductive dissolution is a possible contributor to iron cycling in acidic brines, with high ionic strength promoting oxidation of reduced quinone species by iron oxyhydroxides. Specifically, ferrihydrite was experimentally shown to be a strong abiotic oxidant under saline and acidic conditions which has significance for oxidative degradation of organic matter and dissimilatory iron reduction.

This work represents a controlled exploration of abiotic reactivity in conditions similar to the Soudan Mine groundwater seepages, and future work will explore the effect of using collected groundwater samples from the mine. While this location represents only one environment where these redox reactions are important, these findings have implications to other sulfur-deficient acidic brines or evaporative settings across a global setting, such as acidic brine lakes and acid mine drainage locations that contain precipitated iron oxyhydroxides. For example, abiotic oxidation of organic matter by iron oxyhydroxides could compete with acidophilic microbial iron cycling in the extremely acidic evaporative sites found in Western Australia. For moderately acidic brines, we have shown that estimates of iron oxyhydroxide abiotic reactivity are important for

interpretations of iron cycling. In conclusion, although many of the studies discussed previously have provided contributions to the understanding of biotic reactivity in these rare but distinctive environments, future study of the abiotic iron oxyhydroxide reactivity could greatly improve our understanding of these complex sites.

Acknowledgments

We thank E.C. Alexander and S. Alexander (University of Minnesota) for providing unpublished geochemistry data for Soudan Mine groundwater seeps, B.E. Wilson for nitrogen sorption analyses, and K. Sabyrov for akaganeite synthesis procedure. This work was supported by the John Wertz Fellowship, as part of the Department of Chemistry Fellowships for Excellence in Graduate Studies at the University of Minnesota (J.H.S.), NSF grants ECS-1012193 and CHE-1507496 (R.L.P. and W.A.A.), and Minnesota Environment and Natural Resources Trust Fund as recommended by the LCCMR (B.M.T.). Parts of this work were carried out in the Characterization Facility, University of Minnesota, a member of the NSF-funded Materials Research Facilities Network (www.mrfn.org) via the MRSEC program.

Chapter 6. Conclusions

As described by the culmination of results in this thesis, the reactivity of iron oxide nanoparticles towards oxidized contaminants in groundwater systems will change as a function of environmental variables and extent of reaction. The presence of organic matter and secondary mineral phases altered both short- and long-term reactions between iron oxide nanoparticles, aqueous Fe(II), and nitroaromatic compounds. In addition, other solution variables like pH, ionic strength, and reactant concentration affected the rate and products of reactions, the extent of which depended on the variable and reaction time. While the effects of these variables on short-term reactions of iron oxide nanoparticles are well known, evolving reactivity is not well understood but has the potential to affect both the fate and transport of contaminants and nanoparticles in natural groundwater settings. The results of this study, therefore, provided essential contributions to current groundwater remediation literature as well as established protocols to studying evolving reactivity in these complex and dynamic systems.

On a broad-scale, this work has the potential to help solve the water crisis we are faced with. Most agricultural zones rely on groundwater resources but are often the most contaminated sites, with high concentrations of pesticides containing nitroaromatic functional groups. Industrial and developing areas are also faced with both a higher production of hazardous waste and a growing population. By increasing our understanding of how iron oxide nanoparticles will react in the subsurface, the efficiency and expected outcome of remediation will improve. In addition, the fundamental concept of accessible

reactive surface area as a function of solution variables will also impact current research that is beyond this thesis scope. For example, the findings could affect interpretations of microbial iron cycling in aqueous iron-rich environments, industrial production methods of nanoparticle synthesis, or geological studies of iron oxide formation.

Bibliography

Chapter 1 References

(1) Maupin, M. A.; Kenny, J. F.; Hutson, S. S.; Lovelace, J. K.; Barber, N. L.; Linsey, K. S. *Estimated use of water in the United States in 2010*; U.S. Geological Survey Circular 1405, Reston, VA, 2014.

(2) Lapworth, D. J.; Baran, N.; Stuart, M. E.; Ward, R. S. Emerging organic contaminants in groundwater: A review of sources, fate and occurrence. *Environ. Pollut.* **2012**, *163*, 287–303.

(3) Toccalino, P. L.; Gilliom, R. J.; Lindsey, B. D.; Rupert, M. G. Pesticides in groundwater of the United States: Decadal-scale changes, 1993-2011. *Groundwater* **2014**, *52*, 112–125.

(4) SciFinder. Chemical Abstracts Service: Columbus, OH. Search research topic: "environmental remediation". https://scifinder.cas.org (accessed February 1, 2016).

(5) Higgins, M. R.; Olson, T. M. Life-cycle case study comparison of permeable reactive barrier versus pump-and-treat remediation. *Environ. Sci. Technol.* **2009**, *43*, 9432–9438.

(6) Karn, B.; Kuiken, T.; Otto, M. Nanotechnology and in situ remediation: a review of the benefits and potential risks. *Environ. Heal. Perspect.* **2009**, *117*, 1813–1831.

(7) Tratnyek, P. G.; Johnson, R. L.; Lowry, G. V; Brown, R. A. In situ chemical reduction for source remediation. In *Chlorinated Solvent Source Zone Remediation*; Kueper, B. H., Stroo, H. F., Vogel, C. M., Ward, C. H., Eds.; Springer Science+Business Media, 2014; pp 307–351.

(8) Klausen, J.; Tröber, S. P.; Haderlein, S. B.; Schwarzenbach, R. P. Reduction of substituted nitrobenzenes by Fe(II) in aqueous mineral suspensions. *Environ. Sci. Technol.* **1995**, *29*, 2396–2404.

(9) Kosmulski, M.; Durand-Vidal, S.; Maczka, E.; Rosenholm, J. B. Morphology of synthetic goethite particles. *J. Colloid Interface Sci.* **2004**, *271*, 261–269.

(10) Schaefer, M. V; Gorski, C. A.; Scherer, M. M. Spectroscopic evidence for interfacial Fe(II)-Fe(III) electron transfer in a clay mineral. *Environ. Sci. Technol.* **2011**, *45*, 540–545.

(11) Sherman, D. M. Molecular orbital (SCF-Xα-SW) theory of metal-metal charge transfer processes in minerals. *Phys. Chem. Miner.* **1987**, *14*, 355–363.

(12) Stumm, W. The inner-sphere surface complex. In *Aquatic Chemistry: Interfacial and Interspecies Processes*; Huang, C., O'Melia, C. R., Morgan, J. J., Eds.; American Chemical Society: Washington, D.C., 1995; pp 1–32.

(13) Farley, K. J.; Dzombak, D. A.; Morel, F. M. . A surface precipitation model for the sorption of cations on metal oxides. *J. Colloid Interface Sci.* **1985**, *106*, 226–242.

(14) Williams, A. G. B.; Scherer, M. M. Spectroscopic evidence for Fe(II)-Fe(III) electron transfer at the iron oxide-water interface. *Environ. Sci. Technol.* **2004**, *38*,

4782–4790.
(15) Rosso, K. M.; Smith, D. M. A.; Dupuis, M. An ab initio model of electron transport in hematite (α-Fe2O3) basal planes. *J. Chem. Phys.* **2003**, *118*, 6455–6466.
(16) Gorski, C. A.; Scherer, M. M. Influence of magnetite stoichiometry on Fe(II) uptake and nitrobenzene reduction. *Environ. Sci. Technol.* **2009**, *43*, 3675–3680.
(17) Gorski, C. A.; Nurmi, J. T.; Tratnyek, P. G.; Hofstetter, T. B.; Scherer, M. M. Redox behavior of magnetite: Implications for contaminant reduction. *Environ. Sci. Technol.* **2010**, *44*, 55–60.
(18) Hofstetter, T. B.; Heijman, C. G.; Haderlein, S. B.; Holliger, C.; Schwarzenbach, R. P. Complete reduction of TNT and other (poly)nitroaromatic compounds under iron-reducing subsurface conditions. *Environ. Sci. Technol.* **1999**, *33*, 1479–1487.
(19) Boparai, H. K.; Comfort, S. D.; Satapanajaru, T.; Szecsody, J. E.; Grossl, P. R.; Shea, P. J. Abiotic transformation of high explosives by freshly precipitated iron minerals in aqueous Fe^{II} solutions. *Chemosphere* **2010**, *79*, 865–872.
(20) Gregory, K. B.; Larese-Casanova, P.; Parkin, G. F.; Scherer, M. M. Abiotic transformation of hexahydro-1,3,5-trinitro-1,3,5-triazine by Fe^{II} bound to magnetite. *Environ. Sci. Technol.* **2004**, *38*, 1408–1414.
(21) Klupinski, T. P.; Chin, Y.-P.; Traina, S. J. Abiotic degradation of pentachloronitrobenzene by Fe(II): Reactions on goethite and iron oxide nanoparticles. *Environ. Sci. Technol.* **2004**, *38*, 4353–4360.
(22) Klupinski, T. P.; Chin, Y.-P. Abiotic degradation of trifluralin by Fe(II): Kinetics and transformation pathways. *Environ. Sci. Technol.* **2003**, *37*, 1311–1318.
(23) Strathmann, T. J.; Stone, A. T. Mineral surface catalysis of reactions between Fe^{II} and oxime carbamate pesticides. *Geochim. Cosmochim. Acta* **2003**, *67*, 2775–2791.
(24) Sørensen, J.; Thorling, L. Stimulation by lepidocrocite (γ-FeOOH) of Fe(II)-dependent nitrite reduction. *Geochim. Cosmochim. Acta* **1991**, *55*, 1289–1294.
(25) Chun, C. L.; Hozalski, R. M.; Arnold, W. A. Degradation of drinking water disinfection byproducts by synthetic goethite and magnetite. *Environ. Sci. Technol.* **2005**, *39*, 8525–8532.
(26) Vikesland, P. J.; Valentine, R. L. Iron oxide surface-catalyzed oxidation of ferrous iron by monochloramine: Implications of oxide type and carbonate on reactivity. *Environ. Sci. Technol.* **2002**, *36*, 512–519.
(27) Lee, J.-Y.; Pearson, C. R.; Hozalski, R. M.; Arnold, W. A. Degradation of trichloronitromethane by iron water main corrosion products. *Water Res.* **2008**, *42*, 2043–2050.
(28) Buerge, I. J.; Hug, S. J. Influence of mineral surfaces on chromium(VI) reduction by iron(II). *Environ. Sci. Technol.* **1999**, *33*, 4285–4291.
(29) Liger, E.; Charlet, L.; Van Cappellen, P. Surface catalysis of uranium(VI) reduction by iron(II). *Geochim. Cosmochim. Acta* **1999**, *63*, 2939–2955.
(30) Pecher, K.; Haderlein, S. B.; Schwarzenbach, R. P. Reduction of polyhalogenated methanes by surface-bound Fe(II) in aqueous suspensions of iron oxides. *Environ.*

Sci. Technol. **2002**, *36*, 1734–1741.
(31) Amonette, J. E.; Workman, D. J.; Kennedy, D. W.; Fruchter, J. S.; Gorby, Y. A. Dechlorination of carbon tetrachloride by Fe(II) associated with goethite. *Environ. Sci. Technol.* **2000**, *34*, 4606–4613.
(32) Elsner, M.; Schwarzenbach, R. P.; Haderlein, S. B. Reactivity of Fe(II)-bearing minerals toward reductive transformation of organic contaminants. *Environ. Sci. Technol.* **2004**, *38*, 799–807.
(33) Tobler, N. B.; Hofstetter, T. B.; Straub, K. L.; Fontana, D.; Schwarzenbach, R. P. Iron-mediated microbial oxidation and abiotic reduction of organic contaminants under anoxic conditions. *Environ. Sci. Technol.* **2007**, *41*, 7765–7772.
(34) Hansel, C. M.; Benner, S. G.; Neiss, J.; Dohnalkova, A.; Kukkadapu, R. K.; Fendorf, S. Secondary mineralization pathways induced by dissimilatory iron reduction of ferrihydrite under advective flow. *Geochim. Cosmochim. Acta* **2003**, *67*, 2977–2992.
(35) Garg, S.; Jiang, C.; Waite, T. D. Mechanistic insights into iron redox transformations in the presence of natural organic matter: Impact of pH and light. *Geochim. Cosmochim. Acta* **2015**, *165*, 14–34.
(36) Garg, S.; Jiang, C.; Miller, C. J.; Rose, A. L.; Waite, T. D. Iron redox transformations in continuously photolyzed acidic solutions containing natural organic matter: Kinetic and mechanistic insights. *Environ. Sci. Technol.* **2013**, *47*, 9190–9197.
(37) Garg, S.; Ito, H.; Rose, A. L.; Waite, T. D. Mechanism and kinetics of dark iron redox transformations in previously photolyzed acidic natural organic matter solutions. *Environ. Sci. Technol.* **2013**, *47*, 1861–1869.
(38) Cornell, R. M.; Schwertmann, U. *The Iron Oxides*, 2nd ed.; Wiley-VCH: Weinheim, 2003.
(39) Anschutz, A. J.; Penn, R. L. Reduction of crystalline iron(III) oxyhydroxides using hydroquinone: Influence of phase and particle size. *Geochem. Trans.* **2005**, *6*, 60–66.
(40) Boily, J.-F.; Lützenkirchen, J.; Balmés, O.; Beattie, J.; Sjöberg, S. Modeling proton binding at the goethite (α-FeOOH)–water interface. *Colloids Surf., A* **2001**, *179*, 11–27.
(41) Michel, F. M.; Ehm, L.; Antao, S. M.; Lee, P. L.; Chupas, P. J.; Liu, G.; Strongin, D. R.; Schoonen, M. A. A.; Phillips, B. L.; Parise, J. B. The structure of ferrihydrite, a nanocrystalline material. *Science (80-.).* **2007**, *316*, 1726–1729.
(42) Hiemstra, T.; van Riemsdijk, W. H. Adsorption and surface oxidation of Fe(II) on metal (hydr)oxides. *Geochim. Cosmochim. Acta* **2007**, *71*, 5913–5933.
(43) Barrón, V.; Torrent, J. Surface hydroxyl configuration of various crystal faces of hematite and goethite. *J. Colloid Interface Sci.* **1996**, *177*, 407–410.
(44) Dixit, S.; Hering, J. G. Sorption of Fe(II) and As(III) on goethite in single- and dual-sorbate systems. *Chem. Geol.* **2006**, *228*, 6–15.
(45) Larese-Casanova, P.; Scherer, M. M. Fe(II) sorption on hematite: New insights based on spectroscopic measurements. *Environ. Sci. Technol.* **2007**, *41*, 471–477.

(46) Tanwar, K. S.; Petitto, S. C.; Ghose, S. K.; Eng, P. J.; Trainor, T. P. Fe(II) adsorption on hematite (0001). *Geochim. Cosmochim. Acta* **2009**, *73*, 4346–4365.
(47) Catalano, J. G.; Fenter, P.; Park, C.; Zhang, Z.; Rosso, K. M. Structure and oxidation state of hematite surfaces reacted with aqueous Fe(II) at acidic and neutral pH. *Geochim. Cosmochim. Acta* **2010**, *74*, 1498–1512.
(48) Frierdich, A. J.; Helgeson, M.; Liu, C.; Wang, C.; Rosso, K. M.; Scherer, M. M. Iron atom exchange between hematite and aqueous Fe(II). *Environ. Sci. Technol.* **2015**, *49*, 8479–8486.
(49) Hiemstra, T.; Van Riemsdijk, W. H. A surface structural model for ferrihydrite I: Sites related to primary charge, molar mass, and mass density. *Geochim. Cosmochim. Acta* **2009**, *73*, 4423–4436.
(50) Appelo, C. A. J.; Van der Weiden, M. J. J.; Tournassat, C.; Charlet, L. Surface complexation of ferrous iron and carbonate on ferrihydrite and the mobilization of arsenic. *Environ. Sci. Technol.* **2002**, *36*, 3096–3103.
(51) Pabisiak, T.; Kiejna, A. Fe adsorption on hematite (α-Fe_2O_3) (0001) and magnetite (Fe_3O_4) (111) surfaces. *J. Chem. Phys.* **2014**, *141*, 134707.
(52) Sun, Z.; Su, F.; Forsling, W.; Samskog, P.-O. Surface characteristics of magnetite in aqueous suspension. *J. Colloid Interface Sci.* **1998**, *197*, 151–159.
(53) Heijman, C. G.; Holliger, C.; Glaus, M. A.; Schwarzenbach, R. P.; Zeyer, J. Abiotic reduction of 4-chloronitrobenzene to 4-chloroaniline in a dissimilatory iron-reducing enrichment culture. *Appl. Environ. Microbiol.* **1993**, *59*, 4350–4353.
(54) Strehlau, J. H.; Toner, B. M.; Arnold, W. A.; Penn, R. L. Accessible reactive surface area of iron oxyhydroxides in acidic brines. **2016**, In revision.
(55) Tamaura, Y.; Ito, K.; Katsura, T. Transformation of γ-FeO(OH) to Fe_3O_4 by adsorption of iron(II) ion on γ-FeO(OH). *J. Chem. Soc. Dalt. Trans.* **1983**, 189–194.
(56) Silvester, E.; Charlet, L.; Tournassat, C.; Géhin, A.; Grenèche, J.-M.; Liger, E. Redox potential measurements and Mössbauer spectrometry of Fe^{II} adsorbed onto Fe^{III} (oxyhydr)oxides. *Geochim. Cosmochim. Acta* **2005**, *69*, 4801–4815.
(57) Zhang, Y.; Charlet, L.; Schindler, P. W. Adsorption of protons, Fe(II) and Al(III) on lepidocrocite (γ-FeOOH). *Colloids Surf.* **1992**, *63*, 259–268.
(58) Schultz, J. D.; Strehlau, J. H.; Penn, R. L. Time and concentration dependencies of Fe(II)-induced phase transformation of akaganeite. **2016**, In preparation.
(59) Stemig, A. M.; Do, T. A.; Yuwono, V. M.; Arnold, W. A.; Penn, R. L. Goethite nanoparticle aggregation: effects of buffers, metal ions, and 4-chloronitrobenzene reduction. *Environ. Sci. Nano* **2014**, *1*, 478–487.
(60) Burrows, N. D.; Kesselman, E.; Sabyrov, K.; Stemig, A.; Talmon, Y.; Penn, R. L. Crystalline nanoparticle aggregation in non-aqueous solvents. *CrystEngComm* **2014**, *16*, 1472.
(61) Yuwono, V. M.; Burrows, N. D.; Soltis, J. A.; Do, T. A.; Penn, R. L. Aggregation of ferrihydrite nanoparticles in aqueous systems. *Faraday Discuss.* **2012**, *159*, 235–245.
(62) Legg, B. A.; Zhu, M.; Comolli, L. R.; Gilbert, B.; Banfield, J. F. Impacts of ionic

strength on three-dimensional nanoparticle aggregate structure and consequences for environmental transport and deposition. *Environ. Sci. Technol.* **2014**, *48*, 13703–13710.
(63) Legg, B. A.; Zhu, M.; Comolli, L. R.; Gilbert, B.; Banfield, J. F. Determination of the three-dimensional structure of ferrihydrite nanoparticle aggregates. *Langmuir* **2014**, *30*, 9931–9940.
(64) Frandsen, C.; Bahl, C. R. H.; Lebech, B.; Lefmann, K.; Kuhn, L. T.; Keller, L.; Andersen, N. H.; v. Zimmermann, M.; Johnson, E.; Klausen, S. N.; et al. Oriented attachment and exchange coupling of α-Fe_2O_3 nanoparticles. *Phys. Rev. B* **2005**, *72*, 214406.
(65) Wu, J.; Aslam, M.; Dravid, V. P. Imaging of magnetic colloids under the influence of magnetic field by cryogenic transmission electron microscopy. *Appl. Phys. Lett.* **2008**, *93*, 2014–2017.
(66) Essington, M. E. *Soil and Water Chemistry: An Integrative Approach*; CRC Press: Boca Raton, FL, 2004.
(67) Jeon, B.-H.; Dempsey, B. A.; Burgos, W. D.; Royer, R. A. Reactions of ferrous iron with hematite. *Colloids Surf., A* **2001**, *191*, 41–55.
(68) Handler, R. M.; Frierdich, A. J.; Johnson, C. M.; Rosso, K. M.; Beard, B. L.; Wang, C.; Latta, D. E.; Neumann, A.; Pasakarnis, T.; Premaratne, W. A. P. J.; et al. Fe(II)-catalyzed recrystallization of goethite revisited. *Environ. Sci. Technol.* **2014**, *48*, 11302–11311.
(69) Reddy, T. R.; Frierdich, A. J.; Beard, B. L.; Johnson, C. M. The effect of pH on stable iron isotope exchange and fractionation between aqueous Fe(II) and goethite. *Chem. Geol.* **2015**, *397*, 118–127.
(70) Sposito, G. On points of zero charge. *Environ. Sci. Technol.* **1998**, *32*, 2815–2819.
(71) Baalousha, M.; Manciulea, A.; Cumberland, S.; Kendall, K.; Lead, J. R. Aggregation and surface properties of iron oxide nanoparticles: Influence of pH and natural organic matter. *Environ. Toxicol. Chem.* **2008**, *27*, 1875–1882.
(72) Sverjensky, D. A.; Sahai, N. Theoretical prediction of single-site surface-protonation equilibrium constants for oxides and silicates in water. *Geochim. Cosmochim. Acta* **1996**, *60*, 3773–3797.
(73) Sahai, N.; Sverjensky, D. A. Evaluation of internally consistent parameters for the triple-layer model by the systematic analysis of oxide surface titration data. *Geochim. Cosmochim. Acta* **1997**, *61*, 2801–2826.
(74) Palomino, D.; Stoll, S. Fulvic acids concentration and pH influence on the stability of hematite nanoparticles in aquatic systems. *J. Nanopart. Res.* **2013**, *15*, 1428.
(75) Xie, J.; Gu, X.; Tong, F.; Zhao, Y.; Tan, Y. Surface complexation modeling of Cr(VI) adsorption at the goethite–water interface. *J. Colloid Interface Sci.* **2015**, *455*, 55–62.
(76) Liu, J.; Zhu, R.; Xu, T.; Xu, Y.; Ge, F.; Xi, Y.; Zhu, J.; He, H. Co-adsorption of phosphate and zinc(II) on the surface of ferrihydrite. *Chemosphere* **2016**, *144*, 1148–1155.
(77) Kumar, E.; Bhatnagar, A.; Hogland, W.; Marques, M.; Sillanpaa, M. Interaction of

inorganic anions with iron-mineral adsorbents in aqueous media - A review. *Adv. Colloid Interface Sci* **2014**, *203*, 11–21.
(78) Ottley, C. J.; Davison, W.; Edmunds, W. M. Chemical catalysis of nitrate reduction by iron(II). *Geochim. Cosmochim. Acta* **1997**, *61*, 1819–1828.
(79) Xu, C.; Deng, K.; Li, J.; Xu, R. Impact of environmental conditions on aggregation kinetics of hematite and goethite nanoparticles. *J. Nanopart. Res.* **2015**, *17*, 394.
(80) Wu, Y.; Geng, L.; Wang, X.; Chen, R.; Wei, Y.; Wu, D. Reductive transformation of p-nitrophenol by Fe(II) species: The effect of anionic media. *J. Hazard. Mater.* **2013**, *263*, 556–561.
(81) Escoube, R.; Rouxel, O. J.; Sholkovitz, E.; Donard, O. F. X. Iron isotope systematics in estuaries: The case of North River, Massachusetts (USA). *Geochim. Cosmochim. Acta* **2009**, *73*, 4045–4059.
(82) Boyle, E. A.; Edmond, J. M.; Sholkovitz, E. R. The mechanism of iron removal in estuaries. *Geochim. Cosmochim. Acta* **1977**, *41*, 1313–1324.
(83) Mayer, L. M. Aggregation of colloidal iron during estuarine mixing: Kinetics, mechanism, and seasonality. *Geochim. Cosmochim. Acta* **1982**, *46*, 2527–2535.
(84) Gu, B.; Schmitt, J.; Chen, Z.; Liang, L.; McCarthy, J. F. Adsorption and desorption of natural organic matter on iron oxide: mechanisms and models. *Environ. Sci. Technol.* **1994**, *28*, 38–46.
(85) Vindedahl, A. M.; Strehlau, J. H.; Arnold, W. A.; Penn, R. L. Organic matter and iron oxide nanoparticles: aggregation, interactions, and reactivity. *ES Nano* **2016**, DOI: 10.1039/C5EN00215J.
(86) Zhou, Q.; Maurice, P. a.; Cabaniss, S. E. Size fractionation upon adsorption of fulvic acid on goethite: Equilibrium and kinetic studies. *Geochim. Cosmochim. Acta* **2001**, *65*, 803–812.
(87) Safiur Rahman, M.; Whalen, M.; Gagnon, G. A. Adsorption of dissolved organic matter (DOM) onto the synthetic iron pipe corrosion scales (goethite and magnetite): Effect of pH. *Chem. Eng. J.* **2013**, *234*, 149–157.
(88) Kaiser, K.; Mikutta, R.; Guggenberger, G. Increased stability of organic matter sorbed to ferrihydrite and goethite on aging. *Soil Sci. Soc. Am. J.* **2007**, *71*, 711–719.
(89) Yamamoto, M.; Nishida, A.; Otsuka, K.; Komai, T.; Fukushima, M. Evaluation of the binding of iron(II) to humic substances derived from a compost sample by a colorimetric method using ferrozine. *Bioresour. Technol.* **2010**, *101*, 4456–4460.
(90) Catrouillet, C.; Davranche, M.; Dia, A.; Bouhnik-Le Coz, M.; Marsac, R.; Pourret, O.; Gruau, G. Geochemical modeling of Fe(II) binding to humic and fulvic acids. *Chem. Geol.* **2014**, *372*, 109–118.
(91) Nurmi, J. T.; Tratnyek, P. G. Electrochemical properties of natural organic matter (NOM), fractions of NOM, and model biogeochemical electron shuttles. *Environ. Sci. Technol.* **2002**, *36*, 617–624.
(92) Luan, F.; Xie, L.; Li, J.; Zhou, Q. Abiotic reduction of nitroaromatic compounds by Fe(II) associated with iron oxides and humic acid. *Chemosphere* **2013**, *91*, 1035–1041.

(93) Colón, D.; Weber, E. J.; Anderson, J. L. Effect of natural organic matter on the reduction of nitroaromatics by Fe(II) species. *Environ. Sci. Technol.* **2008**, *42*, 6538–6543.
(94) Hakala, J. A.; Chin, Y.-P.; Weber, E. J. Influence of dissolved organic matter and Fe(II) on the abiotic reduction of pentachloronitrobenzene. *Environ. Sci. Technol.* **2007**, *41*, 7337–7342.
(95) Vindedahl, A. M.; Stemig, M. S.; Arnold, W. A.; Penn, R. L. Character of humic substances as a predictor for goethite nanoparticle reactivity and aggregation. *Environ. Sci. Technol.* **2016**, *50*, 1200–1208.
(96) Nesse, W. D. Sheet Silicates. In *Introduction to Mineralogy*; Oxford University: New York, 2012; pp 266–293.
(97) Solin, S. A. Clays and clay intercalation compounds: Properties and physical phenomena. *Annu. Rev. Mater. Sci.* **1997**, *27*, 89–115.
(98) Luan, F.; Liu, Y.; Griffin, A. M.; Gorski, C. A.; Burgos, W. D. Iron(III)-bearing clay minerals enhance bioreduction of nitrobenzene by Shewanella putrefaciens CN32. *Environ. Sci. Technol.* **2015**, *49*, 1418–1426.
(99) Schultz, C. A.; Grundl, T. J. pH dependence on reduction rate of 4-Cl-nitrobenzene by Fe(II)/montmorillonite systems. *Environ. Sci. Technol.* **2000**, *34*, 3641–3648.
(100) Hofstetter, T. B.; Neumann, A.; Schwarzenbach, R. P. Reduction of nitroaromatic compounds by Fe(II) species associated with iron-rich smectites. *Environ. Sci. Technol.* **2006**, *40*, 235–242.
(101) Neumann, A.; Olson, T. L.; Scherer, M. M. Spectroscopic evidence for Fe(II)-Fe(III) electron transfer at clay mineral edge and basal sites. *Environ. Sci. Technol.* **2013**, *47*, 6969–6977.
(102) Clausen, L.; Fabricius, I.; Madsen, L. Adsorption of pesticides onto quartz, calcite, kaolinite, and α-alumina. *J. Environ. Qual.* **2001**, *30*, 846–857.
(103) Cornejo, J.; Celis, R.; Pavlovic, I.; Ulibarri, M. A. Interactions of pesticides with clays and layered double hydroxides: A review. *Clay Miner.* **2008**, *43*, 155–175.
(104) Boyd, S.; Johnston, C.; Laird, D.; Teppen, B.; Li, H. Comprehensive study of organic contaminant adsorption by clays: Methodologies, mechanisms, and environmental implications. In *Biophysico-Chemical Processes of Anthropogenic Organic Compounds in Environmental Systems*; Xing, B., Senesi, N., Huang, P. M., Eds.; John Wiley & Sons: Hoboken, NJ, 2011; pp 51–72.
(105) Son, Y.-H.; Lee, J.-K.; Soong, Y.; Martello, D.; Chyu, M. Structure−property correlation in iron oxide nanoparticle−clay hybrid materials. *Chem. Mater.* **2010**, *22*, 2226–2232.
(106) Marco-Browna, J. L.; Barbosa-Lema, M. C.; Torres Sánchez, R. M.; Mercader, R. C.; Santos Afonsoa, M. dos. Adsorption of picloram herbicide on iron oxide pillared montmorillonite. *Appl. Clay Sci.* **2012**, *58*, 25–33.
(107) Tombácz, E.; Csanaky, C.; Illés, E. Polydisperse fractal aggregate formation in clay mineral and iron oxide suspensions, pH and ionic strength dependence. *Colloid Polym. Sci.* **2001**, *279*, 484–492.
(108) Wei, S.; Tan, W.; Zhao, W.; Yu, Y.; Liu, F.; Koopal, L. K. Microstructure,

interaction mechanisms, and stability of binary systems containing goethite and kaolinite. *Soil Sci. Soc. Am. J.* **2012**, *76*, 389–398.
(109) Nègre, M.; Leone, P.; Trichet, J.; Défarge, C.; Boero, V.; Gennari, M. Characterization of model soil colloids by cryo-scanning electron microscopy. *Geoderma* **2004**, *121*, 1–16.
(110) Strehlau, J. H.; Schultz, J. D.; Vindedahl, A. M.; Arnold, W. A.; Penn, R. L. Evolving reactivity and cryogenic microscopy of goethite-kaolinite mixed mineral suspensions. **2016**, In preparation.
(111) Gupta, V. K.; Saini, V. K.; Jain, N. Adsorption of As(III) from aqueous solutions by iron oxide-coated sand. *J. Colloid Interface Sci.* **2005**, *288*, 55–60.
(112) Benjamin, M. M.; Sletten, R. S.; Bailey, R. P.; Bennett, T. Sorption and filtration of metals using iron-oxide-coated sand. *Water Res.* **1996**, *30*, 2609–2620.
(113) Phillips, D. H.; Van Nooten, T.; Bastiaens, L.; Russell, M. I.; Dickson, K.; Plant, S.; Ahad, J. M. E.; Newton, T.; Elliot, T.; Kalin, R. M. Ten year performance evaluation of a field-scale zero-valent iron permeable reactive barrier installed to remediate trichloroethene contaminated groundwater. *Environ. Sci. Technol.* **2010**, *44*, 3861–3869.
(114) Chun, C. L.; Penn, R. L.; Arnold, W. A. Kinetic and microscopic studies of reductive transformations of organic contaminants on goethite. *Environ. Sci. Technol.* **2006**, *40*, 3299–3304.
(115) Vindedahl, A. M.; Arnold, W. A.; Penn, R. L. Impact of pahokee peat humic acid and buffer identity on goethite aggregation and reactivity. *Environ. Sci. Nano* **2015**, *2*, 509–517.
(116) Strehlau, J. H.; Stemig, M. S.; Penn, R. L.; Arnold, W. A. Facet-dependent oxidative goethite growth as a function of aqueous solution conditions. **2016**, Submitted.
(117) Pedersen, H. D.; Postma, D.; Jakobsen, R.; Larsen, O. Fast transformation of iron oxyhydroxides by the catalytic action of aqueous Fe(II). *Geochim. Cosmochim. Acta* **2005**, *69*, 3967–3977.
(118) Jeon, B. H.; Dempsey, B. A.; Burgos, W. D. Kinetics and mechanisms for reactions of Fe(II) with iron(III) oxides. *Environ. Sci. Technol.* **2003**, *37*, 3309–3315.
(119) Liu, H.; Li, P.; Zhu, M.; Wei, Y.; Sun, Y. Fe(II)-induced transformation from ferrihydrite to lepidocrocite and goethite. *J. Solid State Chem.* **2007**, *180*, 2121–2128.
(120) Liu, H.; Guo, H.; Li, P.; Wei, Y. The transformation of ferrihydrite in the presence of trace Fe(II): The effect of the anionic media. *J. Solid State Chem.* **2008**, *181*, 2666–2671.
(121) Usman, M.; Abdelmoula, M.; Faure, P.; Ruby, C.; Hanna, K. Transformation of various kinds of goethite into magnetite: Effect of chemical and surface properties. *Geoderma* **2013**, *197-198*, 9–16.
(122) Bursill, L. A.; Withers, R. L. On the multiple orientation relationships between hematite and magnetite. *J. Appl. Cryst.* **1979**, *12*, 287–294.

(123) Kashiwaya, Y.; Yamaguchi, Y.; Kinoshita, H.; Ishii, K. In situ observation of reduction behavior of hematite with solid carbon and crystallographic orientation between hematite and magnetite. *ISIJ Int.* **2007**, *47*, 226–233.
(124) LaKind, J. S.; Stone, A. T. Reductive dissolution of goethite by phenolic reducants. *Geochim. Cosmochim. Acta* **1989**, *53*, 961–971.
(125) Suter, D.; Banwart, S.; Stumm, W. Dissolution of hydrous iron(III) oxides by reductive mechanisms. *Langmuir* **1991**, *7*, 809–813.
(126) Panias, D.; Taxiarchou, M.; Paspaliaris, I.; Kontopoulos, A. Mechanisms of dissolution of iron oxides in aqueous oxalic acid solutions. *Hydrometallurgy* **1996**, *42*, 257–265.
(127) Larsen, O.; Postma, D. Kinetics of reductive bulk dissolution of lepidocrocite, ferrihydrite, and goethite. *Geochim. Cosmochim. Acta* **2001**, *65*, 1367–1379.
(128) Echigo, T.; Aruguete, D. M.; Murayama, M.; Hochella, M. F. Influence of Size, Morphology, Surface Structure, and Aggregation State on Reductive Dissolution of Hematite Nanoparticles with Ascorbic Acid. *Geochim. Cosmochim. Acta* **2012**, *90*, 149–162.
(129) Henn, K. W.; Waddill, D. W. Utilization of nanoscale zero-valent iron for source remediation—A case study. *Remediation* **2006**, *16*, 57–77.
(130) Vikesland, P. J.; Valentine, R. L. Reaction pathways involved in the reduction of monochloramine by ferrous iron. *Environ. Sci. Technol.* **2000**, *34*, 83–90.
(131) Salmani, M. H.; Vakili, M.; Ehrampoush, M. H. A comparative study of copper (ii) removal on iron oxide, aluminum oxide and activated carbon by continuous down flow method. *J. Toxicol. Environ. Heal. Sci.* **2013**, *5*, 150–155.
(132) Devlin, J. F.; Klausen, J.; Schwarzenbach, R. P. Kinetics of nitroaromatic reduction on granular iron in recirculating batch experiments. *Environ. Sci. Technol.* **1998**, *32*, 1941–1947.
(133) Baskan, M. B.; Pala, A. Batch and fixed-bed column studies of arsenic adsorption on the natural and modified clinoptilolite. *Water Air Soil Pollut.* **2014**, *225*, 1798.
(134) Su, C.; Puls, R. W. In situ remediation of arsenic in simulated groundwater using zerovalent iron: Laboratory column tests on combined effects of phosphate and silicate. *Environ. Sci. Technol.* **2003**, *37*, 2582–2587.
(135) Anderson, M. P. Movement of contaminants in groundwater: Groundwater transport - advection and dispersion. In *Groundwater Contamination*; National Academy Press: Washington, D.C., 1984; pp 37–45.
(136) Kundu, S.; Gupta, A. K. As(III) removal from aqueous medium in fixed bed using iron oxide-coated cement (IOCC): Experimental and modeling studies. *Chem. Eng. J.* **2007**, *129*, 123–131.
(137) Statham, T. M.; Mason, L. R.; Mumford, K. A.; Stevens, G. W. The specific reactive surface area of granular zero-valent iron in metal contaminant removal: Column experiments and modelling. *Water Res.* **2015**, *77*, 24–34.
(138) Simon, R.; Colón, D.; Tebes-Stevens, C. L.; Weber, E. J. Effect of redox zonation on the reductive transformation of p-cyanonitrobenzene in a laboratory sediment column. *Environ. Sci. Technol.* **2000**, *34*, 3617–3622.

(139) Tosco, T.; Bosch, J.; Meckenstock, R. U.; Sethi, R. Transport of ferrihydrite nanoparticles in saturated porous media: Role of ionic strength and flow rate. *Environ. Sci. Technol.* **2012**, *46*, 4008–4015.
(140) Ritter, K.; Odziemkowski, M. S.; Simpgraga, R.; Gillham, R. W.; Irish, D. E. An in situ study of the effect of nitrate on the reduction of trichloroethylene by granular iron. *J. Contam. Hydrol.* **2003**, *65*, 121–136.
(141) suk O, J.; Jeen, S.-W.; Gillham, R. W.; Gui, L. Effects of initial iron corrosion rate on long-term performance of iron permeable reactive barriers: Column experiments and numerical simulation. *J. Contam. Hydrol.* **2009**, *103*, 145–156.
(142) Fenner, K.; Canonica, S.; Wackett, L. P.; Elsner, M. Evaluating pesticide degradation in the environment: Blind spots and emerging opportunities. *Science (80-.).* **2013**, *341*, 752–758.
(143) Yan, W.; Lien, H.-L.; Koel, B. E.; Zhang, W. Iron nanoparticles for environmental clean-up: recent developments and future outlook. *Environ. Sci. Process. Impacts* **2013**, *15*, 63.
(144) Manning, B. A.; Hunt, M. L.; Amrhein, C.; Yarmoff, J. A. Arsenic(III) and arsenic(V) reactions with zerovalent iron corrosion products. *Environ. Sci. Technol.* **2002**, *36*, 5455–5461.
(145) Jeen, S. W.; Gillham, R. W.; Przepiora, A. Predictions of long-term performance of granular iron permeable reactive barriers: Field-scale evaluation. *J. Contam. Hydrol.* **2011**, *123*, 50–64.
(146) Andreu, V.; Picó, Y. Determination of pesticides and their degradation products in soil: Critical review and comparison of methods. *Trends Anal. Chem.* **2004**, *23*, 772–789.
(147) Popp, P.; Keil, P.; Möder, M.; Paschke, A.; Thuss, U. Application of accelerated solvent extraction followed by gas chromatography, high-performance liquid chromatography and gas chromatography–mass spectrometry for the determination of polycyclic aromatic hydrocarbons, chlorinated pesticides and polychlorin. *J. Chromatogr. A* **1997**, *774*, 203–211.
(148) van Mourik, L. M.; Leonards, P. E. G.; Gaus, C.; de Boer, J. Recent developments in capabilities for analysing chlorinated paraffins in environmental matrices: A review. *Chemosphere* **2015**, *136*, 259–272.
(149) Picó, Y.; Barceló, D. Transformation products of emerging contaminants in the environment and high-resolution mass spectrometry: A new horizon. *Anal. Bioanal. Chem.* **2015**, *407*, 6257–6273.
(150) Net, S.; Delmont, A.; Sempére, R.; Paluselli, A.; Ouddane, B. Reliable quantification of phthalates in environmental matrices (air, water, sludge, sediment and soil): A review. *Sci. Total Environ.* **2015**, *515-516*, 162–180.
(151) Thullner, M.; Centler, F.; Richnow, H.-H.; Fischer, A. Quantification of organic pollutant degradation in contaminated aquifers using compound specific stable isotop analysis - Review of recent developments. *Org. Geochem.* **2012**, *42*, 1440–1460.
(152) Elsner, M.; Jochmann, M. A.; Hofstetter, T. B.; Hunkeler, D.; Bernstein, A.;

Schmidt, T. C.; Schimmelmann, A. Current challenges in compound-specific stable isotope analysis of environmental organic contaminants. *Anal. Bioanal. Chem.* **2012**, *403*, 2471–2491.
(153) Burrows, N. D.; Penn, R. L. Cryogenic transmission electron microscopy: aqueous suspensions of nanoscale objects. *Microsc. Microanal.* **2013**, *19*, 1542–1553.
(154) Soltis, J. A.; Feinberg, J. M.; Gilbert, B.; Penn, R. L. Phase transformation and particle-mediated growth in the formation of hematite from 2-line ferrihydrite. *Cryst. Growth Des.* **2016**, *16*, 922–932.
(155) El-Bakry, M.; Sheehan, J. Analysing cheese microstructure: A review of recent developments. *J. Food Eng.* **2014**, *125*, 84–96.
(156) Ferrer, M. L.; Garcia-Carvajal, Z. Y.; Yuste, L.; Rojo, F.; Del Monte, F. Bacteria viability in sol-gel materials revisited: Cryo-SEM as a suitable tool to study the structural integrity of encapsulated bacteria. *Chem. Mater.* **2006**, *18*, 1458–1463.
(157) Desbois, G.; Urai, J. L.; Hemes, S.; Brassinnes, S.; De Craen, M.; Sillen, X. Nanometer-scale pore fluid distribution and drying damage in preserved clay cores from Belgian clay formations inferred by BIB-cryo-SEM. *Eng. Geol.* **2014**, *179*, 117–131.
(158) Karimi-Lotfabad, S.; Gray, M. R. Characterization of contaminated soils using confocal laser scanning microscopy and cryogenic-scanning electron microscopy. *Environ. Sci. Technol.* **2000**, *34*, 3408–3414.
(159) Pecharsky, V.; Zavalij, P. *Fundamentals of Powder Diffraction and Structural Characterization of Materials*, 2nd ed.; Springer: New York, 2009.
(160) Patterson, A. L. The Scherrer formula for X-ray particle size determination. *Phys. Rev.* **1939**, *56*, 978–982.
(161) Jun, Y. S.; Lee, B.; Waychunas, G. A. In situ observations of nanoparticle early development kinetics at mineral-water interfaces. *Environ. Sci. Technol.* **2010**, *44*, 8182–8189.
(162) Hu, Y.; Lee, B.; Bell, C.; Jun, Y. S. Environmentally abundant anions influence the nucleation, growth, ostwald ripening, and aggregation of hydrous Fe(III) oxides. *Langmuir* **2012**, *28*, 7737–7746.
(163) Strehlau, J. H.; Hegner, L. A.; Strauss, B. E.; Feinberg, J. M.; Penn, R. L. Simple and efficient separation of magnetic minerals from speleothems and other carbonates. *J. Sediment. Res.* **2014**, *84*, 1096–1106.
(164) Till, J. L.; Guyodo, Y.; Lagroix, F.; Morin, G.; Ona-Nguema, G. Goethite as a potential source of magnetic nanoparticles in sediments. *Geology* **2015**, *43*, 75–78.
(165) Lu, H. M.; Meng, X. K. Morin temperature and Néel temperature of hematite nanocrystals. *J. Phys. Chem. C* **2010**, *114*, 21291–21295.
(166) Carvalho, M. D.; Henriques, F.; Ferreira, L. P.; Godinho, M.; Cruz, M. M. Iron oxide nanoparticles: The influence of synthesis method and size on composition and magnetic properties. *J. Solid State Chem.* **2013**, *201*, 144–152.
(167) Wu, C.; Yin, P.; Zhu, X.; OuYang, C.; Xie, Y. Synthesis of hematite (α-Fe_2O_3) nanorods: Diameter-size and shape effects on their applications in magnetism, lithium ion battery, and gas sensors. *J. Phys. Chem. B* **2006**, *110*, 17806–17812.

(168) Liu, R.; Jiang, Y.; Fan, H.; Lu, Q.; Du, W.; Gao, F. Metal ions induce growth and magnetism alternation of α-Fe_2O_3 crystals bound by high-index facets. *Chem. - Eur. J.* **2012**, *18*, 8957–8963.
(169) Choi, J.; Cha, J.; Lee, J.-K. Synthesis of various magnetite nanoparticles through simple phase transformation and their shape-dependent magnetic properties. *RSC Adv.* **2013**, *3*, 8365–8371.
(170) Gorski, C. A.; Handler, R. M.; Beard, B. L.; Pasakarnis, T.; Johnson, C. M.; Scherer, M. M. Fe atom exchange between aqueous Fe^{2+} and magnetite. *Environ. Sci. Technol.* **2012**, *46*, 12399–12407.
(171) Latta, D. E.; Bachman, J. E.; Scherer, M. M. Fe electron transfer and atom exchange in goethite: Influence of Al-substitution and anion sorption. *Environ. Sci. Technol.* **2012**, *46*, 10614–10623.
(172) Amstaetter, K.; Borch, T.; Larese-Casanova, P.; Kappler, A. Redox transformation of arsenic by Fe(II)-activated goethite (α-FeOOH). *Environ. Sci. Technol.* **2010**, *44*, 102–108.
(173) Boland, D. D.; Collins, R. N.; Glover, C. J.; Payne, T. E.; Waite, T. D. Reduction of U(VI) by Fe(II) during the Fe(II)-accelerated transformation of ferrihydrite. *Environ. Sci. Technol.* **2014**, *48*, 9086–9093.
(174) Li, S.-S.; Li, W.-J.; Jiang, T.-J.; Liu, Z.-G.; Chen, X.; Cong, H.-P.; Liu, J.-H.; Huang, Y.-Y.; Li, L.-N.; Huang, X.-J. Iron Oxide with different crystal phases (α- and γ-Fe2O3) in electroanalysis and ultrasensitive and selective detection of lead(II): An advancing approach using XPS and EXAFS. *Anal. Chem.* **2016**, *88*, 906–914.
(175) Cory, R. M.; Mcknight, D. M. Fluorescence spectroscopy reveals ubiquitous presence of oxidized and reduced quinones in dissolved organic matter fluorescence spectroscopy reveals ubiquitous presence of oxidized and reduced quinones in dissolved organic matter. *Environ. Sci. Technol.* **2005**, *39*, 8142–8149.
(176) Beale, D. J.; Porter, N. A.; Roddick, F. A. The interaction between natural organic matter in raw waters and pesticide residues: A three dimensional excitation-emission matrix (3DEEM) fluorescence investigation. *Water Sci. Technol.* **2013**, *67*, 2428–2436.
(177) Daouk, S.; Frege, C.; Blanc, N.; Mounier, S.; Redon, R.; Merdy, P.; Lucas, Y.; Pfeifer, H. R. Fluorescence spectroscopy to study dissolved organic matter interactions with agrochemicals applied in Swiss vineyards. *Environ. Sci. Pollut. Res.* **2015**, *22*, 9284–9292.
(178) Manciulea, A.; Baker, A.; Lead, J. R. A fluorescence quenching study of the interaction of Suwannee River fulvic acid with iron oxide nanoparticles. *Chemosphere* **2009**, *76*, 1023–1027.
(179) Chen, W.; Westerhoff, P.; Leenheer, J. A.; Booksh, K. Fluorescence excitation-emission matrix regional integration to quantify spectra for dissolved organic matter. *Environ. Sci. Technol.* **2003**, *37*, 5701–5710.
(180) Fellman, J. B.; Miller, M. P.; Cory, R. M.; D'Amore, D. V.; White, D. Characterizing dissolved organic matter using PARAFAC modeling of

fluorescence spectroscopy: A comparison of two models. *Environ. Sci. Technol.* **2009**, *43*, 6228–6234.
(181) Poulin, B. A.; Ryan, J. N.; Aiken, G. R. The effects of iron on optical properties of dissolved organic matter. *Environ. Sci. Technol. Technol.* **2014**, *48*, 10098–10106.
(182) Akcil, A.; Erust, C.; Ozdemiroglu, S.; Fonti, V.; Beolchini, F. A review of approaches and techniques used in aquatic contaminated sediments: Metal removal and stabilization by chemical and biotechnological processes. *J. Clean. Prod.* **2015**, *86*, 24–26.
(183) He, Y. T.; Wilson, J. T.; Su, C.; Wilkin, R. T. Review of abiotic degradation of chlorinated solvents by reactive iron minerals in aquifers. *Groundw. Monit. Rem.* **2015**, *35*, 57–75.
(184) Gong, Y.; Tang, J.; Zhao, D. Application of iron sulfide particles for groundwater and soil remediation: A review. *Water Res.* **2016**, *89*, 309–320.
(185) Adeleye, A. S.; Conway, J. R.; Garner, K.; Huang, Y.; Su, Y.; Keller, A. A. Engineered nanomaterials for water treatment and remediation: Costs, benefits, and applicability. *Chem. Eng. J.* **2016**, *286*, 640–662.

Chapter 2 References

(1) Elsner, M.; Schwarzenbach, R. P.; Haderlein, S. B. Reactivity of Fe(II)-bearing minerals toward reductive transformation of organic contaminants. *Environ. Sci. Technol.* **2004**, *38*, 799–807.

(2) Klausen, J.; Tröber, S. P.; Haderlein, S. B.; Schwarzenbach, R. P. Reduction of substituted nitrobenzenes by Fe(II) in aqueous mineral suspensions. *Environ. Sci. Technol.* **1995**, *29*, 2396–2404.

(3) Hofstetter, T. B.; Heijman, C. G.; Haderlein, S. B.; Holliger, C.; Schwarzenbach, R. P. Complete reduction of TNT and other (poly)nitroaromatic compounds under iron-reducing subsurface conditions. *Environ. Sci. Technol.* **1999**, *33*, 1479–1487.

(4) Klupinski, T. P.; Chin, Y.-P.; Traina, S. J. Abiotic degradation of pentachloronitrobenzene by Fe(II): Reactions on goethite and iron oxide nanoparticles. *Environ. Sci. Technol.* **2004**, *38*, 4353–4360.

(5) Klupinski, T. P.; Chin, Y.-P. Abiotic degradation of trifluralin by Fe(II): Kinetics and transformation pathways. *Environ. Sci. Technol.* **2003**, *37*, 1311–1318.

(6) Dixit, S.; Hering, J. G. Sorption of Fe(II) and As(III) on goethite in single- and dual-sorbate systems. *Chem. Geol.* **2006**, *228*, 6–15.

(7) Reddy, T. R.; Frierdich, A. J.; Beard, B. L.; Johnson, C. M. The effect of pH on stable iron isotope exchange and fractionation between aqueous Fe(II) and goethite. *Chem. Geol.* **2015**, *397*, 118–127.

(8) Luan, F.; Xie, L.; Li, J.; Zhou, Q. Abiotic reduction of nitroaromatic compounds by Fe(II) associated with iron oxides and humic acid. *Chemosphere* **2013**, *91*, 1035–1041.

(9) Vindedahl, A. M.; Stemig, M. S.; Arnold, W. A.; Penn, R. L. Character of humic substances as a predictor for goethite nanoparticle reactivity and aggregation. *Environ. Sci. Technol.* **2016**, *50*, 1200–1208.

(10) Colón, D.; Weber, E. J.; Anderson, J. L. Effect of natural organic matter on the reduction of nitroaromatics by Fe(II) species. *Environ. Sci. Technol.* **2008**, *42*, 6538–6543.

(11) Weng, L.; Van Riemsdijk, W. H.; Koopal, L. K.; Hiemstra, T. Adsorption of humic substances on goethite: Comparison between humic acids and fulvic acids. *Environ. Sci. Technol.* **2006**, *40*, 7494–7500.

(12) Cwiertny, D. M.; Handler, R. M.; Schaefer, M. V.; Grassian, V. H.; Scherer, M. M. Interpreting nanoscale size-effects in aggregated Fe-oxide suspensions: Reaction of Fe(II) with goethite. *Geochim. Cosmochim. Acta* **2009**, *72*, 1365–1380.

(13) Cwiertny, D. M.; Roberts, A. L. On the nonlinear relationship between k_{obs} and reductant mass loading in iron batch systems. *Environ. Sci. Technol.* **2005**, *39*, 8948–8957.

(14) Phillips, D. H.; Van Nooten, T.; Bastiaens, L.; Russell, M. I.; Dickson, K.; Plant, S.; Ahad, J. M. E.; Newton, T.; Elliot, T.; Kalin, R. M. Ten year performance evaluation of a field-scale zero-valent iron permeable reactive barrier installed to remediate trichloroethene contaminated groundwater. *Environ. Sci. Technol.* **2010**,

44, 3861–3869.
(15) Bae, S.; Hanna, K. Reactivity of nanoscale zero-valent iron in unbuffered systems: Effect of pH and Fe(II) dissolution. *Environ. Sci. Technol.* **2015**, *49*, 10539–10543.
(16) Pedersen, H. D.; Postma, D.; Jakobsen, R.; Larsen, O. Fast transformation of iron oxyhydroxides by the catalytic action of aqueous Fe(II). *Geochim. Cosmochim. Acta* **2005**, *69*, 3967–3977.
(17) Chun, C. L.; Penn, R. L.; Arnold, W. A. Kinetic and microscopic studies of reductive transformations of organic contaminants on goethite. *Environ. Sci. Technol.* **2006**, *40*, 3299–3304.
(18) Vindedahl, A. M.; Arnold, W. A.; Penn, R. L. Impact of pahokee peat humic acid and buffer identity on goethite aggregation and reactivity. *Environ. Sci. Nano* **2015**, *2*, 509–517.
(19) Larsen, O.; Postma, D. Kinetics of reductive bulk dissolution of lepidocrocite, ferrihydrite, and goethite. *Geochim. Cosmochim. Acta* **2001**, *65*, 1367–1379.
(20) Pedersen, H. D.; Postma, D.; Jakobsen, R. Release of arsenic associated with the reduction and transformation of iron oxides. *Geochim. Cosmochim. Acta* **2006**, *70*, 4116–4129.
(21) Amal, R.; Raper, J. A.; Waite, T. D. Effect of fulvic acid adsorption on the aggregation kinetics and structure of hematite particles. *J. Colloid Interface Sci.* **1992**, *151*, 244–257.
(22) Hotze, E. M.; Phenrat, T.; Lowry, G. V. Nanoparticle aggregation: Challenges to understanding transport and reactivity in the environment. *J. Environ. Qual.* **2010**, *39*, 1909–1924.
(23) Mylon, S. E.; Chen, K. L.; Elimelech, M. Influence of natural organic matter and ionic composition on aggregation kinetics of hematite particles: Implications to iron depletion estuaries. *Langmuir* **2004**, *20*, 9000–9006.
(24) Bruemmer, G. W.; Gerth, J.; Tiller, K. G. Reaction kinetics of the adsorption and desorption of nickel, zinc and cadmium by goethite. I. Adsorption and diffusion of metals. *J. Soil Sci.* **1988**, *39*, 37–52.
(25) Henn, K. W.; Waddill, D. W. Utilization of nanoscale zero-valent iron for source remediation—A case study. *Remediation* **2006**, *16*, 57–77.
(26) Handler, R. M.; Beard, B. L.; Johnson, C. M.; Scherer, M. M. Atom exchange between aqueous Fe(II) and goethite: an Fe isotope tracer study. *Environ. Sci. Technol.* **2009**, *43*, 1102–1107.
(27) Cornell, R. M.; Schwertmann, U. *The Iron Oxides*, 2nd ed.; Wiley-VCH: Weinheim, 2003.
(28) Anschutz, A. J.; Penn, R. L. Reduction of crystalline iron(III) oxyhydroxides using hydroquinone: Influence of phase and particle size. *Geochem. Trans.* **2005**, *6*, 60–66.
(29) Stookey, L. L. Ferrozine – a new spectrophotometric reagent for iron. *Anal. Chem.* **1970**, *42*, 779–781.
(30) Strehlau, J. H.; Hegner, L. A.; Strauss, B. E.; Feinberg, J. M.; Penn, R. L. Simple and efficient separation of magnetic minerals from speleothems and other

carbonates. *J. Sediment. Res.* **2014**, *84*, 1096–1106.
(31) Arnold, W. A.; Roberts, A. L. Pathways and kinetics of chlorinated ethylene and chlorinated acetylene reaction with Fe(0) particles. *Environ. Sci. Technol.* **2000**, *34*, 1794–1805.
(32) Pecharsky, V.; Zavalij, P. *Fundamentals of Powder Diffraction and Structural Characterization of Materials*, 2nd ed.; Springer: New York, 2009.
(33) Guyodo, Y.; Mostrom, A.; Penn, R. L.; Banerjee, S. K. From nanodots to nanorods: Oriented aggregation and magnetic evolution of nanocrystalline goethite. *Geophys. Res. Lett.* **2003**, *30*, 1512.
(34) Weidler, P. G.; Hug, S. J.; Wetche, T. P.; Hiemstra, T. Determination of growth rates of (100) and (110) faces of synthetic goethite by scanning force microscopy. *Geochim. Cosmochim. Acta* **1998**, *62*, 3407–3412.
(35) Boily, J.-F. Water structure and hydrogen bonding at goethite/water interfaces: Implications for proton affinities. *J. Phys. Chem. C* **2012**, *116*, 4714–4724.
(36) Boily, J.-F.; Lützenkirchen, J.; Balmés, O.; Beattie, J.; Sjöberg, S. Modeling proton binding at the goethite (α-FeOOH)–water interface. *Colloids Surf., A* **2001**, *179*, 11–27.
(37) Echigo, T.; Hatta, T.; Nemoto, S.; Takizawa, S. X-ray photoelectron spectroscopic study on the goethites with variations in crystallinity and morphology: Their effects on surface hydroxyl concentration. *Phys. Chem. Miner.* **2012**, *39*, 769–778.
(38) Russell, B.; Payne, M.; Ciacchi, L. C. Density functional theory study of Fe(II) adsorption and oxidation on goethite surfaces. *Phys. Rev. B - Condens. Matter Mater. Phys.* **2009**, *79*, 1–14.
(39) Barrón, V.; Torrent, J. Surface hydroxyl configuration of various crystal faces of hematite and goethite. *J. Colloid Interface Sci.* **1996**, *177*, 407–410.
(40) Gu, B.; Schmitt, J.; Chen, Z.; Liang, L.; McCarthy, J. F. Adsorption and desorption of natural organic matter on iron oxide: mechanisms and models. *Environ. Sci. Technol.* **1994**, *28*, 38–46.
(41) Fu, H.; Quan, X. Complexes of fulvic acid on the surface of hematite, goethite, and akaganeite: FTIR observation. *Chemosphere* **2006**, *63*, 403–410.

Chapter 3 References

(1) Klausen, J.; Tröber, S. P.; Haderlein, S. B.; Schwarzenbach, R. P. Reduction of substituted nitrobenzenes by Fe(II) in aqueous mineral suspensions. *Environ. Sci. Technol.* **1995**, *29*, 2396–2404.

(2) Hofstetter, T. B.; Heijman, C. G.; Haderlein, S. B.; Holliger, C.; Schwarzenbach, R. P. Complete reduction of TNT and other (poly)nitroaromatic compounds under iron-reducing subsurface conditions. *Environ. Sci. Technol.* **1999**, *33*, 1479–1487.

(3) Klupinski, T. P.; Chin, Y.-P.; Traina, S. J. Abiotic degradation of pentachloronitrobenzene by Fe(II): Reactions on goethite and iron oxide nanoparticles. *Environ. Sci. Technol.* **2004**, *38*, 4353–4360.

(4) Williams, A. G. B.; Scherer, M. M. Spectroscopic evidence for Fe(II)-Fe(III) electron transfer at the iron oxide-water interface. *Environ. Sci. Technol.* **2004**, *38*, 4782–4790.

(5) Elsner, M.; Schwarzenbach, R. P.; Haderlein, S. B. Reactivity of Fe(II)-bearing minerals toward reductive transformation of organic contaminants. *Environ. Sci. Technol.* **2004**, *38*, 799–807.

(6) Hofstetter, T. B.; Schwarzenbach, R. P.; Haderlein, S. B. Reactivity of Fe(II) species associated with clay minerals. *Environ. Sci. Technol.* **2003**, *37*, 519–528.

(7) Schaefer, M. V; Gorski, C. A.; Scherer, M. M. Spectroscopic evidence for interfacial Fe(II)-Fe(III) electron transfer in a clay mineral. *Environ. Sci. Technol.* **2011**, *45*, 540–545.

(8) Hofstetter, T. B.; Neumann, A.; Schwarzenbach, R. P. Reduction of nitroaromatic compounds by Fe(II) species associated with iron-rich smectites. *Environ. Sci. Technol.* **2006**, *40*, 235–242.

(9) Essington, M. E. *Soil and Water Chemistry: An Integrative Approach*; CRC Press: Boca Raton, FL, 2004.

(10) Ioannou, A.; Dimirkou, A. Phosphate adsorption on hematite, kaolinite, and kaolinite-hematite (k-h) systems as described by a constant capacitance model. *J. Colloid Interface Sci.* **1997**, *192*, 119–128.

(11) Wei, S.; Tan, W.; Liu, F.; Zhao, W.; Weng, L. Surface properties and phosphate adsorption of binary systems containing goethite and kaolinite. *Geoderma* **2014**, *213*, 478–484.

(12) Reich, T. J.; Das, S.; Koretsky, C. M.; Lund, T. J.; Landry, C. J. Surface complexation modeling of Pb(II) adsorption on mixtures of hydrous ferric oxide, quartz and kaolinite. *Chem. Geol.* **2010**, *275*, 262–271.

(13) Haderlein, S. B.; Schwarzenbach, R. P. Adsorption of substituted nitrobenzenes and nitrophenols to mineral surfaces. *Environ. Sci. Technol.* **1993**, *27*, 316–326.

(14) Haderlein, S. B.; Weissmahr, K. W.; Schwarzenbach, R. P. Specific adsorption of nitroaromatic explosives and pesticides to clay minerals. *Environ. Sci. Technol.* **1996**, *30*, 612–622.

(15) Carroll-Webb, S. A.; Walther, J. V. A surface complex reaction model for the pH-dependence of corundum and kaolinite dissolution rates. *Geochim. Cosmochim.*

Acta **1988**, *52*, 2609–2623.
(16) Latta, D. E.; Bachman, J. E.; Scherer, M. M. Fe electron transfer and atom exchange in goethite: Influence of Al-substitution and anion sorption. *Environ. Sci. Technol.* **2012**, *46*, 10614–10623.
(17) Quin, T. G.; Long, G. J.; Benson, C. G.; Mann, S.; Williams, R. J. P. Influence of silicon and phosphorus on structural and magnetic properties of synthetic goethite and related oxides. *Clays Clay Miner.* **1988**, *36*, 165–175.
(18) Tombácz, E.; Csanaky, C.; Illés, E. Polydisperse fractal aggregate formation in clay mineral and iron oxide suspensions, pH and ionic strength dependence. *Colloid Polym. Sci.* **2001**, *279*, 484–492.
(19) Hou, T.; Xu, R.; Zhao, A. Interaction between electric double layers of kaolinite and Fe/Al oxides in suspensions. *Colloids Surf., A* **2007**, *297*, 91–94.
(20) Dimirkou, A.; Ioannou, A.; Doula, M. Preparation, characterization and sorption properties for phosphates of hematite, bentonite and bentonite-hematite systems. *Adv. Colloid Interface Sci* **2002**, *97*, 37–61.
(21) Schroth, B. K.; Sposito, G. Surface charge properties of kaolinite. *Clays Clay Miner.* **1997**, *45*, 85–91.
(22) Kosmulski, M. Compilation of PZC and IEP of sparingly soluble metal oxides and hydroxides from literature. *Adv. Colloid Interface Sci* **2009**, *152*, 14–25.
(23) Burrows, N. D.; Penn, R. L. Cryogenic transmission electron microscopy: aqueous suspensions of nanoscale objects. *Microsc. Microanal.* **2013**, *19*, 1542–1553.
(24) Vindedahl, A. M.; Arnold, W. A.; Penn, R. L. Impact of pahokee peat humic acid and buffer identity on goethite aggregation and reactivity. *Environ. Sci. Nano* **2015**, *2*, 509–517.
(25) Yuwono, V. M.; Burrows, N. D.; Soltis, J. A.; Do, T. A.; Penn, R. L. Aggregation of ferrihydrite nanoparticles in aqueous systems. *Faraday Discuss.* **2012**, *159*, 235–245.
(26) Nègre, M.; Leone, P.; Trichet, J.; Défarge, C.; Boero, V.; Gennari, M. Characterization of model soil colloids by cryo-scanning electron microscopy. *Geoderma* **2004**, *121*, 1–16.
(27) Anschutz, A. J.; Penn, R. L. Reduction of crystalline iron(III) oxyhydroxides using hydroquinone: Influence of phase and particle size. *Geochem. Trans.* **2005**, *6*, 60–66.
(28) Pruett, R. J.; Webb, H. L. Sampling and analysis of KGa-1B well-crystallized kaolin source clay. *Clays Clay Miner.* **1993**, *41*, 514–519.
(29) Stookey, L. L. Ferrozine – a new spectrophotometric reagent for iron. *Anal. Chem.* **1970**, *42*, 779–781.
(30) Huertas, F. J.; Chou, L.; Wollast, R. Mechanism of kaolinite dissolution at room temperature and pressure, part II: kinetic study. *Geochim. Cosmochim. Acta* **1999**, *63*, 3261–3275.
(31) Xie, Z.; Walther, J. V. Incongruent dissolution and surface area of kaolinite. *Geochim. Cosmochim. Acta* **1992**, *56*, 3357–3363.
(32) Strehlau, J. H.; Stemig, M. S.; Penn, R. L.; Arnold, W. A. Facet-dependent

oxidative goethite growth as a function of aqueous solution conditions. **2016**, Submitted.
(33) Schulze, D. G. The influence of aluminum on iron oxides. VIII. Unit-cell dimensions of Al-substituted goethites and estimation of Al from them. *Clays Clay Miner.* **1984**, *32*, 36–44.
(34) Liu, H.; Chen, T.; Frost, R. L.; Chang, D.; Qing, C.; Xie, Q. Effect of aging time and Al substitution on the morphology of aluminous goethite. *J. Colloid Interface Sci.* **2012**, *385*, 81–86.
(35) Schwertmann, U.; Taylor, R. M. The influence of silicate on the transformation of lepidocrocite to goethite. *Clays Clay Miner.* **1972**, *20*, 159–164.
(36) Schulze, D. G.; Schwertmann, U. The influence of aluminium on iron oxides: X. Properties of Al-substituted goethites. *Clay Miner.* **1984**, *19*, 521–539.
(37) Strehlau, J. H.; Hegner, L. A.; Strauss, B. E.; Feinberg, J. M.; Penn, R. L. Simple and efficient separation of magnetic minerals from speleothems and other carbonates. *J. Sediment. Res.* **2014**, *84*, 1096–1106.
(38) Liu, Q.; Yu, Y.; Torrent, J.; Roberts, A. P.; Pan, Y.; Zhu, R. Characteristic low-temperature magnetic properties of aluminous goethite [α -(Fe, Al)OOH] explained. *J. Geophys. Res.* **2006**, *111*, B12S34.
(39) Chun, C. L.; Penn, R. L.; Arnold, W. A. Kinetic and microscopic studies of reductive transformations of organic contaminants on goethite. *Environ. Sci. Technol.* **2006**, *40*, 3299–3304.
(40) Tombácz, E.; Libor, Z.; Illés, E.; Majzik, A.; Klumpp, E. The role of reactive surface sites and complexation by humic acids in the interaction of clay mineral and iron oxide particles. *Org. Geochem.* **2004**, *35*, 257–267.
(41) Fialips, C.-I.; Petit, S.; Decarreau, A.; Beaufort, D. Influence of synthesis pH on kaolinite “crystallinity” and surface properties. *Clays Clay Miner.* **2000**, *48*, 173–184.
(42) Petit, S.; Madejová, J.; Decarreau, A.; Martin, F. Characterization of octahedral substitutions in kaolinites using near infrared spectroscopy. *Clays Clay Miner.* **1999**, *47*, 103–108.

Chapter 4 References

(1) Klausen, J.; Tröber, S. P.; Haderlein, S. B.; Schwarzenbach, R. P. Reduction of substituted nitrobenzenes by Fe(II) in aqueous mineral suspensions. *Environ. Sci. Technol.* **1995**, *29*, 2396–2404.

(2) Hofstetter, T. B.; Heijman, C. G.; Haderlein, S. B.; Holliger, C.; Schwarzenbach, R. P. Complete reduction of TNT and other (poly)nitroaromatic compounds under iron-reducing subsurface conditions. *Environ. Sci. Technol.* **1999**, *33*, 1479–1487.

(3) Boparai, H. K.; Comfort, S. D.; Satapanajaru, T.; Szecsody, J. E.; Grossl, P. R.; Shea, P. J. Abiotic transformation of high explosives by freshly precipitated iron minerals in aqueous Fe^{II} solutions. *Chemosphere* **2010**, *79*, 865–872.

(4) Gregory, K. B.; Larese-Casanova, P.; Parkin, G. F.; Scherer, M. M. Abiotic transformation of hexahydro-1,3,5-trinitro-1,3,5-triazine by Fe^{II} bound to magnetite. *Environ. Sci. Technol.* **2004**, *38*, 1408–1414.

(5) Klupinski, T. P.; Chin, Y.-P.; Traina, S. J. Abiotic degradation of pentachloronitrobenzene by Fe(II): Reactions on goethite and iron oxide nanoparticles. *Environ. Sci. Technol.* **2004**, *38*, 4353–4360.

(6) Klupinski, T. P.; Chin, Y.-P. Abiotic degradation of trifluralin by Fe(II): Kinetics and transformation pathways. *Environ. Sci. Technol.* **2003**, *37*, 1311–1318.

(7) Williams, A. G. B.; Scherer, M. M. Spectroscopic evidence for Fe(II)-Fe(III) electron transfer at the iron oxide-water interface. *Environ. Sci. Technol.* **2004**, *38*, 4782–4790.

(8) Sherman, D. M. Molecular orbital (SCF-Xα-SW) theory of metal-metal charge transfer processes in minerals. *Phys. Chem. Miner.* **1987**, *14*, 355–363.

(9) Farley, K. J.; Dzombak, D. A.; Morel, F. M. . A surface precipitation model for the sorption of cations on metal oxides. *J. Colloid Interface Sci.* **1985**, *106*, 226–242.

(10) Cundy, A. B.; Hopkinson, L.; Whitby, R. L. D. Use of iron-based technologies in contaminated land and groundwater remediation: A review. *Sci. Total Environ.* **2008**, *400*, 42–51.

(11) Noubactep, C.; Caré, S.; Crane, R. Nanoscale metallic iron for environmental remediation: Prospects and limitations. *Water Air Soil Pollut.* **2012**, *223*, 1363–1382.

(12) Karn, B.; Kuiken, T.; Otto, M. Nanotechnology and in situ remediation: a review of the benefits and potential risks. *Environ. Heal. Perspect.* **2009**, *117*, 1813–1831.

(13) Strehlau, J. H.; Stemig, M. S.; Penn, R. L.; Arnold, W. A. Facet-dependent oxidative goethite growth as a function of aqueous solution conditions. **2016**, In preparation.

(14) Strehlau, J. H.; Toner, B. M.; Arnold, W. A.; Penn, R. L. Accessible reactive surface area of iron oxyhydroxides in acidic brines. **2016**, In revision.

(15) Dixit, S.; Hering, J. G. Sorption of Fe(II) and As(III) on goethite in single- and dual-sorbate systems. *Chem. Geol.* **2006**, *228*, 6–15.

(16) Brezonik, P. L.; Arnold, W. A. *Water Chemistry: An Introduction to the Chemistry of Natural and Engineered Aquatic Systems*; Oxford University: New York, 2011.

(17) Philippe, A.; Schaumann, G. E. Interactions of dissolved organic matter with natural and engineered inorganic colloids: A review. *Environ. Sci. Technol.* **2014**, *48*, 8946–8962.
(18) Vindedahl, A. M.; Strehlau, J. H.; Arnold, W. A.; Penn, R. L. Organic matter and iron oxide nanoparticles: aggregation, interactions, and reactivity. *ES Nano* **2016**, DOI: 10.1039/C5EN00215J.
(19) Grillo, R.; Rosa, A. H.; Fraceto, L. F. Engineered nanoparticles and organic matter: A review of the state-of-the-art. *Chemosphere* **2015**, *119*, 608–619.
(20) Andrade-Eiroa, Á.; Canle, M.; Cerdá, V. Environmental applications of excitation-emission spectrofluorimetry: An in-depth review I. *Appl. Spectrosc. Rev.* **2013**, *48*, 1–49.
(21) Zhou, J.; Wang, J.-J.; Baudon, A.; Chow, A. T. Improved fluorescence excitation-emission matrix regional integration to quantify spectra for fluorescent dissolved organic matter. *J. Environ. Qual.* **2013**, *42*, 925–930.
(22) Cory, R. M.; Miller, M. P.; McKnight, D. M.; Guerard, J. J.; Miller, P. L. Effect of instrument-specific response on the analysis of fulvic acid fluorescence spectra. *Limnol. Oceanogr. Methods* **2010**, *8*, 67–78.
(23) Poulin, B. A.; Ryan, J. N.; Aiken, G. R. The effects of iron on optical properties of dissolved organic matter. *Environ. Sci. Technol. Technol.* **2014**, *48*, 10098–10106.
(24) Waite, T. D.; Morel, F. M. M. Ligand exchange and fluorescence quenching studies of the fulvic acid-iron interaction: Effects of pH and light. *Anal. Chim. Acta* **1984**, *162*, 263–274.
(25) Anschutz, A. J.; Penn, R. L. Reduction of crystalline iron(III) oxyhydroxides using hydroquinone: Influence of phase and particle size. *Geochem. Trans.* **2005**, *6*, 60–66.
(26) Viollier, E.; Inglett, P. W.; Hunter, K.; Roychoudhury, A. N.; Van Cappellen, P. The ferrozine method revisited: Fe(II)/Fe(III) determination in natural waters. *Appl. Geochemistry* **2000**, *15*, 785–790.
(27) Rinnan, Å.; Booksh, K. S.; Bro, R. First order Rayleigh scatter as a separate component in the decomposition of fluorescence landscapes. *Anal. Chim. Acta* **2005**, *537*, 349–358.
(28) Guy, R. D.; Narine, D. R.; DeSilva, S. Organocation speciation. I. A comparison of the interactions of methylene blue and paraquat with bentonite and humic acid. *Can. J. Chem.* **1980**, *58*, 547–554.
(29) Meier, M.; Namjesnik-Dejanovic, K.; Maurice, P. A.; Chin, Y.-P.; Aiken, G. R. Fractionation of aquatic natural organic matter upon sorption to goethite and kaolinite. *Chem. Geol.* **1999**, *157*, 275–284.
(30) Vindedahl, A. M.; Stemig, M. S.; Arnold, W. A.; Penn, R. L. Character of humic substances as a predictor for goethite nanoparticle reactivity and aggregation. *Environ. Sci. Technol.* **2016**, *50*, 1200–1208.
(31) Chekli, L.; Phuntsho, S.; Roy, M.; Shon, H. K. Characterisation of Fe-oxide nanoparticles coated with humic acid and Suwannee River natural organic matter. *Sci. Total Environ.* **2013**, *461-462*, 19–27.

(32) Lv, J.; Zhang, S.; Wang, S.; Luo, L.; Cao, D.; Christie, P. Molecular-scale investigation with ESI-FT-ICR-MS on fractionation of dissolved organic matter induced by adsorption on iron oxyhydroxides. *Environ. Sci. Technol.* **2016**, *50*, 2328–2336.

Chapter 5 References

(1) Jones, B. F.; Deocampo, D. M. Geochemistry of saline lakes. In *Treatise on Geochemistry, Volume 5*; Drever, J. I., Ed.; Elsevier: Oxford, 2003; pp 393–424.
(2) Todd, D. K. Quality of groundwater. In *Groundwater Hydrology*; John Wiley & Sons: New York, 1980; pp 267–315.
(3) Risacher, F.; Fritz, B. Origin of salts and brine evolution of Bolivian and Chilean salars. *Aquat. Geochem.* **2009**, *15*, 123–157.
(4) Benison, K. C.; Karmanocky, F. J. Could microorganisms be preserved in Mars gypsum? Insights from terrestrial examples. *Geology* **2014**, *42*, 615–618.
(5) Burton, E. D.; Bush, R. T.; Sullivan, L. A. Sedimentary iron geochemistry in acidic waterways associated with coastal lowland acid sulfate soils. *Geochim. Cosmochim. Acta* **2006**, *70*, 5455–5468.
(6) Benison, K. C.; Bowen, B. B. Extreme sulfur-cycling in acid brine lake environments of Western Australia. *Chem. Geol.* **2013**, *351*, 154–167.
(7) Johannesson, K. H.; Lyons, W. B.; Yelken, M. A.; Gaudette, H. E.; Stetzenbach, K. J. Geochemistry of the rare-earth elements in hypersaline and dilute acidic natural terrestrial waters: Complexation behavior and middle rare-earth element enrichments. *Chem. Geol.* **1996**, *133*, 125–144.
(8) Carter, J.; Viviano-Beck, C.; Loizeau, D.; Bishop, J.; Le Deit, L. Orbital detection and implications of akaganéite on Mars. *Icarus* **2015**, *253*, 296–310.
(9) España, J. S. The behavior of iron and aluminum in acid mine drainage: Speciation, mineralogy, and environmental significance. In *Thermodynamics, Solubility and Environmental Issues*; Letcher, T. M., Ed.; Elsevier B.V.: Amsterdam, 2007; pp 137–150.
(10) Zhu, M.; Legg, B.; Zhang, H.; Gilbert, B.; Ren, Y.; Banfield, J. F.; Waychunas, G. A. Early stage formation of iron oxyhydroxides during neutralization of simulated acid mine drainage solutions. *Environ. Sci. Technol.* **2012**, *46*, 8140–8147.
(11) Jacobs, J. A.; Lehr, J. H.; Testa, S. M. *Acid Mine Drainage, Rock Drainage, and Acid Sulfate Soils: Causes, Assessment, Prediction, Prevention, and Remediation*; John Wiley & Sons: Hoboken, NJ, 2014.
(12) Liu, H.; Chen, T.; Frost, R. L. An overview of the role of goethite surfaces in the environment. *Chemosphere* **2014**, *103*, 1–11.
(13) Orsetti, S.; Laskov, C.; Haderlein, S. Electron transfer between iron minerals and quinones: estimating the reduction potential of the Fe(II)-goethite surface from AQDS speciation. *Environ. Sci. Technol.* **2013**, *47*, 14161–14168.
(14) Li, X.; Liu, T.; Liu, L.; Li, F. Dependence of the electron transfer capacity on the kinetics of quinone-mediated Fe(III) reduction by two iron/humic reducing bacteria. *RSC Adv.* **2014**, *4*, 2284–2290.
(15) Maria Valente, T.; Antunes, M.; Sequeira Braga, A.; Prudêncio, M. I.; Marques, R.; Pamplona, J. Mineralogical attenuation for metallic remediation in a passive system for mine water treatment. *Environ. Earth Sci.* **2011**, *66*, 39–54.
(16) Baalousha, M. Aggregation and disaggregation of iron oxide nanoparticles:

Influence of particle concentration, pH and natural organic matter. *Sci. Total Environ.* **2009**, *407*, 2093–2101.
(17) Hu, J.-D.; Zevi, Y.; Kou, X.-M.; Xiao, J.; Wang, X.-J.; Jin, Y. Effect of dissolved organic matter on the stability of magnetite nanoparticles under different pH and ionic strength conditions. *Sci. Total Environ.* **2010**, *408*, 3477–3489.
(18) Hayes, K. F.; Leckie, J. O. Modeling ionic strength effects on cation adsorption at hydrous oxide/solution interfaces. *J. Colloid Interface Sci.* **1987**, *115*, 564–572.
(19) Hayes, K. F.; Papelis, C.; Leckie, J. O. Modeling ionic strength effects on anion adsorption at hydrous oxide/solution interfaces. *J. Colloid Interface Sci.* **1988**, *125*, 717–726.
(20) Antelo, J.; Avena, M.; Fiol, S.; López, R.; Arce, F. Effects of pH and ionic strength on the adsorption of phosphate and arsenate at the goethite-water interface. *J. Colloid Interface Sci.* **2005**, *285*, 476–486.
(21) Chekli, L.; Phuntsho, S.; Roy, M.; Lombi, E.; Donner, E.; Shon, H. K. Assessing the aggregation behaviour of iron oxide nanoparticles under relevant environmental conditions using a multi-method approach. *Water Res.* **2013**, *47*, 4585–4599.
(22) Dickson, B. L.; Giblin, A. M. Features of acid-saline systems of Southern Australia. *Appl. Geochem.* **2009**, *24*, 297–302.
(23) Toner, B. M.; Berquó, T. S.; Michel, F. M.; Sorensen, J. V; Templeton, A. S.; Edwards, K. J. Mineralogy of iron microbial mats from Loihi Seamount. *Front. Microbiol.* **2012**, *3*, 1–18.
(24) Glazer, B. T.; Rouxel, O. J. Redox speciation and distribution within iron-dominated microbial habitats at Loihi Seamount. *Geomicrobiol. J.* **2009**, *26*, 606–622.
(25) Wieland, A.; Zopfi, J.; Benthien, M.; Ku, M. Biogeochemistry of an iron-rich hypersaline microbial mat. *Microb. Ecol.* **2005**, *49*, 34–49.
(26) Dichristina, T. J.; Arnold, R. G.; Lidstrom, M. E.; Hoffmann, M. R. Dissimilative iron reduction by the marine eubacterium *alteromonas putrefaciens* strain 200. *Wat. Sci. Tech.* **1989**, *20*, 69–79.
(27) Langley, S.; Gault, A.; Ibrahim, A.; Renaud, R.; Fortin, D.; Clark, I. D.; Ferris, F. G. A comparison of the rates of Fe(III) reduction in synthetic and bacteriogenic iron oxides by *Shewanella putrefaciens* CN32. *Geomicrobiol. J.* **2009**, *26*, 57–70.
(28) Michel, F. M.; Ehm, L.; Antao, S. M.; Lee, P. L.; Chupas, P. J.; Liu, G.; Strongin, D. R.; Schoonen, M. A. A.; Phillips, B. L.; Parise, J. B. The structure of ferrihydrite, a nanocrystalline material. *Science.* **2007**, *316*, 1726–1729.
(29) Toner, B. M.; Briscoe, L. J.; Michel, F. M.; Alexander, S. C.; Alexander, E. C.; Gralnick, J. A. Iron microbial mat formation from deep continental brines, Goldschmidt 2011 Conference Abstracts. *Miner. Mag.* **2011**, *75*, 2022.
(30) Anschutz, A. J.; Penn, R. L. Reduction of crystalline iron(III) oxyhydroxides using hydroquinone: Influence of phase and particle size. *Geochem. Trans.* **2005**, *6*, 60–66.
(31) Schwertmann, U.; Cornell, R. M. *Iron Oxides in the Laboratory*, 2nd ed.; Wiley-

VCH: Weinheim, 2000.
(32) Bligh, M. W.; Waite, T. D. Formation, reactivity, and aging of ferric oxide particles formed from Fe(II) and Fe(III) sources: Implications for iron bioavailability in the marine environment. *Geochim. Cosmochim. Acta* **2011**, *75*, 7741–7758.
(33) Stookey, L. L. Ferrozine – a new spectrophotometric reagent for iron. *Anal. Chem.* **1970**, *42*, 779–781.
(34) Burrows, N. D.; Hale, C. R. H.; Penn, R. L. Effect of ionic strength on the kinetics of crystal growth by oriented aggregation. *Cryst. Growth Des.* **2012**, *12*, 4787–4797.
(35) Deliyanni, E. A.; Bakoyannakis, D. N.; Zouboulis, A. I.; Matis, K. A.; Nalbandian, L. Akaganeite-type β-FeO(OH) nanocrystals: preparation and characterization. *Micropor. Mesopor. Mat.* **2001**, *42*, 49–57.
(36) Hiemstra, T.; van Riemsdijk, W. H. Adsorption and surface oxidation of Fe(II) on metal (hydr)oxides. *Geochim. Cosmochim. Acta* **2007**, *71*, 5913–5933.
(37) Hiemstra, T.; Van Riemsdijk, W. H. A surface structural model for ferrihydrite I: Sites related to primary charge, molar mass, and mass density. *Geochim. Cosmochim. Acta* **2009**, *73*, 4423–4436.
(38) Song, X.; Boily, J. Surface hydroxyl identity and reactivity in akaganeite. *J. Phys. Chem. C* **2011**, *115*, 17036–17045.
(39) Dixit, S.; Hering, J. G. Sorption of Fe(II) and As(III) on goethite in single- and dual-sorbate systems. *Chem. Geol.* **2006**, *228*, 6–15.
(40) Jones, A. M.; Griffin, P. J.; Collins, R. N.; Waite, T. D. Ferrous iron oxidation under acidic conditions – The effect of ferric oxide surfaces. *Geochim. Cosmochim. Acta* **2014**, *145*, 1–12.
(41) Brezonik, P. L.; Arnold, W. A. *Water Chemistry: An Introduction to the Chemistry of Natural and Engineered Aquatic Systems*; Oxford University: New York, 2011.
(42) Schwarzenbach, R. P.; Gschwend, P. M.; Imboden, D. M. *Environmental Organic Chemistry*, 2nd ed.; John Wiley & Sons: Hoboken, NJ, 2003.
(43) Silvester, E.; Charlet, L.; Tournassat, C.; Géhin, A.; Grenèche, J. M.; Liger, E. Redox potential measurements and Mössbauer spectrometry of FeII adsorbed onto Fe^{III} (oxyhydr)oxides. *Geochim. Cosmochim. Acta* **2005**, *69*, 4801–4815.
(44) Navrotsky, A.; Mazeina, L.; Majzlan, J. Size-driven structural and thermodynamic complexity in iron oxides. *Science.* **2008**, *319*, 1635–1638.
(45) Stemig, A. M.; Do, T. A.; Yuwono, V. M.; Arnold, W. A.; Penn, R. L. Goethite nanoparticle aggregation: effects of buffers, metal ions, and 4-chloronitrobenzene reduction. *Environ. Sci. Nano* **2014**, *1*, 478–487.
(46) Filella, M.; Zhang, J.; Newman, M. E.; Buffle, J. Analytical applications of photon correlation spectroscopy for size distribution measurements of natural colloidal suspensions: Capabilities and limitations. *Colloids Surf., A* **1997**, *120*, 27–46.
(47) Korehi, H.; Blöthe, M.; Schippers, A. Microbial diversity at the moderate acidic stage in three different sulfidic mine tailings dumps generating acid mine drainage. *Res. Microbiol.* **2014**, *165*, 713–718.

(48) Stachowicz, M.; Hiemstra, T.; van Riemsdijk, W. H. Multi-competitive interaction of As(III) and As(V) oxyanions with Ca^{2+}, Mg^{2+}, PO_4^{3-}, and CO_3^{2-} ions on goethite. *J. Colloid Interface Sci.* **2008**, *320*, 400–414.
(49) Antelo, J.; Arce, F.; Fiol, S. Arsenate and phosphate adsorption on ferrihydrite nanoparticles. Synergetic interaction with calcium ions. *Chem. Geol.* **2015**, *410*, 53–62.
(50) Ali, M. A.; Dzombak, D. A. Effects of simple organic acids on sorption of Cu^{2+} and Ca^{2+} on goethite. *Geochim. Cosmochim. Acta* **1996**, *60*, 291–304.
(51) Weng, L. P.; Koopal, L. K.; Hiemstra, T.; Meeussen, J. C. L.; Van Riemsdijk, W. H. Interactions of calcium and fulvic acid at the goethite-water interface. *Geochim. Cosmochim. Acta* **2005**, *69*, 325–339.
(52) Deliyanni, E. A.; Bakoyannakis, D. N.; Zouboulis, A. I.; Matis, K. A. Sorption of As(V) ions by akaganeite-type nanocrystals. *Chemosphere* **2003**, *50*, 155–163.
(53) Kim, J.; Li, W.; Philips, B. L.; Grey, C. P. Phosphate adsorption on the iron oxyhydroxides goethite (α-FeOOH), akaganeite (β-FeOOH), and lepidocrocite (γ-FeOOH): a 31P NMR study. *Energy Environ. Sci.* **2011**, *4*, 4298.
(54) Song, X.; Boily, J.-F. Competitive ligand exchange on akaganéite surfaces enriches bulk chloride loadings. *J. Colloid Interface Sci.* **2012**, *376*, 331–333.
(55) Kozin, P. A.; Boily, J.-F. Proton binding and ion exchange at the akaganeite/water interface. *J. Phys. Chem. C C* **2013**, *117*, 6409–6419.
(56) Norén, K.; Persson, P. Adsorption of monocarboxylates at the water/goethite interface: The importance of hydrogen bonding. *Geochim. Cosmochim. Acta* **2007**, *71*, 5717–5730.
(57) Hansel, C. M.; Benner, S. G.; Fendorf, S. Competing Fe(II)-induced mineralization pathways of ferrihydrite. *Environ. Sci. Technol.* **2005**, *29*, 7147–7153.
(58) Boland, D. D.; Collins, R. N.; Miller, C. J.; Glover, C. J.; Waite, T. D. Effect of solution and solid-phase conditions on the Fe(II)- accelerated transformation of ferrihydrite to lepidocrocite and goethite. *Environ. Sci. Technol.* **2014**, *48*, 5477–5485.

Appendix A. Simple and efficient separation of magnetic minerals from speleothems and other carbonates

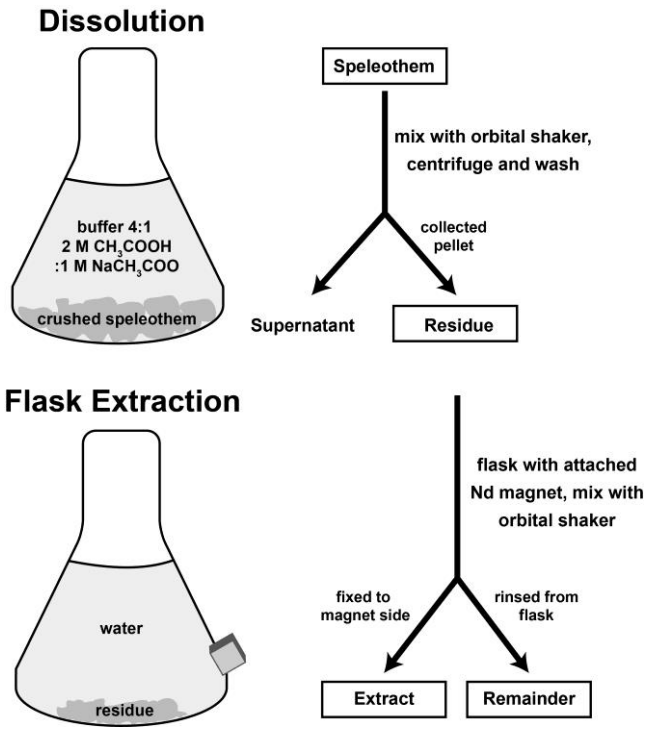

This chapter describes the outcome of a collaborative research project carried out by Jennifer H. Strehlau, Lindsay A. Hegner, and Becky E. Strauss and advised by Joshua M. Feinberg and R. L. Penn. This is IRM publication 1401.

A report on this research has been published:

Strehlau, J. H.; Hegner, L. A.; Strauss, B. E.; Feinberg, J. M.; Penn, R. L.

Journal of Sedimentary Research, 2014, 84, 1096-1106

Summary

Trace concentrations of iron oxide minerals in carbonate sediments can preserve fine details about Earth processes, from high-resolution recordings of the Earth's ancient magnetic field to microscopic remnants of extraterrestrial impacts. This paper presents a novel flask extraction method which uses a neodymium magnet and an orbital shaker for simple and efficient separation of magnetic minerals from carbonate sediments. A mineral assemblage of magnetic standards (titanomagnetite, magnetite, goethite, and hematite) combined with other mineral standards (kaolinite, quartz, and nanoscale TiO_2) was subjected to the extraction procedure and compared to a natural speleothem sample. Exposure of the magnetic standards to a mildly acidic acetate buffer (pH ~ 4) did not cause physical or chemical alteration. The strongly magnetic minerals were reproducibly extracted, with greater than 90% efficiency (by mass), from mixtures of the mineral standards. XRD and low-temperature magnetic characterization demonstrated phase purity of the extracts. Quantitative comparison with two commonly used literature methods showed that the flask extraction method was more reproducible and efficient. The addition of surfactant ($Na(PO_3)_6$) did not significantly improve extraction efficiency. Sequential dissolution and flask extraction of a simulated speleothem containing magnetic particles resulted in consistent extraction efficiencies for samples containing large (> 1 μm) strongly magnetic grains, but a reduction in efficiency was observed for smaller (< 1 μm) grain sizes. No method successfully extracted the weakly magnetic goethite and hematite. However, unprecedented, representative characterization of these minerals was possible through quantitative analysis of the remainder after the collection of the magnetic extract.

This approach may facilitate detailed characterization of a wide range of carbonates, such as pelagic limestone, dolostone, unlithified carbonate ooze, speleothems, and freshwater and pedogenic carbonates. Such mineral extractions can lead to new insights into paleoenvironmental processes as well as an improved understanding of the recording of the Earth's magnetic field.

Introduction

Carbonate speleothems in a natural cave are secondary deposits typically composed of calcite or aragonite crystallites.[1] Assemblages of magnetic minerals trapped within this carbonate matrix have been demonstrated to be effective tools for recording the direction and intensity of the Earth's magnetic field at the time of carbonate precipitation.[2] The combination of high-resolution ^{230}Th isotopic dating of speleothems with paleomagnetic measurements makes them useful archives of Earth's ancient magnetic field behavior.[2,3] Noncarbonate material trapped in a speleothem's crystallite matrix often includes minerals derived from surficial soil, sediment, and bedrock, such as quartz, phyllosilicates, and feldspars.[4,5] Smaller concentrations of ferrimagnetic iron oxide minerals, such as magnetite (Fe_3O_4) and titanomagnetite ($Fe_{3-x}Ti_xO_4$), and antiferromagnetic minerals like goethite (β-FeOOH) and hematite (α-Fe_2O_3), have also been described in speleothem samples through rock magnetic characterization and direct microscopic observation.[2,6–8]

Latham et al. first demonstrated that magnetizations preserved in speleothems capture the Earth's magnetic field at the time of deposition and correlate well to established paleomagnetic records.[9] This work was followed by a series of studies showing that the magnetic minerals in speleothems lock in an accurate recording of the Earth's geomagnetic

field direction, largely accounted for by detrital remanent magnetization (DRM), shortly after their deposition.[10–12] The nearly continuous recording of remanence[13,14] and readily identifiable signatures of post-depositional alteration with no evidence for compaction effects[2,4,15] make speleothems an appealing alternative to more commonly used paleomagnetic archives like igneous rocks and marine sediments.

While DRM from allochthonous magnetic grains is commonly described as the primary remanence mechanism in stalagmites,[2] it is theoretically possible for magnetic minerals to precipitate directly on the surface of a growing stalagmite under certain conditions.[8] As these autochthonous magnetic minerals grow through a critical volume, they lock in a weak magnetization aligned parallel to the Earth's magnetic field, producing a chemical remanent magnetization (CRM). The origin of the remanence of magnetic minerals in stalagmites, whether a DRM or a CRM, continues to be an important question in paleomagnetic research, especially with respect to the identification of grains that may hold a CRM.[2,6–8,16] The answers to these questions will in turn determine whether the concentration and composition of the magnetic minerals in stalagmites are in any way related to local environmental conditions at the surface above a cave, such as mean annual precipitation and temperature.

The low concentration of magnetic minerals in speleothems compared with concentrations in most igneous and sedimentary rocks presents a considerable challenge, requiring large initial sample sizes to yield a representative and readily characterized magnetic subsample. For instance, Strauss et al. described discrepancies between estimates of the grain size of magnetic minerals provided by rock magnetic methods and those

provided by microscopic imaging, introducing the possibility of nonrepresentative sampling during microscopy preparation.[8] Additionally, certain extraction techniques involve steps that may alter the surface texture of the magnetic minerals via acid etching or cause compositional transformations (e.g., goethite to hematite). If undetected, this alteration can lead to misinterpretation of the formation and transport history of the magnetic mineral assemblage. These challenges emphasize the importance of developing a nondestructive, high-yield dissolution technique for the extraction of magnetic minerals in speleothems and carbonates in general.

Early attempts to extract magnetic minerals from speleothems have been partially successful. The standard practice for magnetic mineral extraction begins with the dissolution of the carbonate in an acidic solution. Extraction relies on the application of a small magnetic field to the resulting solution to separate the magnetic minerals; to this end, paleomagnetic researchers have used various techniques ranging in complexity. For example, Perkins described a complex peristaltic pump-driven system with a magnetic joint that achieved extraction efficiencies over 75% with marine sediment samples dominated by strongly magnetic minerals,[17] and added the surfactant sodium hexametaphosphate ($Na(PO_3)_6$) to residues before extraction to discourage flocculation of mineral grains, thereby improving extraction efficiencies.[6] A simpler design for extraction from siliciclastics (including silts, fine sands, and soils) suspends sediments in water, and a magnet wrapped in a plastic bag is submerged into the mixture and manually agitated.[18] Comparison and quantification of efficiencies and compositional yields between techniques using combinations of standard materials have not yet been performed but

would aid in the evaluation of methods to extract magnetic minerals from speleothems and other carbonates.

The aims of this paper are to quantitatively compare methods of speleothem dissolution and magnetic separation and to perform subsequent microscopy and compositional analysis, X-ray diffraction, and magnetic characterization in tandem. A novel, simple, and highly efficient flask magnetic extraction method is described. Three types of samples are compared: heterogeneous mixtures of pure mineral samples, synthetic carbonates precipitated in the presence of pure samples of magnetic minerals, and a natural speleothem. These methods of magnetic mineral separation are applicable to a wide variety of carbonate materials, such as unlithified carbonate ooze, pelagic limestone, dolostone, speleothems, and freshwater and pedogenic carbonates. The magnetic mineral assemblages in such carbonates offer unique insights into paleoenvironmental processes as well as the mechanisms by which the Earth's magnetic field is recorded over geologic time.

Approach and Methods

Mineral Standards

Mineral standards included titanomagnetite, magnetite, goethite, hematite, kaolinite, quartz, and TiO_2 nanoparticles. Each mineral standard was chosen for its common occurrence in carbonate mineral assemblages and its importance for paleomagnetism studies, with the exception of TiO_2. The nanoparticle size and diamagnetic properties of TiO_2 allow assessment of the effects of small, diamagnetic minerals in speleothem residues on the efficiency and mineralogy of a given extraction method. Kaolinite ($Al_2Si_2O_5(OH)_4$) was selected as a representative clay mineral. Kaolinite, quartz,

and TiO_2 are herein defined as the residue standards and abbreviated as KQT when used together.

Mineral standards were either purchased or synthesized. More detailed information is provided in the Supporting Information, and characterization is described in the Results section of this study. Submillimeter titanomagnetite grains were purchased from Gold-Nugget Designs, a private online supplier. Nanoscale magnetite particles were synthesized by partial oxidation of an Fe(II) solution, using a method described by Schwertmann and Cornell.[19] Large goethite nanorods were synthesized using the method of Mazeina and Navrotsky.[20] Hematite nanoparticles were synthesized by the method of Schwertmann and Cornell.[19] KGa-1b, a well-crystallized kaolinite from Washington County, Georgia, U.S.A., was purchased from the Source Clay Minerals Repository (University of Missouri–Columbia, U.S.A.). Ottawa sand of 20–30 mesh (Fisher Sci.) was used as the quartz standard. Titanium Dioxide P25 (Degussa) was used for TiO_2 nanoparticles.

Carbonate Materials

Two carbonate-based materials were used for evaluation of the combined dissolution and extraction procedure: 1) synthetic carbonate containing a magnetic mineral assemblage and 2) natural speleothem sample NC11-1, described in Strauss et al.[8]

Synthetic calcite was crystallized by the slow addition of a $CaCl_2$ solution to a suspension of magnetic particles in Na_2CO_3 solution.[21] A suspension of 1 mg/mL magnetic particles (titanomagnetite, magnetite, or goethite) in 50 mL of 0.40 M Na_2CO_3 was prepared and ultrasonicated for 2 min. At a rate of approximately 5 mL/min, a total of 20 mL of 1.1 M $CaCl_2$ was added to the magnetic suspension by adding 0.83 mL every 10 s,

with constant agitation in between additions. A precipitate immediately formed. After complete addition and 20 min of settling, 40 mL of supernatant was removed by pipette and the suspension dried at 35 °C. The dried solid was then washed with Milli-Q (Millipore, 18.2 MΩ·cm) water using a Büchner filtration system with 55 mm cellulose round filters (Whatman) to remove soluble side products. The remaining solid was dried at room temperature.

Sample NC11-1 is a short massive stalagmite, approximately 15 cm tall and 24 cm in diameter, with abundant detrital material preserved in the calcite matrix and indicated by dark brown layers parallel to annual growth surfaces. NC11-1 was collected by the owner of Niagara Cave (43° 30′ 50.02″ N, 92° 3′ 18.02″ W), located in southeast Minnesota.[22] The top of this stalagmite has been U-Th dated to 539 ± 102 years (Calvin Alexander, personal communication, 2013). NC11-1 is known to include titanomagnetite, magnetite, hemoilmenite, and goethite in its magnetic mineral assemblage.[8]

Dissolution and Flask Extraction

The dissolution and flask extraction method described here results in the acquisition of three subsamples from each speleothem specimen (Fig. A.1). In brief, the speleothem is dissolved in a mildly acidic buffer solution and centrifuged to collect the *residue*, which contains the entirety of the noncarbonate mineral assemblage and often a large amount of silicates relative to a small concentration of magnetic minerals. Flask extraction of the residue yields two subsamples: 1) minerals collected with an applied magnetic field, defined as the *extract*, and 2) minerals that were left behind, defined as the *remainder*.

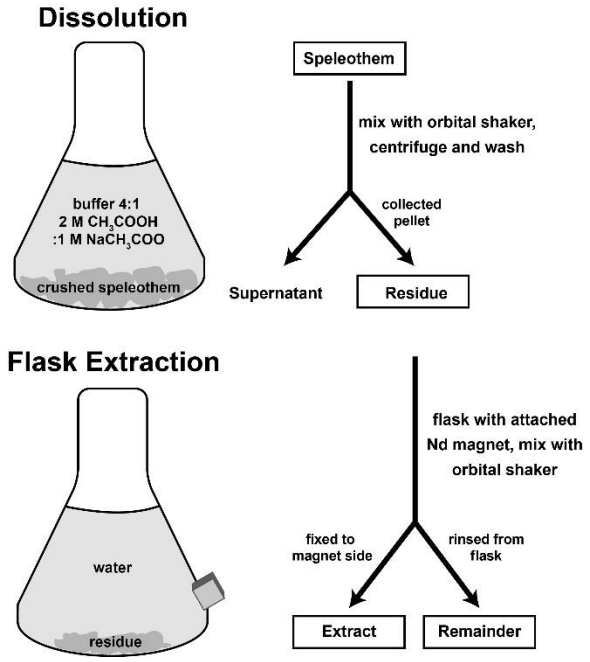

Figure A.1: Schematic of the dissolution and flask extraction processes, including the pathway of collection for the residue, extract, and remainder from a speleothem sample.

The acetate buffer solution used for the speleothem dissolution procedure was described by Perkins[6] and is repeated here as a 4:1 ratio of 2 M CH_3COOH (Mallinckrodt) and 1 M $NaCH_3COO$ (Aldrich). In a 250 mL Erlenmeyer flask, approximately 5 to 6 g of the carbonate material was added to 200 mL of the buffer. When a natural speleothem was used, it was coarsely ground to < 1 cm^3 using a ceramic mortar and pestle, as described by Strauss et al.[8] The flask was continuously mixed on a Cole Parmer Orbital Shaker 51300 Series at 220 rotations per minute (rpm) for 1–3 days or until the sample was completely dissolved. The contents of the flask were then transferred to a polypropylene centrifuge tube and centrifuged at 14000 g (g-force) for 3 min in an Eppendorf 5804 centrifuge. The supernatant was removed, and the residue washed three times with Milli-Q water. The residue was either dried for characterization or transferred to a 50 mL Erlenmeyer flask for

magnetic extraction. For comparison, weighed magnetic standards without accompanying carbonate were also subjected to the dissolution procedure using either the acetate buffer or 2 M acetic acid. Dissolved iron was quantified by ferrozine analysis as in Stookey using an Agilent 8453 UV-Vis spectrophotometer with a detection limit of 0.01 mM Fe(II).[23]

The flask extraction procedure applied to the residue is similar in design to the method briefly described by Strauss et al.,[8] but it does not use a differential magnetic extraction technique. Instead, the procedure described here uses only one magnetic extraction step. Milli-Q water (~ 30 mL) was added to a 50 mL Erlenmeyer flask with either the residue collected after dissolution or standard mineral mixtures. In extraction trials involving mineral standards, known masses of the strongly magnetic minerals were used (summarized in Tables A.1–3) and repeated in triplicate. Standard mixtures were prepared by combining the strongly magnetic minerals with 10 mg goethite or 10 mg hematite and/or 0.25 g kaolinite, 0.25 g quartz, and 5 mg TiO_2 (KQT). In some trials, 50 µL of 0.1 g/mL sodium hexametaphosphate ($Na(PO_3)_6$) was added to the residue prior to suspension. A 1 cm^3 neodymium magnet (with an ~ 10–400 mT field at a distance of 1 mm) was affixed to the outside of the flask, just above the convex curve at the bottom, as shown in Figure A.1. The flask was secured on an orbital shaker at 220 rpm for 15 min. With the magnet still firmly attached, the cloudy suspension containing the remainder was carefully decanted to a centrifuge tube, taking care not to disturb any particles adhering to the glass adjacent to the magnet. The flask was carefully rinsed with approximately 5 mL of Milli-Q water without disturbing the particles attracted to the magnet, and the rinse was

also added to the centrifuge tube. The resulting suspension was centrifuged at 14,000 g for 3 min, the supernatant decanted, and the remainder dried.

To rinse the magnetic extract, 2–4 mL of Milli-Q water was added to the flask after the remainder had been separated and the magnet was removed. The flask was gently swirled to dislodge any particles previously held by the magnet. The magnet was reattached to the flask to repeat the magnetic extraction for a total of three rinses; the rinse was discarded. To collect the magnetic extract, the magnet was removed and 1–2 mL of Milli-Q water was used to transfer the particles to containers for drying at room temperature. A microbalance was used to weigh extracts from sample NC11-1.

Other Extraction Methods

The complex pump extraction set-up, hereafter referred to as the *pump* method, was fashioned after Reynolds et al., similar to the system described in Perkins and Peterson et al.[6,24,25] Combinations of mineral standards were suspended in 10 mL of Milli-Q water and then added to the reservoir with 200 mL Milli-Q water. The suspension was driven by a Masterflex L/S (Cole Parmer) peristaltic pump at ~ 200 mL/min and passed through Tygon L/S flexible plastic tubing (Saint Gobain) oriented vertically, with a joint that contained a Nd magnet covered with a plastic sleeve to collect the magnetic material. After 90 min, the magnetic extracts were washed from the sleeve with Milli-Q water and collected for analysis. The remaining suspension in the reservoir was collected as the remainder.

A simple extraction method, in which a magnet wrapped in a plastic bag is submerged into a sediment mixture, was modified from the method used for magnetic extraction of lake sediments by Israde-Alcántara et al. and is hereafter referred to as the

bag method.[18] In our trials, combinations of standards were added to 20 mL of Milli-Q water contained in a glass Pyrex dish. The same Nd magnet was wrapped tightly with thin plastic and held so that there would be as little interference by the plastic between the magnet and particles as possible. The covered magnet was then manually agitated in the glass dish for 2 min. The covered magnet with affixed particles was transferred to another glass Pyrex dish and rinsed in 30 mL of Milli-Q water for 2 min by the same agitation method. The magnet was then carefully removed as to not disturb the extracted particles collected on the plastic. With the magnet removed, the particles were collected by rinsing with 1–2 mL of Milli-Q water and then dried. The initial dish containing the remainder in suspension was also dried for analysis.

Characterization

Scanning electron microscopy (SEM) was performed on a JEOL 6500 microscope with a Thermo-Noran Vantage EDS system for elemental analysis. Transmission electron microscopy (TEM) was performed at 120 kV on a FEI T12 high-resolution TEM (HRTEM) with a LaB_6 electron source, a Gatan charge-coupled device (CCD) camera, and an Oxford model 6767 EDS system. Particles were suspended in Milli-Q water (~ 100 µg/mL for SEM and ~ 10 µg/mL for TEM), and 1–3 drops placed directly on a 12 mm square of carbon tape (SPI Supplies) for SEM or a 3 mm 200 mesh holey carbon-coated copper grid (SPI Supplies) for TEM, then dried in air. Approximate particle sizes were estimated from SEM or TEM calibrated images.

X-ray diffraction (XRD) patterns were acquired using a PANalytical X'Pert Pro X-ray diffractometer with a Co source and X'Celerator detector. Data were collected from

15° to 90° 2θ over a minimum collection time of 50 min. The detection limit for compositional mixtures is approximately 1% by volume. Resulting peaks were compared to the corresponding powder diffraction files (PDFs): #19-0629 (magnetite), #29-0713 (goethite), #33-0664 (hematite), and #46-1045 (quartz). The PDF file for magnetite was used to identify both the magnetite and titanomagnetite grains, as the change in *d* spacing was not significant enough to detect a separate shifted peak. Peak intensities and positions for kaolinite and TiO_2 were determined by collecting XRD patterns of the pure mineral standards.

For magnetic characterization, samples were analyzed through two low-temperature experiments conducted on Quantum Designs Magnetic Property Measurement System (MPMS) cryogenic magnetometers with nominal sensitivities of 10^{-10} Am^2:

1) In a Field Cooled-Zero Field Cooled (FC-ZFC) experiment, samples are cooled from room temperature to 10 K in a 2.5 T field, given a 2.5 T isothermal remanent magnetization (IRM) at 10 K, and warmed back to room temperature in zero field. This process is then repeated, albeit with the cooling step in zero field.

2) In a low-temperature cycling of room-temperature saturation isothermal remanent magnetization (RTSIRM) experiment, a 2.5 T IRM is imparted to each sample at room temperature. Magnetization is then measured during cooling to 10 K and warming back to room temperature in zero field.

Results

Characterization of Standards

All standards were characterized using a combination of electron microscopy, MPMS, and XRD. Electron micrographs of titanomagnetite, magnetite, goethite, and hematite standards are shown in Figure A.2. FC-ZFC and RTSIRM curves for the magnetic standards are shown in the Supporting Information. XRD patterns were consistent with the PDF patterns for each mineral standard.

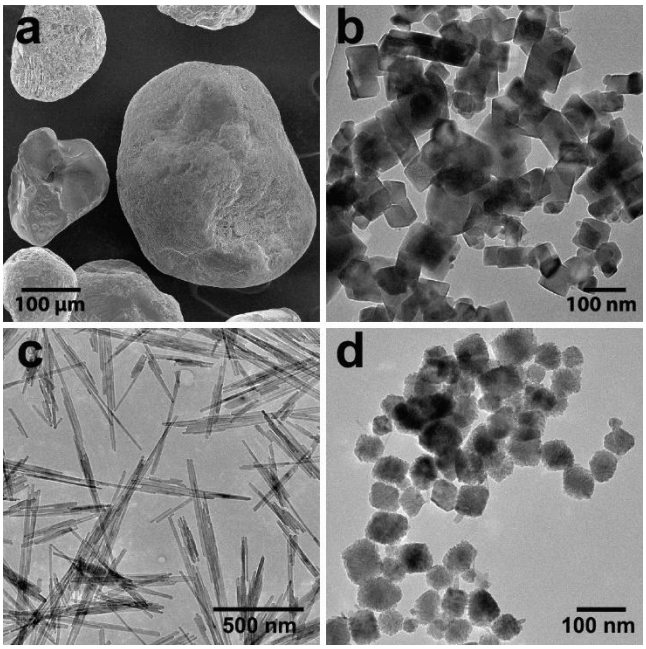

Figure A.2: Microscopy of magnetic standards. A) SEM image of natural submillimeter titanomagnetite grains after exposure to the dissolution buffer. Textures seen on grains are representative of both before and after buffer exposure. B–D) TEM images of synthetically prepared (B) magnetite nanoparticles, (C) goethite nanorods, and (D) hematite nanoparticles.

Titanomagnetite grains were approximately 200 µm in diameter and rounded, with several grains exhibiting textures produced by igneous exsolution processes (example shown in top left of Fig. A.2). The dimensions of these grains are consistent with the size

of particles deposited on stalagmites during flooding events.[26] Compositional analysis by EDS indicated that the grains are titanomagnetite of varied composition; the few grains with exsolution textures displayed Fe:O ratios consistent with hemoilmenite, a solid solution of hematite (Fe_2O_3) and ilmetnite ($FeTiO_3$). Low-temperature magnetic characterization displayed evidence of the Verwey transition, suggesting that there is a range of compositions within the titanomagnetite standard, at least a portion of which is Ti-poor. In contrast, the synthetic magnetite nanoparticles were approximately 100 nm in size and euhedral in shape, and EDS analysis indicates that the material is composed only of iron and oxygen. Low-temperature magnetic characterization of the magnetite also displayed the Verwey transition through cooling; however, on warming the remanence was constant until 90 K, when partial demagnetization occurred. These results are similar to the stoichiometric 100 nm magnetite nanoparticles described by Özdemir et al.[27]

Synthetic goethite particles were acicular in shape, approximately 500 nm long and 10 nm wide, although the distribution of particle sizes was broad. Low-temperature magnetic characterization revealed a systematic separation between the field-cooled (FC) and zero field-cooled (ZFC) curves, consistent with the magnetic behavior of goethite. Synthetic hematite nanoparticles were polygonal to rounded in shape, approximately 50 nm in size, and had coarse surface textures. Low-temperature magnetic analyses showed behavior consistent with the Morin transition of hematite, although the observed transition occurred at a lower temperature than expected (260 K) due to the small particle size of hematite.[28]

The composition and morphologies of the residue standards (kaolinite, quartz, and TiO_2) are well described by the manufacturers; therefore, SEM and TEM analyses are not shown. Reported grain sizes were 0.1–3.5 μm for kaolinite (KGa-1b),[29] 600–800 μm for quartz (Ottawa sand standard, Fisher), and 25 nm for TiO_2 (Degussa). Low-temperature magnetic characterization of these standards (see Supporting Information) did not display any magnetic behavior that could interfere with the measurement of the magnetic standards, with the exception of the quartz standard, which demonstrated a muted Verwey transition, suggestive of minute magnetite impurities. However, in comparison with the magnitude of the signal from the titanomagnetite and magnetite standards, this response is expected to be insignificant.

Effects of Dissolution Buffer

The titanomagnetite standard was characterized by SEM for grain morphology and composition before and after exposure to the acetate dissolution buffer (pH ~ 4). Similar grain sizes, morphologies, compositions, and rare exsolution textures were observed in the pre- and post-treated titanomagnetite. Ferrozine analysis of the post-dissolution supernatant from several trials containing 10 mg of either titanomagnetite, magnetite or goethite in 50 mL of the acetate dissolution buffer yielded no detectable levels greater than the detection limit of 0.01 mM dissolved Fe(II) or Fe(III), further evidence that the buffer did not significantly alter the iron oxides by dissolution. In contrast, after exposure to a more acidic 2 M acetic acid (pH ~ 2), ferrozine analysis of the post-dissolution supernatant detected dissolved Fe(II) or Fe(III) (up to 0.03 mM for the nanoscale magnetite after four days of exposure), demonstrating that this more acidic solution partially dissolves iron-

containing minerals. Finally, ferrozine analysis of the supernatant collected after dissolution of NC11-1 demonstrated no detectable dissolved Fe(II) or Fe(III).

Flask Extraction

Triplicate trials were conducted using simulated residues made from combinations of standards. These trials included 1) the strongly magnetic minerals alone or with residue standards, and 2) titanomagnetite and either goethite or hematite with residue standards. Efficiency is reported as the mass of the material extracted as a percentage of the initial mass of the strongly magnetic minerals added, defined as the percent recovery.

I. (Titano)magnetite.--- Results of flask extraction using standards are summarized in Table 1. Extraction efficiencies were reproducible, with recoveries > 90%. The addition of residue standards did not affect the percent recovery of titanomagnetite; however, the percent recovery of magnetite in systems with small mass loading did decrease. It is possible that the magnetite nanoparticles adhered to either the glassware or residue standards, making extraction more difficult with increasing particle interactions. For example, earlier studies have shown nanometer-scale magnetite grains strongly adhered to clay particles due to differences in electrostatic potential.[30] When both titanomagnetite and magnetite were added to the same extraction trial, no significant difference in percent recovery was observed compared to each magnetic standard alone. In general, trials employing the surfactant solution yielded smaller percent-recovery values than trials without surfactant.

Table A.1: Summary of trials using the flask extraction method. Trials contained titanomagnetite (TMag), magnetite (Mag), or a combination of both, either alone or with residue standards kaolinite, quartz, and TiO_2 (KQT). Initial range of strongly magnetic mineral masses added and average percent recoveries with standard deviations are summarized as a function of surfactant ($Na(PO_3)_6$) addition from triplicate trials.

System	Magnetic Standard(s)	No Surfactant		With Surfactant	
		Magnetic Mass (mg)	Recovery (%)	Magnetic Mass (mg)	Recovery (%)
Magnetic Only	TMag	5.1 - 7.6	99 ± 4	5.3 - 6.9	98 ± 10
	Mag	5.3 - 8.6	100 ± 2	5.2 - 9.6	96 ± 9
	TMag + Mag	9.4 - 13.1	96 ± 3	11.8 - 13.0	95 ± 6
Magnetic + KQT	TMag	4.8 - 8.8	99 ± 5	5.9 - 8.2	93 ± 6
		160.1	97*		
	Mag	4.9 - 8.9	95 ±19	5.7 - 8.3	105 ± 12
		145.6	100*		
	TMag + Mag	8.8 - 16.4	99 ± 3	12.4 - 12.9	102 ± 2

*Trials containing large amounts of TMag and Mag with KQT were performed once.

Three of the trials that were subjected to the flask extraction procedure were further analyzed by XRD, including titanomagnetite with residue standards, magnetite with residue standards, and a combination of titanomagnetite and magnetite with residue standards. XRD patterns of the extract and remainder in each case are shown in Figure A.3. Results demonstrate that extracts contained only the strongly magnetic minerals and no detectable residue standards for all three trials. XRD patterns of remainders demonstrate the presence of the residue standard minerals without detectable (titano)magnetite.

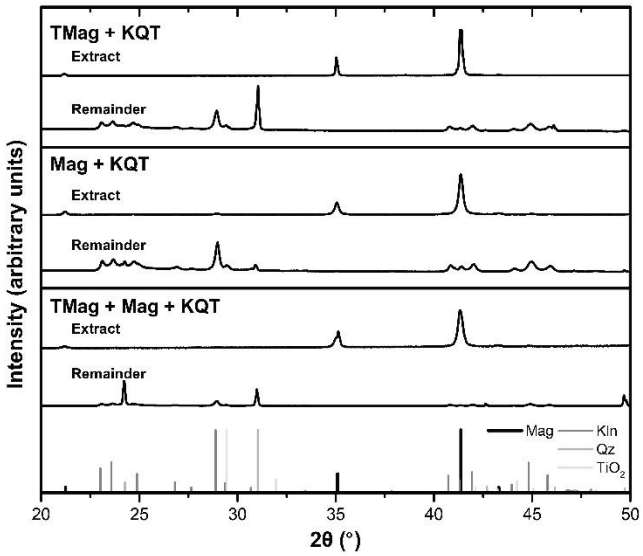

Figure A.3: Compositional analysis of the magnetic extract and remainder from representative flask extraction trials containing either titanomagnetite (TMag, TM), magnetite (Mag, M) or a combination of both, and with residue standards kaolinite (Kln, K), quartz (Qz, Q), and TiO_2 (T), together as KQT, as demonstrated by XRD patterns of the extract and remainder in each trial.

II. Goethite and Hematite.--- Separate flask extraction trials containing titanomagnetite, residue standards, and either goethite or hematite were conducted to test extraction effectiveness for the weakly magnetic minerals. The extract and remainder from these trials were analyzed by XRD. The XRD patterns are shown in Figure A.4, demonstrating that only the strongly magnetic titanomagnetite was detected in the extract. Further, goethite or hematite was detected only in the remainder, in which no titanomagnetite was detected.

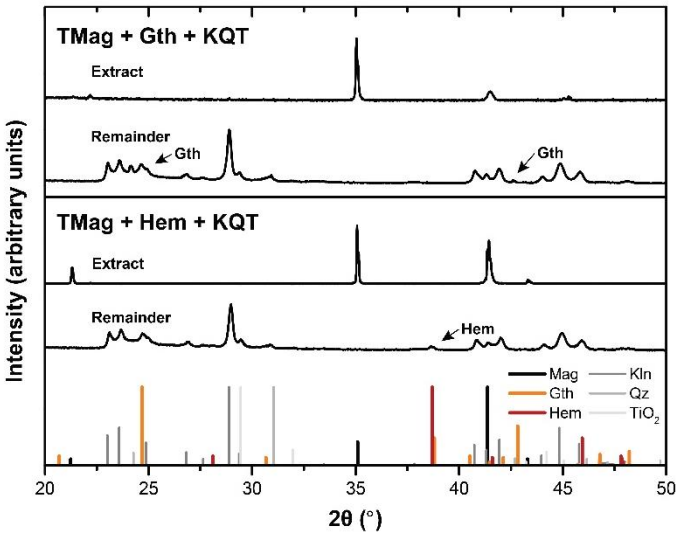

Figure A.4: Compositional analysis of the magnetic extract and remainder from flask extractions containing titanomagnetite (TMag) and either goethite (Gth) or hematite (Hem), with residue standards kaolinite (Kln), quartz (Qz), and TiO_2 (together as KQT). Peaks noted with arrows indicate the detection of the weakly magnetic goethite or hematite in the remainder.

XRD results are consistent with low-temperature magnetic characterization of the pre-extraction sample, extract, and remainder (Fig. A.5). In samples containing titanomagnetite and either goethite or hematite, the dominant character of the magnetic remanence is held by titanomagnetite, swamping any evidence that might indicate goethite or hematite. Characterization of the extract yields a similar response, albeit at higher magnitudes of magnetization, indicating that titanomagnetite is the primary holder of remanence in the extract. In contrast, characterization of the remainder reveals a contribution from either the goethite or hematite. For goethite, a clear, systematic separation of the FC-ZFC curves, which is not observed in either the pre-extraction sample

or the extract, can be readily detected in the remainder. A Morin transition, consistent with the presence of hematite, is observed only in the hematite trial remainder.

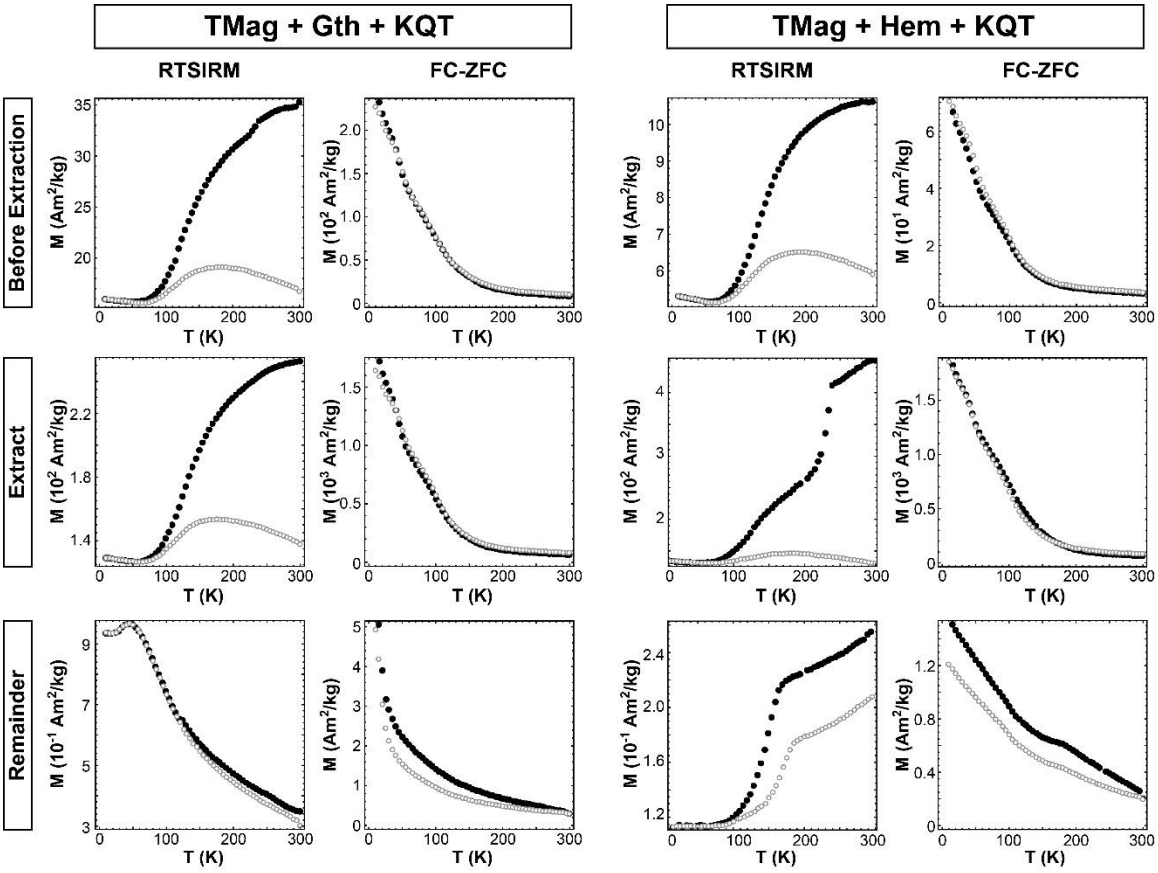

Figure A.5: Low-temperature magnetic characterization of magnetization (M) collected by MPMS of flask extraction trials containing titanomagnetite (TMag) and either goethite (Gth) or hematite (Hem), both with residue standards kaolinite, quartz, and TiO_2 (KQT). Before extraction (top row), magnetic extract (middle row), and remainder (bottom row) for representative trials are shown, with RTSIRM measurements (filled black circles on cooling, open gray circles on warming) at left and FC-ZFC measurements (filled black circles on FC, open gray circles on ZFC) at right of each pair.

III. Comparison with Other Extraction Methods.--- Mixtures of titanomagnetite, goethite, and residue standards were subjected to the flask, pump, and bag

extraction methods, enabling detailed comparison between techniques. The mass of titanomagnetite added and the corresponding percent recoveries for all three methods are listed in Table 5.2. In most cases, both the pump and bag methods recovered significantly less magnetic material than the flask method (~ 10–30% less) and were less reproducible. Additionally, both the pump and bag methods included at least one trial with percent recoveries exceeding the theoretical 100% limit. This excess in percent recovery was not observed in trials with the flask method and is attributed to the presence of residue standards (KQT) in the extract; XRD patterns of extracts and remainders (Fig. A.6) confirm the presence of residue standards in the extracts of the pump and bag methods. However, no method extracted goethite at sufficient concentrations to be detectable by XRD. For both the pump and bag methods, percent recoveries generally decreased or remained about the same with the addition of the surfactant.

Table A.2: Extraction efficiencies of three trials with titanomagnetite (TMag), goethite, and residue standards kaolinite, quartz, and TiO_2 using the flask, pump, and bag extraction methods. Initial mass of titanomagnetite and percent recoveries of each trial are summarized as a function of surfactant ($Na(PO_3)_6$) addition. Percent recoveries larger than 100% indicate the presence of residue standards in the extract.

	Flask		**Pump**		**Bag**	
	TMag (mg)	**Recovery (%)**	**TMag (mg)**	**Recovery (%)**	**TMag (mg)**	**Recovery (%)**
No Surfactant	4.2	98	8.4	114	4.5	109
	6.0	93	6.0	67	4.3	86
	6.8	96	7.1	59	7.9	89
Average		**96 ± 2**		**80 ± 30**		**95 ± 13**
With Surfactant	4.2	105	8.4	73	4.7	123
	5.5	95	5.2	92	5.4	78
	6.9	99	5.9	98	7.9	73
Average		**99 ± 5**		**88 ± 13**		**92 ± 28**

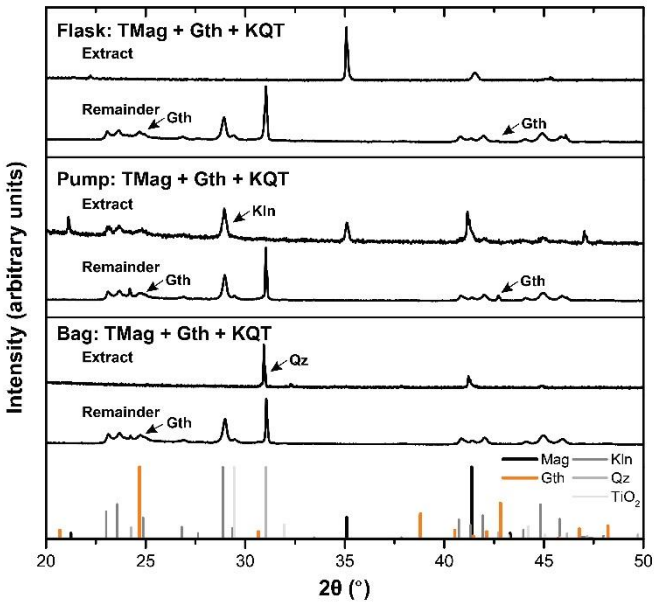

Figure A.6: Compositional analysis of the magnetic extract and remainder in representative trials using the flask (top section), pump (middle section), and bag (bottom section) extraction methods with identical samples containing titanomagnetite (TMag), goethite (Gth), and residue standards kaolinite (Kln), quartz (Qz), and TiO_2 (together as KQT). Peaks noted with arrows indicate residue standards detected in the magnetic extracts or goethite detected in the remainder.

Extractions from Carbonates: Synthetic Calcite and Sample NC11-1

Carbonate precipitated in the presence of titanomagnetite, magnetite or goethite was processed using dissolution followed by the flask extraction technique to test recovery of magnetic material with inclusion of the dissolution step. Percent recoveries after dissolution and flask extraction are provided in Table A.3, where the extracted mass is divided by the theoretical magnetic mass in the carbonate added to the dissolution. Percent recovery of titanomagnetite after carbonate dissolution was > 90%. However, the percent recovery of magnetite was lower than for trials with no dissolution (refer to Table A.1). As with previous trials, no detectable goethite was collected in the extract. For both magnetite

and goethite, particles adhered to centrifuge tube walls, which may account for the lower percent recovery of magnetite when dissolution is included.

Table A.3: Masses of titanomagnetite (TMag)-, magnetite (Mag)-, and goethite (Gth)-spiked synthetic calcite (Cal) added to the dissolution process and percent recoveries of the magnetic standard following flask extraction.

Sample	Total Mass Added to Dissolution (g)	Magnetic Mass Added (mg)	Recovery (%)
TMag-Cal	1.403	47	94%
Mag-Cal	1.475	44	70%
Gth-Cal	1.476	42	0%*

*No measurable amount of weakly magnetic goethite was extracted.

To demonstrate the application of the flask method to a natural speleothem, 5 to 6 g of sample NC11-1 was subjected to the dissolution and flask extraction procedures, yielding ~ 50 mg of residue (mass concentration of roughly 1%). Following the flask extraction, approximately 0.1 mg of strongly magnetic extract was collected (mass concentration of roughly 0.2% of the residue and 0.002% of the bulk sample). Low-temperature magnetic characterization of a representative residue, extract, and remainder of NC11-1 is presented in Figure 7. The residue plots are consistent with bulk sample characterization,[8] showing that the dominant magnetic mineral is strongly magnetic titanomagnetite or magnetite. Characterization of the extract and the remainder, however, reveal the presence of goethite in sample NC11-1, indicated by the systematic separation between FC and ZFC curves.

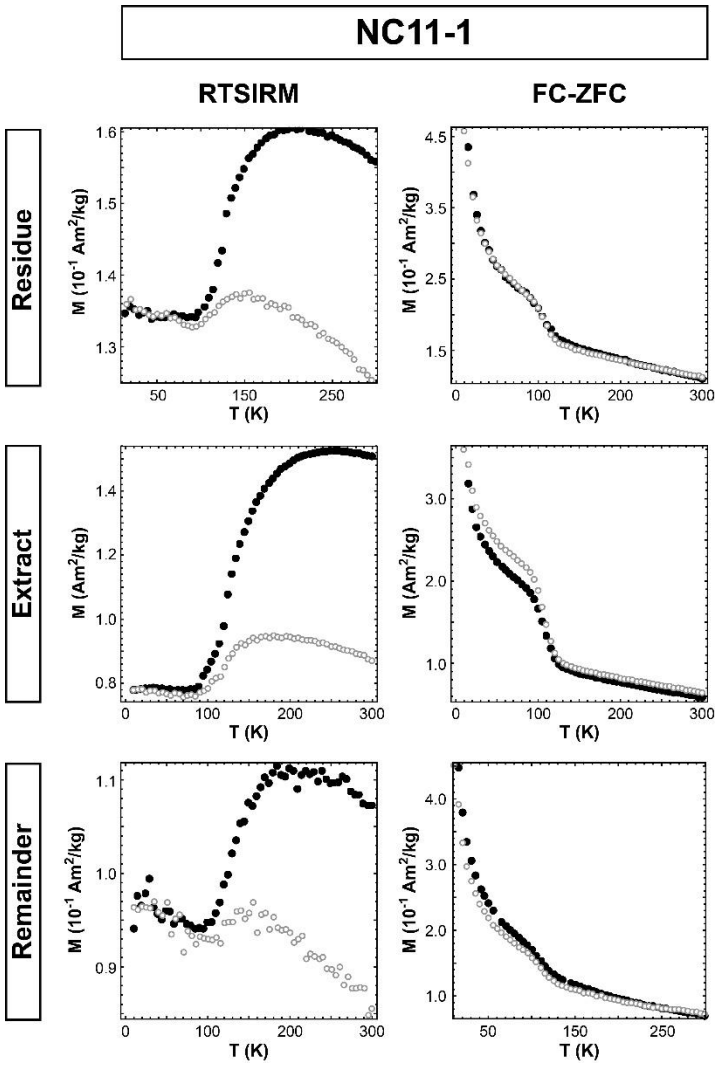

Figure A.7: Low-temperature magnetic characterization of magnetization (M) collected by MPMS of representative samples of NC11-1 following dissolution and flask extraction. The residue (top), extract (middle), and remainder (bottom) are shown, with RTSIRM measurements (filled black circles on cooling, open gray circles on warming) at left and FC-ZFC measurements (filled black circles on FC, open gray circles on ZFC) at right of each pair.

Discussion

Necessity of a Mildly Acidic Buffer in Dissolution

Removal of insoluble minerals from the carbonate matrix of speleothems involves simple acidic dissolution, accompanied by the evolution of gaseous CO_2. However, to assess morphology and composition of grains for the study of the origin of remanence, the dissolution process must not chemically or physically alter the magnetic mineral assemblage. Characterization via electron microscopy before and after exposure to the acetate buffer solution used here demonstrates no detectable changes in surface texture, morphology, or composition. The absence of detectable dissolved Fe(II) or Fe(III) in the supernatant following dissolution further supports this conclusion. In comparison, dissolution experiments employing the more acidic 2 M acetic acid (pH ~ 2) resulted in detectable amounts of dissolved Fe(II) or Fe(III). Therefore, we emphasize the importance of maintaining a mildly acidic pH at all times.

Assessment of the Flask Extraction Method

The flask extraction design first described by Strauss et al. (2013) and further improved upon in this paper has been shown to be more efficient than previous methods described in the literature. A key advantage of the flask extraction design is its simplicity and the use of inexpensive and readily obtained materials. It is also consistently reproducible and relatively quick to perform. The percent recoveries obtained in the trials using various combinations of magnetic minerals and residue standards (Tables A.1 and 2) demonstrate the efficiency of the flask method, which yields recoveries greater than 90% without the addition of a surfactant. Compositional analysis of the extracts by XRD resulted in detection of only titanomagnetite and/or magnetite (Figs. A.3, 4, and 6). The flask extraction method successfully isolates high percentages of strongly magnetic

minerals from a speleothem sample with nearly complete separation of any remainder minerals like clays or silicates.

Previously described methods have been partially successful in the extraction of the magnetic mineral assemblages in speleothems;[6,8] however, this is the first study to quantitatively compare the results. The pump and bag methods serve as models of the range of complexity of common practices. The pump method is fairly complicated to assemble, while the bag method is relatively simple. The pump method requires expensive components and a large space for set-up. Compared to the flask method, the pump method produces inconsistent percent recoveries and collects additional residue standards in the magnetic extract. We attribute this to the complexity of the pump extraction design. In the pump system at the Institute for Rock Magnetism, joints in the tubing combined with segments of vertical flow moving against gravity frequently result in a build-up of sediment, with visible amounts of titanomagnetite (observed as black material in samples of known composition) trapped in these areas. In contrast, the bag method has several desirable qualities in common with the flask method, such as a simple design, inexpensive materials, and short extraction times. However, results demonstrate lower percent recoveries of the strongly magnetic minerals and significant collection of unwanted residue standards. It is important to note that these previously described methods have been broadly successful in obtaining magnetic extract from residues, though our data demonstrate that the flask extraction method provides a substantial improvement in recovery and requires less starting material.

Finally, the surfactant does not improve extraction results and is at times detrimental to extraction efficiency (Tables A.1 and 2). The addition of the surfactant generally resulted in poorer and less reproducible recoveries in all three methods. In trials that contained both the nanoscale magnetite and surfactant, visible black residue remained on the walls of the flask after rinsing and removal of the extract. By limiting the aggregation of the magnetite, the addition of surfactant could enhance the electrostatic attraction of the magnetite grains to the negatively charged glass wall of the flask. Thus, we conclude that the surfactant is an unnecessary component in magnetic extraction from speleothems. We therefore exclude this step from the flask extraction procedure, adding to the simplicity and cost-effectiveness of this method.

Magnetic extraction of goethite and hematite

Previous studies have demonstrated the co-extraction of weakly magnetic particles in magnetic extracts through microscopy.[6–8] Strauss et al. applied an extraction procedure similar in design but used magnets at different proximities to the flask, producing variable magnetic intensities with the goal of differentially extracting strongly and weakly magnetic grains.[8] While this procedure was successful in collecting magnetite, titanomagnetite, goethite, and other magnetite iron oxide grains, it was uncertain whether the phase composition of the recovered materials were representative of the amounts present in the bulk sample. The use of well-characterized and well-separated mineral standards demonstrates that weakly magnetic minerals will not necessarily accompany the strongly magnetic minerals during magnetic extraction. At the same time, the very efficient removal of the strongly magnetic minerals means that the weakly magnetic minerals can be readily

characterized in the remainder. Results from trials combining titanomagnetite with either goethite or hematite demonstrate that no detectable goethite or hematite is extracted. Complementary low-temperature magnetic characterization of the extracts in each case produced similar results (Fig. A.5), where the magnetic behavior observed was characteristic of only titanomagnetite. While the flask method cannot extract goethite or hematite from the insoluble mineral assemblage, the highly efficient extraction of the strongly magnetic material represents substantial improvement in sample preparation for detecting and quantifying the presence of the weakly magnetic minerals in the remainder. This challenge is not limited to the flask extraction method described here. We hypothesize that the successful collection of weakly magnetic minerals may have been achieved in previous studies due to adhesion to the strongly magnetic minerals. This problem has likely presented unrecognized difficulty for previous researchers attempting to extract weakly magnetic minerals for characterization.

Characterization of the remainder represents an opportunity to obtain quantitative information about the weakly magnetic minerals. For example, low-temperature magnetic characterization of remainders following flask extraction on samples containing weakly magnetic minerals (Fig. A.5) reveal magnetic behavior not detectable in the original sample. In pre-extraction materials, neither the separation of FC and ZFC curves (for samples containing goethite and titanomagnetite) nor a Morin transition (for samples containing hematite and titanomagnetite) are observed. However, after the efficient removal of titanomagnetite through extraction, both of these behaviors are readily observed

in their respective remainders. Similarly, XRD patterns (Fig. A.4) of remainders from trials employing goethite or hematite demonstrate detectable amounts of these minerals.

Broader impacts

The dissolution and flask extraction method described here improves on previous techniques for magnetic extraction from speleothems in two primary ways: 1) the mass of speleothem required has been reduced, and 2) the efficiency and reproducibility of extraction have been substantially improved.

Required sample mass is of particular importance in speleology, as speleothems are rare and irreplaceable. The need for dissolution of any speleothem sample is problematic, as this means that further studies on the bulk sample cannot be performed. By using the flask extraction method, we have reduced the required sample mass for dissolution from 60 g in Perkins,[6] 12 g used by Strauss et al.,[8] to < 10 g. This technique enables the study of smaller speleothems with higher spatial and temporal resolution, where earlier methods would have required complete dissolution.

The flask extraction method has higher reproducibility and recovery efficiency, representing substantial improvement upon previous extraction methods. Furthermore, the magnetic separation does not pull substantial amounts of weakly magnetic minerals from the insoluble mineral assembly while nearly all of the strongly magnetic material is collected. Magnetic extracts free of residue minerals are more readily characterized by microscopy, XRD, and magnetic methods. In addition, the shorter time required for extraction means that a greater diversity of samples can be characterized in a smaller time frame.

Efficient magnetic extraction from speleothems is a useful tool for addressing current questions regarding the respective origin, roles, and reliability of DRMs and CRMs in speleothems. Strauss et al. applied a preliminary version of the dissolution and flask extraction methods described in this study to natural stalagmite sample NC11-1 and extracted usable amounts of strongly magnetic minerals for electron microscopic analyses, finding evidence for the presence of magnetic minerals that could hold a DRM (e.g., magnetite and titanomagnetite grains with morphologies indicating physical transport).[8] However, the results of this study suggest that the majority of weakly magnetic minerals like goethite and hematite are left behind in the remainder, which is typically discarded and not analyzed. Thus, the remainder likely holds the greatest potential for the analysis of such weakly magnetic minerals and may be crucial to elucidating the process of CRM acquisition in stalagmites. We conclude that the magnetic extract and remainder should be analyzed in tandem. By way of example, characterization of the remainder from the flask extraction of sample NC11-1 (Fig. A.7) demonstrates the presence of goethite, which was difficult to detect in both the bulk sample[8] and the residue.

The application of the flask extraction method is not limited to the separation of magnetic minerals from speleothems, but extends to a broad list of materials, from pelagic limestones and dolostones to unlithified marine sediments to freshwater carbonates. For example, pelagic marine carbonates contain biogenic magnetic minerals that may provide clues to the types of ocean environments in which they were formed.[31] By magnetically separating the biogenic magnetic minerals from these sediments and analyzing by TEM, researchers have been able to interpret magnetic mineral morphologies as evidence of

certain magnetotactic bacteria, which may serve as a proxy for environmental conditions at time of deposition.[32–34] More specifically, studies of the magnetic mineral assemblages within carbonate-rich marine sediments across the ~ 55 Ma Paleocene–Eocene Thermal Maximum, one of the largest and least understood periods of climate variability, have been used to create environmental paleothermometers[35] and to infer a possible cometary impact as a trigger.[36] Application of an efficient extraction technique such as the flask extraction method would allow for more representative characterization of magnetic mineral assemblages, thereby providing a clearer picture of these environmental paleothermometers.

In addition, Roberts et al. described the complications of detecting goethite or hematite in marine sediments, as magnetite is the dominant magnetic mineral present and oftentimes dictates the magnetic properties detected.[33] Similarly, Channell et al. detected hematite in marine sediments by rock magnetic characterization but did not observe hematite in magnetic extracts collected by a peristaltic pump-driven magnetic extraction system.[34] The results described here suggest that these weaker magnetic minerals may be efficiently analyzed through the characterization of residue portions after primary extraction is complete.

The flask extraction method could also be used for magnetic separation from noncarbonate materials, enabling the collection of magnetic minerals for characterization in an extensive list of geological materials, including sands, soils, and other noncarbonate sediments. We therefore propose that this improved, highly efficient magnetic separation technique and additional characterization of remainders following magnetic extraction will

improve upon previous observations in a wide range of sediments. Future study includes an analysis of flask extraction efficiencies using these materials.

Acknowledgements

We acknowledge E. Calvin Alexander Jr. and Jennifer A. Soltis for providing samples for this research, and Mike J. Jackson for giving insight and advice. Thank you to Mark Bishop for providing access to the Niagara Cave sample. This research was supported by the John Wertz graduate fellowship in Chemistry (for Jennifer H. Strehlau), the Heisig/Gleysteen Chemistry Summer Research Program (for Lindsay A. Hegner), a Ralph W. Stone graduate fellowship from the National Speleological Society (for Becky E. Strauss), and National Science Foundation grants ECS-1012193 and EAR-1316385. Parts of this work were carried out in the Characterization Facility, University of Minnesota, which receives partial support from NSF through the MRSEC program. Magnetic measurements were conducted at the Institute for Rock Magnetism, University of Minnesota.

References

(1) Fairchild, I. J.; Baker, A. *Speleothem Science: From Process to Past Environments*; Wiley-Blackwell: Chichester, West Sussex, 2012.

(2) Lascu, I.; Feinberg, J. M. Speleothem magnetism. *Quat. Sci. Rev.* **2011**, *30*, 3306–3320.

(3) Fairchild, I. J.; Frisia, S.; Borsato, A.; Tooth, A. F. Speleothems. In *Geochemical Sediments and Landscapes*; Nash, D. J., McLaren, S. J., Eds.; Blackwells: Oxford, UK, 2007; pp 200–245.

(4) Bar-Matthews, M.; Matthews, A.; Ayalon, A. Environmental controls of speleothem mineralogy in a karstic dolomitic terrain (Soreq Cave, Israel). *J. Geol.* **1991**, *99*, 189–207.

(5) Essington, M. E. *Soil and Water Chemistry: An Integrative Approach*; CRC Press: Boca Raton, FL, 2004.

(6) Perkins, A. M. Observations under electron microscopy of magnetic minerals extracted from speleothems. *Earth Planet. Sci. Let.* **1996**, *139*, 281–289.

(7) Rusanov, V.; Gilson, R. G.; Lougear, A.; Trautwein, A. X. Mössbauer, magnetic, X-ray fluorescence and transmission electron microscopy study of natural magnetic materials from speleothems: haematite and the Morin transition. *Hyperfine Interact.* **2000**, *128*, 353–373.

(8) Strauss, B. E.; Strehlau, J. H.; Lascu, I.; Dorale, J. A.; Penn, R. L.; Feinberg, J. M. The origin of magnetic remanence in stalagmites: observations from electron microscopy and rock magnetism. *Geochem., Geophys. Geosyst.* **2013**, *14*, 5006–5025.

(9) Latham, A. G.; Schwarcz, H. P.; Ford, D. C.; Pearce, G. W. Paleomagnetism of stalagmite deposits. *Nature* **1979**, *280*, 383–385.

(10) Latham, A. G.; Schwarcz, H. P.; Ford, D. C. The paleomagnetism and U-Th dating of Mexican stalagmite, DAS2. *Earth Planet. Sci. Let.* **1986**, *79*, 195–207.

(11) Latham, A. G. Paleomagnetism, rock magnetism and U-Th dating of speleothem deposits, Ph.D. thesis, Dep. of Geology, McMaster Univ., Hamilton, Ontario, Canada, 1981.

(12) Morinaga, H.; Inokuchi, H.; Yaskawa, K. Magnetization of a stalagmite in Akiyoshi Plateau as a record of the geomagnetic secular variation in West Japan. *J. Geomag. Geoelectr.* **1986**, *38*, 27–44.

(13) Herries, A. I. R.; Adams, J. W.; Kuykendall, K. L.; Shaw, J. Speleology and magnetobiostratigraphic chronology of the GD 2 locality of the Gondolin hominin-bearing paleocave deposits, North West Province, South Africa. *J. Hum. Evol.* **2006**, *51* (6), 617–631.

(14) Dreybrodt, W.; Romanov, D. Regular stalagmites: The theory behind their shape. *Acta Carsol.* **2008**, *37*, 175–184.

(15) Frisia, S.; Borsato, A.; Fairchild, I. J.; McDermott, F. Calcite fabrics, growth mechanisms, and environments of formation in speleothems from the Italian Alps and Southwestern Ireland. *J. Sediment. Res.* **2000**, *70*, 1183–1196.

(16) Latham, A. G.; Ford, D. C.; Schwarcz, H. P.; Birchall, T. Secular variation from Mexican stalagmites: their potential and problems. *Phys. Earth Planet. Inter.* **1989**, *56*, 34–48.

(17) Hounslow, M. W.; Maher, B. a. Quantitative extraction and analysis of carriers of magnetization in sediments. *Geophys. J. Int.* **1996**, *124* (1), 57–74.

(18) Israde-Alcántara, I.; Bischoff, J. L.; Domínguez-Vázquez, G.; Li, H.-C.; DeCarli, P. S.; Bunch, T. E.; Wittke, J. H.; Weaver, J. C.; Firestone, R. B.; West, A.; et al. Evidence from central Mexico supporting the Younger Dryas extraterrestrial impact hypothesis. *PNAS, Early Ed.* **2012**, *109* (13), E738–E747.

(19) Schwertmann, U.; Cornell, R. M. *Iron Oxides in the Laboratory*, 2nd ed.; Wiley-VCH: Weinheim, 2000.

(20) Mazeina, L.; Navrotsky, A. Surface enthalpy of goethite. *Clays Clay Miner.* **2005**, *53*, 113–122.

(21) Wray, J. L.; Daniels, F. Precipitation of calcite and aragonite. *J. Am. Chem. Soc.* **1957**, *79*, 2031–2034.

(22) Bretz, J. H. Caves in the Galena formation. *J. Geol.* **1938**, *46*, 828–841.

(23) Stookey, L. L. Ferrozine – a new spectrophotometric reagent for iron. *Anal. Chem.* **1970**, *42*, 779–781.

(24) Reynolds, R. L.; Sweetkind, D. S.; Axford, Y. *An inexpensive magnetic mineral separator for fine-grained sediment*; Denver, 2001.

(25) Peterson, N.; von Dobeneck, T.; Vali, H. Fossil bacterial magnetite in deep-sea sediments from the South Atlantic Ocean. *Nature* **1986**, *320* (17), 611–615.

(26) Dasgupta, S.; Saar, M. O.; Edwards, R. L.; Shen, C.-C.; Cheng, H.; Alexander Jr., E. C. Three thousand years of extreme rainfall events recorded in stalagmites from Spring Valley Caverns, Minnesota. *Earth Planet. Sci. Let.* **2010**, *300*, 46–54.

(27) Özdemir, Ö.; Dunlop, D. J.; Moskowitz, B. M. Changes in remanence, coercivity and domain state at low temperature in magnetite. *Earth Planet. Sci. Let.* **2002**, *194*, 343–358.

(28) Zysler, R.; Fiorani, D.; Testa, A.; Suber, L.; Agostinelli, E.; Godinho, M. Size dependence of the spin-flop transition in hematite nanoparticles. *Phys. Rev. B* **2003**, *68*, 212408.

(29) Sutheimer, S. H.; Maurice, P. A.; Zhou, Q. Dissolution of well and poorly crystallized kaolinites: Al speciation and effects of surface characteristics. *Am. Mineral.* **1999**, *84*, 620–628.

(30) Sun, W. W.; Kodama, K. P. Magnetic anisotropy, scanning electron microscopy, and X ray pole figure goniometry study of inclination shallowing in a compacting clay-rich sediment. *J. Geophys. Res.* **1992**, *97*, 19599–19615.

(31) Roberts, A. P.; Florindo, F.; Chang, L.; Heslop, D.; Jovane, L.; Larrasoaña, J. C. Magnetic properties of pelagic marine carbonates. *Earth-Sci. Rev.* **2013**, *127*, 111–139.

(32) Chang, L.; Roberts, A. P.; Williams, W.; Fitz Gerald, J. D.; Larrasoaña, J. C.; Jovane, L.; Muxworthy, A. R. Giant magnetofossils and hyperthermal events. *Earth Planet. Sci. Let.* **2012**, *351-352*, 258–269.

(33) Roberts, A. P.; Chang, L.; Heslop, D.; Florindo, F.; Larrasoaña, J. C. Searching for single domain magnetite in the “pseudo-single-domain” sedimentary haystack: Implications of biogenic magnetite preservation for sediment magnetism and

relative paleointensity determinations. *J. Geophys. Res.* **2012**, *117*, B08104.

(34) Channell, J. E. T.; Hodell, D. A.; Margari, V.; Skinner, L. C.; Tzedakis, P. C.; Kesler, M. S. Biogenic magnetite, detrital hematite, and relative paleointensity in Quaternary sediments from the Southwest Iberian Margin. *Earth Planet. Sci. Let.* **2013**, *376*, 99–109.

(35) Schumann, D.; Raub, T. D.; Kopp, R. E.; Guerquin-Kern, J.-L.; Wu, T.-D.; Rouiller, I.; Smirnov, A. V; Sears, S. K.; Lücken, U.; Tikoo, S. M.; et al. Gigantism in unique biogenic magnetite at the Paleocene-Eocene Thermal Maximum. *Proc. Natl. Acad. Sci. U. S. A.* **2008**, *105* (46), 17648–17653.

(36) Kent, D. V.; Cramer, B. S.; Lanci, L.; Wang, D.; Wright, J. D.; Van der Voo, R. A case for a comet impact trigger for the Paleocene/Eocene thermal maximum and carbon isotope excursion. *Earth Planet. Sci. Lett.* **2003**, *211*, 13–26.

Supporting Information

Standard Minerals & Synthetic Procedures

Magnetic mineral standards were either purchased or synthesized, including titanomagnetite, magnetite, goethite and hematite, and are described in detail below. Solutions and suspensions in syntheses were prepared using Milli-Q water (Millipore, 18.2 MΩ·cm) in glassware that was soaked in a 0.1 M oxalic acid bath at pH 3.5 for 2 days. Chemicals for syntheses were purchased from Fisher Scientific and of anhydrous, ACS grade unless otherwise noted.

Submillimeter titanomagnetite grains were acquired from Gold-Nugget Designs, a private supplier. The purchased magnetic grains originated from a beach sand enriched in magnetite near Otter Point State Recreation Site, Oregon, approximately four miles north of Gold Beach, Oregon, U.S.A. The supplier extracted the strongly magnetic grains seven consecutive times by using a rare-earth magnet to reduce the nonmagnetic concentration.

Nanoscale magnetite particles were synthesized by partial oxidation of an Fe(II) solution, described by Schwertmann and Cornell (2000). In a 500 mL separation flask, 280 mL of 0.51 M $FeSO_4 \cdot 7H_2O$ was heated to 90 °C using a water bath under constant flow of N_2 (Matheson, UHP). In a separate beaker, 120 mL of a solution containing 0.27 M KNO_3 and 2.92 M KOH was prepared and deoxygenated for 30 min with N_2. The hydroxide solution was added dropwise to the Fe(II) solution over 45 min, resulting in a black precipitate. The black suspension was then heated at 90 °C for 45 min under N_2, cooled to room temperature, transferred to centrifuge tubes and centrifuged at 8200 g for 2 min using an Eppendorf 5804 centrifuge. The supernatant was discarded and the particles were washed three times with Milli-Q water and dried in an anaerobic chamber under 95% N_2/5% H_2. Once dried, the particles were removed from the chamber and stored at room temperature in aerobic conditions.

Large goethite nanorods were synthesized using the method of Mazeina and Navrotsky (2005). Using a peristaltic pump, 500 mL of 2.5 M KOH was added to 120 mL of 0.5 M $Fe(NO_3)_3 \cdot 9H_2O$ at a rate of approximately 20 mL/min with stirring. The resulting dark brown precipitate was aged at 60 °C for 100 hr, then transferred to dialysis tubing and submerged in 2 L Milli-Q water. Dialysis water was changed three times per day with a minimum of three hours in between changes. After three days, the particle suspension was moved to a Nalgene bottle, diluted and stored in a refrigerator. Suspension of known mass loading was volumetrically delivered into extraction flasks, or air-dried particles were directly massed into standard mixtures.

Hematite nanoparticles were synthesized by the method of Schwertmann & Cornell (2000). While stirring, 60 mL of 1 M KOH was added quickly to 100 mL of 0.2 M $Fe(NO_3)_3 \cdot 9H_2O$, followed by a dilution with 40 mL Milli-Q water. The brown suspension was stirred for 20 sec, then 57 mg of oxalic acid ($C_2H_2O_4 \cdot 2H_2O$) was added. After an additional 5 min of stirring, the suspension was transferred to dialysis tubing and dialyzed in 2 L Milli-Q water. Following the dialysis procedure employed with the above goethite particles, the suspension was aged in a Nalgene bottle at 90 °C for 29 hr to form hematite and stored likewise to the goethite.

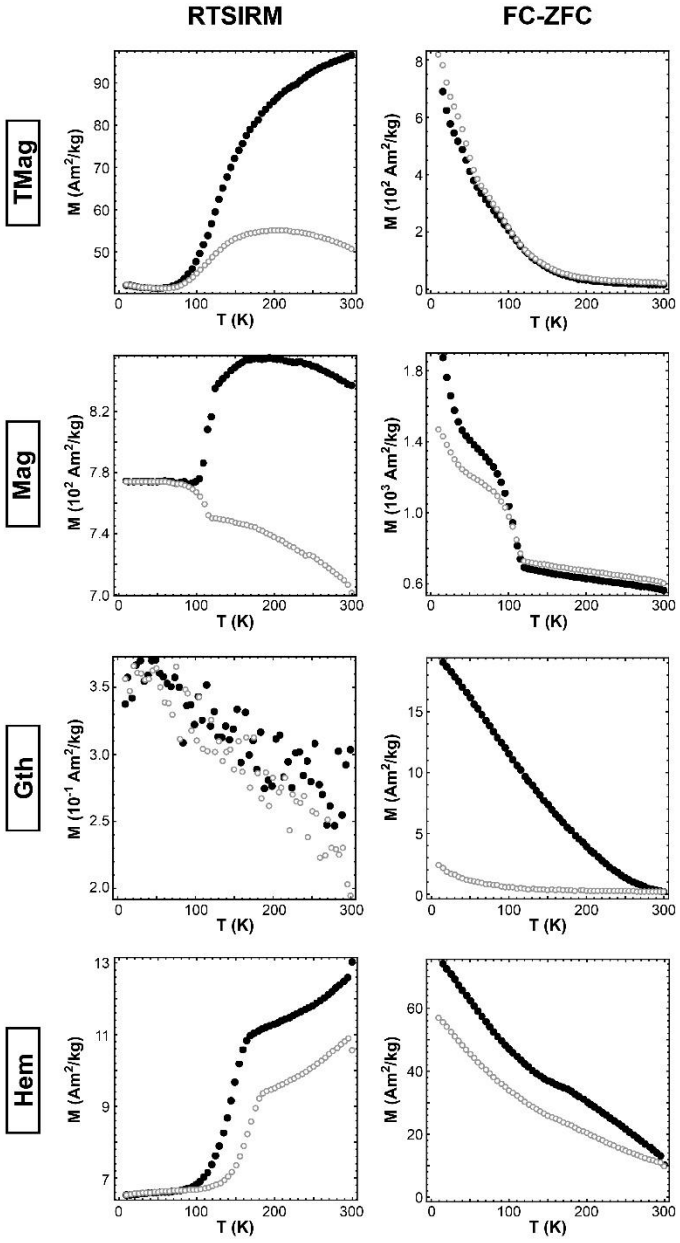

Figure A.8: Low-temperature magnetic characterization of magnetic standards titanomagnetite (TMag), magnetite (Mag), goethite (Gth), and hematite (Hem) collected by MPMS. RT-SIRM measurments (filled black circles on cooling, open gray circles on warming) at left and FC-ZFC measurements (filled black circles on FC, open gray circles on ZFC) on right.

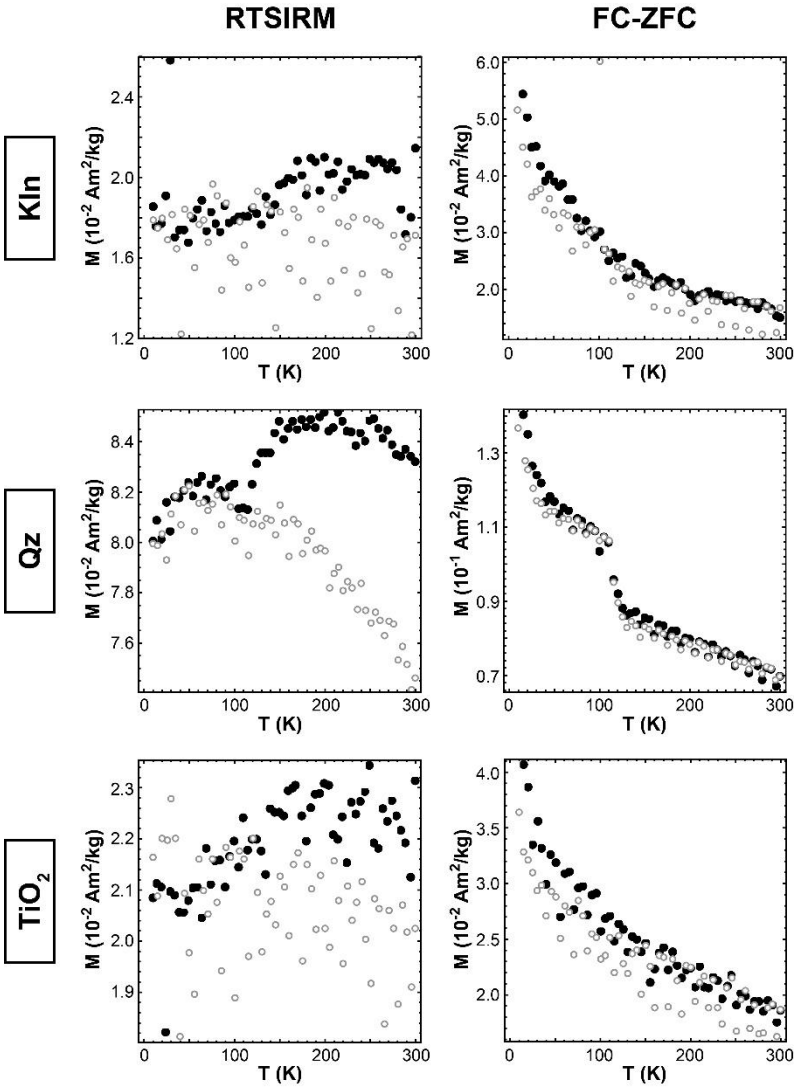

Figure A.9: Low-temperature magnetic characterization of residue standards kaolinite (Kln), quartz (Qz) and TiO_2 collected by MPMS, including RT-SIRM measurments (filled black circles on cooling, open gray circles on warming) at left and FC-ZFC measurements (filled black circles on FC, open gray circles on ZFC) on right.

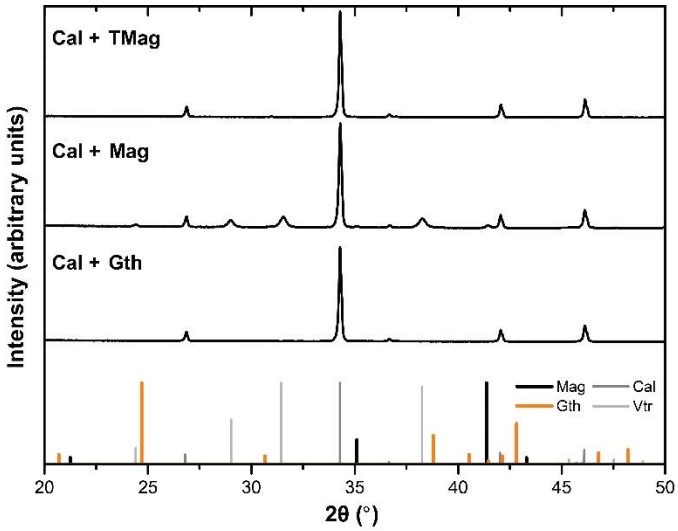

Figure A.10: XRD patterns of synthetic calcite (Cal) crystallized in the presence of ~2% w/w titanomagnetite (TMag), magnetite (Mag), or goethite (Gth). Vaterite (Vtr, $CaCO_3$ polymorph) seen in the magnetite-synthetic calcite sample is a result of drying at room temperature conditions (Wray and Daniels 1957).

Table A.4: Data of flask extraction trials using TMag, Mag or both with and without surfactant (corresponds to manuscript Table 1).

Trial	Description	$Na(PO_4)_3$	Tmag (g)	Mag (g)	Total (g)	K (g)	Q (g)	T (g)	Water (mL)	Extract (g)	Recovery (%)
1	TMag	N	0.0068	0	0.0068	0	0	0	30	0.0064	94
2	TMag	N	0.0076	0	0.0076	0	0	0	30	0.0078	103
3	TMag	N	0.0051	0	0.0051	0	0	0	30	0.0051	100
										Average	**99**
										St. Dev.	**4**
1	Tmag + surf	Y	0.0053	0	0.0053	0	0	0	30	0.0046	87
2	Tmag + surf	Y	0.0069	0	0.0069	0	0	0	30	0.007	101
3	Tmag + surf	Y	0.0068	0	0.0068	0	0	0	30	0.0072	106
										Average	**98**
										St. Dev.	**10**
1	Mag	N	0	0.0053	0.0053	0	0	0	30	0.0052	98
2	Mag	N	0	0.0086	0.0086	0	0	0	30	0.0086	100
3	Mag	N	0	0.0072	0.0072	0	0	0	30	0.0074	103
										Average	**100**
										St. Dev.	**2**
1	Mag + surf	Y	0	0.0052	0.0052	0	0	0	30	0.0045	87
2	Mag + surf	Y	0	0.0096	0.0096	0	0	0	30	0.0095	99
3	Mag + surf	Y	0	0.0055	0.0055	0	0	0	30	0.0057	104
										Average	**96**
										St. Dev.	**9**
1	TMag + Mag	N	0.0057	0.0058	0.0115	0	0	0	30	0.0112	97
2	TMag + Mag	N	0.0073	0.0058	0.0131	0	0	0	30	0.0122	93
3	TMag + Mag	N	0.004	0.0054	0.0094	0	0	0	30	0.0093	99
										Average	**96**
										St. Dev.	**3**
1	TMag + Mag + surf	Y	0.0052	0.0067	0.0119	0	0	0	30	0.0117	98
2	TMag + Mag + surf	Y	0.0057	0.0061	0.0118	0	0	0	30	0.0104	88
3	TMag + Mag + surf	Y	0.0059	0.0071	0.0130	0	0	0	30	0.013	100
										Average	**95**
										St. Dev.	**6**

Table A.5: Data of flask extraction trials using TMag, Mag or both with KQT and with/without surfactant (corresponds to manuscript Table 1).

Trial	Description	$Na(PO_4)_3$	Tmag (g)	Mag (g)	Total (g)	K (g)	Q (g)	T (g)	Water (mL)	Extract (g)	Recovery (%)
1	Tmag + KQT	N	0.0050	0	0.0050	0.2583	0.2965	0.0052	30	0.0047	94
2	Tmag + KQT	N	0.0048	0	0.0048	0.2474	0.2863	0.0061	30	0.005	104
3	Tmag + KQT	N	0.0088	0	0.0088	0.2503	0.2508	0.0037	30	0.0087	99
										Average	**99**
										St. Dev.	**5**
4	TMag Large Amount + KQT	N	0.1601	0	0.1601	0.2797	0.2824	0.0091	30	0.1548	97
1	Tmag + KQT + surf	Y	0.0059	0	0.0059	0.2559	0.2488	0.0039	30	0.0051	86
2	Tmag + KQT + surf	Y	0.0071	0	0.0071	0.3315	0.2909	0.004	30	0.007	99
3	Tmag + KQT + surf	Y	0.0082	0	0.0082	0.2798	0.2523	0.0053	30	0.0076	93
										Average	**93**
										St. Dev.	**6**
1	Mag + KQT	N	0	0.0049	0.0049	0.2700	0.2428	0.0061	30	0.0036	73
2	Mag + KQT	N	0	0.0052	0.0052	0.2042	0.2803	0.0046	30	0.0056	108
3	Mag + KQT	N	0	0.0089	0.0089	0.3497	0.3127	0.006	30	0.0092	103
										Average	**95**
										St. Dev.	**19**
4	Mag Large Amount + KQT	N	0	0.1456	0.1456	0.2564	0.1994	0.0064	30	0.1454	100
1	Mag + KQT + surf	Y	0	0.0057	0.0057	0.2627	0.2689	0.0028	30	0.0052	91
2	Mag + KQT + surf	Y	0	0.0083	0.0083	0.2318	0.2954	0.0088	30	0.0092	111
3	Mag + KQT + surf	Y	0	0.0076	0.0076	0.2265	0.3064	0.0081	30	0.0085	112
										Average	**105**
										St. Dev.	**12**
1	TMag + Mag + KQT	N	0.0086	0.0074	0.0160	0.2913	0.3139	0.0039	30	0.0153	96
2	TMag + Mag + KQT	N	0.0078	0.0086	0.0164	0.2174	0.3387	0.0047	30	0.0161	98
3	TMag + Mag + KQT	N	0.0043	0.0045	0.0088	0.2275	0.2981	0.004	30	0.009	102
										Average	**99**
										St. Dev.	**3**
1	TMag + Mag + KQT + surf	Y	0.0079	0.0045	0.0124	0.2953	0.3637	0.0044	30	0.0128	103
2	TMag + Mag + KQT + surf	Y	0.0054	0.0075	0.0129	0.3106	0.2914	0.0067	30	0.0131	102
3	TMag + Mag + KQT + surf	Y	0.0045	0.0082	0.0127	0.3739	0.2772	0.0058	30	0.0127	100
										Average	**102**
										St. Dev.	**2**

Table A.6: Data of flask, pump and bag extraction trials using TMag, Gth and KQT with and without surfactant (corresponds to manuscript Table A.2).

Trial	Description	$Na(PO_4)_3$	Tmag (g)	Gth (g)	K (g)	Q (g)	T (g)	Water (mL)	Extract (g)	Recovery (%)
	FLASK									
1	Tmag + Gth + KQT	N	0.0042	0.01	0.3834	0.3054	0.0043	30	0.0041	98
2	Tmag + Gth + KQT	N	0.006	0.01	0.2546	0.2888	0.0096	30	0.0056	93
3	Tmag + Gth + KQT	N	0.0068	0.01	0.2577	0.2935	0.0087	30	0.0065	96
									Average	**96**
									St. Dev.	**2**
1	Tmag + Gth + KQT + surf	Y	0.0042	0.01	0.2928	0.2689	0.0062	30	0.0044	105
2	Tmag + Gth + KQT + surf	Y	0.0055	0.01	0.2477	0.3386	0.0063	30	0.0052	95
3	Tmag + Gth + KQT + surf	Y	0.0069	0.01	0.288	0.279	0.0053	30	0.0068	99
									Average	**99**
									St. Dev.	**5**
	PUMP									
1	Tmag + Gth + KQT	N	0.0084	0.01	0.3436	0.3218	0.0063	210	0.0096	114
2	Tmag + Gth + KQT	N	0.0060	0.01	0.3151	0.3444	0.0044	210	0.0040	67
3	Tmag + Gth + KQT	N	0.0071	0.01	0.3007	0.2625	0.0078	210	0.0042	59
									Average	**80**
									St. Dev.	**30**
1	Tmag + Gth + KQT + surf	Y	0.0084	0.01	0.3435	0.3491	0.0071	210	0.0061	73
2	Tmag + Gth + KQT + surf	Y	0.0052	0.01	0.3553	0.3208	0.0049	210	0.0048	92
3	Tmag + Gth + KQT + surf	Y	0.0059	0.01	0.2489	0.3015	0.0054	210	0.0058	98
									Average	**88**
									St. Dev.	**13**
	BAG									
1	Tmag + Gth + KQT	N	0.0045	0.01	0.3291	0.3202	0.0040	20	0.0049	109
2	Tmag + Gth + KQT	N	0.0043	0.01	0.3025	0.3033	0.0038	20	0.0037	86
3	Tmag + Gth + KQT	N	0.0079	0.01	0.3296	0.2956	0.0033	20	0.0070	89
									Average	**101**
									St. Dev.	**24**
1	Tmag + Gth + KQT + surf	Y	0.0047	0.01	0.3375	0.3345	0.0038	20	0.0058	123
2	Tmag + Gth + KQT + surf	Y	0.0054	0.01	0.3125	0.3049	0.0059	20	0.0042	78
3	Tmag + Gth + KQT + surf	Y	0.0079	0.01	0.3572	0.3033	0.0050	20	0.0058	73
									Average	**92**
									St. Dev.	**28**

Appendix B. Supporting information for Chapter 2

Section B.1: Additional experimental methods

SRNOM was purchased from the International Humic Substance Society (IHSS). Acetonitrile (HPLC grade), $FeCl_2 \cdot 4H_2O$, methanol (HPLC grade), and NaOH were purchased from Fisher, $NaHCO_3$ from Sigma Aldrich, ferrozine from Alfa Aesar, 4-ClNB from Acros, NH_4CH_3COO and H_2SO_4 from Mallinckrodt, and HCl from BDH Aristar. All aqueous experiments were performed in carbonate buffer (10 mM, pH 7.0), anaerobically prepared by adding $NaHCO_3$ to deoxygenated ultrapure (18.2 MΩ·cm, Milli-Q) water and adjusting pH with 1 M H_2SO_4. The stock Fe(II) solution was prepared by adding ~ 0.23 g $FeCl_2 \cdot 4H_2O$ to 0.2 mL of 1 M HCl and the appropriate amount of ultrapure water so that the final concentration was 175 mM. This stock solution was remade every seven days. For Fe(II) concentration analyses, a 5 mg/mL ferrozine stock in ultrapure water was prepared.

An Agilent 1100 Series system and ultraviolet detector was used to quantify 4-ClNB concentration. Each sample (20 μL) was injected into the system, equipped with a Zorbax SB-C18 column (4.6 × 150 mm, 5 μm) and set to measure absorbance at 254 nm. The mobile phase (0.7 mL/min) was 70 : 30 acetonitrile : 1 g/L ammonium acetate at pH 7.

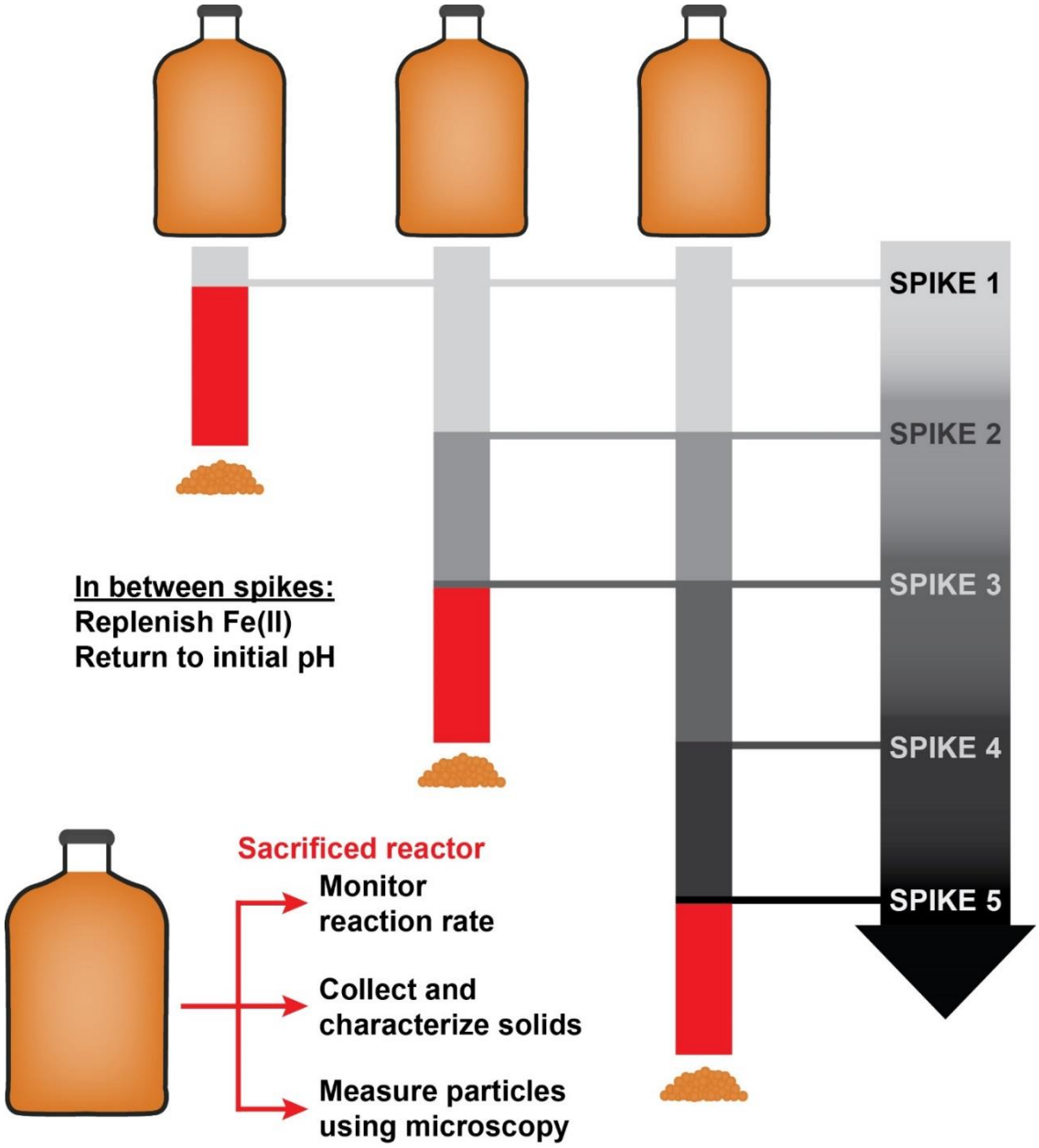

Figure B.1: Flowchart for the sequential-spike batch reactors. Adjustments to initial conditions included 1) quantifying $[Fe(II)_{aq}]$ with ferrozine analysis, 2) adjusting pH to 7 (or 6.5) with 0.5 M NaOH, 3) adding Fe(II) stock solution so that $[Fe(II)_{aq}] = 1$ (or 0.5 mM), and 4) equilibrating 21 – 24 h before initiating the next 4-ClNB spike.

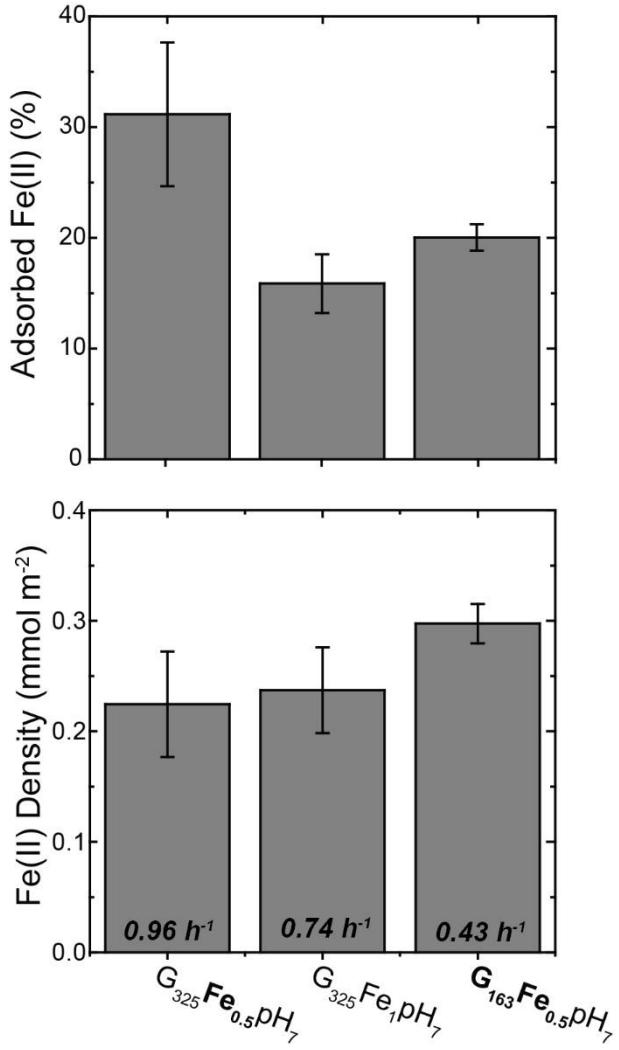

Figure B.2: Percent adsorbed Fe(II) and Fe(II) density on goethite after 21 hours of equilibration for samples with adjusted goethite mass loading and Fe(II) concentration. Initial conditions: $G_{325}Fe_1pH_7$ = 0.325 g/L goethite, 1 mM Fe(II); $\mathbf{G_{163}Fe_{0.5}}pH_7$ = 0.163 g/L goethite, 0.5 mM Fe(II); $G_{325}\mathbf{Fe_{0.5}}pH_7$ = 0.325 g/L goethite, 0.5 mM Fe(II). Reported are the averages and standard deviations of triplicate trials. Numerical values in bold italics are the k_{obs} values for each reaction condition.

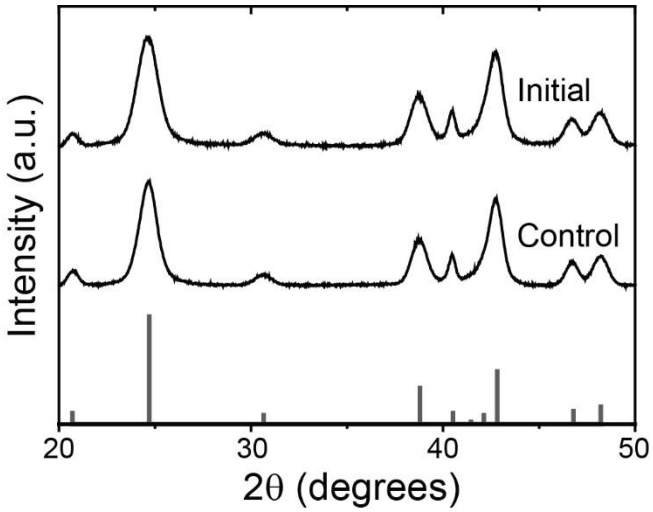

Figure B.3. XRD patterns of the initial nanoparticles and goethite after 18 days of stirring in buffer with 1 mM Fe(II) (control). Powder diffraction file for goethite = #029-0713, straight lines.

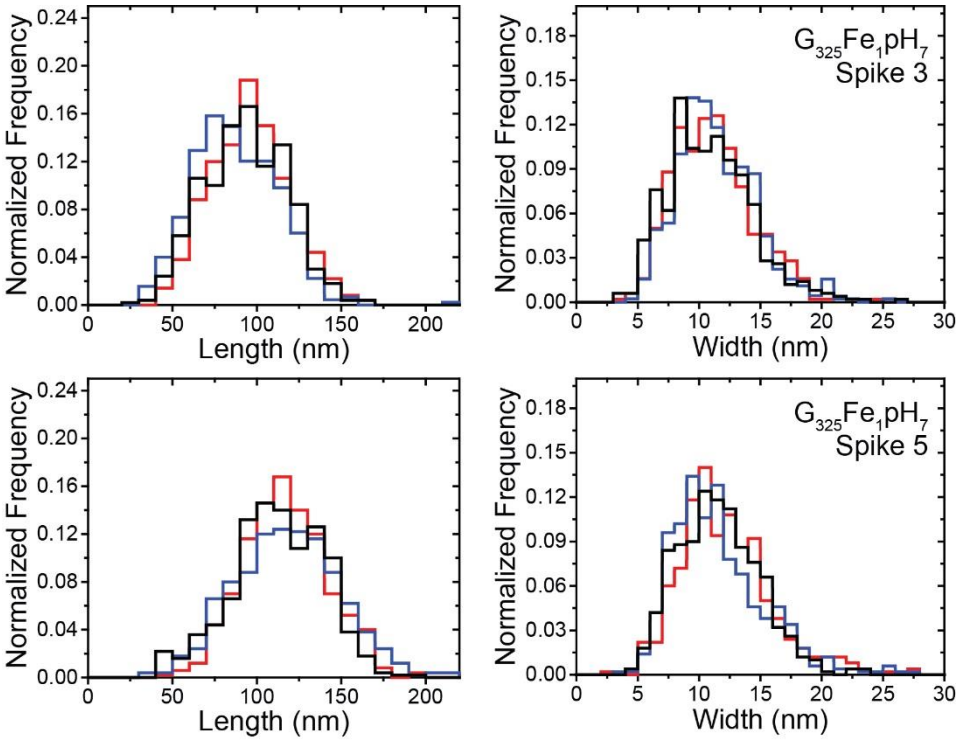

Figure B.4. Measurements from triplicate trials for $G_{325}Fe_1pH_7$ after three (top row) or five (bottom row) spikes of 4-ClNB.

Table B.1. Uncertainties of particle measurements taken 20 times on separate days.

	Length Uncertainty	**Width Uncertainty**
Mean (pixels)	**1.3**	**1.1**
Mean (nm)	**0.8**	**0.7**
Max (nm)	1.2	0.9
Min (nm)	0.4	0.5

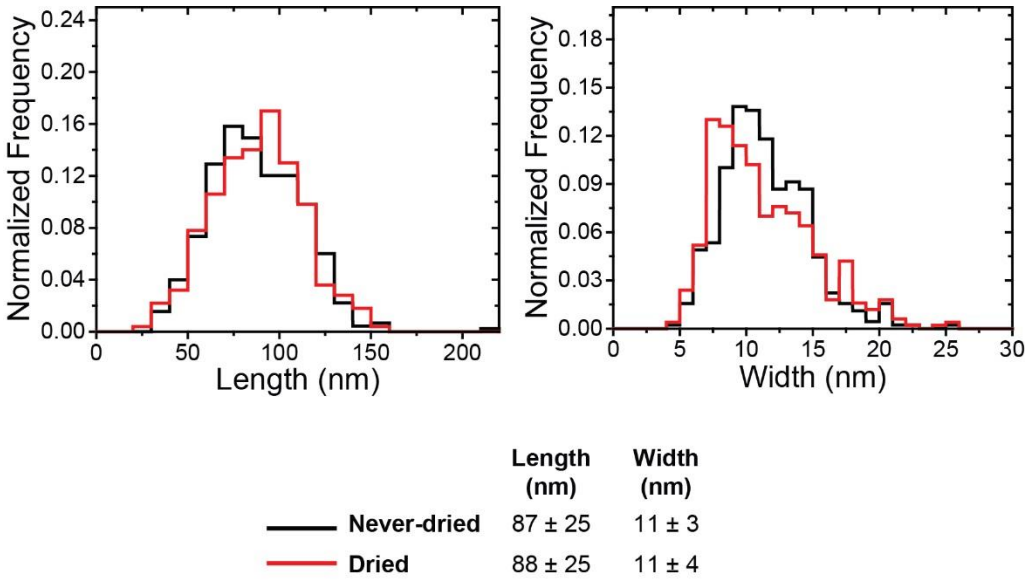

Figure B.5. Histograms of length and width measurements of the same sample ($G_{325}Fe_1pH_7$) prepped for TEM by either sampling directly from the reactor and diluting (never-dried, black line) or resuspending dried particles and sonicating (dried, red line).

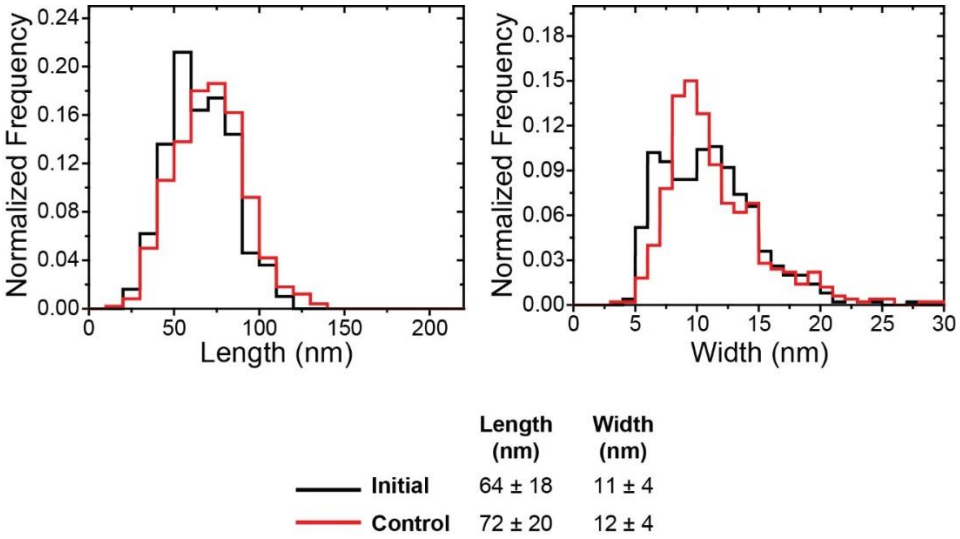

Figure B.6. Histograms of length and width measurements of the initial nanoparticles (black line) and goethite after 18 days of stirring in buffer with 1 mM Fe(II) (control, red line).

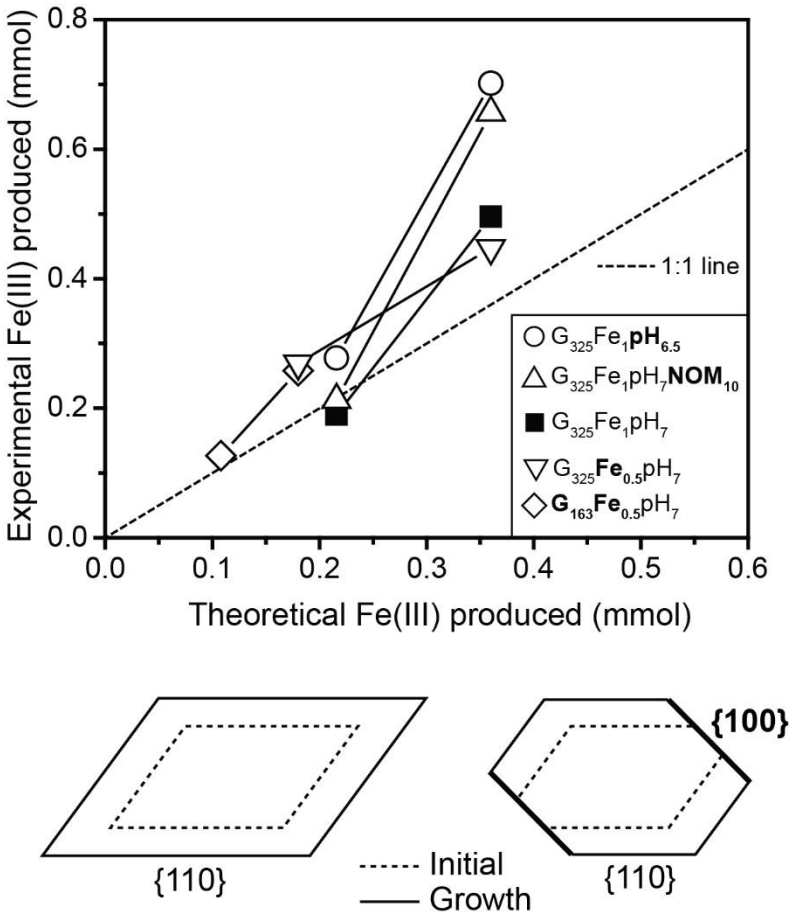

Figure B.7. Experimental Fe(III) produced compared to theoretical values calculated from reaction stoichiometry. Experimental Fe(III) was estimated by calculating the volume of new goethite growth given the average length and width measurements of particles (listed in Table 2.2). A cross-sectional rhombus composed of {110} faces was assumed, as in the previous work of Anschutz and Penn (2005). A density of 4.26 g/cm^3 (Cornell and Schwertmann, 2003) was used for goethite. Conditions that resulted in wider particles (pH 6.5 and added SRNOM) have overestimates of produced Fe(III), indicating that the {100} faces are less reactive and thus would contribute more surface area with continued reaction (as demonstrated by the schematic).

Appendix C. Supporting information for Chapter 3

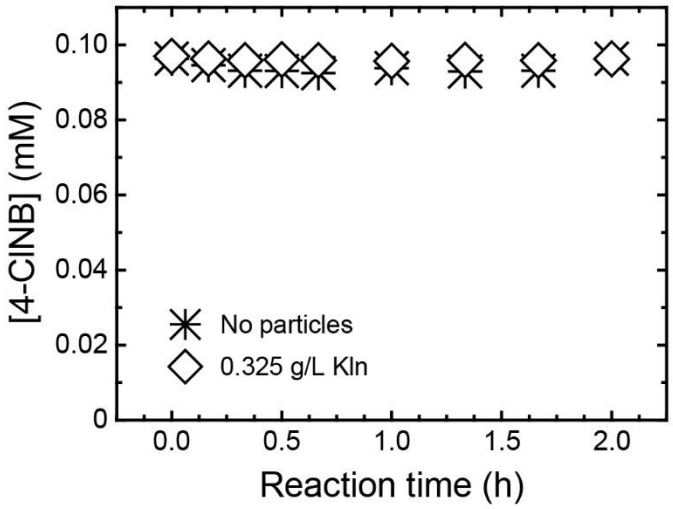

Figure C.1: Reduction of 4-ClNB in reactors containing Fe(II) and no particles or Fe(II) and 0.325 g/L kaolinite, demonstrating undetectable reaction and minimal adsorption of 4-ClNB on kaolinite.

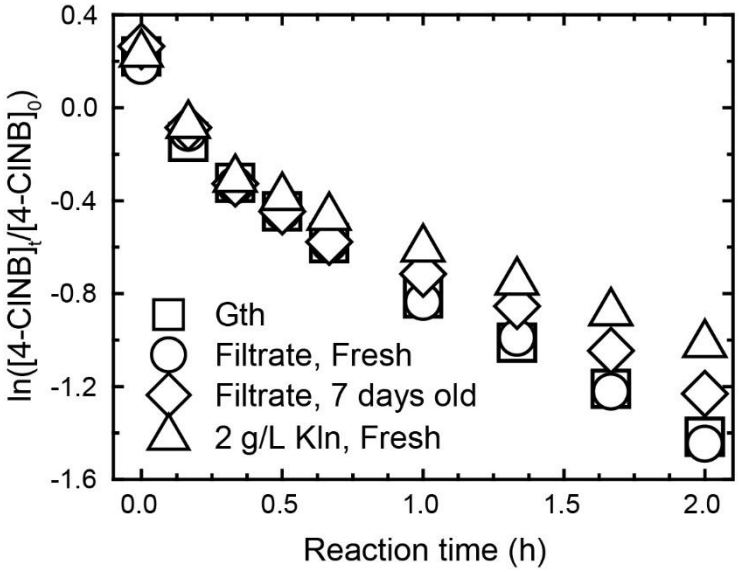

Figure C.2: Reduction of 4-ClNB in reactors 0.325 g/L goethite and equivalent volume of kaolinite stock solution filtrate freshly prepared or after 7 days of equilibration. Data from goethite only (black squares) and goethite with 2 g/L kaolinite (blue triangles) are replicated from Figure 3.1 for easier comparison here.

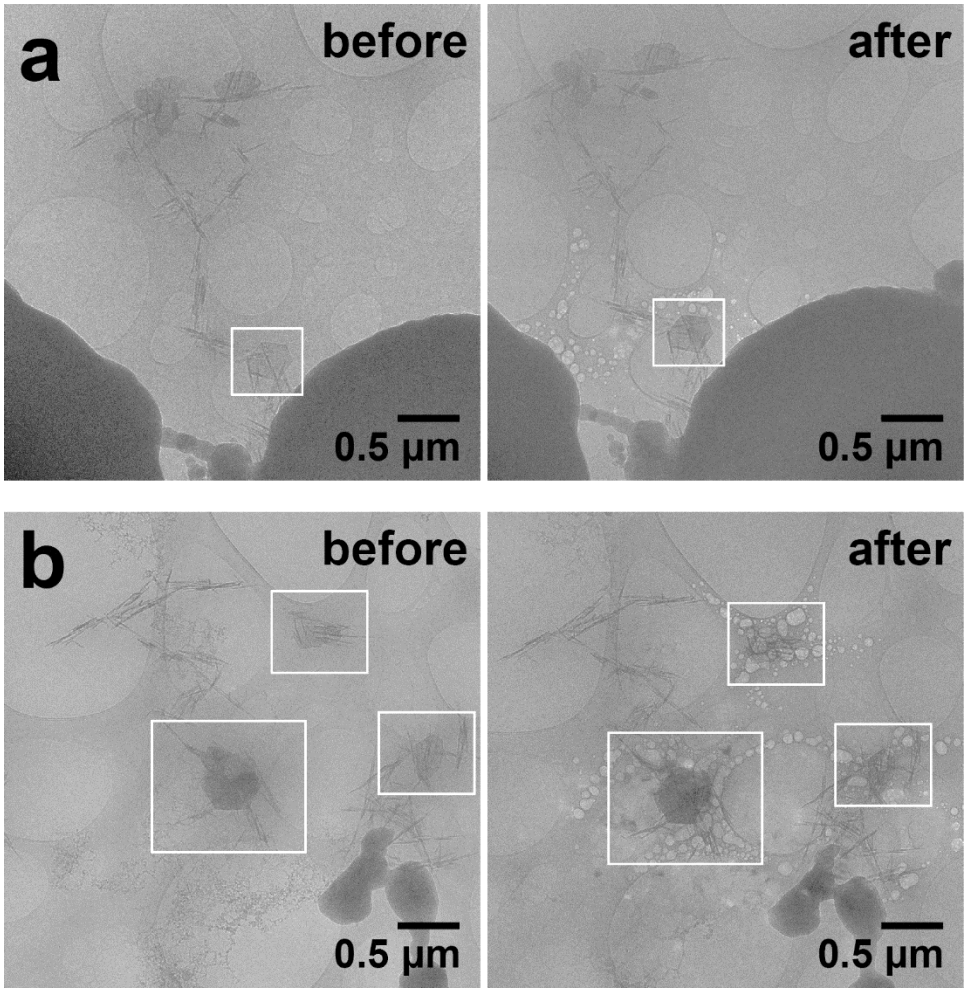

Figure C.3: Cryo-TEM images of two goethite-kaolinite aggregates in suspensions containing 0.325 g/L Gth and 2 g/L Kln. Images taken before (a,c) and after (b,d) 1 min of electron beam exposure, demonstrating that the hexagonal shaped particles are kaolinite as opposed to ice or other artifacts of cryo-imaging.

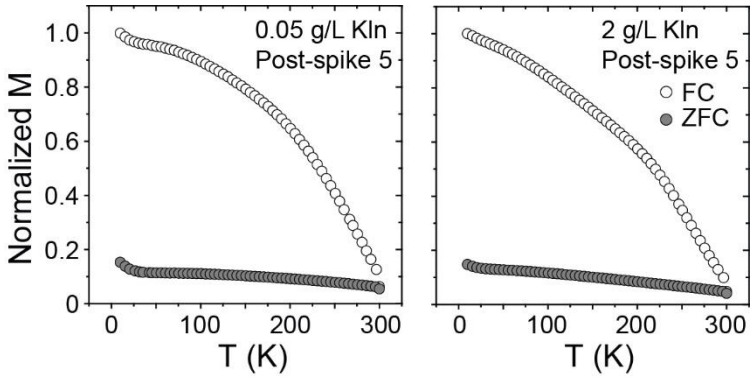

Figure C.4: Low-temperature magnetic characterization of post-reaction solids from 0.325 g/L goethite and either 0.05 or 2 g/L kaolinite in 10 mM carbonate buffer at pH 7 with [Fe(II)]*i* = 1 mM after five spikes of 4-ClNB. FC = field cooled. ZFC = zero-field cooled. Magnetization normalized to the maximum of the FC curve for each sample. Both samples demonstrated magnetic properties characteristic of only goethite.

Table C.1: Concentrations of Si and Al in filtrates and goethite as analyzed by ICP-OES. Goethite was 0.325 g/L for all cases. Control experiment was goethite and 1 mM Fe(II) equilibrating in buffer for 18 days. Dialysis experiment was goethite and 1 mM Fe(II) equilibrating in buffer for 18 days in the presence of a dialysis membrane filled with equivalent 2 g/L kaolinite. Goethite analyzed for the dialysis experiment did not come into direct contact with kaolinite solids.

Filtrates

Kaolinite (g/L)	**Stage**	**Equilibration (d)**	**[Si] (ppm)**	**[Al] (ppm)**
0	Control	18	3.0	0.06
0.05	Spike 1	1	0.5	0
0.05	Spike 5	18	3.0	0.04
2	Dialysis	18	4.8	0.08
2	Spike 1	1	3.2	0
2	Spike 5	30	6.3	0.05

Goethite after 18 days equilibration

Kaolinite (g/L)	**Stage**	**Equilibration (d)**	**[Si] (wt%)**	**[Al] (wt%)**
0	Control	18	0.2	0
2	Dialysis	18	0.6	0.2

Appendix D. Supporting information for Chapter 5

Section D.1. Materials

All glassware, Nalgene bottles, and Teflon coated magnetic stir bars were soaked in 0.1 M oxalic acid at pH 3.5 for two days and rinsed with Milli-Q water prior to use. All solutions were made using ultrapure Milli-Q water (18.2 MΩ·cm). $Fe(NO_3)_3 \cdot 9H_2O$ (ACS grade), $FeCl_3 \cdot 6H_2O$ (ACS grade), $FeCl_2 \cdot 4H_2O$ (>99%), and NaOH (50% w/w) were purchased from Fisher. $CaCl_2 \cdot 2H_2O$ (ACS grade) was purchased from Macron. Ferrozine (B-(2-pyridyl)-5,6-bis(4-sulfophenyl)-1,2,4-triazine disodium salt hydrate, >98%) was purchased from TCI. Concentrated HCl was purchased from Aristar, and glacial acetic acid (ACS grade) was purchased from BDH. 1,4-Benzoquinone (>99%) was purchased from Acros. $NaHCO_3$ (ACS grade), hydroquinone (>99%) and acetonitrile (CHROMASOLV grade) were purchased from Sigma. Benzoquinone, hydroquinone, and $FeCl_2 \cdot 4H_2O$ were all stored anaerobically. Norm-Ject Tuberkulin 1 mL plastic syringes

and Pall Acrodisc 13 mm syringe filters with 0.2 μm Nylon membrane were used for sampling and filtering particle suspensions. Anaerobic experiments were conducted in a Coy anaerobic chamber (95% N_2/5% H_2, Matheson).

Section D.2. Nanoparticle synthesis

Goethite: Goethite nanoparticles were synthesized using a modified version of the method from Anschutz and Penn. By peristaltic pump addition, 500 mL of 0.48 M $NaHCO_3$ (Sigma Aldrich) was added to 500 mL of 0.40 M $Fe(NO_3)_3 \cdot 9H_2O$ at a rate of approximately 7 mL/min with constant stirring. The dark brown suspension was transferred to several 250 mL Nalgene bottles, and each bottle was microwaved for a total of 60 s with a pause at 30 s for manual mixing. Boiling was reached within the first 30 s interval for all bottles. The contents of each bottle were combined into a 1 L Nalgene bottle set in an ice bath. When the entire suspension reached 20 °C, the particles were purified by dialysis in Spectra/Por 7 dialysis membrane tubing (MWCO 2,000) and placed in 2 L of Milli-Q water at 5 °C, with water changes three times per day over three days with a minimum of 3 h between each water change. The suspension was transferred to a 1 L Nalgene bottle, adjusted to pH 12 using 5 M NaOH, and aged at 90 °C for 92 h. The resulting orange goethite nanoparticles were cooled and allowed to settle to remove 200 mL of clear supernatant. The nanoparticles were stored as a suspension with known mass loadings in a Nalgene bottle at 5 °C to be delivered by volumetric pipette.

Akaganeite: Akaganeite nanoparticles were synthesized by aging 100 mL of 0.035 M $FeCl_3 \cdot 6H_2O$ in a Teflon-lined hydrothermal bomb (Parr Instrument) at 200 °C for 90 min. After cooling to room temperature, the dark brown suspension was neutralized with 5 M NaOH. The particles were washed three times with Milli-Q water using an Eppendorf 5804 centrifuge at 14000 g for 3 min. After washing and suspending in 50 mL of Milli-Q water, the suspension was adjusted to pH 4.5 with 2 M HCl for storage at 5 °C in a Nalgene bottle with a measured mass loading.

Ferrihydrite: Ferrihydrite nanoparticles were prepared by rapid addition of 11.5 mL of 1 M KOH to a stirring 25 mL solution of 0.20 M $Fe(NO_3)_3 \cdot 9H_2O$ as described in Schwertmann and Cornell. The resulting brown suspension stirred for 20 s and immediately was loaded into dialysis tubing for purification, as described in the goethite synthesis procedure above. Fresh ferrihydrite nanoparticles were prepared after three weeks of storage at 5 °C in Nalgene bottles.

References

Anschutz A. J. and Penn R. L. (2005) Reduction of crystalline iron(III) oxyhydroxides using hydroquinone: Influence of phase and particle size. *Geochem. Trans.* **6**, 60–66.

Schwertmann U. and Cornell R. M. (2000) *Iron Oxides in the Laboratory*. Wiley-VCH, Weinheim. pp. 113–119.

Section D.3. Nanoparticle characterization

Particle composition, size, morphology, and surface area were determined by a combination of X-ray diffraction (XRD), transmission electron microscopy (TEM), and nitrogen sorption analysis (see SI). XRD patterns were collected from 20° to 80° 2θ over a collection time of 50 min using a PANalytical X'Pert Pro X-ray diffractometer with a Co source and X'Celerator detector. Resulting peaks were compared to the corresponding powder diffraction files (PDFs): #29-0713 (goethite), #34-1266 (akaganeite), and #29-0712 (ferrihydrite). TEM grids were prepared by air-drying 1 to 2 drops of a ~10 µg/mL particle suspension on a 3 mm 200 mesh holey carbon coated copper grid (SPI Supplies), and images were obtained with a FEI T12 high-resolution TEM at 120 kV. Particle dimensions for goethite and akaganeite were averaged from measurements of at least 300 particles using Image J (National Institute of Health, 1.47v). Nitrogen sorption was performed using a Quantachrome Autosorb iQ instrument. Samples were outgassed for 12 h at 100 °C to remove surface contaminants prior to analysis. For ferrihydrite, this temperature has been shown to be sufficient in removing contaminants without resulting in phase transformations.[38] XRD analysis of the post-nitrogen sorption ferrihydrite sample confirmed that phase transformation did not occur during sample pretreatment. Total surface area was calculated by the Brunauer-Emmett-Teller (BET) adsorption model from points between 0 and 0.35 P/P_0.

Section D.4. Mass loading experiments

Mass loading experiments performed by delivering a volume (0.1 - 0.5 mL, five volumes total) of the suspension to a weigh boat with known mass then letting them dry at room temperature for 2 d or until the dried mass remained constant. The dried mass was plotted against the delivered volume and fitted with a linear trendline (intercept set at zero) to obtain the mass loading. Accuracy of the mass loading experiments were good (R^2 = 0.98 - 1.0), accomplishing a reactor mass concentration with low error (on average 0.325 g/L ± 0.003 g/L). These measurements were performed frequently, approximately once every 1 - 2 months to account for any evaporation in the solution. As the stock solutions were stored at 5 °C and kept capped, mass loading for each iron oxyhydroxide varied no more than 0.1% per month.

Section D.5. HPLC parameters

The Agilent 1100 series HPLC was equipped with an Agilent Zorbax SB-C18 column (4.6 mm × 150 mm × 5 µm). The mobile phase was an 80:20 mixture of 40 mM acetate buffer at pH 3.75 and acetonitrile, the flow rate was 1.0 mL, and the injection volume was 10 µL, at which benzoquinone and hydroquinone had retention times of 3.9 min and 2.4 min, respectively. Five standards (0.02 to 0.1 mM) for both quinones were prepared by diluting the stock solutions with acetate buffer (there was no significant difference in calibration curves when standards were prepared in acetate buffer with 0 or 0.67 M $CaCl_2$).

Section D.6. Fe(II) adsorption

Suspensions were prepared in 20 mL glass scintillation vials by volumetrically adding nanoparticle suspensions so as to achieve 0.325 g/L in each batch reactor. The vials were then moved into the anaerobic chamber and diluted with deoxygenated 10 mL of water or 0.67 M $CaCl_2$. An aliquot of the Fe(II) stock solution was added to attain 0.342 mM Fe(II) initially. The pH of the suspension was adjusted to cover a range of pH 3 to 7 using 10 mM HCl or NaOH prepared in either water or 0.67 M $CaCl_2$. Water or 0.67 M $CaCl_2$ was then added to bring the final volume to 15 mL. The vials were capped and stirred continuously for 21 h, after which the pH was measured. Approximately 1 mL of the suspension was then sampled using a plastic syringe and filtered. Triplicate cuvettes were prepared such that each contained 3 mL of water or 0.67 M $CaCl_2$, 0.25 mL of 5 mg/mL ferrozine in water and 0.25 mL of the filtered sample. Absorbance values for each sample were measured in triplicate at 562 nm using an Agilent 8453 UV-Vis spectrophotometer. Dissolved Fe(II) concentration was calculated from a five-point calibration curve (0.01 to 0.08 mM Fe(II)). The average dissolved Fe(II) for each sample was compared to the average of two controls that contained no particles to calculate the percent of Fe(II) adsorbed.

To obtain the percent of occupied reactive sites, the number of reactive sites was calculated from TEM surface area and the calculated number of surface sites per unit surface area (goethite: 3.0 nm^{-1} for {110} faces and 7.0 nm^{-1} for end faces, akaganeite[44]: 3.1 nm^{-1} for {100} faces and 3.5 nm^{-1} for {010} faces, and ferrihydrite[45]: 7.2 nm^{-1} for

total surface area) provides a comparison of the fraction of reactive sites occupied by Fe(II) for each iron oxyhydroxide (Figure 5.1d-e).

Goethite: Hiemstra T. and van Riemsdijk W. H. (2007) Adsorption and surface oxidation of Fe(II) on metal (hydr)oxides. *Geochim. Cosmochim. Acta* **71**, 5913–5933.

Ferrihydrite: Hiemstra T. and Van Riemsdijk W. H. (2009) A surface structural model for ferrihydrite I: Sites related to primary charge, molar mass, and mass density. *Geochim. Cosmochim. Acta* **73**, 4423–4436.

Akaganeite: Song X. and Boily J. (2011) Surface hydroxyl identity and reactivity in akaganeite. *J. Phys. Chem. C* **115**, 17036–17045.

Figure D.1: TEM micrographs of synthetic a) goethite, b) akaganeite, and c) ferrihydrite.

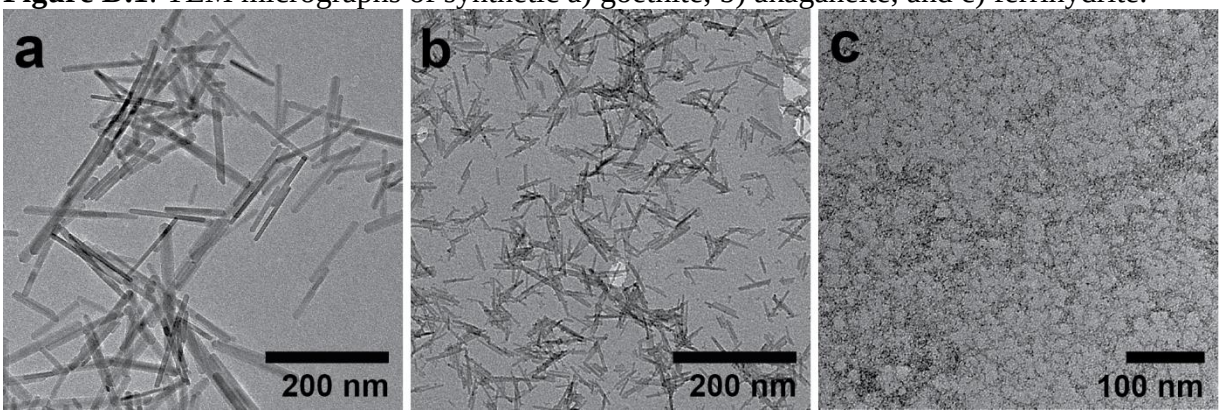

Figure D.2: X-ray diffraction patterns of goethite (Gth), akaganeite (Ak), and ferrihydrite (Fh). I = before reaction, II = after benzoquinone reduction in 0 M $CaCl_2$, III = after benzoquinone reduction in 0.67 M $CaCl_2$, IV = after hydroquinone oxidation in 0 M $CaCl_2$, and V = after hydroquinone oxidation in 0.67 M $CaCl_2$. Sample holder peak indicated by arrow. Based on the amount of Fe(II) oxidized in the benzoquinone reactions, mineral mass could increase up to 5% (well within the detection limit). PDF#s: 29-0713 (Gth), 34-1266 (Ak), 29-0712 (Fh).

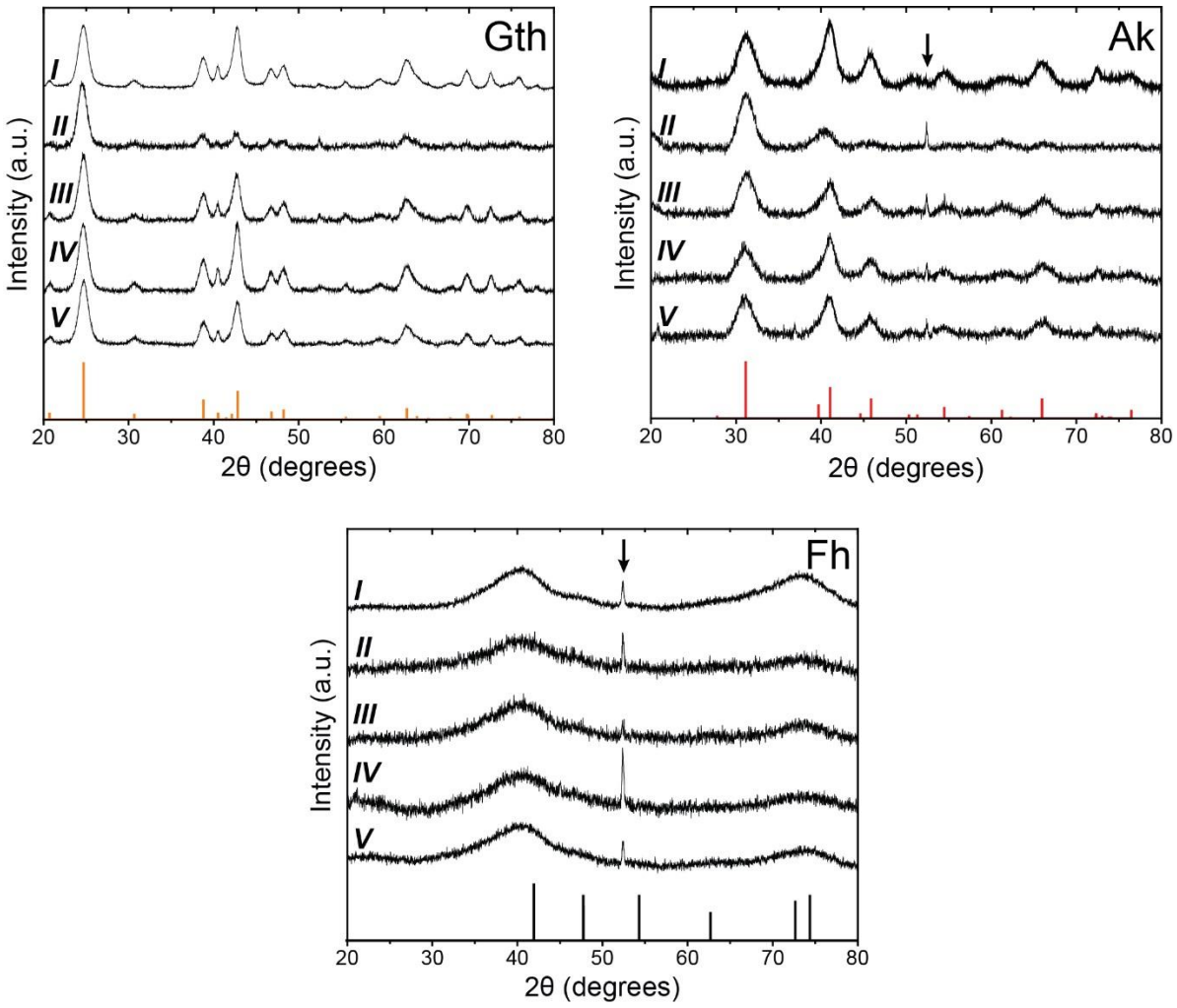

Figure D.3: Benzoquinone (Q) degradation by Fe(II) in solutions containing no nanoparticles and 40 mM acetate buffer at pH 4.5 with initial 0.1 mM benzoquinone and 0.342 mM Fe(II). Open symbols are suspensions prepared with 0 M $CaCl_2$ and closed symbols with 0.67 M $CaCl_2$. Linear regression provided k_{obs} values, with R^2 values in parentheses, of 0.017 ± 0.002 h^{-1} (0.95) and 0.003 ± 0.002 h^{-1} (0.17) for 0 M and 0.67 M $CaCl_2$, respectively.

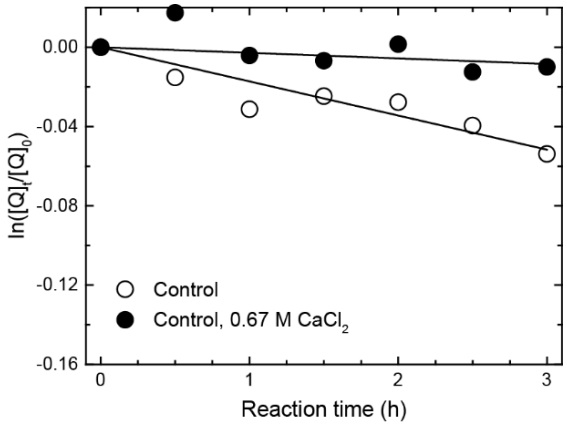

Figure D.4: Benzoquinone (Q) production in solutions containing no nanoparticles and 40 mM acetate buffer at pH 4.5 with an initial hydroquinone concentration of 1 mM. Open symbols are suspensions prepared with 0 M $CaCl_2$ and closed symbols with 0.67 M $CaCl_2$. Linear regression provided d[Q]/dt values, with R^2 values in parentheses, of 0.08 ± 0.16 µM hr^{-1} (-0.12) and -0.34 ± 0.08 µM hr^{-1} (0.69) for 0 M and 0.67 M $CaCl_2$, respectively.

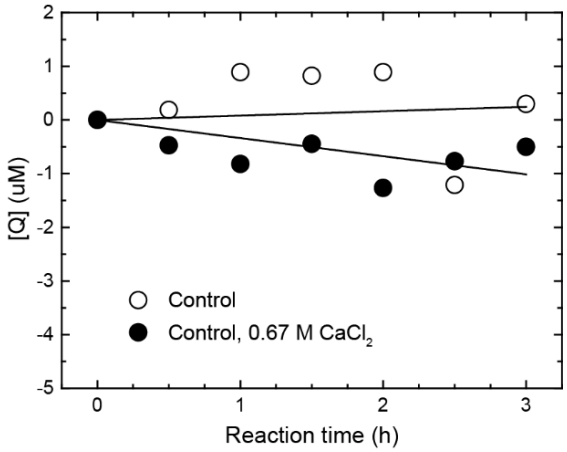

Figure D.5: Benzoquinone (Q) production by goethite (Gth), akaganeite (Ak), and ferrihydrite (Fh) in 40 mM acetate buffer at pH 4.5 and 0.67 M $CaCl_2$ over 32 h.

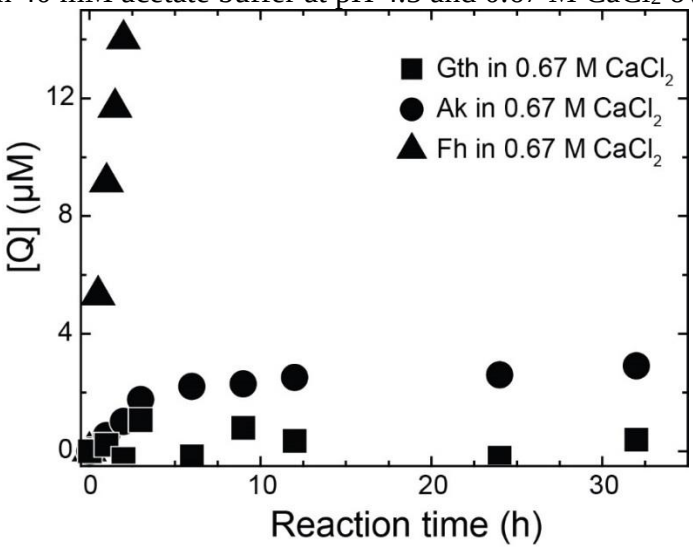

Figure D.6: Log number-based mean hydrodynamic diameter of ferrihydrite as a function of reaction time with hydroquinone as measured using dynamic light scattering. Reaction conditions include 40 mM acetate buffer at pH 4.5, 0 M $CaCl_2$, and 0.1 mM hydroquinone (equivalent to open triangles seen in Figure 5.3b). Each data point was calculated as an average of 5 runs. Outlier runs for each data point were determined either by the quantitative detection limit of 3000 nm or by the Q-test.

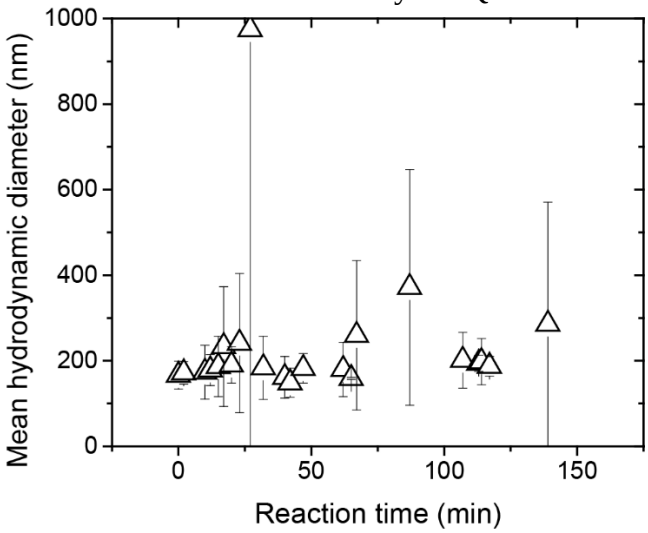

Table D.1: Pseudo-first order reaction rates for benzoquinone reduction by adsorbed Fe(II) on goethite (Gth) and ferrihydrite (Fh) in 40 mM acetate buffer at pH 4.5 and various $CaCl_2$ concentrations. Errors are the 95% confidence intervals.

[$CaCl_2$] (M)	Gth k_{obs} (h^{-1})	Fh k_{obs} (h^{-1})
0	1.02 ± 0.02	0.64 ± 0.09
0.005	0.51 ± 0.01	0.41 ± 0.04
0.02	0.30 ± 0.01	0.24 ± 0.01
0.05	0.18 ± 0.01	0.150 ± 0.005
0.67	0.16 ± 0.02	0.073 ± 0.004

Figure D.7: Benzoquinone (Q) degradation by adsorbed Fe(II) on a mixture of goethite, akaganeite, and ferrihydrite at different mass loadings in 40 mM acetate buffer at pH 4.5. Open symbols are suspensions prepared with 0 M $CaCl_2$ and closed symbols with 0.67 M $CaCl_2$. Total mass loading of the three iron oxyhydroxides was either 0.975 g/L or 0.325 g/L at equal mass ratios.